

The Effect of Flow on the Development and Retention of Iron Sulfide Corrosion Product
Layers

A dissertation presented to
the faculty of
the Russ College of Engineering and Technology of Ohio University

In partial fulfillment
of the requirements for the degree
Doctor of Philosophy

Ezechukwu J. Anyanwu

May 2019

© 2019 Ezechukwu J. Anyanwu. All Rights Reserved.

This dissertation titled
The Effect of Flow on the Development and Retention of Iron Sulfide Corrosion Product
Layers

by

EZECHUKWU J. ANYANWU

has been approved for
the Department of Chemical and Biomolecular Engineering
and the Russ College of Engineering and Technology by

Marc Singer

Associate Professor of Chemical and Biomolecular Engineering

Dennis Irwin

Dean, Russ College of Engineering and Technology

ABSTRACT

ANYANWU EZECHUKWU J., Ph.D., May 2019, Chemical Engineering

The Effect of Flow on the Development and Retention of Iron Sulfide Corrosion Product Layers

Director of Dissertation: Marc Singer

The impact of fluid flow on the mechanical integrity and protectiveness of corrosion product layers formed on the surface of carbon steel pipelines is a crucial aspect of corrosion in CO₂/H₂S environments typically encountered in oil and gas production. Produced fluids may travel inside pipelines at velocities that can generate high shear stresses on the pipe wall. The effect of shear stress on the development of corrosion product layers, and more specifically iron sulfide layers, or the retention of already developed layers is not known. In addition, high fluid velocities generate high mass transfer rates which impact the corrosion behavior of carbon steel substrates. The effect of high mass transfer rates on the characterization of iron sulfide layers is also yet to be fully understood. The goal of this project is to explore ways to identify the individual contributing effects of wall shear stress and mass transfer rate to the development and retention of iron sulfide layers in representative flow conditions and relate this to the corrosion behavior of a carbon steel substrate. This will help characterize the protectiveness, or lack thereof, of FeS layers and enable the selection of appropriate asset integrity management program.

The first part of this project focused on the development of experimental test setups, the glass cell with impeller flow and the channel cell in the single-phase flow

loop, which enable representative flow conditions and control of water chemistry. The flow in these systems was characterized using electrochemical methods by developing a Sherwood correlation. The associated shear stress impacting the specimen surface was also characterized through computational fluid dynamics (CFD) techniques. The developed mass transfer correlations were used to model the experimentally determined corrosion rate results successfully.

In the next part of this project, the glass cell with an impeller flow experimental setup was used to study the role of the iron carbide network, in a ferritic/pearlitic UNS G10180 carbon steel, on the development of iron sulfide layers. This was done by comparing the morphologies of the FeS layers formed on 99.9% pure Fe and UNS G10180 when these substrates were exposed to 1 wt.% NaCl solution sparged with 10% H₂S in a mixture with N₂, at 30°C and pH 5.00 and pH 6.00. The major findings from this study was the preferential precipitation of iron sulfides within and on top of the iron carbide matrix, especially in environments promoting the exposure of iron carbides (low FeS saturation conditions). The presence of iron carbides in UNS G10180 carbon steel also favored the attachment of the iron sulfide layers to the steel substrate surface.

The third part of this project focused on the study of the effect of flow on the development and retention of iron sulfide layers by exposing UNS G10180 and 99.9% pure Fe to different flow environments in the channel flow of the single-phase flow loop (SPFL) with test conditions similar to those of the glass cell test at pH 6.00. The result showed that iron sulfide layers could still form at any velocity tested. Experiment performed in CO₂ environment showed that the formation of FeCO₃ was impeded at high

flow velocities due to the shear stress related mechanical removal of the iron carbide residues. This was not the case for iron sulfide. The retention experiments revealed that this shear stress was not enough to remove an already developed iron sulfide layer. This study also revealed that the undermining corrosion was more pronounced at high velocity (due to higher mass transfer rates) and in the presence of the iron carbide corrosion product residues.

Finally, the mechanical properties of the mackinawite layers formed both in low and high flow conditions were characterized by conducted indentation measurements, for the hardness of the layers and scratch adhesion test, for the interfacial shear strength of the layers. All the measured values of interfacial shear stress were of the order of hundreds of MPa, at least five order of magnitude higher than the typical shear stress generated by fluid flow in a pipeline. The presence of iron carbide corrosion product residues increased hardness of the mackinawite layers by an average of 229.67%. Indentation results also showed that the hardness of the mackinawite layers formed in high flow velocity increased by an average of 35.3%. In addition, the mackinawite layer formed in low flow conditions possessed an interfacial shear strength three times lower than those obtained at high flow conditions. With the measurement of lower interfacial shear strength of mackinawite on substrates that showed higher undermining corrosion at the respective flow velocities, this study has highlighted the importance of attachment to the overall protective behavior of the FeS layer.

DEDICATION

This work is dedicated to

My loving parents Sir. Hyacinth Anyanwu and Dr. Lady Augustina Anyanwu,

my loving wife, Chinenye

my adorable son, Chiduterem Anyanwu

and other family members

for their continued love and support

ACKNOWLEDGMENTS

I would like to express my sincere thanks to my advisor, Prof. Marc Singer for his guidance during my Ph.D. Studies. He has maintained a high level of commitment and dedication throughout the period of my research and this has in turn kept me motivated. I believe that my understanding and ability to critically analyze and apply engineering concepts, especially in the field of corrosion science and technology, have greatly improved from my constant interaction with him.

I would like to appreciate my family for their tremendous support during this long journey. To my parents, your constant prayer and undying love has been the source of my strength through these years. To my beloved brothers, I am truly grateful for your all round support. Knowing that I can count on you two for anything gave me that peace of mind that I needed to concentrate. To my loving sisters, thank you so much for caring and looking out for me even from far away. To the Aririeri and Anunne family, thank you for showing so much love to myself and my family. To my nephews, nieces, brothers in-law, sisters in-law and parents in-law, thank you so much for making the family a big and happy one.

My sincere appreciation goes to my project leader Dr. Bruce Brown for being so patient and willing to help during my period of conducting experiment, and also to Al Schubert and Cody Shafer for their help in the developing my experiment setups.

I am grateful to Dr. David Young for his immense help at critical times during my studies. Through your humor and constant assistance you have made my period in the Institute for Corrosion and Multiphase Technology (ICMT) a memorable one.

I am also grateful to Prof. Srdjan Nesic (ICMT Director), Dr. Katherine Cimat, Dr. John Staser, Dr. Dina Lopez for their contributions to my research and for agreeing to serve in my graduate committee.

I would also like to express my sincere gratitude to the people who were my buddy during the time I conducted my experiments in the H₂S room, Juan Dominguez, Shujun Gao, Alexis Barxias, Cody Shafer and Martin Colahan.

Great thanks go to the people at ICMT for creating such a wonderful working environment. I especially acknowledge Becky Gill, Claudia Prietto, Zheng Ma, and Dr. Tuba Unsal.

Finally, I would like to thank my loving wife Chinenye and my adorable son Chiduterem for giving me so much joy and happiness.

Most importantly, I give glory to God Almighty for with him I was able to accomplish this.

TABLE OF CONTENTS

	Page
Abstract.....	3
Dedication	6
Acknowledgments	7
List of Tables.....	12
List of Figures	14
Chapter 1: Introduction.....	26
Chapter 2: Literature Review	30
2.1 Solution Chemistry.....	31
2.2 Electrochemical Reaction Mechanisms.....	34
2.3 Formation of Iron Sulfide Corrosion Product Layer.....	37
2.4 Physicochemical Properties of Iron Sulfide Phases	40
2.5 Effects of Flow on Development and Retention of Iron Sulfide Layers.....	44
2.5.1 Effect of Mass Transfer	45
2.5.2 Mechanical Effects	48
Chapter 3: Research Objectives	51
3.1 Knowledge Gaps.....	51
3.1 Objectives and Hypotheses.....	52
3.2 Test Methodology and Safety.....	53
Chapter 4: Development and Characterization of Experimental Setups	57
4.1 Introduction and Research Goal.....	57
4.2 Description of Glass Cell with Impeller Setup.....	61
4.2.1 Mass Transfer Characterization of Glass Cell with Impeller.....	65
4.2.2 Shear Stress Calculation on the Specimen Surface.....	74
4.2.3 Development of Iron Sulfide Layers in Controlled Solution Chemistry...88	88
4.3 The Single-Phase Flow Loop.....	98
4.3.1 Mass Transfer in the Single-Phase Flow Loop.	101
4.3.2 Channel Flow Simulation and Wall Shear Stress Calculations	102
4.4 Summary.....	108
Chapter 5: Impact of Iron Carbide on Iron Sulfide Layer Development.....	110
5.1 Introduction and Research Goal.....	110

5.2	Experimental Setup and Methodology	113
5.2.1	Equipment	113
5.2.2	Material Preparation and Microstructure Analysis	114
5.2.3	Test Methodology and Procedure	115
5.2.4	Test Matrix.....	116
5.3	Results and Discussion	116
5.3.1	Microstructure of Test Specimens.....	116
5.3.2	Iron Sulfide Layer Development in Environment Promoting Fe ₃ C Formation (pH 5.00)	117
5.3.3	Iron Sulfide Layer Development under High FeS Saturation (pH 6.00).128	
5.4	Proposed Mechanism for FeS Development	143
5.4.1	FeS Development on UNS G10180 Substrate	143
5.4.2	FeS Development on 99.9% Pure Fe Substrate	145
5.5	Summary.....	146
Chapter 6: Effect of Flow on the Development and retention of Iron Sulfide Layers		147
6.1	Introduction and Research Goal.....	147
6.2	Experimental Setup and Methodology	149
6.2.1	Equipment	149
6.2.2	Material.....	150
6.2.3	Test Methodology and Procedure	150
6.2.4	Test Matrix.....	152
6.3	Results and Discussion	154
6.3.1	Development of Iron Sulfide Layer on UNS G10180 Substrate	157
6.3.2	Development of Iron Sulfide Layer on 99.9% Pure Fe Substrate.....	172
6.3.3	Retention of iron sulfide layer on UNS G10180.....	181
6.4	Summary.....	185
Chapter 7: Characterization of the Mechanical Properties of Iron Sulfide Layers		186
7.1	Introduction and Research Goal.....	186
7.1.1	Indentation Measurement	187
7.1.2	Scratch Testing.....	189
7.2	Experimental Methods	195
7.2.1	Equipment for Iron Sulfide Layer Development	195
7.2.2	Equipment for Mechanical Testing of Iron Sulfide layers	196

7.2.3	Materials Test.....	196
7.2.4	Procedure for the Mechanical Testing of the Developed Iron Sulfide Layers	197
7.3	Results and Discussion	197
7.3.1	Effect of Temperature on the Mechanical Properties of Iron Sulfide Layers	199
7.3.2	Effect of Substrate material on the Mechanical Properties of Iron Sulfide Layers Formed in Low Flow Conditions	225
7.3.3	Effect of Substrate on the Mechanical Properties of Layers Developed in High flow conditions.....	234
7.4	Conclusions.....	240
Chapter 8: Conclusions and Future Work.....		241
8.1.	Conclusions.....	241
8.2.	Future Work.....	243
References.....		245
Appendix A: Development of Iron Sulfide Layer in a 2-Liter Glass Cell Without Solution Chemistry Control		267
Appendix B: Characterization of the Mechanical Strength of Mackinawite Layers in the Presence of Other Iron Sulfide Phases.....		277
Appendix C: Modelling of Corrosion Rates		286

LIST OF TABLES

	Page
Table I: Different expressions for FeS precipitation reaction and the corresponding equations for FeS saturation.....	39
Table II: Summary of the physicochemical properties of different iron sulfide phases[31,82]	42
Table III: Mesh properties and statistics	78
Table IV: Test matrix for the development of Iron Sulfide Layers in Controlled Solution Chemistry	89
Table V: Chemical composition of the UNS G10180 mild steel specimens	114
Table VI: Test Matrix for studying the impact of iron carbide on iron sulfide layer development	116
Table VII: Test Matrix for the study of the effect of flow on the development of iron sulfide on UNS G10180 steel and 99.9% pure Fe.....	152
Table VIII: Test Matrix for the study of the effect of flow on the retention of iron sulfide on UNS G10180 and 99.9% pure Fe	153
Table IX: Failure modes from layer and substrate hardness[158]	193
Table X: Summary of measured hardness of UNS G10180 from indentation tests using a Vickers indenter	198
Table XI: Summary of measured hardness of mackinawite layer formed on UNS G10180 exposed to 1 wt.% solution at pH 6.00, 0.1bar of H ₂ S, 30°C, and 250rpm impeller rotation speed from from indentation tests using a Vickers indenter	202
Table XII: Summary of results obtained for mechanical characterization of mackinawite layer formed on UNSG 1018 is exposed to a solution sparged, pH 6.0 and impeller speed of 250 rpm.....	211
Table XIII: Summary of measured hardness of mackinawite layer formed on UNS G10180 exposed to 1 wt.% solution at pH 6.0, 80°C, and 250rpm impeller rotation speed from indentation tests using a Vickers indenter	214
Table XIV: Summary of results obtained for mechanical characterization of mackinawite layer formed on UNS G1018 exposed to a solution sparged with 10%H ₂ S/N ₂ at 80°C, pH 6.00 and impeller speed of 250rpm	223
Table XV: Summary of measured hardness of mackinawite layer formed on 99.9% pure Fe exposed to 1 wt.% solution at pH 6.0, 0.1bar H ₂ S 30°C, and 250rpm impeller rotation speed from from indentation tests using a Vickers indenter.....	227
Table XVI: Summary of results obtained for mechanical characterization of mackinawite layer formed on UNSG 1018 and 99.9% pure Fe after 3 days exposure to 1 wt. % NaCl	

solution at 30°C, pH 6.0, 0.1bar H ₂ S and 250rpm impeller rotational speed of 250 rpm.	233
Table XVII: Summary of measured hardness of mackinawite layer formed on UNS G10180 and 99.9% pure Fe after 4 days exposure to 1 wt.% solution at pH 6.0, 30°C, 0.1bar H ₂ S and 10.4m/s fluid velocity.....	235
Table XVIII: Summary of results obtained for mechanical characterization of mackinawite layer formed on UNSG 1018 and 99.9% pure Fe after 3 days exposure to 1 wt. % NaCl solution at 30°C, pH 6.0, 0.1bar H ₂ S and 10.4m/s.....	239
Table XIX: Chemical composition in wt.% of the selected API 5L X65 mild steel.....	268
Table XX: Test conditions for the glass cell experiment	269
Table XXI: Test conditions for the development of an iron sulfide layer in the 7L Hastelloy autoclave	278

LIST OF FIGURES

	Page
Figure 1: Change in equilibrium concentration of sulfide species with respect to pH in an open system at H ₂ S partial pressure of 0.1bar and temperature of 30°C.....	33
Figure 2: Change in equilibrium concentration of sulfide species with respect to pH in a closed system at H ₂ S partial pressure of 0.1bar and a temperature of 30°C at a gas to liquid volume ratio of 1:1	34
Figure 3: Schematic representation of the different resistances to mass transfer of species from the bulk to the substrate surface in the presence of a corrosion product layers[38].	46
Figure 4: Glass cell with specimen holders, impeller assembly and water chemistry control system	61
Figure 5: Top view of glass cell showing the concentric arrangement of specimens and the Rushton 6 impeller.....	62
Figure 6: Resin consisting of a sulphonated polystyrene structural moiety and a mobile cation.....	64
Figure 7: Polarization curves at impeller rotational speed ranging from 50-250rpm at electrolyte solution of (a.) 30°C (b.) 40°C (c.) 50°C.....	68
Figure 8: A straight line fit of the mass transfer correlation developed for the impeller flow in the glass cell	70
Figure 9: Impeller rotational speed in glass cell vs linear velocity in 0.2m diameter pipe at equal mass transfer coefficient.....	71
Figure 10: Comparison of the modelled potentiodynamic sweep with the curve from the cathodic polarization of 99.9% pure Fe in 1 bar N ₂ , pH 5.0, 30°C and 250 rpm impeller velocity.....	74
Figure 11: Glass cell geometry designed in Solidworks showing the Stator, specimen holder and rotor domain.....	76
Figure 12: Meshing of the glass with impeller system into discrete cells (a.) stator domain (b.) rotor and specimen holder domains	77
Figure 13: Velocity vectors of water in glass at temperature of 30°C and impeller rotational speed of (a.) 250rpm and (b.) 50rpm	82
Figure 14: Velocity contours of water in glass at temperature of 30°C and impeller rotational speed of (a.) 250rpm and (b.) 50rpm	83
Figure 15: Wall shear stress at specimen location resulting from fluid flow at impeller rotational speeds of (a.) 250rpm and (b.) 50rpm.....	84
Figure 16: (a.) Wall shear stress obtained from CFD simulation of glass cell with a rotating impeller (b.) Calculated shear stress in a 0.2m diameter pipe at equivalent velocity.....	85

Figure 17: Glass cell arrangement with installed floating element probe for the direct measurement of shear stress at the specimen location.....	86
Figure 18: Wall shear stress from direct measurements at impeller rotational speed of 250rpm using the floating element probe installed on the specimen location.	87
Figure 19: Comparison of wall shear stress at different impeller rotational speed obtained from CFD simulation and direct measurement.	88
Figure 20: Solution pH and Fe^{2+} concentration during a 4-day exposure of 99.9% pure Fe in solution saturated with 10% by volume of H_2S at pH of 5, 30°C and impeller rotational speed of (a.) 50rpm and (b.) 250rpm	89
Figure 21: Comparison of measured corrosion rates of pure Fe with predicted values at impeller rotational speed of 50rpm and 250rpm in solution at pH 6.0, temperature of 30°C, and 10% vol. of H_2S in a mixture with nitrogen	91
Figure 22: Comparison of corrosion rate measurements using LPR and weight loss methods.	92
Figure 23: Surface SEM/EDS of FeS layer formed on 99.9% pure Fe at 30°C, 0.1bar of H_2S and 50rpm impeller rotational speed (a.) 1 day (b) 3 days (c) 4 days	93
Figure 24: Surface SEM/EDS of the FeS layer formed on 99.9% pure Fe specimen exposed to a solution sparged with 10 vol.% H_2S/N_2 at pH 6.00, 30°C, and 50rpm impeller rotational speed for(a.) 1 day (b) 3 days (c) 4 days	93
Figure 25: Cross-section of the FeS layer formed on 99.9% pure Fe specimen exposed to a solution sparged with 10 vol.% H_2S/N_2 at pH 6.00, 30°C, and 50rpm impeller rotational speed for(a.) 1 day (b) 3 days (c) 4 days.....	94
Figure 26: Cross section of the FeS layer formed on 99.9% pure Fe specimen exposed to a solution sparged with 10 vol.% H_2S/N_2 at pH 6.0, 30°C, and 250rpm impeller rotational speed for(a.) 1 day (b) 3 days (c) 4 days.....	94
Figure 27: Thickness of corrosion product layer formed on 99.9% pure Fe in 1%. wt. NaCl solution at 30°C, 0.1bar of H_2S and 50rpm after day 1, day 3 and day 4.....	95
Figure 28: Thickness of corrosion product layer formed on 99.9% pure Fe in 1%. wt. NaCl solution at 30°C, 0.1bar of H_2S and 250rpm after day 1, day 3 and day 4.....	96
Figure 29: Nyquist plots for 99.9% pure Fe exposed to 1 wt. %. NaCl solution at 30°C, 0.1bar of H_2S and 50rpm after day 0 (1hr), day 1, day 2, day 3 and day 4	97
Figure 30: Nyquist plots for 99.9% pure Fe exposed to 1 wt. %. NaCl solution at 30°C, 0.1bar of H_2S and 250rpm after day 0 (1hr), day 1, day 2, day 3 and day 4	97
Figure 31: Single phase flow loop system showing the solution conditioning section, channel flow test section, autoclave.	99
Figure 32: Diagram of the channel flow test cell showing the location of the reference electrode, working electrode, weight loss specimen, channel and the flow direction (a.) Schematic of the external body (b.) Schematic of the internal body.....	100

Figure 33: Assembly of the test cell showing the modified fluid entry region which ensures the removal of the flow entry region.....	101
Figure 34: Comparison of mass transfer coefficient of H ₂ S in a fully turbulent channel using Sherwood correlations from different authors	102
Figure 35: Geometry of the channel cell showing the flow entry region, the channel region (housing the test cell) and flow exit region.....	103
Figure 36: Meshing of channel cell into discrete elements	104
Figure 37: Velocity profile of the channel region at the lowest flow capacity (V = 1.1m/s, Re = 2614) of the single-phase flow loop.....	105
Figure 38: Velocity profile of the channel region at the highest flow capacity (V = 10.4m/s, Re = 24216) of the single-phase flow loop.....	106
Figure 39: Contours of wall shear stress generated by a fully turbulent flow in the channel region at (a.) fluid velocity of 1.1m/s and (b.) fluid velocity of 10.4m/s	107
Figure 40: Comparison of wall shear obtained from the Patel and Dean friction factors with wall shear stress calculation from CFD simulations.....	108
Figure 41: Microstructure of (a.) 99.9% pure Fe substrate (b.) UNS G10180 substrate, revealed after etching in 5% Nital solution, showing phases and grain boundaries.	117
Figure 42: Bulk solution pH and ferrous ion concentration during the corrosion experiment in 1 wt.% NaCl solution, at pH 5.00, and for 0.1bar of H ₂ S at system temperature of 30°C and impeller rotational speed of 250rpm (a.) 99.9% pure Fe substrate and (b.) UNS G10180.....	118
Figure 43: Bulk FeS saturation during corrosion experiment in 1 wt.% NaCl solution, at pH 5.00, and for 0.1bar of H ₂ S at system temperature of 30°C and impeller rotational speed of 250rpm (a.) 99.9% pure Fe substrate and (b.) UNS G10180.....	118
Figure 44: Weight loss corrosion rates of 99.9% pure Fe and UNS G10180 in 1 wt.% NaCl solution, at pH 5.00, for 0.1 bar of H ₂ S, 30°C and impeller rotational speed of 250rpm.....	119
Figure 45: LPR corrosion rate measurements of 99.9% pure Fe and UNS G10180, in 1 wt.% NaCl solution, at pH 5.00, for 0.1 bar of H ₂ S, 30°C and impeller rotational speed of 250rpm.....	120
Figure 46: Open circuit potential (vs. Ag/AgCl) of 99.9% pure Fe and UNS G10180 in 1 wt.% NaCl solution, at pH 5.00, for 0.1 bar of H ₂ S, 30°C and impeller rotational speed of 250rpm.....	121
Figure 47: Cross-section of FeS layer formed after 1 day exposure in 1 wt.% NaCl solution at 30°C, at pH 5.00, for 0.1bar of H ₂ S and 250rpm impeller rotational speed (a.) 99.9% pure Fe substrate (b) UNS G10180 substrate.....	122
Figure 48: Cross-section of FeS layer formed after 3 days exposure in 1 wt.% NaCl solution at 30°C, at pH 5.00, for 0.1bar of H ₂ S and 250rpm impeller rotational speed (a.) 99.9% pure Fe substrate (b) UNS G10180 substrate.....	122

Figure 49: Cross-section of FeS layer formed after 4 days exposure in 1 wt.% NaCl solution at 30°C, at pH 5.00, for 0.1bar of H ₂ S and 250rpm impeller rotational speed (a.) 99.9% pure Fe substrate (b) UNS G10180 substrate.....	123
Figure 50: EDS mapping of FeS layer formed on 99.9% pure Fe substrate after a 4 days exposure period in 1 wt.% NaCl solution, at pH 5.00, at 30°C, for 0.1bar of H ₂ S and 250rpm impeller rotational speed.....	124
Figure 51: EDS mapping of FeS layer formed on UNS G1018 substrate after 4-day exposure period in 1 wt.% NaCl solution, at pH 5.00, at 30°C, for 0.1bar of H ₂ S and 250rpm impeller rotational speed.....	125
Figure 52: SEMs and XRD analyses of corrosion product layers formed on (a.) 99.9% pure Fe and (b.) UNS G10180 after a 4 day exposure in 1 wt. % NaCl solution, at pH 5.00, and for 0.1bar of H ₂ S at a system temperature of 30°C and impeller rotational speed of 250rpm.....	126
Figure 53: Fraction of corroded Fe in the FeS layer after exposure of 99.9% pure Fe and UNS G10180 substrates to 1 wt.% NaCl solution, at pH 5.00, and for 0.1bar of H ₂ S at system temperature of 30°C and impeller rotational speed of 250rpm.	127
Figure 54: Bulk solution pH and ferrous ion concentration during corrosion experiments in 1 wt. % NaCl solution, a pH 6.00, and for 0.1bar of H ₂ S at system temperature of 30°C and impeller rotational speed of 250rpm (a.) 99.9% pure Fe substrate and (b.) UNS G10180.....	129
Figure 55: Bulk FeS saturation during corrosion experiment in 1 wt.% NaCl solution, at pH 6.00, and for 0.1bar of H ₂ S at system temperature of 30°C and impeller rotational speed of 250rpm (a.) 99.9% pure Fe substrate and (b.) UNS G10180.....	130
Figure 56: Weight loss corrosion rates of 99.9% pure Fe, and UNS G10180, in 1 wt.% NaCl solution, at pH 6.00, for 0.1 bar of H ₂ S, 30°C and impeller rotational speed of 250rpm.....	130
Figure 57: Open circuit potential (vs. Ag/AgCl) of 99.9% pure Fe, and UNS G10180, in 1 wt.% NaCl solution, at pH 6.00, for 0.1 bar of H ₂ S, 30°C and impeller rotational speed of 250rpm.....	131
Figure 58: LPR corrosion rate measurements of 99.9% pure Fe and UNS G10180, in 1 wt.% NaCl solution, at pH 6.00, for 0.1 bar of H ₂ S, 30°C and impeller rotational speed of 250rpm.....	132
Figure 59: Cross-section of FeS layer formed after 1-day exposure in 1 wt.% NaCl solution at 30°C, at pH 6.00, for 0.1bar of H ₂ S and 250rpm impeller rotational speed (a.) 99.9% pure Fe substrate (b) UNS G10180 substrate.....	133
Figure 60: Cross-section of FeS layer formed after 3 days exposure in 1 wt.% NaCl solution at 30°C, at pH 6.00, for 0.1bar of H ₂ S and 250rpm impeller rotational speed (a.) 99.9% pure Fe substrate (b) UNS G10180 substrate.....	133

Figure 61: Cross-section of FeS layer formed after 4 days exposure in 1 wt. % NaCl solution at 30°C, at pH 6.00, for 0.1bar of H ₂ S and 250rpm impeller rotational speed (a.) 99.9% pure Fe substrate (b) UNS G1018 substrate.....	134
Figure 62: EDS mapping of FeS layer formed on 99.9% pure Fe substrate after 4-day exposure in 1 wt.% NaCl solution at 30°C, at pH 6.00, and 0.1bar of H ₂ S and 250rpm impeller rotational speed.....	135
Figure 63:EDS mapping of FeS layer formed on UNS G10180 substrate after 4-day exposure in 1 wt.% NaCl solution at 30°C, at pH 6.00, and 0.1bar of H ₂ S and 250rpm impeller rotational speed.....	136
Figure 64: EDS spot analysis of the layer at different locations on the UNS G10180 substrate after 4 days exposure period in 1 wt.% NaCl solution at 30°C, pH 6.00, 0.1bar of H ₂ S and 250rpm impeller rotational speed (a.) outside the pearlite region (b.) in the pearlite region.....	137
Figure 65: Surface SEM images of FeS layer formed on 99.9% pure Fe substrate exposed to 1 wt.% NaCl solution at 30°C, pH 6.00, 0.1bar of H ₂ S and 250rpm impeller rotational speed after (a.) 1 day, (b.) 3 days and (c.) 4 days.....	138
Figure 66: Surface SEM images of FeS layer formed on UNS G10180 exposed to 1 wt.% NaCl solution at 30°C, pH 6.00, 0.1bar of H ₂ S and 250rpm impeller rotational speed after (a.) 1 day, (b.) 3 days and (c.) 4 days	138
Figure 67: XRD analyses of corrosion product layers formed on (a.) 99.9% pure Fe and (b.) UNS G10180 after 4 days exposure in 1 wt.% NaCl solution, pH 6.00, and 0.1 bar of H ₂ S at system temperature of 30°C and impeller rotational speed of 250rpm	139
Figure 68: Fraction of corroded Fe in the FeS layer after exposure of 99.9% pure Fe and UNS G10180 substrates to 1 wt.% NaCl solution, pH 6.00, and 0.1bar of H ₂ S at system temperature of 30°C and impeller rotational speed of 250rpm.	140
Figure 69: Topography of 99.9% pure Fe surface after removing the corrosion product layer with Clarke solution after exposure times of (a.) 1 day (b.) 3 days and (c.) 4 days.	141
Figure 70: Topography of UNS G10180 surface after removing the corrosion product layer with Clarke solution after exposure times of (a.) 1 day (b.) 3 days and (c.) 4 days.	141
Figure 71: Topography of the UNS G10180 surface after removing the corrosion product layer with Clarke solution after 4 days (Repeat experiment).....	142
Figure 72: Fluid velocities and sample exposure times for FeS retention experiment on UNS G10180 substrates.....	154
Figure 73: Modelled anodic and cathodic potentiodynamic curves for 10% vol. H ₂ S/N ₂ at pH 6.00, 30°C and flow velocity of 1.1m/s	156
Figure 74: Modelled anodic and cathodic potentiodynamic curves for 10% vol. H ₂ S/N ₂ at pH 6.00, 30°C and flow velocity of 10.4m/s	156

Figure 75: Corrosion rate trend of UNS G10180 during a 4 days exposure to 1 wt.% NaCl solution sparged with a 10% vol. H ₂ S in admixture with nitrogen at pH 6.0, 30°C and flow velocities of 1.1 m/s and 10.4 m/s	158
Figure 76: Corrosion rate measurement by weight loss compared with time-averaged corrosion rates from LPR measurement after 4 days exposure of UNS G10180 to 1 wt.% NaCl solution sparged with 10% vol. H ₂ S in admixture with nitrogen at pH 6.0, 30°C and flow velocities of 1.1m/s and 10.4m/s	159
Figure 77: Surface SEM and cross section analysis of corrosion product layers developed after 4 days exposure to 1 wt.% NaCl solution sparged with 10% H ₂ S in a mixture with N ₂ at pH of 6.00, 30°C and flow velocity of 1.1m/s and 10.4m/s	161
Figure 78: Effect of layer porosity on the total mass transfer coefficient of H ₂ S from the bulk through the layer to the specimen surface at equal layer thickness	162
Figure 79: EDS maps detecting iron and sulfur in the corrosion product layers developed after 4 days exposure to 1wt.% NaCl solution sparged with 10% H ₂ S in admixture with N ₂ at pH of 6.00, 30°C and flow velocity of 1.1m/s and 10.4m/s	165
Figure 80: XRD analysis of iron sulfide layers developed on UNSG 10180 mild steel specimens after 4 days of exposure to 1 wt.% NaCl solution sparged with a 10% vol. H ₂ S in admixture with N ₂ at pH 6.00, 30°C and flow velocities of (a.) 1.1 m/s and (b.) 10.4m/s	166
Figure 81: Moles of Fe corroded compared with moles of Fe precipitated (Fe in FeS layers) after exposure of UNS G10180 mild steel substrates to 1 wt.% NaCl solution, at pH 6.00, and 0.1bar of H ₂ S at 30°C and flow velocities of 1.1 m/s and 10.4m/s	168
Figure 82: Fraction of corroded Fe in the FeS layers after exposure of UNS G10180 mild steel substrates to 1 wt.% NaCl solution, at pH 6.0, and 0.1bar of H ₂ S at 30°C and flow velocities of 1.1 m/s and 10.4m/s	168
Figure 83: Level of steel surface before corrosion, with FeS layer and after removal of FeS layer developed after exposure of UNS G10180 to 1 wt.% NaCl solution at pH 6.0, and 0.1bar of H ₂ S at 30°C and flow velocities of 1.1 m/s and 10.4m/s	169
Figure 84: Specimen surface with FeS layer and the mapped specimen surface after the removal of the mackinawite layer formed after exposure of UNS G10180 to 1 wt.% NaCl solution at pH 6.0, and 0.1bar of H ₂ S at 30°C and flow velocities of 1.1 m/s and 10.4m/s	170
Figure 85: Corrosion rate trend of 99.9% pure Fe during a 4 days exposure to 1 wt.% NaCl solution sparged with a 10% vol. H ₂ S in admixture with N ₂ at pH 6.00, 30°C and flow velocities of 1.1 m/s and 10.4 m/s	172
Figure 86: Corrosion rate measurement by weight loss compared with time averaged corrosion rates from LPR measurement after 4 day exposure of 99.9% pure Fe to 1 wt.% NaCl solution sparged with a 10% vol. H ₂ S in admixture with N ₂ at pH 6.00, 30°C and flow velocities of 1.1 m/s and 10.4 m/s	173

Figure 87: Surface SEM and cross-section analyses of corrosion product layers developed on 99.9% pure Fe after 4 days of exposure to 1 wt.% NaCl solution sparged with 10% H ₂ S in admixture with N ₂ at pH of 6.00, 30°C and flow velocity of 1.1m/s and 10.4m/s	174
Figure 88: EDS maps detecting iron and sulfur in the corrosion product layers developed after a 4 day exposure of 99.9% pure Fe to 1wt.% NaCl solution sparged with 10% H ₂ S in admixture with N ₂ at pH 6.00, 30°C and flow velocity of 1.1m/s and 10.4m/s	176
Figure 89: Moles of Fe corroded compared with moles of Fe precipitated (Fe in FeS layers) after exposure of 99.9% pure Fe substrates to 1 wt. % NaCl solution, pH 6.0, and 0.1bar of H ₂ S at 30°C and flow velocities of 1.1 m/s and 10.4m/s.....	177
Figure 90: Fraction of corroded Fe in the FeS layers after exposure of 99.9% pure Fe substrates to 1 wt. % NaCl solution, at pH 6.0, and 0.1bar of H ₂ S at 30°C and flow velocities of 1.1 m/s and 10.4m/s	177
Figure 91: Level of steel surface before corrosion, with FeS layer and after removal of FeS layer developed after exposure of 99.9% pure Fe to 1 wt.% NaCl solution at pH 6.00, and 0.1bar of H ₂ S at 30°C and flow velocities of 1.1 m/s and 10.4 m/s	179
Figure 92: Specimen surface with FeS layer and the mapped specimen surface after the removal of the mackinawite layer formed after exposure of 99.9% pure Fe to 1 wt.% NaCl solution at pH 6.00, and 0.1bar of H ₂ S at 30°C and flow velocities of 1.1 m/s and 10m/s.....	179
Figure 93: Corrosion rate trend of the retention test of iron sulfide layer developed on UNS G10180 during a 4-day exposure to 1 wt.% NaCl solution sparged with a 10% vol. H ₂ S in admixture with N ₂ at pH 6.00, 30°C and initial flow velocities of 1.1 m/s	181
Figure 94: Surface SEM and cross-section analyses of FeS layers after the retention experiment.....	182
Figure 95: EDS analysis of corrosion product layer after the retention experiment confirming the formation of iron sulfide	183
Figure 96: Specimen with FeS layer (a.) and profilometry (b.) of its surface after the removal of the mackinawite layer formed in the FeS retention experiment.	184
Figure 97: A typical loading and unloading curve from an indentation test[148]	188
Figure 98: A schematic of a Vickers indenter tip with dimensions	189
Figure 99: Schematics of different types of cohesive failure (a.) chevron cracks (b.) arc tensile cracks (c.) hertzian cracks (d.) conformal cracks (design idea courtesy of Claudia Prietto)	191
Figure 100: Schematics of different types of cohesive failure (a.) buckling cracks (b.) wedging spallation (c.) recovery spallation (d.) gross spallation (design idea courtesy of Claudia Prietto)	192
Figure 101: Schematics of the forces and dimensions associated with an indenter tip in contact with a surface during a scratch test.....	193

Figure 102: Tip geometry for (a.) Conical, (b.) Berkovich and (c.) Vickers indenter [11]	196
Figure 103: Loading and unloading curve from hardness measurements on (a.) a bare UNS G-10180 carbon steel and (b.) a bare 99.9% pure Fe.....	198
Figure 104: Surface SEM of FeS layer developed on UNS G10180 immersed in 1%. wt. NaCl solution at 30 ⁰ C, pH 6.0, 0.1bar of H ₂ S and 250rpm impeller speed (a.) 1 day exposure (b.) 3 days exposure.....	199
Figure 105: Cross section of FeS layers on UNS G10180 immersed in 1%. wt. NaCl solution at 30 ⁰ C, pH 6.0, 0.1bar of H ₂ S and 250rpm impeller speed (a.) 1-day exposure (b.) 3 days exposure.....	200
Figure 106: XRD analysis of FeS layer formed after 3 days exposure time in 1%. wt. NaCl solution at 30 ⁰ C, pH 6.0, 0.1bar of H ₂ S and 250rpm impeller rotational speed....	200
Figure 107: Loading and unloading curve from hardness measurements of mackinawite layer formed on UNS G10180 immersed in 1%. wt. NaCl solution at 30 ⁰ C, pH 6.0, 0.1bar of H ₂ S and 250rpm impeller speed after (a.) 1 day (b.) 3days	201
Figure 108: Progressive load scratch test from 0.1mN to 300mN on the mackinawite layer formed after 1 day exposure of UNS G10180 to 1 wt.% solution at pH 6.00, 0.1bar of H ₂ S, 30 ⁰ C, and 250rpm impeller rotation speed, conducted at a scratch speed of 0.25mm/min and loading rate of 75mN/min.....	203
Figure 109: EDS Analysis of progressive load scratch from 0.1mN to 300mN on mackinawite layer formed after 1 day exposure of UNS G10180 to 1 wt.% solution at pH 6.00, 0.1bar of H ₂ S, 30 ⁰ C, and 250rpm impeller rotation speed, (a.) 0.1mN (b.) 150mN and (c.) 300mN.....	204
Figure 110:(a.) Scratch track and (b.) EDS mapping of scratch mark from a constant load test at 200mN constant load test on a mackinawite layer formed after 1-day exposure to 1 wt.% Solution at pH 6.00, 0.1bar of H ₂ S, 30 ⁰ C, and 250rpm Impeller Rotation Speed.	205
Figure 111: (a.) Scratch track and (b.) EDS mapping of scratch track from a constant load test at 230mN constant load test on a mackinawite layer formed after 1-day Exposure to 1 wt.% Solution at pH 6.0, 0.1bar of H ₂ S, 30 ⁰ C, and 250rpm Impeller Rotation Speed. ...	206
Figure 112: EDS analysis of scratched area from a 230mN constant load test on a mackinawite layer formed after 1-day Exposure to 1 wt.% Solution at pH 6.0, 0.1bar of H ₂ S, 30 ⁰ C, and 250rpm Impeller Rotation Speed.....	207
Figure 113: Profilometry of scratch track left by a shear stress of (a.) 400 MPa and (b.) 470 MPa on a Mackinawite layer developed UNS G10180 after 1 days exposure to 1 wt. % NaCl solution at 30 ⁰ C, pH 6.0, 0.1bar H ₂ S and 250rpm impeller rotational speed....	208
Figure 114: (a.) Scratch track and (b.) EDS mapping of scratch track from a constant load test at 250mN (500MPa) constant load test on a mackinawite layer formed after 3-day Exposure to 1 wt.% Solution at pH 6.0, 0.1bar of H ₂ S, 30 ⁰ C, and 250rpm Impeller Rotation Speed.	209

Figure 115: Profilometry of scratch track left by a shear stress of 500 MPa on a Mackinawite layer developed UNS G10180 after 3 days exposure to 1 wt. % NaCl solution at 30°C, pH 6.0, 0.1bar H ₂ S and 250rpm impeller rotational speed.	210
Figure 116: Scratch mark from a 0.1mN constant load test on layers developed in 1 wt. % solution sparged with 10% H ₂ S/N ₂ at 30°C, pH 6.00 and 250rpm (a.) 1-day exposure (b.) 3 days exposure	211
Figure 117: Cross section of FeS layers developed on UNS G10180 immersed in 1%. wt. NaCl solution at 80°C, pH 6.0, 0.1bar of H ₂ S and 250rpm impeller speed (a.) 1-day exposure (b.) 3 days exposure	212
Figure 118: Surface SEM of FeS layer developed on UNS G10180 immersed in 1%. wt. NaCl solution at 80°C, pH 6.00, 0.1bar of H ₂ S and 250rpm impeller speed (a.) 1 day exposure (b.) 3 days exposure	213
Figure 119: XRD analysis of FeS layer formed on UNS G10180 after 3 days exposure to 1%. wt. NaCl solution at 80°C, pH 6.00, 0.1bar of H ₂ S and 250rpm impeller speed.....	213
Figure 120: Loading and unloading curve from hardness measurements of mackinawite layer formed on UNS G10180 at 80°C after (a.) 1 day (b.) 3 days.....	214
Figure 121: Progressive load scratch test from 0.1mN to 300mN on the mackinawite layer formed after 1 day exposure of UNS G10180 to 1 wt.% solution at pH 6.0, 80°C, and 250rpm impeller rotation speed, conducted at a scratch speed of 0.25mm/min and loading rate of 75mN/min.	215
Figure 122: EDS Analysis of progressive load scratch from 0.1mN to 300mN on mackinawite layer formed on UNS G10480 after 1-day exposure to 1 wt.% solution at pH 6.0, 80°C, and 250rpm impeller rotation speed at (a.) 0.1mN (b.) 150mN and (c.) 300mN	217
Figure 123: (a.) Scratch mark from a constant load test at 100mN (b.) EDS mapping of scratch mark with uniform distribution of Fe and S	218
Figure 124: (a.) Scratch mark from a constant load test at 150mN (b.) EDS analysis of scratch mark showing distinct area of high iron intensities.	219
Figure 125: Profilometry of scratched area resulting from a shear stress of (a.) 310 MPa and (b.) 410 MPa	220
Figure 126: (a.) Scratch mark from a constant load test at 150mN (b.) EDS analysis of scratch mark showing distinct area of high iron intensities.	221
Figure 127: Profilometry of the scratched area resulting from a shear stress of 370MPa	222
Figure 128: Scratch mark from a 0.1mN constant load test on layers developed in 1 wt. % solution sparged with 10% H ₂ S/N ₂ at 80°C, pH 6.00 and 250rpm (a.) 1 day exposure (b.) 3 days exposure	223

Figure 129: Summary of the interfacial shear strength of mackinawite layers formed in 30°C and 80°C solutions compared to the highest possible flow related shear stress in pipelines	224
Figure 130: (a.) Surface SEM and (b.) Cross section of FeS layer developed on 99.9% pure Fe after 3 days exposure to 1 wt. % NaCl solution at 30°C, pH 6.0, 0.1bar H ₂ S and 250rpm impeller rotational speed	225
Figure 131: EDS analysis of FeS layer developed on 99.9% pure Fe after 3 days exposure to 1 wt. % NaCl solution at 30°C, pH 6.00, 0.1bar H ₂ S and 250rpm impeller rotational speed	226
Figure 132: Loading and unloading curve from hardness measurements of mackinawite layer formed on 99.9% pure Fe after 3 days exposure to 1 wt. % NaCl solution at 30°C, pH 6.0, 0.1bar H ₂ S and 250rpm impeller rotational speed	227
Figure 133: Progressive load scratch test from 0.1mN to 300mN on the mackinawite layer formed on 99.9% pure Fe after 3 days exposure to 1 wt.% solution at pH 6.00, 30°C, and 250rpm impeller rotation speed, conducted at a scratch speed of 0.25mm/min and loading rate of 75mN/min.	229
Figure 134: EDS analysis of progressive load scratch from 0.1mN to 300mN on mackinawite layer formed on 99.9% pure Fe after 3 days exposure to 1 wt. % NaCl solution at 30°C, pH 6.00, 0.1bar H ₂ S and 250rpm impeller rotation speed at (a.) 0.1mN (b.) 150mN and (c.) 300mN	230
Figure 135: Scratch track left by a shear stress of 500MPa on a Mackinawite layer developed on 99.9% Pure Fe after 3 days exposure to 1 wt. % NaCl solution at 30°C, pH 6.0, 0.1bar H ₂ S and 250rpm impeller rotational speed. (b.) EDS analysis of scratch track showing distinct area of high iron intensities.....	231
Figure 136: Profilometry of scratch track left by a shear stress of 500MPa on a Mackinawite layer developed on 99.9% Pure Fe after 3 days exposure to 1 wt. % NaCl solution at 30°C, pH 6.0, 0.1bar H ₂ S and 250rpm impeller rotational speed	232
Figure 137: Loading and unloading curve from hardness measurements of mackinawite layer formed on (a.) UNS G10180 and (b.) 99.9% pure Fe substrate after 4 days exposure to 1 wt. % NaCl solution at 30°C, pH 6.0, 0.1bar H ₂ S and 10.4m/s fluid velocity.....	234
Figure 138: EDS analysis of scratch tracks from 1470 MPa shear stress on a mackinawite layer formed on UNS G10180 and 99.9% pure Fe after 4 days exposure to 1 wt. % NaCl solution at 30°C, pH 6.0, 0.1bar H ₂ S and 10.4m/s fluid velocity.	237
Figure 139: Profilometry of scratch track left by a shear stress of 1470MPa on a Mackinawite layer developed on (a.) UNS G10180 and (b.) 99.9% Pure Fe after 3 days exposure to 1 wt. % NaCl solution at 30°C, pH 6.0, 0.1bar H ₂ S and 10.4m/s	238
Figure 140: 2L glass cell set-up for electrochemical test (image courtesy of Cody Shafer, ICMT).....	268

Figure 141: Corrosion rate measurement (from LPR and weight loss) of X-65 carbon steel sample in 1 wt. % NaCl solution, pH 6.00, 30°C and 0.1mbar of H ₂ S compared with predicted corrosion rate values from Zheng's model.	271
Figure 142: Open circuit potential measurement of X-65 carbon steel sample in 1 wt. % NaCl solution, pH 6.00, 30°C and 0.1mbar of H ₂ S compared with predicted corrosion rate values Zheng's model.	272
Figure 143: Solution pH measurements for experiment conducted at 30°C, pH ₂ S = 1mbar, [Fe ²⁺] = 0 and initial solution pH = 6.00.....	273
Figure 144: Supersaturation (SS) of FeS in solution for experiment conducted at 30°C, pH ₂ S = 1mbar, [Fe ²⁺] = 0 and initial solution pH= 6.00.....	273
Figure 145: Surface morphology of iron sulfide layers after 2 days exposure in solution at 30°C, 1mbar H ₂ S, pH 6.00 (a) Test 1 (b) Repeat experiment.....	274
Figure 146: Surface morphology of iron sulfide layers after 3 days exposure in solution at 30°C, 1mbar H ₂ S, pH 6.00 (a) Test 1 (b) Repeat experiment.....	274
Figure 147: Cross section of iron sulfide layers after 2 days exposure in solution at 30°C, 1mbar H ₂ S (a) Test 1 (b) Repeat experiment.....	275
Figure 148: Cross section of iron sulfide layers after 3 days exposure in solution at 30°C, 1mbar H ₂ S (a) Test 1 (b) Repeat experiment.....	275
Figure 149: XRD analysis of the X65 carbon steel surface after testing in 1 wt. % NaCl solution, pH 6.00, 30°C and with 1mbar of H ₂ S.....	276
Figure 150: 7L Hastelloy autoclave for FeS layer development (image courtesy of Cody Shafer, ICMT).....	277
Figure 151: (a.) Surface SEM and (b.) Cross section of UNS G10180 exposed to 1 wt.% NaCl solution with 2 bars H ₂ S, pH 4.00, 80°C and 2 weeks exposure.	279
Figure 152: EDS Analysis of iron sulfide layer formed on UNS G10180 exposed to 1 wt.% NaCl solution with 2 bars H ₂ S, pH 4.00, 80°C and 2 weeks exposure.	280
Figure 153: XRD analysis of iron sulfide layer formed on UNS G10180 exposed to 1 wt.% NaCl solution with 2 bar H ₂ S, pH 4.00, 80°C and 2 weeks exposure.....	281
Figure 154: Progressive load test from 0.1mN to 400mN on iron sulfide layers formed on UNS G10180 exposed to 1 wt.% NaCl solution with 2 bar H ₂ S, pH 4.00, 80°C and 2 weeks exposure	281
Figure 155: Scratch tracks corresponding to the (a.) 800mN, (b.) 400mN and (c.) 0.1mN from the progressive load scratch test.	282
Figure 156: Constant load tests at different normal forces	283
Figure 157: (a.) Scratch track and (b.) EDS mapping of scratch track left by a shear stress of 1.3 GPa on a layer formed on UNS G10180 after 2 weeks exposure to 1wt.% NaCl after exposure to 2bar H ₂ S, pH 4.00, 80°C.....	284

Figure 158: EDS spot analyses on areas inside and outside the scratch track from a shear stress of 1.3GPa on a layer formed on UNS G10180 after 2 weeks exposure to 1wt.% NaCl after exposure to 2 bar H₂S, pH 4.00, 80°C.....284

CHAPTER 1: INTRODUCTION

Pipeline transmission is the most common mode of product transportation in the oil and gas industries due to its economic and structural advantages[1]. The latest report, published in 2017, by the American Petroleum Institute and the Association of Oil Pipe Lines stated that across America alone there are 207,792 miles of pipelines used to transport product from production sites to refineries, and finally to the consumer market[2]. This constitutes a 9% increase from the reported mileage of pipelines in 2014[2,3]. Owing to its economic advantage over other materials, carbon steel materials have been commonly used in the fabrication and construction of these pipelines[4] and, due to the potentially high corrosive nature of the fluids being transported[5], corrosion mitigation has been a constant challenge that needs to be tackled in order to ensure asset integrity. A study released by US federal highway administration in 2002 showed that the direct annual cost of corrosion in the U.S was \$276 billion, then equivalent to 3.1% of the nation's Gross Domestic Product (GDP)[6]. Out of this, \$1.4billion was attributed to the costs of corrosion in oil and gas exploration and production. The findings from this study highlighted the urgent need for strategies to achieve better corrosion mitigation practices. Pipeline failure remains a concern to oil and gas operators because of resulting shutdowns in operations, risk to life, and environmental damage (including the possible release of toxic gases such as H₂S).

Exploration and subsequent production of oil and gas from sour (H₂S containing) geologic hydrocarbon reservoirs has been ongoing for over half a century, with companies expending significant efforts to minimize risks associated with their

operations.[4,7] Operations in sour gas fields have potential hazards associated with pipeline failure and release of H₂S gas to the environment[5]. Even with the progress that has been made in the last decade, this area of research continues to generate a lot of interest especially in areas relating to localized corrosion[8–11] and influence of environmental factors[12,13]. A major concern in conducting small scale laboratory studies is performing experiments in environments which are representative of field conditions, especially in order to develop superior mitigation strategies. This is especially true in studies related to flow and its effect on corrosion.

Flow is one of the major factors that influences corrosion processes because it impacts both mass transport of electroactive species[14–19] and wall shear stress[20,21] and can consequently affect the formation/retention of corrosion product layers. The mass transfer effects on corrosion rates depends on the limiting process of the corrosion reactions. A corroding system is said to be mass transfer limited if the rate of transport of electroactive species is not sufficiently fast to keep up with the rate of the electrochemical reactions. In this case, the corrosion rates measured are sensitive to flow since an increase in the flow rate directly increases the convective mass transport rate of corrosive species to the reaction site [19]. In contrast, a corrosion process is said to be under charge transfer control, when there is an abundance of corrosive species at the reaction site, and when the corrosion process is purely limited by the kinetics of the electrochemical reactions (how fast oxidation and reduction reactions occur, i.e. charge transfer). The corrosion rate in this case is not dependent on the mass transport of species and, thus, is insensitive to the flow velocity. Some corroding systems that were initially under charge transfer control

can become mass transfer controlled if a protective corrosion product layer develops. In this case, the corrosion product layer forms a diffusion barrier to the transport of species and makes the corrosion process sensitive to flow. This is the case in the formation of iron carbonate corrosion product layers, in sweet (CO_2) conditions, and iron sulfide layers, in sour (H_2S) conditions. The protectiveness of these corrosion product layers has been shown to be dependent, among other factors, on steel microstructure. For example, iron carbonate layers with better protective properties form on a carbon steel with a ferritic/pearlitic microstructure in comparison to that with martensitic microstructure, even with similar carbon contents[22]. This is primarily due to the presence of iron carbide corrosion product residue which provides anchoring structures that favor iron carbonate precipitation. In high flow conditions, the damage of these mechanically weak and porous iron carbide corrosion product residues can affect the protective properties of the iron carbonate layers. This was demonstrated in the study conducted by Di Bonaventura, *et. al.*, [23,24] where it was shown that a shear stress of 100Pa removes the iron carbide layers from a carbon steel surface, resulting in the lack of an anchoring structure for the formation of protective iron carbonate layers. In H_2S environments, it is generally accepted that the formation of the first iron sulfide layers is very fast[25,26]. Therefore, it is important to understand if the formation of protective iron sulfide layers can be impeded by high shear conditions similarly to what has been reported, albeit for FeCO_3 , in CO_2 conditions. The flow system used by Bonaventura [23] could achieve high levels of turbulence and shear stresses, and thus, were representative. This system comprises of a flow through a channel, where the test specimens were mounted flush to

the surface of the channel. This system is known as the thin channel flow cell. Another setup used by this author [23] was a central impeller mounted on the lid of a 4L glass cell inside which several steel specimens were placed. However, the adaptation of these relatively complex systems to sour corrosion studies naturally brings some level of safety concerns due to the toxicity of H_2S . Rotating cylinder electrodes (RCE) in glass cell setups have been commonly used in sour environments. However, the impact of centrifugal forces generated in the rotation of the cylindrical specimens directly acts on the corrosion product layers can artificially affect their protectiveness. This is RCE setup is consequently not representative of the actual flow conditions and could lead to the generation of corrosion rate results that are misleading.

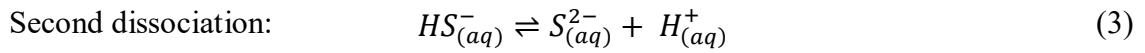
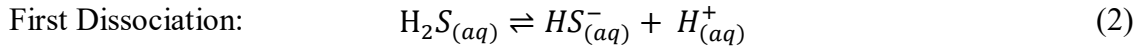
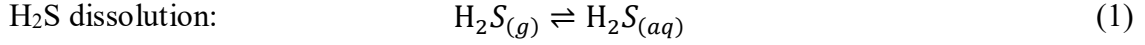
In the current research, new experimental set-ups were developed with the aim of achieving representative flow conditions and of limiting experimental artefacts. Initial studies were conducted to understand the impact of iron carbide on the development of iron sulfide layers. Subsequently, the integrity of these layers was tested under high shear stress conditions. Further investigations of the adhesive properties of the corrosion product layer were also conducted.

CHAPTER 2: LITERATURE REVIEW

H₂S occurs naturally in oil and gas fields. One possible mechanism, valid at low temperature conditions from 0°C to 80°C involves the reduction of sulfur by sulfur reducing bacteria [27,28]. However, in high temperature geological settings, the metabolization of these sulphate reducing bacteria becomes impossible. In this case thermochemical sulfate reduction becomes the major process of H₂S production [28]. In the presence of H₂S, carbon steel materials become very prone to different forms of corrosion, ranging from localized to uniform, which typically leads to an accelerated degradation of such materials[29,30]. In addition to economic losses associated with infrastructure failure, there is a high level of safety concern that arises with sour well pipeline failure. For these reasons, H₂S corrosion has been a great concern, and has been investigated extensively for the past 80 years by researcher in different fields of study [7,26,31–37]. Even with the immense strides made towards the understanding of H₂S corrosion mechanism in last decade[19,38–41], this topic still remains a subject of debate between researchers in the field of corrosion. To understand the corrosive behavior of carbon steel in aqueous sour environment three major subjects has been discussed in this chapter: the solution chemistry, the electrochemical reactions and the formation of the resultant iron sulfide corrosion product layers. In addition, this chapter seeks to further discuss the current studies that have been conducted on the impact of flow on iron sulfide layer formation.

2.1 Solution Chemistry

The following reactions lead to the formation of different sulfide species in aqueous sour conditions starting with the dissolution of gaseous H₂S to the first and second dissociation of aqueous H₂S [42–44].



The equilibrium expressions for equations 1, 2 and 3 are as follows:

$$\text{Equilibrium expression for H}_2\text{S dissolution:} \quad K_{\text{H}_2\text{S}} = \frac{C_{\text{H}_2\text{S}}}{P_{\text{H}_2\text{S}}} \quad (4)$$

$$\text{Equilibrium expression for first dissociation of H}_2\text{S:} \quad K_1 = \frac{C_{\text{H}^+} C_{\text{HS}^-}}{C_{\text{H}_2\text{S}}} \quad (5)$$

$$\text{Equilibrium expression for second dissociation of H}_2\text{S:} \quad K_2 = \frac{C_{\text{H}^+} C_{\text{S}^{2-}}}{C_{\text{HS}^-}} \quad (6)$$

Suleimenov and Krupp[45] formulated the equation for calculating the solubility constant of H₂S, and is given in the expression presented in Equation 7. The equation for the first dissociation constant of H₂S presented in Equation 8 was reported by Suleimenov and Seward[46] while that for the second dissociation of H₂S was formulated by Kkaraka, *et al.*, [47]. These expressions have been validated and are generally used to calculate the aqueous concentration of sulfide species in solution.

$$K_{\text{H}_2\text{S}} = 10^{-(634.27+0.2709T_K-0.11132 \times 10^{-3}T_K^2-\frac{16719}{T_K}-261.9 \log_{10} T_K)} \quad (7)$$

$$K_1 = 10^{782.43945+0.361261T_K-1.6722 \times 10^{-4}T_K^2-\frac{20565.7315}{T_K}-142.741722 \ln T_K} \quad (8)$$

$$K_2 = 10^{-(23.93 - 0.030446T_K + 2.4831 \times 10^{-5}T_K^2)} \quad (9)$$

Where K_{H_2S} is in molar/bar, K_1 and K_2 are in mol, and T_k is the temperature in Kelvin.

In an aqueous sour environment, there are 5 species present in solution (assuming pure water): OH^- , H^+ , H_2S , HS^- and S^{2-} . With the three equilibrium expressions presented (Equation 4-6), there is a need for two additional equation to solve for the 5 unknown species concentration. The two additional equations are the equilibrium expression for the dissociation of water (Equation 10) and the electroneutrality equation (Equation 11), which accounts for the charge balance of ions in solution.

$$K_W = C_{H^+}C_{OH^-} \quad (10)$$

$$C_{H^+} = C_{OH^-} + C_{HS^-} + C_{S^{2-}} \quad (11)$$

The equilibrium concentration of the sulfide species in an open system at different solution pH values was calculated using these equations as presented in Figure 1. These calculations were carried out at a solution temperature of 30°C and H_2S partial pressure of 0.1bars.

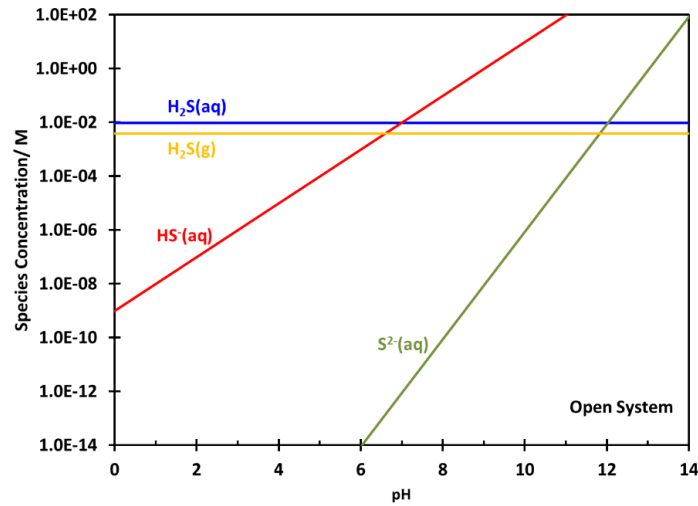


Figure 1: Change in equilibrium concentration of sulfide species with respect to pH in an open system at H_2S partial pressure of 0.1bar and temperature of $30^\circ C$

In a closed system, the number of moles of the species in solution, N , is conserved. Therefore, Equation 12 shows the sum of the sulfide species concentration is equal irrespective of the pH of the solution.

$$N_{H_2S(g)} + N_{H_2S(aq)} + N_{HS^-(aq)} + N_{S^{2-}(aq)} = \text{constant} \quad (12)$$

Where N the number of moles.

Figure 2 shows the equilibrium concentration of the different sulfide species in closed system with an initial H_2S partial pressure of 0.1bar, a temperature of $30^\circ C$ and a liquid to gas volume ratio of 1:1.

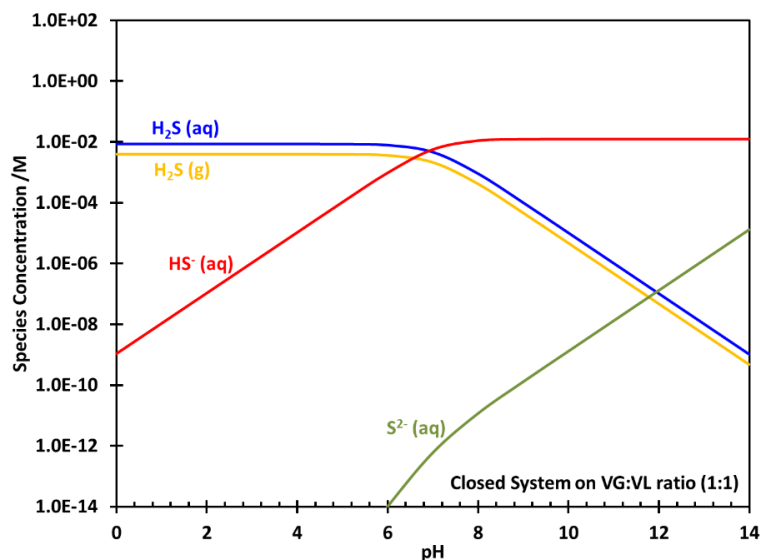


Figure 2: Change in equilibrium concentration of sulfide species with respect to pH in a closed system at H_2S partial pressure of 0.1bar and a temperature of $30^\circ C$ at a gas to liquid volume ratio of 1:1

With the knowledge of the solution chemistry, the concentration of corrosive species and their contribution to the corrosion process in a particular condition can be better understood.

2.2 Electrochemical Reaction Mechanisms

Anodic Reaction:

In the electrochemical reaction mechanisms of aqueous H_2S corrosion of steel, the anodic reaction involves the oxidation of an iron atom to a ferrous ion accompanied by the release of two electrons. This reaction is known as the iron oxidative dissolution reaction.

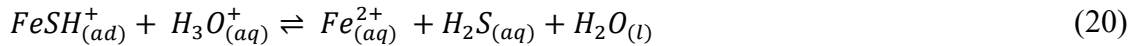
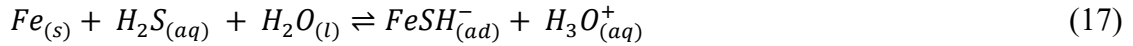


In acidic solutions, the mechanism of iron dissolution as proposed by Bockris, *et al.*, [48] is as follows:



Equation 15 is the rate determining step (RDS) of the process.

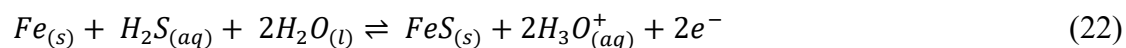
A mechanism of a similar form, shown in Equations 14 - 16, was proposed by Ma, *et al.*, [13,49] for iron dissolution in H₂S. These reactions, shown in Equations 17-20, are generally accepted as the mechanism of iron dissolution in an H₂S solution.



It can be observed that the equations presented for the mechanism of iron dissolution in acidic solutions combine to give the simple anodic reaction shown by Equation 13. This is also the case with the reactions for the mechanism of iron dissolution in H₂S conditions. Therefore, the species OH⁻, FeOH, FeOH⁺, and FeSH⁻, FeSH and FeSH⁺, can be considered as the intermediates for the different mechanisms of iron dissolution in different environments which leads to Equation 13 as the overall reaction. The FeSH⁻ and FeSH are the intermediates that are adsorbed on the surface [7]. Depending on the solution chemistry, FeSH⁺ can form FeS according to the reaction shown in Equation 21.

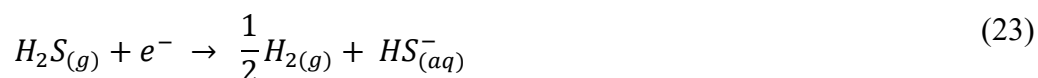


The combination of Equations 17, 18, 19 and 21 gives Equation 22, which represents the direct reaction of iron with H₂S on the steel surface.



Cathodic Reactions:

The major cathodic reactions in an aqueous H₂S environment are the reduction of hydrogen ions, dissolved H₂S and water molecules. With the exception of water reduction, the contribution of each reduction reaction to the overall cathodic current depends on the concentration of the reducible species in solution.

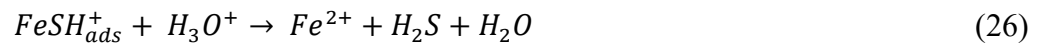
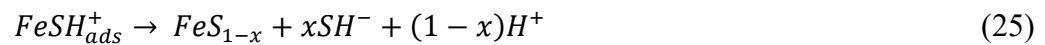


As shown in Equations 2 and 3, H₂S in its aqueous form undergoes first and second dissociations to form sulfide and bisulfide ions. The product of these reactions, H⁺, promotes the hydrogen ion reduction reaction (Equation 22). However, evidence of H₂S chemisorption on a steel surface, and its subsequent reduction, has also been reported. [39,50–53] Zheng, *et al.*, [39] postulated that the diminution in the water reduction reaction observed in the presence of H₂S was due to the replacement of water molecules with H₂S on the steel surface. It was also reported that the limiting current associated with the reduction of H₂S responded to changes in electrolyte velocity. In the absence of H₂S, the

H^+ and H_2O reduction reactions are the major cathodic reactions. However, in the presence of H_2S , the dominant reaction can be the H_2S reduction reaction (if the H_2S content is high enough), while the contribution from the hydrogen reduction reaction depends on the pH. This is especially true at pH above 5.00. Studies have shown that below this pH, down to pH 3.00, the direct reduction of H_2S is not significant.[54] This is a similar case with other weak acids.

2.3 Formation of Iron Sulfide Corrosion Product Layer

The initially proposed mechanism of FeS formation was by the direct reaction of Fe with H_2S . [26,55] This mechanism involves the dissolution of H_2S in aqueous environment and its subsequent diffusion to the metal surface, where it undergoes a reaction with the Fe to form a mackinawite layer. According to Shoesmith, [56] the initial mackinawite layer dissolves by combining with H_2S to form an $Fe(SH)^+$ and HS^- . Furthermore, it was proposed that the $Fe(SH)^+$ can either hydrolyze to Fe^{2+} or form FeS on the steel surface according to the following reaction[56,57]:



Sun [58,59], used a similar concept to Shoesmith[56] to develop the following equation for the direct reaction mechanism:



The formation of the mackinawite layer at saturation levels of less than one was presented as evidence for the direct reaction mechanism. Consequently, the initial

mackinawite layers are often fairly continuous and adherent, and thus more resistant mechanically to flow and less influenced by the bulk water chemistry. However, subsequent mackinawite layers can form by precipitation and deposition from the bulk solution. These layers tend to be less adherent and more dependent on mass transfer effects.[59] Smith, *et al.*, [60] proposed a mechanism of iron sulfide growth which agreed with that presented by Sun [58,59]. In this mechanism, the initial iron sulfide layer cracks due to development of internal stresses and giving way to the formation of new iron sulfide layers. This repeated formation and reformation of iron sulfide layers was proposed as the method of layer growth. Several pieces of evidence were presented as reasons for the proposed mechanism. However, Zheng, *et al.*, [39] disputed the direct reaction mechanism of iron with H₂S by a model entirely based on electrochemical reactions. This model is generally adopted for the H₂S corrosion process leading to the formation of iron sulfide layer. For iron sulfide layers to form on the metal surface, the saturation level with respect to ferrous (Fe²⁺) and sulfide (S²⁻) species in solution has to be in excess of one. Different reports have shown that mackinawite forms as the initial iron sulfide layer due to its fast formation kinetics.[61–63] Depending on the sulfide species considered, Table I shows the different precipitation reactions and corresponding equation that can be used to calculate the iron sulfide layer saturation.

Table I: Different expressions for FeS precipitation reaction and the corresponding equations for FeS saturation

Precipitation reactions for FeS formation	Corresponding equation for FeS saturation
$Fe_{(aq)}^{2+} + H_2S_{(aq)} \xrightleftharpoons{K_{sp,H_2S}} FeS_{(s)} + 2H_{(aq)}^+$ (28)	$S_{FeS} = \frac{C_{Fe^{2+}} + C_{H_2S}}{K_{sp,H_2S} \times C_{H^+}^2}$ (31)
$Fe_{(aq)}^{2+} + HS_{(aq)}^- \xrightleftharpoons{K_{sp,HS^-}} FeS_{(s)} + H_{(aq)}^+$ (29)	$S_{FeS} = \frac{C_{Fe^{2+}} + C_{HS^-}}{K_{sp,HS^-} \times C_{H^+}}$ (32)
$Fe_{(aq)}^{2+} + S_{(aq)}^{2-} \xrightleftharpoons{K_{sp,S^{2-}}} FeS_{(s)}$ (30)	$S_{FeS} = \frac{C_{Fe^{2+}} + C_{S^{2-}}}{K_{sp,S^{2-}}}$ (33)

The concept of scaling tendency, introduced by van Hunnik, *et al.*, [64], is used to evaluate the protective nature of corrosion product layer.

$$ST = \frac{PR}{CR} \quad (34)$$

According to this concept, the corrosion process in a layer forming condition is controlled by the competing effect of two dynamic processes; precipitation rate (PR) and the corrosion rate (CR). The precipitation of the iron sulfide layers provides a diffusion barrier to the corrosion species while the corrosion rates undermines the protectiveness of these layers. The kinetics of these processes is dependent on the system conditions such as pH, temperature and the availability of species close to the metal surface. Precipitation rate of FeS [65–67], presented in Equation 35, is strongly dependent on the saturation of FeS which is greatly influenced by the solution pH and concentrations Fe^{2+} and H_2S .

$$PR_{FeS} \left(\frac{mol}{m^2s} \right) = 7.02 \times 10^{14} \times e^{-\frac{40000}{RT}} K_{sp,S^{2-}} (S_{FeS} - 1) \quad (35)$$

The constants in Equation 35 were determined experimentally [38] while FeS saturation, S_{FeS} , can be calculated using Equation 33 and $K_{sp,S^{2-}}$, the solubility constant

for mackinawite (in mol^2), can be calculated with the expression by Benning, *et al.*, [68] (Equation 36). R is the gas constant, 8.314J/mol.K , and T is the temperature in Kelvin.

$$K_{sp,S^2-}(\text{mol}^2) = 10^{\frac{2848.779}{T}-6.347} K_1 K_2 \quad (36)$$

K_1 and K_2 (in mol) are the first and second dissociation constants of H_2S presented Equations 8 and 9 respectively [46,47].

Corrosion rates, since they are being responsive to concentration of corrosive species in solution, are also influenced by flow through the enhancement of species mass transport. Since precipitation rate is independent of flow, it is not yet understood if high flow conditions affect layer morphology, through wall shear stress impacts, or protectiveness, through increased mass transport. Other factors that can also impact on the corrosion process are the physicochemical properties of the iron sulfide corrosion product formed on the corroding surface.

2.4 Physicochemical Properties of Iron Sulfide Phases

System temperature and partial pressure of H_2S are parameters that play a crucial role both on the kinetics of electrochemical reactions and on the formation of iron sulfide layers [19,26,38,66]. An increase in temperature typically favors the formation of corrosion product layers by increasing the kinetics of reactions and transformation to more thermodynamically stable iron sulfide layers [40]. The effects of temperature, pH, pH_2S and ferrous ion concentration on the thermodynamics of iron sulfide formation was studied by Ning, *et al.*, [16] and Pourbaix diagrams of phases in the H_2S - H_2O -Fe system were constructed using thermodynamic data from the literature. The following sequence for the formation of iron sulfide layers have been proposed by different authors [18,69]:

mackinawite – pyrrhotite – pyrite ($\text{FeS} - \text{Fe}_{1-x}\text{S} - \text{FeS}_2$). [18]. Wijkord, *et al.*, [18] showed that in a system at 1.5MPa H_2S partial pressure, sulfur-rich iron sulfide phases formed at higher temperature and increased exposure time. Ning, *et al.*, [70] conducted a similar study of developing different iron sulfide phases at different temperatures, exposure times and H_2S partial pressures. X-ray diffraction (XRD) data showed mackinawite as the only iron sulfide phase formed after short term exposure time (42hours) in solutions sparged with 0.2mbar and 1mbar of H_2S (in admixture with nitrogen) for a temperature maintained at 25°C. At a higher temperature of 60°C with other conditions maintained at the same values, greigite and pyrite were detected. [70] Lennie, *et al.*, [71] reported a more direct effect of temperature on the transformation of mackinawite to a higher sulfur content iron sulfide phase, in this case pyrrhotite. Pyrrhotite was partially transformed by heating synthetic mackinawite at a temperature range of 257°C to 272°C in vacuum. The transformation of mackinawite to pyrite has also been reported at temperature below 100°C in oxidizing sour solutions [68]. These different phases of iron sulfides possess different physicochemical properties, which affect their protectiveness to the underlying metal [72–75]. Gao, *et al.*, [76], for example, showed that an increase in solution temperature favors the formation of higher sulfide containing FeS phases. Starting from 80°C, and with an incremental increase in temperature of 40°C up to 200°C, the phase of iron sulfide developed were in the order mackinawite, troilite, pyrrhotite and pyrite; protectiveness of these FeS phases, with the exception of pyrite, increased in a similar trend. In the case of pyrite, several reports suggest that its electrically conductive properties [77–80] cause a galvanic coupling between it and the steel substrate resulting in

localized corrosion[72,81]. A summary of the physicochemical properties of iron sulfides frequently encountered in corrosion product layers is shown in Table II.

Table II: Summary of the physicochemical properties of different iron sulfide phases[31,82]

Name	Chemical Formula	Crystal Structure	Properties
Amorphous	FeS	Non-crystalline	Unstable, converts quickly to mackinawite
Mackinawite	FeS	Tetragonal, 2D layer structure	Metastable, primary precipitate from aqueous solution. Common low T corrosion product.
Cubic FeS	FeS	Cubic	Unstable, can transform to mackinawite, pyrrhotite or troilite. Occurs in top of the line corrosion (TLC).
Troilite	FeS	Hexagonal	Stoichiometric member of the $Fe_{1-x}S$ group ($x=0$). High temperature corrosion product.
Pyrrhotite	$Fe_{1-x}S$ ($x = 0$ to 0.17)	Monoclinic Fe_7S_8 or Hexagonal $Fe_{10}S_{11}$	Most abundant iron sulfide, rare in marine environments but common in corrosion.
Smythite	Fe_3S_4	Trigonal- Hexagonal	Metastable phase. Rare but found to in the company of carbonate.
Greigite	Fe_3S_4	Cubic	Metastable, thiospinel of iron, occurs in marine systems.

Table II Continued

Pyrite	FeS ₂	Cubic	Thermodynamically stable iron disulfide.
Marcasite	FeS ₂	Orthorhombic	Metastable, occur naturally in geological formation. Not common in corrosion.

Being the first and most common [83–85] iron sulfide corrosion product layer formed, it is important to highlight some of the important properties of mackinawite. Mackinawite has a tetragonal crystal structure with the iron atom connected to four sulfur atoms in a tetrahedral form within the layer structure that constitutes crystal lattice [31,86]. This FeS phase oxidize easily by the loss of electrons from the ferrous ions within the lattice [87]. Earlier studies on mackinawite stoichiometry proposed mackinawite as an iron rich FeS with the reasoning that elemental sulfur forms as a product of the dissolution of mackinawite in HCl [88]. However, in recent years, it has been generally accepted that mackinawite has a stoichiometric balance of Fe and S [88]. The current research is focused on mackinawite due to its significance as a corrosion product layer. By applying the thermodynamic model developed by Ning, *et al.*, [40], conditions were carefully selected to ensure the development of this FeS phase.

In addition to the effects conferred by the physicochemical properties of layers on a corroding surface, the adhesion and growth rate of the corrosion products can be strongly influenced by the microstructure of the steel [22,89,90]. Corrosion product layers generally act as diffusion barriers, which prevent substrate metals from having direct

contact with the corrosive electrolyte[4,91]. In the corrosion process of carbon steel, the presence of a cementite network may favor the formation of a corrosion product layer especially in a ferritic-pearlitic microstructure. This cementite/iron carbide acts as a cathodic site in a galvanic couple with the ferrite as the anode and leads to an increase in corrosion rate of the base metal especially in non-layer forming conditions[19,22,89]. In this process, the ferrite corrodes away and exposes cementite, which provides a relatively sheltered location where the chemistry favors high saturation levels. This phenomenon is particularly evident in CO₂ environments, where reports show that the presence of residual Fe₃C structures promote FeCO₃ nucleation and growth.[22] In H₂S conditions, the fast precipitation kinetics may interact with the development of an iron carbide structure resulting in a mechanism of corrosion product layer development that may be different from that encountered in CO₂ environments. The understanding of the role of iron carbide in FeS development will provide an insight into the retention of these layer in adverse flow conditions.

2.5 Effects of Flow on Development and Retention of Iron Sulfide Layers

Flow related corrosion studies started with the use of rotating disk electrodes in the 1950s[92]. However, studies in this system did not have much practical relevance since the flow in this system is laminar and does not relate to turbulent flow conditions typically encountered in the field. Thereafter, test setups with different flow geometries, such as rotating cylinder electrodes (RCE) [59][17,93–97] and pipe flows[98][99], have been used to capture the turbulent properties of flow as they exist in field conditions. While these experimental setups may have their peculiarities, such as the centrifugal force effects observed with the use of RCE[100–102] and the need to contain large

volume of fluids in the use of a pipe flow loop[103], they continue to be used for flow related corrosion studies especially due to their well characterized hydrodynamic properties. Sun, *et al.*, [104] attempted to avoid these problems by developing an autoclave system where the test solution was contained in a vessel and agitated with the aid of a rotating impeller while the specimens were in stationary positions . With the understanding that flow can influence corrosion processes either through an enhanced mass transfer process or by direct mechanical interaction with the corroding surface, it is important to properly characterize these flow characteristics for any newly developed experimental setup being used for corrosion testing. This was not reported in this study.

2.5.1 Effect of Mass Transfer

Corrosion is an electrochemical process that takes place on a solid liquid interface and requires the presence of the corrosive species at the reaction sites [105]. Flow inherently affects the corrosion process by enhancing the mass transport of corrosive species to the metal surface. The mass transport effect of flow is important only if the corrosion process is under mass transfer control. This is typically the case when a material is corroding at such a high rate that the transport of reducible species to the surface becomes a rate limiting step [19].

In H₂S conditions, the presence of FeS layers provides a mass transfer barrier which has to be considered in the understanding of the entire corrosion process. Also Morris[106] showed that in acidic conditions, where the formation of layers is less likely, corrosion processes can also be under charge transfer control depending on the conditions. As a result, the rate determining step is no more the mass transport but the

electrochemical reduction rate of H_2S in which case the entire corrosion process is said to be under charge transfer control, and is less sensitive to flow[105]. Some studies on the impact of flow on corrosion product layer characteristics have been conducted in conditions where the corrosion process, even before the formation of layers, is under mass transfer control and, thus, is sensitive to flow conditions[19,94]. In this case, the measurement of corrosion rates alone cannot help determine the effect of flow on the formation/characteristics of corrosion product layers as the “layer-free” corrosion rate is already flow dependent. In layer forming conditions, morphological characteristics such as the thickness, porosity and tortuosity, are important factors that may influence their protectiveness[38]. A thicker, less porous and tortuous layer is expected to reduce mass transport of species through the layers resulting in a diminution of corrosion rates. Figure 3 shows a schematic representation of the different resistance to the mass transfer of species from the bulk to the substrate surface in the presence of a corrosion product layer.

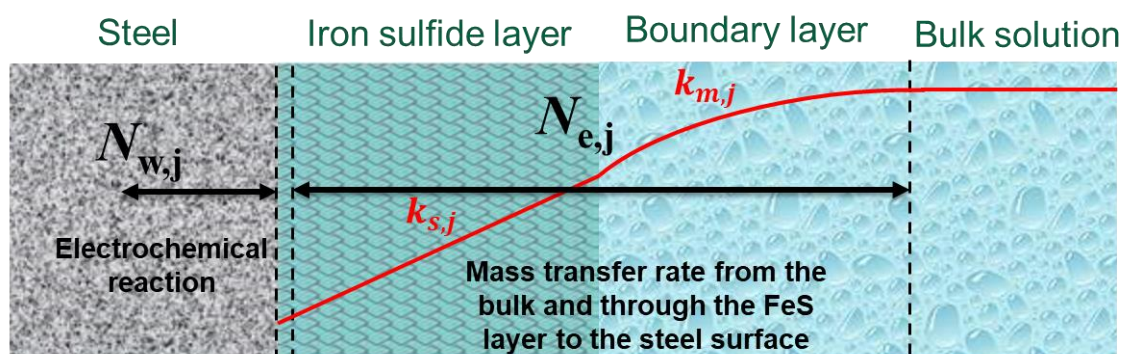


Figure 3: Schematic representation of the different resistances to mass transfer of species from the bulk to the substrate surface in the presence of a corrosion product layers[38].

$N_{e,j}$ is the flux of species (in mol./m².s), j , from and to the bulk to the surface. $N_{w,j}$ is the mass flux of species, j , from and to the surface to the bulk (in mol./m².s). The mass transfer coefficient of species from the bulk through the layer to the steel surface is the harmonic mean of the mass transfer coefficient through the boundary layer, $k_{m,j}$, and the mass transfer coefficient through the corrosion product layer, $k_{s,j}$.

$$\frac{1}{k_{T,j}} = \frac{1}{k_{s,j}} + \frac{1}{k_{m,j}} \quad (37)$$

The mass transfer coefficient through the corrosion product layer is a function of the layer properties such as the porosity, ε , diffusion coefficient, D , layer tortuosity, τ and thickness, δ_s .

$$k_{s,j} = \frac{\varepsilon\tau D_j}{\delta_s} \quad (38)$$

The tortuosity of the layer is dependent on the porosity of the layer ($\tau = \varepsilon^{1/2}$).

The mass transfer coefficient through the bulk, $k_{m,j}$, can be estimated using the appropriate Sherwood correlation for the specific flow system. It can be observed from Equation 37 that as the value of the mass transfer coefficient through the bulk becomes very high (as the case in high fluid velocity conditions), the overall mass transfer coefficient becomes closer to the mass transfer coefficient through the layer, since it becomes the major resistance to mass transfer. Similarly, as the value of the mass transfer coefficient through the layer becomes very high (which is the case for a highly porous layer) the overall mass transfer coefficient approaches the value of the mass transfer coefficient through the bulk.

Zheng, *et al.*, [19] investigated the role of flow on the growth of corrosion product layers developed on an API X65 steel exposed to 0.05 bar H₂S, 80°C and at pH values of

4.0, 5.0. The authors reported that at pH 4.0, a thicker but more porous iron carbide layer filled with iron sulfide precipitated at 600rpm solution stirring rate in comparison to at 60rpm. Even with the thicker layer, higher corrosion rates were measured at higher solution stirring speed. The difference in the layer morphology and corrosion rates was less significant at pH 5.0. It was suggested that the corrosion rates were responsible for the nature of the corrosion product layers developed since higher iron dissolution will lead to an increase in FeS saturation at the steel surface. The authors also concluded that the corrosion product layers offered no protection to the substrate due to their loose and detached nature. Since test conditions in this study meant that the layer-free corrosion processes were under mass transfer control, any retarding influence of the corrosion product layer on the corrosion process could be easily masked by the dominant flow sensitive mass transfer of the species from the bulk. To have a clear understanding of the impact of flow on the morphology of layers vis- à-vis their protectiveness, experiment have to be conducted in conditions where the corrosion process, in the absence of a layer, is under charge transfer control. In this condition, the initial corrosion rates at the different flow velocities are similar, and any difference in the corrosion rate trends can be directly attributed to the formation of corrosion product layers. Also, in all these studies, little thought has been given to the mechanical properties of the layers developed and their integrity in high shear stress conditions.

2.5.2 Mechanical Effects

Sun, *et al.*, [59], reported that a reduction of the thickness of iron sulfide layers results from flow induced hydrodynamic forces. The thinning of these iron sulfide layers by

chemical dissolution was ruled out by Sun, *et al.*, [59] based on the fact that the solution was supersaturated and thus provided no driving force for iron sulfide dissolution. Higher shear stress expected at this flow rate was cited as the reason for the mechanical removal of weakly attached iron sulfide layers from the metal surface.

However, the ability to test the effect of hydrodynamic induced wall shear stress while maintaining the species mass transfer coefficients constant is always a challenge associated with flow related studies. Different approaches have been used to address this problem.

Li, *et al.*, [21] studied the effect of flow on an iron carbonate layer by investigating the maximum wall shear stress that can be obtained in a single and multi-phase flow system at atmospheric pressure whilst also characterizing the mechanical strength of the layer. Wall shear stress values were obtained using a floating element wall shear stress measuring device. The mechanical strength of the iron carbonate layer was studied using Atomic Force Microscopy (AFM), where the corrosion product was scratched off the surface and the force needed for this operation was measured. The lateral force required to remove the iron carbonate layer was determined to be about 10^7 Pa. This has to be compared with the maximum wall shear stress obtained from the single-phase and multi-phase flow systems which was reported to be 10^2 Pa. With these findings it was concluded that wall shear stress generated by flow is unlikely to remove the iron carbonate layers formed on carbon steel material. By directly relating the shear stress calculated from AFM studies to flow conditions, the author ignored the additional impact of an enhanced species mass transport could also have on the corrosion process in such

high flow conditions. With an enhanced mass transport of reducible species to the metal surface, corrosion rates are expected to be higher, thereby undermining the protectiveness of the layer. Based on this understanding, there is a clear need to investigate the impact of flow related shear stress on the integrity of iron sulfide corrosion product layers. By conducting studies in both in situ and ex situ conditions, the synergistic role between mass transfer and wall shear stress on the protectiveness of the layer can be highlighted.

CHAPTER 3: RESEARCH OBJECTIVES

3.1 Knowledge Gaps

Based on the reviewed literature, the following gaps specific to the effect of flow on the formation, retention and characteristics of corrosion product layers forming in sour environments have been identified:

- Little effort has been made to study the flow impact on the properties of corrosion product layers in sour environments, especially in well-defined flow conditions representative of those encountered in the field. This is in part due to the high level of safety concerns associated with corrosion experimentations in H₂S environments.
- Studies have shown that a shear stress of 100 Pa removes an iron carbide layer from the metal surface which undermines the formation of a protective iron carbonate layer. So far, it is unknown if iron sulfide layers can be developed or retained on steel in high shear stress flow conditions.
- The extent to which iron carbides promote the growth of FeS layers remains uncertain.
- The mechanical properties of iron sulfide layers may be related to their protectiveness against localized corrosion. To date, the adhesive properties of iron sulfide layers and how they relate to corrosion behavior of substrates remains unknown.

3.1 Objectives and Hypotheses

The following key objectives are proposed to fill the knowledge gaps identified in the previous section:

- Develop experimental systems/procedures to consistently grow iron sulfide layers under representative flow conditions.
- Define the influence of flow on the development and retention of iron sulfide layers, as well as their morphological characteristics, whilst considering the role of iron carbide.
- Characterize the mechanical strength of the iron sulfide layers under investigation.
- Model the impact of flow on the corrosion behavior of carbon steel in film forming conditions.

In achieving the above set of research objectives, the following hypotheses will be tested:

1. High flow velocities generate high mass transfer coefficients through the boundary layer and influence the morphology of corrosion product layers in a way that enables higher mass transfer rates thereby promoting higher undermining corrosion rates.
2. By enhancing mass transfer rates and consequently promoting corrosion, high flow rates favor low scaling tendencies and impede the formation of protective corrosion product layers.
3. Iron sulfide layers cannot be damaged by shear stress generated by flow in typical conditions encountered in oil and gas production.

4. The presence of iron carbide in the steel microstructure provides an “anchoring structure” for the formation of FeS precipitates.

3.2 Test Methodology and Safety

The methodology presented in this section is designed to fulfill the proposed research objectives and, in doing so, the following tasks will be accomplished:

Task #1: Develop and characterize new corrosion test set-ups enabling controlled water chemistry and representative flow conditions.

This task involved developing and characterizing corrosion testing systems which enables uniform mass transfer conditions, maintained a stable solution chemistry and eliminated any possible impacts of centrifugal forces typically encountered in the standard RCE setup.

The first testing system that was developed was the glass cell setup with impeller flow similar to that used by Ieamsupamong[107]. This setup possessed a controlled solution chemistry and system. In this system, ion exchange resins were connected to the test cell, with the aid of a flow through system, to control the excess H^+ and Fe^{2+} concentrations in the bulk solution. In order to avoid any centrifugal force effects on corrosion product layers (situation typical of RCE setup), specimens were held in stationary positions concentric to the circumference of an impeller, while the impeller was rotated at the center to induce flow. Flow studies were conducted in this setup to obtain the mass transfer coefficients, and to calculate wall shear stress values obtainable on specimen surfaces. Mass transfer coefficients were determined by investigating the dependence of the Sherwood number (Sh) on the Reynolds number (Re) and the Schmidt

number (Sc) in a ferri-ferro cyanide coupled system. The Sherwood correlation developed for this system was validated in non-layer forming conditions. Computational fluid dynamics (CFD) simulations conducted with ANSYS 17.0 CFX software were used to determine the wall shear stress on the flat face of the specimen at different impeller rotational speeds. The flow simulations were conducted using the shear stress transport model, which is most appropriate for complex flow systems[108]. The calculated shear stress values were validated by direct measurement of the shear stress at the specimen location using a floating element probe.

The second system that was developed was the single-phase flow loop system. This system was designed to achieve high shear stress turbulent flow conditions of up to 400Pa. The flow in this system was simulated with the aid of CFD to ascertain the flow characteristics in the electrode regions. The mass transfer in this system was calculated while the wall shear stress values obtained from CFD simulations were compared with those derived theoretically.

Task #2: Determine the role of iron carbide on iron sulfide layer development.

In carrying out this task, the corrosion behavior of UNS G10180, a carbon steel with ferritic/pearlitic microstructure, was compared with that of 99.9% pure iron substrate in the same layer forming sour environment. The glass cell system with impeller flow was used in the execution of this task. To highlight the role of iron carbide on iron sulfide layer formation, two testing conditions were used: an environment which promoted iron carbide formation (through a high corrosion rate), and an environment with high FeS saturation (favoring rapid FeS formation and lowering corrosion rates).

The changes in the morphologies and identity of the corrosion product layers were analyzed while their protectiveness was established from the monitored corrosion rates of the substrate.

Task #3: Study the combined role of iron carbide and flow on the development and retention of iron sulfide layers.

This task was accomplished with the execution of high shear stress corrosion experiments in the channel cell of the single-phase flow loop system. The corrosion behaviors of UNS G10180 and 99.9% pure Fe specimens were investigated at variable electrolyte velocities. The impacts of shear stress were investigated by comparing the morphologies of the corrosion product layers developed at low and high shear stress conditions. The contributing effects of iron carbides and shear stress were better understood by relating corrosion rate trends with FeS layer morphologies. The surface of the substrates after removal of the corrosion product layers were also analyzed for any possible localized attack.

Task #4: Characterize the mechanical properties of iron sulfide layers under investigation.

The hardness and adhesive strength of well-defined iron sulfide layers were investigated using a mechanical tester. The iron sulfide layers were developed in the glass cell with impeller flow in conditions identical to that in which the FeS retention experiments were conducted (Task #3). Scratch tests were conducted on the iron sulfide layers and the occurrence of adhesive failures was established from the SEM and EDS analysis of the scratch tracks. Results obtained from this task were converted to shear stress with the aim of making comparisons with results from the FeS retention

experiments. The impact of iron carbide on the interfacial shear strength of FeS layers was also investigated using two substrates, UNS G10180 and 99.9% pure Fe.

Task #5: Modelling of experimental results.

The corrosion behavior was modelled with an already existing in house corrosion model, Freecorp™ V1.0. As stated earlier, this corrosion software was built based on the corrosion model developed by Zheng, *et al.*[39] Since this model does not account for the flow geometries used in this study, the Sherwood correlations for the impeller and channel flow were inputted in this model in order to obtain equivalent corrosion rate predictions. The corrosion rates obtained from this prediction were compared with experimental results. The development of this model has been discussed in Appendix C.

Safety:

All experiments were conducted in accordance with strict H₂S safety procedures as practiced in the Institute of Corrosion and Multiphase Technology (ICMT), Ohio University. The personnel conducting the laboratory experiments were trained and certified by a certified H₂S trainer and are required to undergo a yearly refresher course. Personnel performing experiments in the H₂S room are equipped with a self-contained breathing apparatus (SCBA) and always have a buddy outside with whom he/she maintains constant communication. Finally, no H₂S leakage, irrespective of the amount, was allowed while running experiments. The H₂S in the exit gas stream of the experimental set-up was neutralized by passing through a 1M NaOH solution and then into an activated carbon scrubber before being released to a combustion system. These safety measures were strictly adhered to in order to achieve maximum laboratory safety during experimentation.

CHAPTER 4: DEVELOPMENT AND CHARACTERIZATION OF EXPERIMENTAL SETUPS

4.1 Introduction and Research Goal

Results from almost all small-scale laboratory corrosion tests are viewed with the prospect of using them to predict corrosion in larger scale and real world systems. In order to develop corrosion prediction models, experimental test matrices focus on changing only one test parameter at a time with the aim of maintaining the environmental conditions in the test cell over the entire length of the test. Uncontrolled changes in parameters, such as pH and ferrous ion concentration, will affect the corrosion and precipitation rates in both carbon dioxide and hydrogen sulfide environments[19][109]; this makes data analysis for corrosion prediction problematic. The most desirable data comes from experiments that maintain parameters which influence the water chemistry (pH, gas partial pressures, ferrous ion concentration and temperature) and mass transfer characteristics (the rotation speed of cylinder electrodes, disk electrodes, stir bars and impellers), as consistently as possible, and report any changes observed during experiments. A set of systems using ion exchange resins has been developed and validated to control the solution pH and the ferrous ion concentration during corrosion experiments.

When the concentration of ferrous ions in solution increases due to ongoing corrosion of steel specimens, the solution pH will increase as the balance of ionic species will shift to maintain a neutral charge[38]. This transient increase in solution pH will influence the final results of the corrosion test and, if not properly documented, can cause complete misinterpretations of data and trends. In addition, corrosion prediction models

developed/calibrated from this data would generate inaccurate results. ASTM G31[110] recommends having a greater than 20 mL/cm² solution to specimen surface area ratio as an indirect attempt to minimize transient changes in solution pH and water chemistry, but this procedure does not guarantee that no such changes will occur.

Changes in pH are not as dramatic in CO₂ saturated test environments as compared to H₂S saturated test environments. This is due to the buffering effects of H₂CO₃ (carbonic acid) and the total amount of CO₂ present in solution. When purging with carbon dioxide, there is a continuous dissolution of CO_{2(g)} into solution and the slow hydration step for CO_{2(aq)} provides a constant carbonic acid concentration independent of solution pH (Equations 39 and 40) [111].



However, in hydrogen sulfide conditions, there is always a significant change in the pH of the solution during corrosion test because the dissolved H₂S does not have as much buffering capacity as that observed for the carbonic acid/carbonate/bicarbonate system.

Although H₂S is more soluble than CO₂ under the same environmental conditions, there is a greater number of carbonate species than sulfide species in solution under the same partial pressure and temperature[39]. For this reason, experiments with only H₂S and no CO₂ should be conducted in a system with stable solution chemistry for more accurate corrosion prediction.

Another major challenge associated with the development of new experimental setups capable of generating diverse flowing conditions is the necessity of a clear understanding of the hydrodynamic properties of the flow and their contribution to the entire corrosion process. Hydrodynamic parameters, such as mass transfer coefficients and shear stress, can affect the corrosion behavior of carbon steel depending on the mechanism that governs the corrosion process[112]. In the absence of a corrosion product layer, mass transfer of electroactive species is critical, particularly if the corrosion process is under diffusion control[53]. Under this condition, the mass transport of species from the bulk cannot keep up with the fast rate of electrochemical reactions at the metal surface. Therefore, by directly increasing the velocity of fluid, the mass flux of species to the site of their electrochemical reaction increases, resulting in higher corrosion rates. This does not hold if the corrosion process is activation controlled, where the limiting step is the slow electrochemical reactions. In this case, corrosive species are readily present at the metal surface and corrosion rates, therefore, are unresponsive to changes in fluid velocity. In layer forming conditions, the story becomes more complicated because of the convoluted effects of both mass transfer and shear stress on the whole corrosion process. The formation of a corrosion product layer creates a diffusion barrier, which electroactive species have to navigate through before reaching the metal surface[111][33]. However, such corrosion product layers can be removed chemically or mechanically, with the former being dependent on water chemistry, and the latter on high shear conditions[113]. Morphological changes which may result from mechanical

impacts on layers may affect the entire corrosion process by changing the mass transfer rates of species through these layers to the surface.

A long-standing challenge in conducting flow related corrosion studies in small scale test systems is the selection of an experimental setup with appropriate flow geometry. The flow regime should have well-defined hydrodynamic and mass transfer characteristics. In the past, researchers have used rotating electrodes (disks and cylinder) to conduct flow related studies because of their well-established hydrodynamic features and mass transfer characteristics[53][18][17]. However, a common problem in the use of rotating electrodes for flow studies is the effect of the centrifugal forces generated by the rotating flow on the corrosion product layer[113]. As an example, it has been reported that, in a H₂S environment, rotational speed of a disk electrode may affect the phase distribution of the iron sulfide layer formed[18]. In this case, iron sulfides of uniform stoichiometry were reportedly formed at stagnant and low speed conditions (0.27m/s peripheral velocity), whereas at high velocity (3.2m/s peripheral velocity), the iron content of the FeS layers decreased from the center of the rotating disk, where pyrrhotite and troilite were identified, to the outer circumference, where mackinawite was dominant. In rotating cylinder flow, centrifugal forces may give rise to the formation of more porous corrosion product layers[100]. The possible effects of centrifugal forces on the whole corrosion process add more complexity to the interpretation of corrosion results obtained in rotating flow geometries. This influence is not easily accounted for as it may vary with environmental conditions and rotation rate.

For better understanding of the corrosion behavior of steel materials, there is a need to simplify a testing system in such a way to avoid flowing conditions not representative of pipe flow (centrifugal force effects for example). Therefore, the motivation for this work was to develop and characterize a corrosion experiment setup which has variable fluid (electrolyte) velocity and shear characteristics. Furthermore, this newly developed test equipment has to maintain consistent mass transfer coefficients for multiple metal specimens in the test cell without the influence of centrifugal force.

4.2 Description of Glass Cell with Impeller Setup

The new experimental set up, shown in Figure 4 consists of a glass cell with specimens arranged in stationary positions concentric to the circumference of a central rotating Rushton-type impeller.

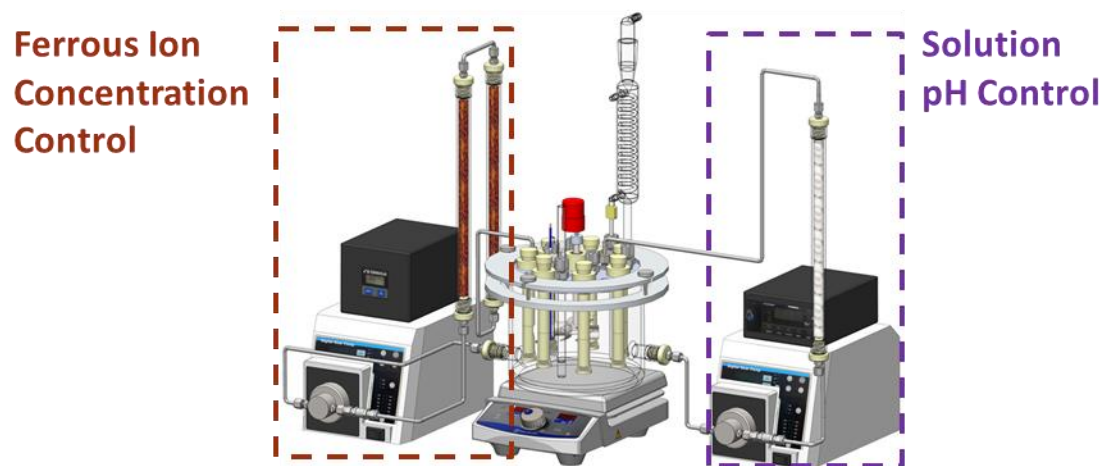


Figure 4: Glass cell with specimen holders, impeller assembly and water chemistry control system

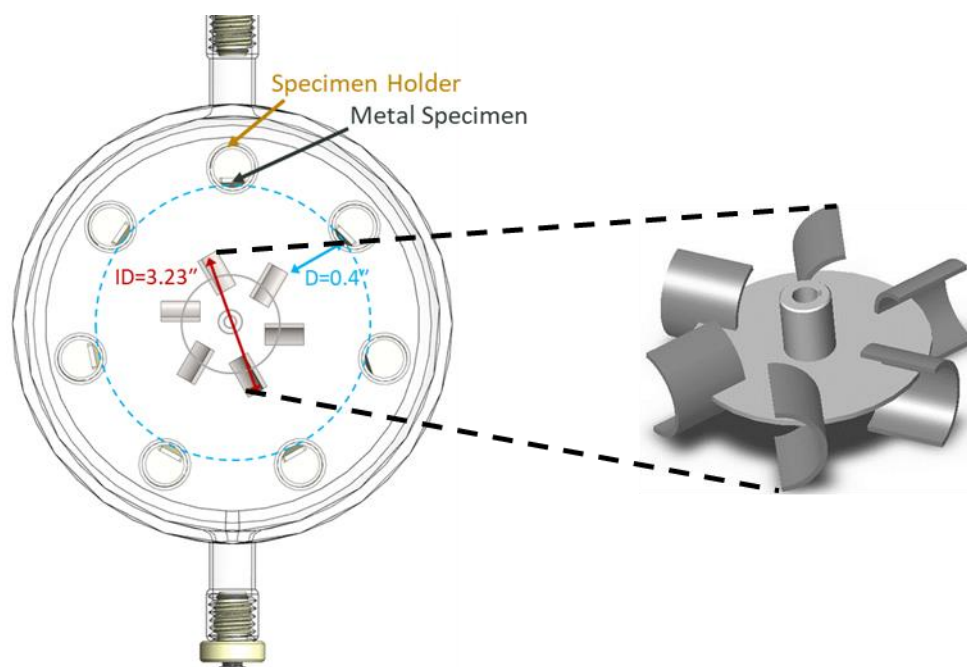


Figure 5: Top view of glass cell showing the concentric arrangement of specimens and the Rushton 6 impeller

The top view of the glass cell, in Figure 5, shows that all the specimens are at an equal distance from the circumference of the impeller. This specimen arrangement ensures that all the mass transfer and wall shear stress characteristics, generated by the impeller generated flow, are equal across the surface of all the specimen. In addition to having a controlled flow, a water chemistry control system is connected to the glass cell to maintain H^+ and Fe^{2+} concentrations in the bulk system. There are two main parts to this solution chemistry control process, the measurement of specie concentration in solution and controlled replenishment to maintain solution chemistry for the desired condition. The H^+ ion concentration is measured *in situ* with a pH probe immersed in the solution. The pH probe is connected to a pH control meter which turns on a pump when the solution pH goes above a set value. The pump draws solution from the glass cell,

passes it through a column containing an H-form ion-exchange resin, and delivers it back into the glass cell. This process continues until the solution pH is restored to the set value. A slightly different method is used for the control of the Fe^{2+} in the bulk solution. The Fe^{2+} concentration is measured *ex situ* by extracting a solution sample from the glass cell and conducting spectrophotometric measurements. Depending on the ferrous ion concentration measured, a timer is adjusted to control the on-and-off cycle of a pump that pushes solution through a column containing a Na-form resin where ferrous ions in the solution are replaced with sodium ions.

The resins used for this operation are cross-link polymeric compounds with mobile cations which can be replaced with ions of equal charge and higher affinity [114]. The ability of this resin to efficiently exchange cations makes it very useful for this operation. Typically, larger ions with high valence have higher affinity and replace ions of smaller size and less valence. The order of affinity of common ions in the resin employed in this work is: $\text{Hg}^{2+} < \text{Li}^+ < \text{H}^+ < \text{Na}^+ < \text{K}^+ \approx \text{NH}_4^+ < \text{Cd}^{2+} < \text{Cs}^+ < \text{Ag}^+ < \text{Mn}^{2+} < \text{Fe}^{2+} < \text{Cu}^{2+} < \text{Ni}^{2+} < \text{Co}^{2+} < \text{Ca}^{2+} < \text{Sr}^{2+} < \text{Pb}^{2+} < \text{Al}^{3+} < \text{Fe}^{3+}$. Figure 6 shows the chemical structure of the resin, which consists of a sulphonated polystyrene functional group and the mobile cation.

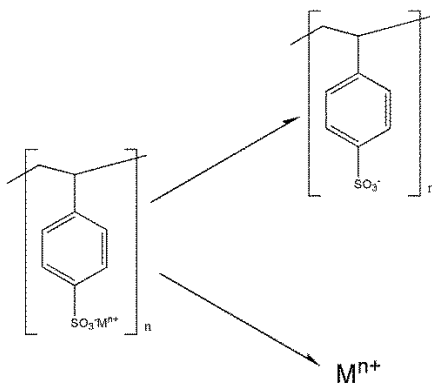
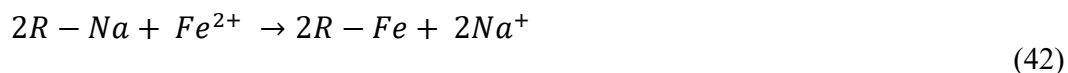


Figure 6: Resin consisting of a sulphonated polystyrene structural moiety and a mobile cation

The Na-form and H-form resins have been used with great success in CO₂ corrosion experiments [114], and their application and effectiveness are tested in H₂S environments in the current study. The H-form resin replenishes the bulk H⁺ concentration by releasing the H⁺ mobile cation from the H-form resin and replacing it with sodium ion from the bulk solution (see Equation 41).



Similarly, the excess Fe²⁺ in the bulk is removed when Fe²⁺ replaces the Na⁺ as the mobile cation attached to the polymeric backbone.



Unlike for well-studied rotating cylinder and straight pipe flow, where mass transfer behavior is characterized with the Eisenberg [16] and Berger and Hau [115] correlations, the hydrodynamic properties of the flow in this experimental setup are unknown. In order to achieve a full understanding of the hydrodynamic properties of the new glass cell setup, the mass transfer of the electrochemical species as well as the flow related shear

stress exerted on the specimens need to be characterized. Therefore, the objectives for the current work were:

- Characterize the mass transfer of electroactive species in solution by investigating the dependence of the Sherwood number (Sh) on the Reynolds number (Re) and the Schmidt number (Sc).
- Calculate wall shear stress exerted on specimen surfaces at different impeller speeds by conducting computational fluid dynamics (CFD) simulations.
- Validate the developed Sherwood correlations and wall shear stresses obtained.

To achieve the first objective, a ferri-ferro cyanide coupled system was used to characterize the mass transfer of species in the solution while the second objective was achieved by conducting a computational fluid dynamic simulation using ANSYS CFX software. To test the validity of generated results, the developed Sherwood correlation was tested in non-layer forming corrosive environments, i.e., to avoid formation of corrosion products. Similarly, the CFD simulations were validated by comparing wall shear stress values calculated at different impeller speeds with those directly measured with a floating element probe.

4.2.1 Mass Transfer Characterization of Glass Cell with Impeller

The reduction of ferricyanide ions to ferrocyanide ions at a nickel electrode has been widely used to characterize mass transport in electrochemical systems [16]–[18].



By measuring the mass transport controlled limiting current associated with the above reduction reaction, the mass transfer coefficient, k_m , can be calculated using the equation:

$$k_m = \frac{i_{lim}}{nFC_b} \quad (44)$$

Where i_{lim} is the limiting current density ($A.m^{-2}$), n is the number of electron transferred in the electrochemical reaction (1 equiv mol^{-1}), F is the Faraday constant ($96485 \text{ C mol}_{\text{equiv}}^{-1}$) and C_b is the concentration of the ferricyanide ions in solution (mol.L^{-1})

Equation 44 is used only when the electrochemical reaction at the electrode surface is under complete mass transport control, as indicated by a clear limiting current plateau.

Development of Sherwood Correlation

The composition of the electrolyte used for this study is 0.5M sodium hydroxide, 0.005M $K_3Fe(CN)_6$ and 0.01M $K_4Fe(CN)_6$. Freshly deionized water with 0.5M sodium hydroxide was sparged with a fast stream of nitrogen for 2 hours and the concentration of the dissolved oxygen measured by connecting the exit stream gas to an oxygen sensor. Nitrogen sparging continued until the concentration of dissolved oxygen was below 5ppb. $K_3Fe(CN)_6$ and $K_4Fe(CN)_6$ were introduced into the solution while the oxygen concentration was monitored (<5ppb). To avoid any oxygen contamination, the cell was isolated from the atmosphere by connecting the port for the exit gas to a water trap. The glass cell was shrouded with a reflective insulating aluminum wrapper to avoid the ultraviolet degradation of the electrolyte during the experiment.

A nickel electrode was pretreated by polishing with silicon carbide abrasive paper to a 600-grit finish and rinsing with isopropanol in an ultrasonic bath, to ensure a uniform surface area. The counter electrode was a platinum-coated titanium mesh and the reference electrode was an Ag/AgCl electrode. Potentiodynamic sweeps were conducted

at different impeller speeds ranging from 50 to 250rpm (at 50 rpm intervals) and at temperatures of 30°C, 40°C and 50°C. The cathodic curves were obtained by polarizing from the open circuit potential (OCP) to a potential of 0.87V below the OCP. The OCP was monitored to ensure that it returned to its original value before the execution of another sweep. The nickel electrode was polarized in the anodic direction up to 0.325V above the open circuit potential. The scan speed for both cathodic and anodic sweeps was 0.5mV/s. After the current vs. potential measurements, the average of the current density at the plateau portion of the cathodic curves was used for analysis.

Results

Figure 7 shows the potential vs. current density curves obtained at the different rotational speeds and temperatures.

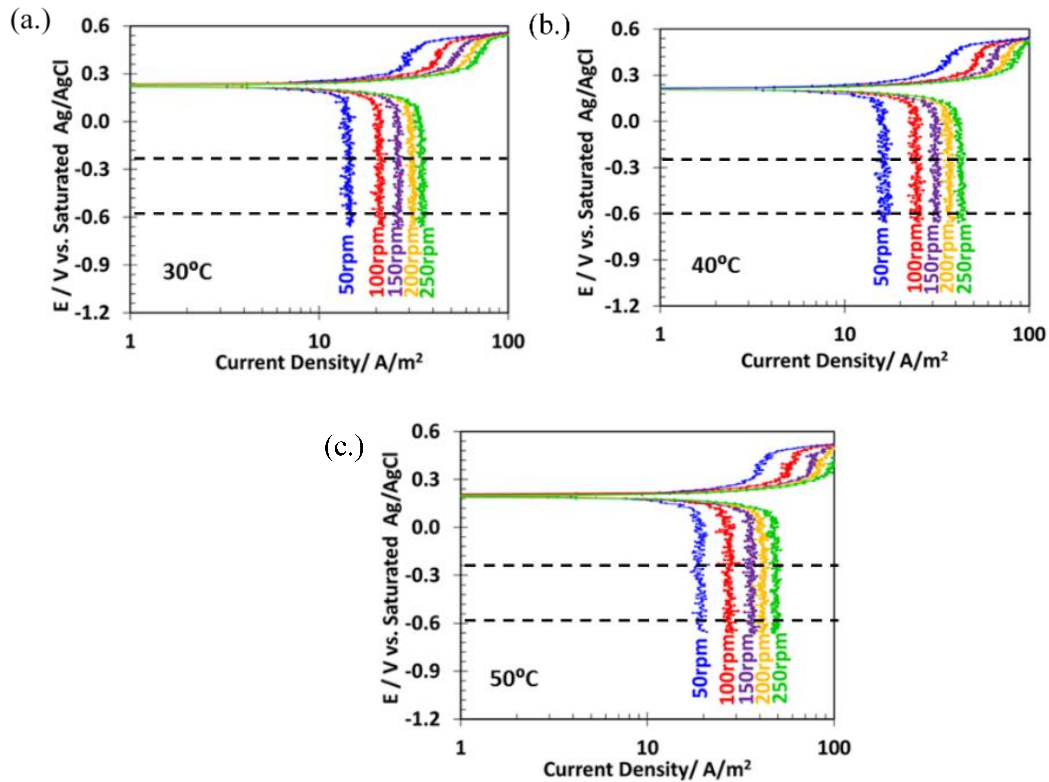


Figure 7: Polarization curves at impeller rotational speed ranging from 50-250rpm at electrolyte solution of (a.) 30°C (b.) 40°C (c.) 50°C

The curves show that the OCP was in the range of 0.24V to 0.20V vs Ag/AgCl while the limiting current plateau started from 0.17V below the OCP. These are similar to the values obtained by Ieamsupong[107] under similar conditions. The average of the limiting current within the potential range of -0.24V to -0.6V vs. Ag/AgCl (shown by the dotted lines) was used as the i_{lim} in Equation 44 for calculating the mass transfer for each of the conditions.

These results, with other electrolyte properties, fit to the correlation of the form:

$$Sh = aRe^x Sc^y \quad (45)$$

This correlation is widely known as the Sherwood correlation. The Sherwood (Sh), Reynolds (Re) and Schmidt (Sc) numbers are defined as follows:

$$\text{Sh} = \frac{k_m d}{D} \quad (46)$$

$$\text{Re} = \frac{d^2 N}{\nu} \quad (47)$$

$$\text{Sc} = \frac{\nu}{D} \quad (48)$$

Where, k_m = mass transfer coefficient (m/s), D = diffusion coefficient of the electrochemical specie (m^2/s), d = diameter of impeller (m), ν = kinematic viscosity (m^2/s), N = Revolutions per second.

Equation 45 can be rearranged in a logarithmic form to get Equation 49:

$$\log(\text{Sh}) = \log a + x \log(\text{Re}) + y \log(\text{Sc}) \quad (49)$$

By conducting a multiple regression analysis on the values of the $\log \text{Sh}$, $\log \text{Re}$ and $\log \text{Sc}$ at different rotational speeds and temperature, the a , x and y coefficients in Equation 49 were determined to be 1.034, 0.612 and 0.33. By substituting these coefficients in Equation 45 the mass transfer correlation for the impeller flow in the glass cell shown in Equation 50 was developed.

$$\text{Sh} = 1.034 \text{Re}^{0.612} \text{Sc}^{1/3} \quad (50)$$

A plot of $\text{Sh}/\text{Sc}^{1/3}$ vs. $\text{Re}^{0.612}$ shown Figure 8 yields a straight-line graph with a slope of 1.0338, origin at 0 and an R^2 value of 0.9752.

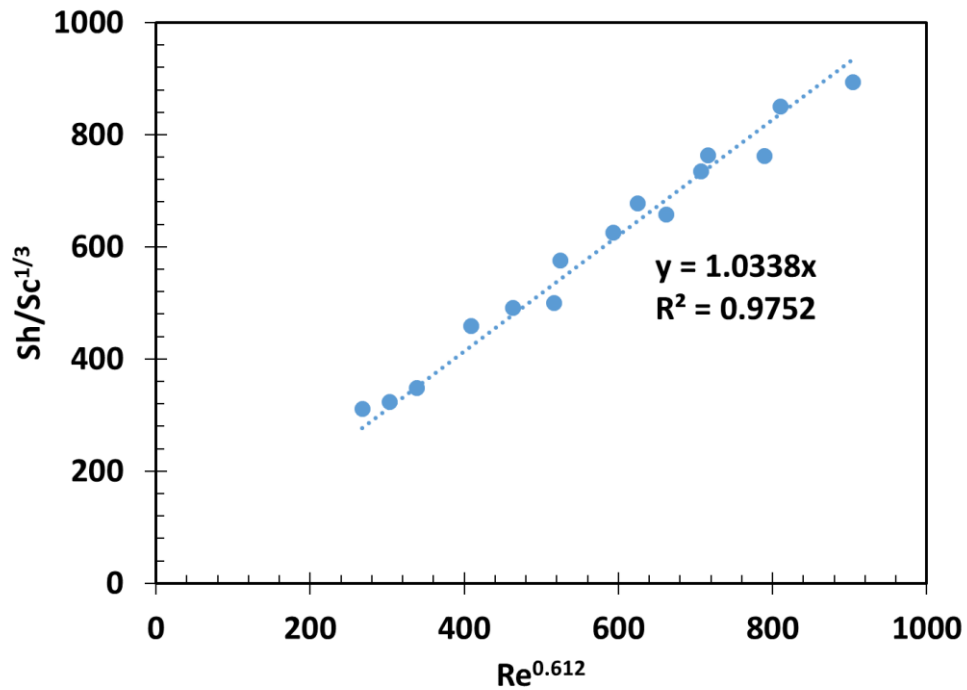


Figure 8: A straight line fit of the mass transfer correlation developed for the impeller flow in the glass cell

The Sherwood correlation for the mass transport of species in a straight pipe is given by [115]:

$$Sh = 0.0165 Re^{0.86} Sc^{0.33} \quad (51)$$

By matching the mass transfer coefficient in straight pipe flow and impeller flow, the expression for the pipe velocity equivalent to different impeller speeds was developed (Equation 52). Figure 9 shows the velocity in a 0.2m diameter pipe equivalent to different impeller rotational speeds.

$$V = \left(62.42 \times N^{0.612} \times d_{pipe}^{0.140} \times d_{imp}^{0.224} \times \nu^{0.248} \right)^{1.163} \quad (52)$$

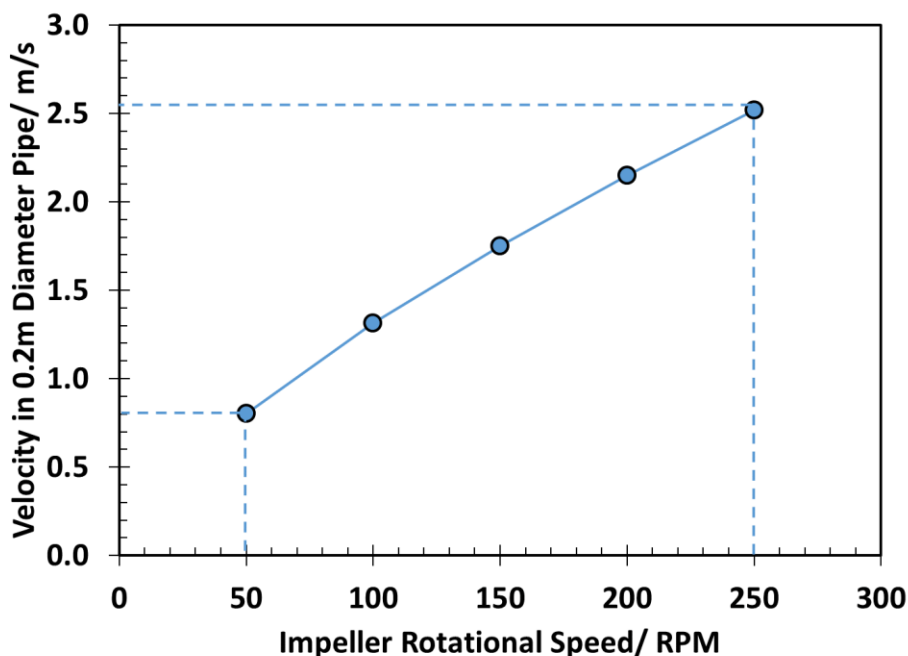


Figure 9: Impeller rotational speed in glass cell vs linear velocity in 0.2m diameter pipe at equal mass transfer coefficient.

Validation of Mass Transfer Correlation

A 99.9% pure Fe substrate was cathodically polarized at a speed of 1 mV/sec in a solution sparged with 1 bar nitrogen at pH of 5.00, 30°C and 250 rpm. At this condition, the dominant cathodic reaction was the hydrogen reduction reaction. The limiting current is controlled by mass transfer and should be sensitive to flow. The mass transfer correlation developed for the flow in this system was checked by modelling the cathodic polarization curve at different impeller velocities and comparing the results with the curves from experiments.

Modelling of Polarization Curves

Cathodic Reaction

The total current density for the cathodic reaction is the sum of the current due to the hydrogen ion reduction and the water reduction reaction.

Hydrogen reduction reaction:

For the hydrogen reduction reaction (Equation 53), the total current density is the harmonic mean of the charge transfer current and the mass transfer limiting current [116].

$$\frac{1}{i_{H^+}} = \frac{1}{i_{ct,H^+}} + \frac{1}{i_{lim,H^+}^d} \quad (53)$$

The charge transfer current density can be calculated with the Tafel equation:

$$i_{ct,H^+} = i_{0,H^+} \times 10^{-\frac{\eta}{b_c}} \quad (54)$$

Where $b_c = 0.120$ V/decade at 30°C, and i_{0,H^+} is the exchange current density for hydrogen = 0.014A/m², and η is the overpotential in V.

The diffusion limiting current, i_{lim,H^+}^d , shown in the Equation 55 is given by:

$$i_{lim,H^+}^d = k_{m,H^+} F C_{H^+} \quad (55)$$

k_{m,H^+} is the flow dependent mass transfer coefficient of the hydrogen calculated by substituting Sh in Equation 50 with Equation 46 the developed mass transfer correlations.

$$Sh = \frac{k_{m,H^+} d_{RCE}}{D_{H^+}} = 1.034 Re^{0.612} Sc^{1/3} \quad (56)$$

C_{H^+} is the hydrogen ion concentration.

Water reduction reaction:



With the ample presence of water at the metal surface, the water reduction reaction can be said to be under charge transfer control. The current density associated with this process can be calculated by using the Tafel equation:

$$i_{H_2O} = i_{0,H_2O} \times 10^{-\frac{\eta}{b_c}} \quad (58)$$

Where b_c is the Tafel slope (0.120V/decade) and i_{0,H_2O} is the exchange current density for water.

Anodic Reaction

The anodic reaction in the present experiment is iron dissolution.



This reaction is under charge transfer control and shows Tafel behavior especially close to the open circuit potential.

$$i_{Fe^{2+}} = i_{0,Fe^{2+}} \times 10^{\frac{\eta}{b_a}} \quad (60)$$

Figure 10 shows a good agreement between the experimentally measured cathodic curve and the modelled potentiodynamic sweep with the mass transfer correlation obtained for this system.

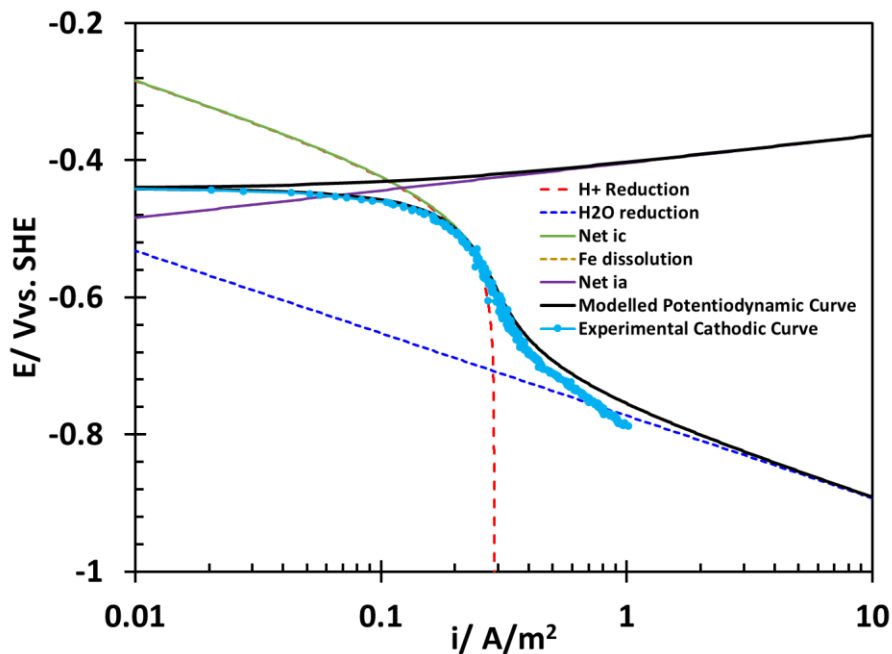


Figure 10: Comparison of the modelled potentiodynamic sweep with the curve from the cathodic polarization of 99.9% pure Fe in 1 bar N_2 , pH 5.0, 30°C and 250 rpm impeller velocity

4.2.2 Shear Stress Calculation on the Specimen Surface

To determine the shear stress on the specimen surface, a computational fluid dynamic simulation of the flow in the glass cell created by a rotating Rushton Scada 6 impeller was conducted. In conducting flow simulations, the use of a correct turbulence model was critical to the convergence of calculations and the correctness of the results. In the simulation of turbulent flow, two-equation models are generally used to capture the momentum transfer caused by turbulent eddies. These models are based on the Boussinesq hypothesis which assumes that the Reynolds stress tensor is proportional to the product of the strain rate and the isotropic turbulent viscosity[117,118]. This is a sensible assumption since the majority of the models used for flow simulations are based

on the Reynold's averaging of the Navier-Stokes equation. The most common of such models, K- ϵ , solves the transport equations for the turbulent kinetic energy, K, and the turbulent energy dissipation rates, ϵ .

The K- ϵ model has been used extensively in the past due to its simplicity and serves as a starting point for flow field simulations[119–124]. However, the main limitation of this model is its poor treatment of near wall regions. Due to the inability of this model to integrate near wall layers in its calculation, it applies a standard wall treatment, which does not reflect the real behavior of the viscous sublayers.[125] This problem was addressed by the development of the K- ω model, which is based on turbulent kinetic energy, K, and turbulence eddy frequency, ω [118]. The K- ω model captures the actual near wall behavior by applying the Dirichlet boundary conditions, in this case for no-slip [126]. While this near wall treatment gives more details about the viscous sublayer, it tends to be over sensitive in the shear free regions by assuming transition flow regimes as being fully turbulent. Since the K- ϵ model gives good results in the free stream regions and the K- ω model offers better near wall treatment, these two models were blended, and with the addition of a turbulence limiter close to the walls, the shear stress transport (SST) model was formulated [127].

A blending function was integrated into this model for the purpose of switching from the k- ϵ model at the shear free region to the k- ω model at the boundary layer regions close to the wall[108]. Users of the SST model have merited it for good prediction in adverse pressure gradients and separating flow conditions[118,127]; for this reason, the SST model has been implemented in the simulation of the impeller flow in the glass cell.

The simulation process involved the design of the geometry, creating a suitable mesh and setting the boundary conditions and the simulation model for proper calculation.

Computational Fluid Dynamic Simulation of Impeller Flow in a Glass Cell and Calculation of Wall Shear Stress

Geometry: Figure 11 shows the geometry of the glass cell and impeller designed in Solidworks™ and imported into the ANSYS design modeler.

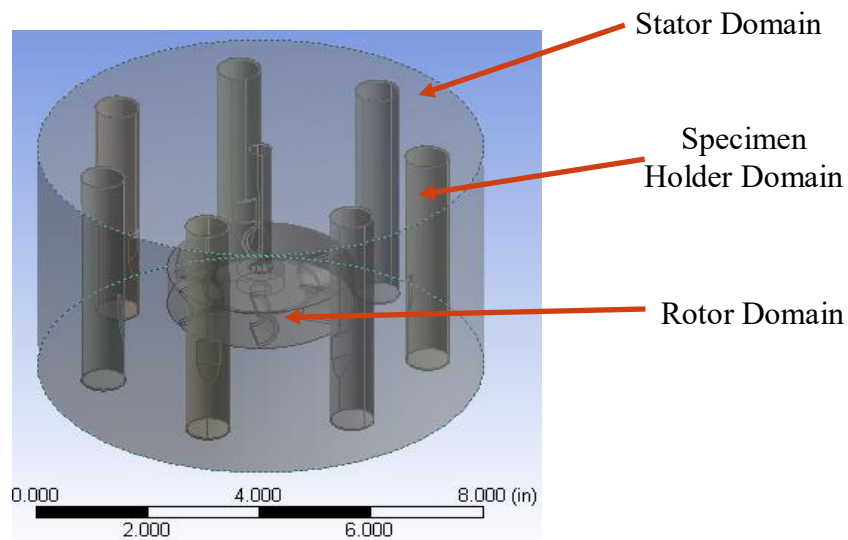


Figure 11: Glass cell geometry designed in Solidworks showing the Stator, specimen holder and rotor domain

To simulate the impeller flow in the glass cell, the geometry shown in Figure 11 has the diameter of the glass cell (8") and a height corresponding to the solution level (4.85"). The bottom clearance of the glass cell from the impeller is 1.37" and the bottom clearance from the specimen holder is 0.28".

As indicated in Figure 11, the glass cell is categorized into three different domains:

- Rotor (rotating) domain: Region around the impeller assembly.
- Specimen holder domain: Region around the specimen holder.
- Stator (stationary) domain: Region outside the rotor and the specimen holder domain.

For easy handling, these domains were made distinct from each other with the Boolean function in the ANSYS designmodeler. However, the areas where the domains connect are depicted by an interface. Therefore, the two interfaces in this system are the stator/specimen holder domain interface and the stator/rotor domain interface.

Meshing:

Domains are required to be divided into discrete cells for the purpose of solving the equations. Meshing is critical to the resolution and accuracy of the simulation results since equations are solved at cell or nodal locations. The mesh around areas of interest are typically refined for better accuracy of the results. Figure 12 shows the mesh created for the current system.

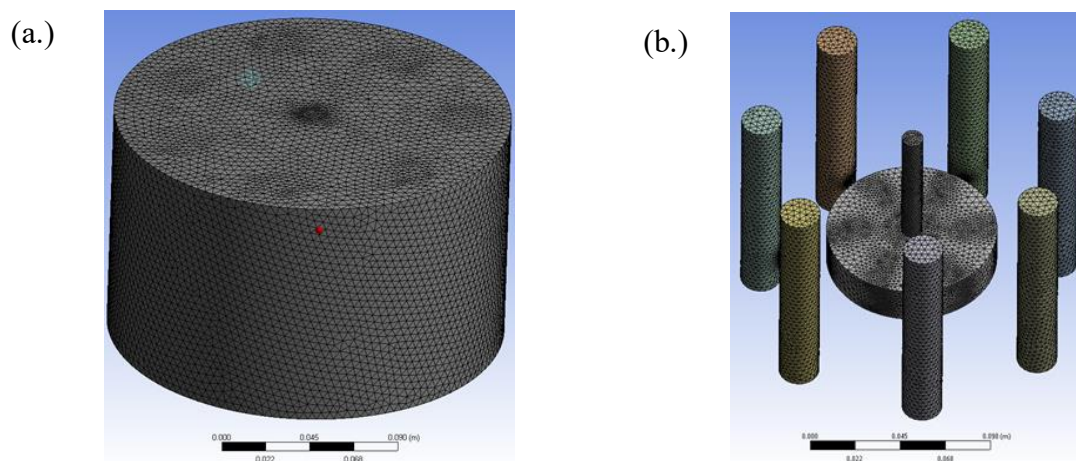


Figure 12: Meshing of the glass with impeller system into discrete cells (a.) stator domain (b.) rotor and specimen holder domains

Due to the complexity of the geometry, triangular mesh elements were used to capture all the areas of the system. Since the key areas of interest are the specimen locations and the impeller tip, the mesh around these areas were more refined in order to achieve a better resolution of results. Wall y^+ is used to evaluate if the mesh used for simulations is appropriately refined. For a good wall treatment, a target y^+ of below 100 was used as a criterion for the mesh size. This was based on the studies performed by Menter, *et al.*, [108], where the variation of the wall shear stress calculated in Couette flow simulations, using a shear stress transport simulation model, was less than 2% for wall y^+ of 0.2, 9 and 100. A smaller y^+ and better wall treatment can be achieved with a shorter nodal distance. Equation 59 shows that the wall y^+ is dependent on the friction velocity (u^*), the first nodal distance from the wall (y) and the kinematic viscosity (ν).

$$y^+ = \frac{u^* y}{\nu} \quad (61)$$

Where $u^* = \sqrt{\frac{\tau_w}{\rho}}$

The properties and statistics of the mesh shown in Figure 12 are presented in Table III.

Table III: Mesh properties and statistics

Element Properties	Specification
Minimum face size	$4.5 \times 10^{-5} \text{m}$
Maximum face size	$4.5 \times 10^{-3} \text{m}$
Element growth rate	1.2
Number of elements	511292
Number of nodes	107607

Problem Setup:

The material used in the current simulation was water at 30°C, atmospheric pressure and buoyancy properties of 9.8m/s corresponding to the force of gravity. A no slip boundary condition was applied to the specimen holder walls and the body of the glass cell. At the rotor/stator domain interface and specimen holder/stator domain interface, a conservative flux for mass and momentum was applied to ensure the transfer of mass and momentum across the interfaces were conserved. An opening boundary condition was applied to the top of the geometry in order not to impose any restriction to the flow. A transient state calculation was carried out for a total time of 10 hours with a time step starting from 60 seconds to 1800 seconds.

Turbulence model:

As stated earlier, the turbulent flow generated by the impeller in the glass cell was simulated using the shear stress transport model. This model calculates two main transport equation, the turbulent kinetic energy and the dissipation rate equation [108,128].

The transport equation for the specific turbulent kinetic energy, k (m^2s^{-2}), for this model is given as:

$$\frac{\partial(\rho k)}{\partial t} + \frac{\partial(\rho u_j k)}{\partial x_j} = \tilde{P}_k - \beta^* \rho \omega k + \frac{\partial}{\partial x_j} \left[(\mu + \sigma_k \mu_t) \frac{\partial k}{\partial x_j} \right] \quad (62)$$

Specific turbulent dissipation rate, ω (s^{-1}):

$$\begin{aligned} \frac{\partial(\rho \omega)}{\partial t} + \frac{\partial(\rho u_i \omega)}{\partial x_i} \\ = \frac{\gamma}{\nu_t} P - \beta^* \rho \omega^2 + \frac{\partial}{\partial x_i} \left[(\mu + \sigma_\omega \mu_t) \frac{\partial \omega}{\partial x_i} \right] + 2(1 - F_1) \rho \omega_w^2 \frac{1}{\omega} \frac{\partial k}{\partial x_i} \frac{\partial \omega}{\partial x_i} \end{aligned} \quad (63)$$

The first terms on the left side of Equations 62 and 63 represent the rate of change of k or ω respectively, while the second terms are the rate convective transport terms. The right side of the equations are comprised of the production rate term, the destruction rate term, and the diffusion transport term. The blending function, F_1 , as earlier described and shown in Equation 28, is given by:

$$F_1 = \tanh \left\{ \left(\min \left[\max \left(\frac{\sqrt{k}}{\beta^* \omega y}, \frac{500\nu}{y^2 \omega} \right), \frac{4\rho\sigma_{\omega 2} k}{CD_{k\omega} y^2} \right] \right)^4 \right\} \quad (64)$$

In the shear free region, F_1 is equal to zero and Equation 63 becomes the k - ϵ model, while at the boundary layer region, F_1 is equal to one and Equation 63 becomes the k - ω model.

In Equation 64, y is the distance to the nearest wall and $CD_{k\omega} = \max \left(2\rho\sigma_{\omega 2} \frac{1}{\omega} \frac{\partial k}{\partial x_i} \frac{\partial \omega}{\partial x_i}, 10^{-10} \right)$.

In order to prevent excessive turbulence in the stagnation zones, a turbulent production limiter, given in Equation 65, is incorporated into the SST model.

$$P_k = \mu_t \left[\frac{\partial U_i}{\partial x_i} + \frac{\partial U_j}{\partial x_j} \right] \rightarrow \tilde{P}_k = \min (P_k, 10 \cdot \beta^* \rho \omega k) \quad (65)$$

μ_t in Equation 63 is the eddy viscosity and is defined by:

$$\nu_t = \frac{k}{\omega} \quad (66)$$

This equation for the eddy viscosity does not factor in the transport of turbulent shear stress which is its limitation of the k - ω model. The turbulent shear stress transport

is based on the assumption that shear stress in the boundary layer region is proportional to the turbulent kinetic energy, k:

$$\tau = \rho a_1 k \quad (67)$$

The shear-stress transport (SST) model thus satisfies the transport of turbulent shear stress in its eddy viscosity model by the following equation;

$$v_t = \frac{a_1 k}{\max(a_1 \omega, SF_2)} \quad (68)$$

The above equations ensure that in a situation of adverse pressure gradient Equation (67) is satisfied and in other situations Equation (66) is satisfied. This is the main advantage of the SST model over the k- ω model.

Definition of terms:			
ρ	density (kg/m ³)	γ	modeling constant
u	incident free-stream (m/s)	σ_ω	modeling constant
\tilde{P}_K	effective production rate of k (kg/m.s ³)	σ_k	modeling constant
P	rate of production of ω (kg/m ³ .s ²)	a_1	modeling constant
μ	eddy viscosity (kg/m.s)	F_1	blending function
ν_t	kinematic eddy viscosity (m ² /s)	F_2	blending function
y	first nodal distance from the wall (m)	β^*	modeling constant
$CD_{k\omega}$	cross-diffusion term (kg/m.s ²)	S	Strain rate (s ⁻¹)

Results:

After the execution of the calculation for 10 simulation hours, the results were analyzed using the ANSYS CFX-post. The lateral view (at the impeller center level) of the velocity vectors at 250rpm and 50rpm impeller speeds presented in Figure 13 shows the velocity and direction of the fluid flow. Since these simulations are transient, the images are a snapshot of the impeller position with respect to the specimen holders. For this reason, the velocity profile from each impeller blade is different. In the velocity contours presented in Figure 14, the maximum velocity occurred at the tip of the impeller and travelled towards the specimen holder region. This velocity distribution is commonly observed in impeller flow simulations irrespective of the shape of the impeller blade or the clearance of the impeller from the bottom of the stator region[118][129][123,130].

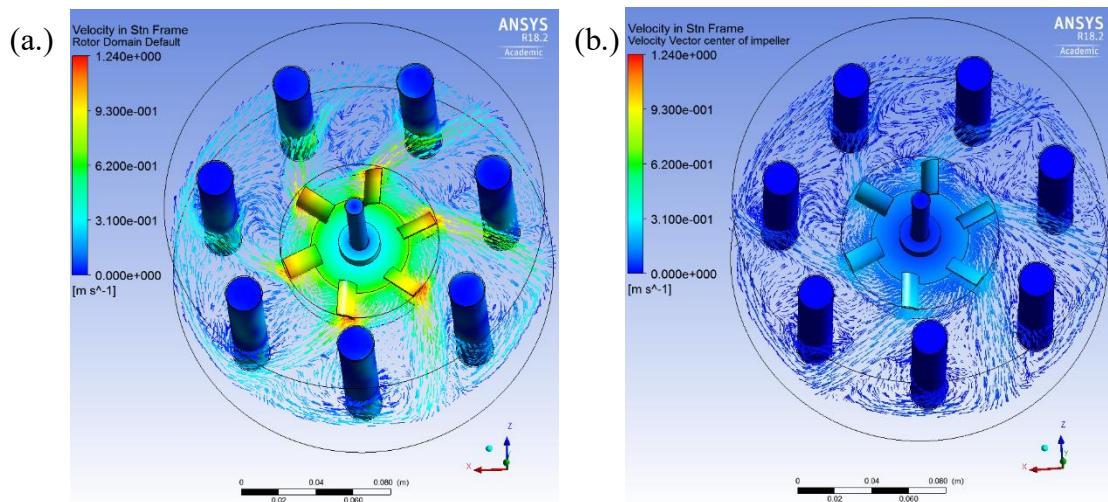


Figure 13: Velocity vectors of water in glass at temperature of 30°C and impeller rotational speed of (a.) 250rpm and (b.) 50rpm

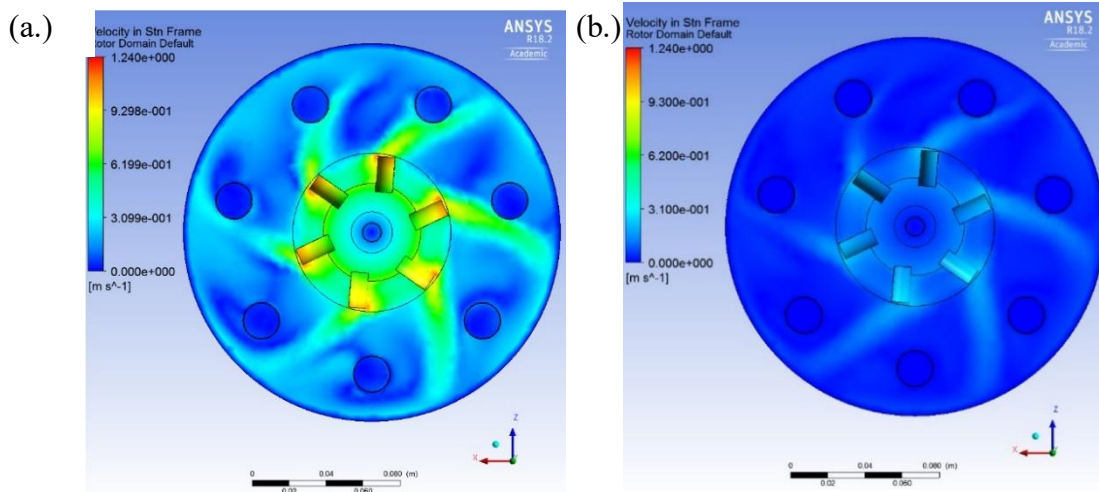


Figure 14: Velocity contours of water in glass at temperature of 30°C and impeller rotational speed of (a.) 250rpm and (b.) 50rpm

As the impeller rotates, specimens experience different flow intensities at a frequency that is dependent on the impeller rotational speed. The wall shear stress at the different specimen locations differ from each other since the simulation type is transient and the information about the hydrodynamic properties of the fluid can only be obtained at particular timeframes. In order to have a common ground for comparison, the specimen location with the maximum shear stress was adopted for calculation. The maps presented in Figure 15 show that the maximum wall shear stress values at the specimen wall location at 250rpm and 50rpm were 2.4Pa and 0.9Pa, respectively. The scales of the contours in Figure 15 (a.) and Figure 15 (b.) were made to capture the wall shear stress distribution on the specimen wall at the different impeller rotational speeds. However, the average of the wall shear stress of all the nodal point on the specimen location at each impeller rotational speed was calculated and is presented in Figure 16(a.).

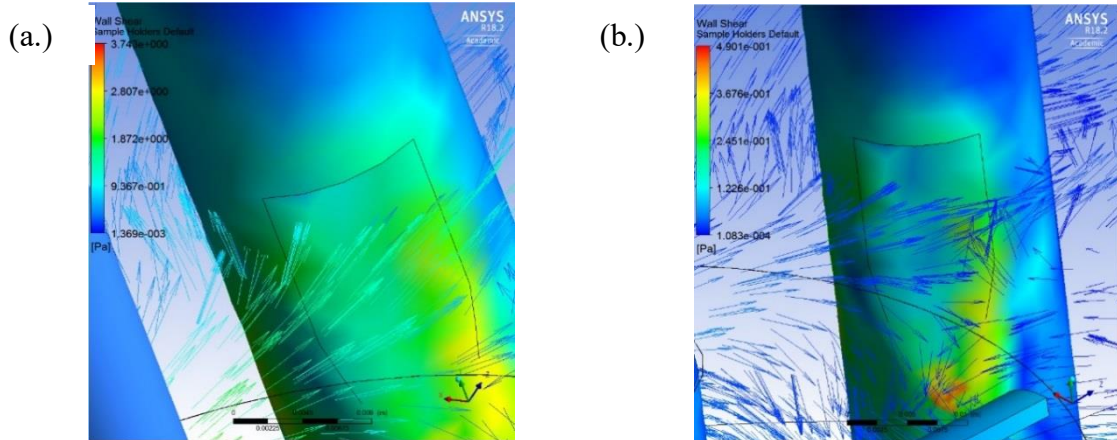


Figure 15: Wall shear stress at specimen location resulting from fluid flow at impeller rotational speeds of (a.) 250rpm and (b.) 50rpm

The plot of the wall shear stress at different impeller rotational speeds shows that the relationship between them is non-linear, a major revelation from the current CFD simulation. The shear stress at equivalent pipe velocity (for a 0.2m diameter pipe) presented in Figure 16 (b.) shows that the pipe flow geometries generate approximately eight times higher shear stress than the impeller flow in the glass cell. This is a desirable characteristic of the flow in this glass cell since the aim of developing this system is to limit any possible wall shear stress effects.

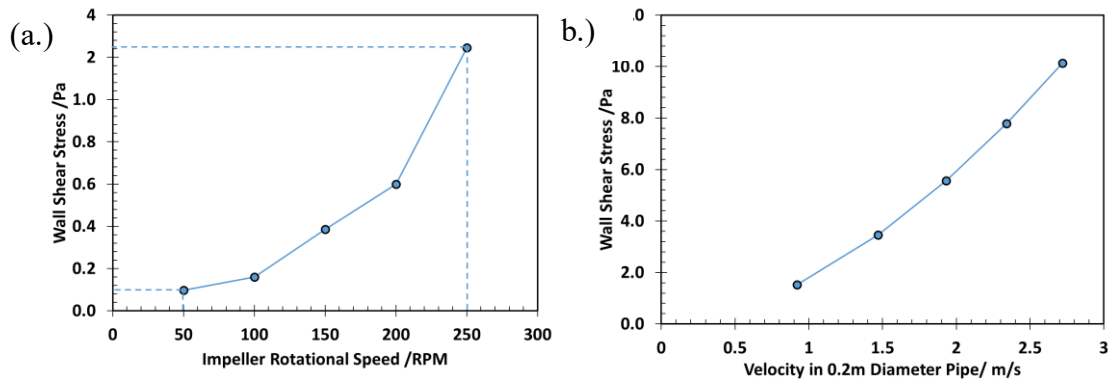


Figure 16: (a.) Wall shear stress obtained from CFD simulation of glass cell with a rotating impeller (b.) Calculated shear stress in a 0.2m diameter pipe at equivalent velocity

The wall y^+ at the specimen location for the current simulation ranged from 5.4 at 50rpm to 18.1 at 250rpm. These y^+ values are within the acceptable limits for a good wall treatment [108] and, thus, lends more credibility to the calculated wall shear stress values.

Validation of Calculated Shear Stress Values

To validate the shear stress values calculated from CFD simulations, a floating element probe identical to that used by Li, *et al.*, [20], was mounted in the specimen location to directly measure the wall shear stress. Direct shear stress measurements using this type of probe have been shown to be accurate and details about its components can be found in the paper published by Li, *et al.*, [20]. The floating element probe comprises of an assembly of a floating element, a cantilever and two optical fiber strain gauges. Fluid flow across the floating element causes a lateral displacement of the cantilever which in turn changes the optical spectra reflected by the strain gauges. These spectra are then processed, and with the use of some mechanical calculations, are converted to wall shear stress [20]. Figure 17 shows the glass cell arrangement, where the wall shear stress

probe was flush mounted at the specimen location with the concentric arrangement of the corrosion specimens around the impeller being maintained.

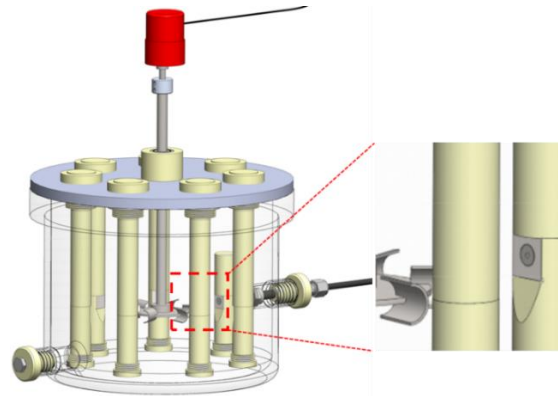


Figure 17: Glass cell arrangement with installed floating element probe for the direct measurement of shear stress at the specimen location.

Measurements were collected for 4 to 5 seconds at rotational speeds from 50 rpm to 250 rpm in increments of 50 rpm. The average of the shear stress data acquired between 2 and 3 rotational speeds was compared with those calculated from the CFD simulations. Figure 18 shows a typical data set acquired from a test at 250rpm impeller rotational speed.

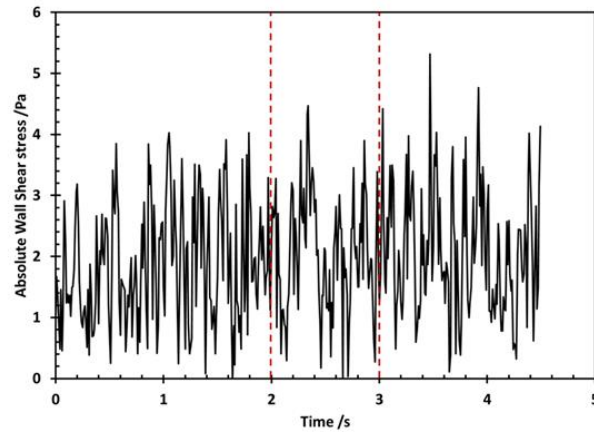


Figure 18: Wall shear stress from direct measurements at impeller rotational speed of 250rpm using the floating element probe installed on the specimen location.

The results presented in Figure 19 show that the WSS from direct measurements have higher values than those from simulations. These higher shear stresses may result from the turbulence caused by the non-continuous surface of the installed WSS probe or the several assumptions made in the CFD simulations. Nonetheless, the shear stress values from the direct measurements are within the same magnitude as the shear stress obtained from the CFD simulations.

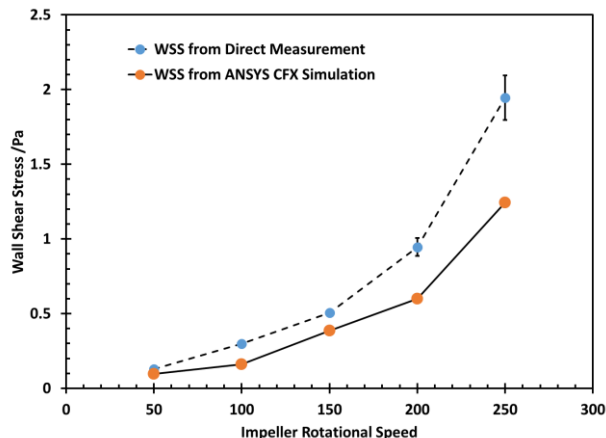


Figure 19: Comparison of wall shear stress at different impeller rotational speed obtained from CFD simulation and direct measurement.

4.2.3 Development of Iron Sulfide Layers in Controlled Solution Chemistry

The corrosion behavior of 99.9% pure Fe was investigated in 1 wt. % NaCl solution, deoxygenated with N_2 then sparged with 10% by volume of H_2S in admixture with N_2 , at bulk solution pH 6.00 and $30^\circ C$. The corrosion rates were monitored at impeller rotational speeds of 50 rpm and 250 rpm by conducting LPR measurements throughout the exposure period using a Gamry 600 potentiostat. A three-electrode system was used, where an Ag/AgCl probe was used as the reference electrode while a platinum coated mesh was used as the counter electrode and the test specimen was the working electrode. The LPR measurement was conducted by polarizing the working electrode $\pm 5mV$ versus the open circuit potential with a scan rate of $0.125mV/s$. All LPR corrosion rates were obtained by dividing the polarization resistance by a B value of $0.023 V/decade$. This experiment was designed to test the efficiency of the developed corrosion testing setup, in terms of its usage and its effective solution chemistry control (especially in an H_2S environment), for an extended testing period. Figure 20(a.) and Figure 20(b.) shows

good control of the solution pH and Fe^{2+} concentration, with the bulk solution pH being within 0.03 of the set pH while the ferrous ion concentration measured throughout the experiment was maintained below 0.2ppm.

Table IV: Test matrix for the development of Iron Sulfide Layers in Controlled Solution Chemistry

Operating Parameter	Specification
Material	99.9% pure iron
H_2S Partial Pressure	0.1 bar
Total Pressure	1.01 bar (balance N_2)
Electrolyte	1 wt.% NaCl
Solution pH	6.0
Temperature	30°C
Expected FeS Phase	Mackinawite
Impeller Speed	50rpm, 250rpm
Test Duration	4 days
Measurement Methods	LPR, EIS

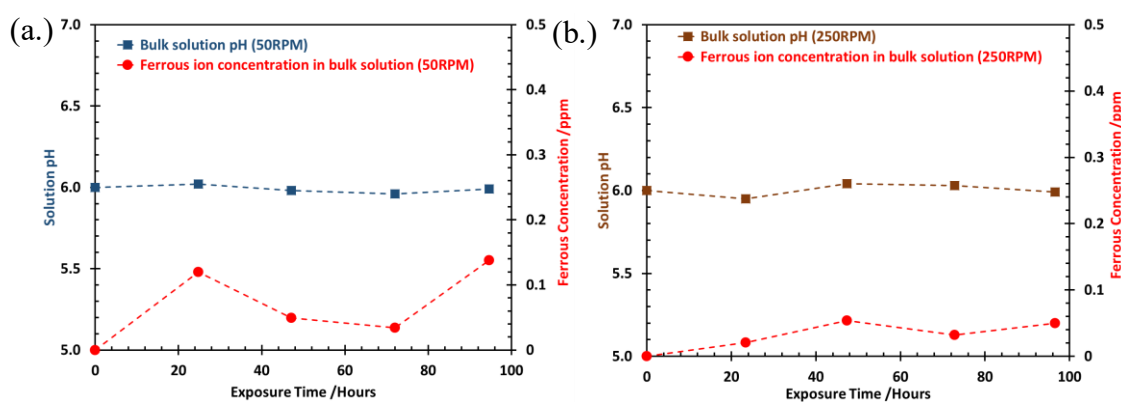


Figure 20: Solution pH and Fe^{2+} concentration during a 4-day exposure of 99.9% pure Fe in solution saturated with 10% by volume of H_2S at pH of 5, 30°C and impeller rotational speed of (a.) 50rpm and (b.) 250rpm

To check the validity of the corrosion rates measured in the glass cell setup, comparisons were made with corrosion rates obtained from using ICMT's in-house corrosion prediction software, FREECORP. The FREECORP corrosion prediction software is based on the corrosion rate model developed by Zheng, *et al.*[38] However, impeller flow was not one of the flow systems considered in this model. Therefore, the correlation between pipe velocity & impeller flow presented in Equation 52 was used to calculate the pipe velocity for each impeller rotational speed. It is worth noting that Equation 52 was developed by equating the mass transfer coefficients in impeller flow with that in pipe flow.

Figure 21, shows the comparison of the measured corrosion rates with the results obtained from the model. Prior to the formation of a protective layer, the corrosion process was under charge transfer control and the constants for calculating the corrosion rates were sensitive to the substrate metal. Zheng's model[38], referred to in Figure 21, was developed based on a carbon steel substrate while a 99.9% pure Fe was used to conduct the current experiment. This may have caused some differences between the measured and the predicted corrosion rates over the initial exposure time, especially at 250rpm. However, as the corrosion product layer became more protective, the corrosion process was controlled by the transport of species through the corrosion product layer and thus, became mass transfer limited. This is evident in the similarity in the steady state corrosion rates between the experimental and the predicted results in the later period of exposure.

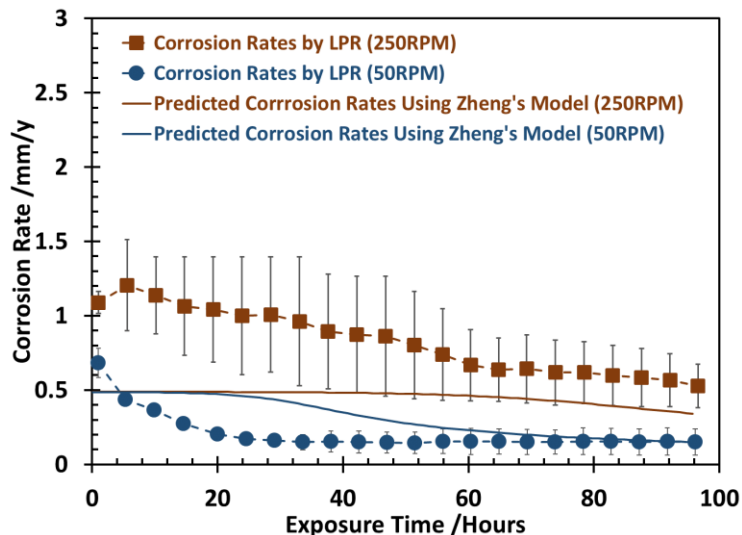


Figure 21: Comparison of measured corrosion rates of pure Fe with predicted values at impeller rotational speed of 50rpm and 250rpm in solution at pH 6.0, temperature of 30°C, and 10% vol. of H₂S in a mixture with nitrogen

Comparison of the time averaged corrosion rate from LPR with the calculated corrosion rate from weight loss, Figure 22, suggests that the corrosion rates from LPR methods are overestimated, especially at 250rpm. Further investigation of the cause of the observed discrepancy in corrosion rates was conducted using electrochemical impedance spectroscopy (EIS) methods.

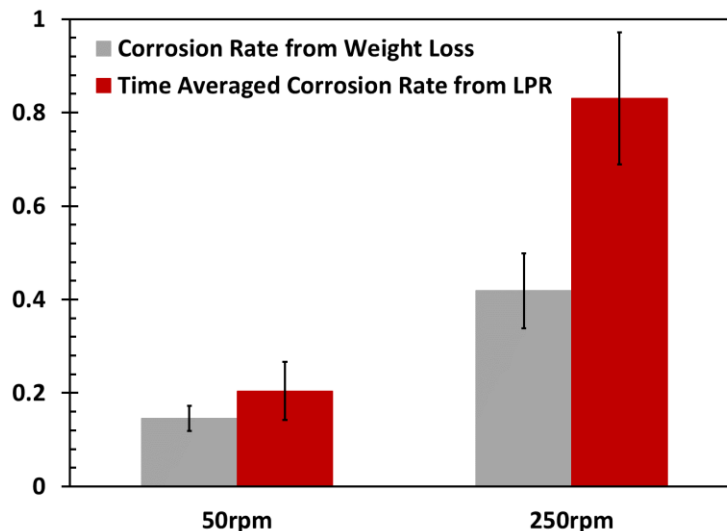


Figure 22: Comparison of corrosion rate measurements using LPR and weight loss methods.

Corrosion Product Layer Development

The reason for developing this new experimental setup is to investigate the impact of flow on the development of corrosion product layers without the influence of centrifugal forces or changing water chemistries on the layers. The development of the corrosion product layers in the current study was monitored by conducting SEM/EDS analyses of the specimens extracted after 1-day, 3-day and 4-day exposure periods. In addition, further characterization of the changes in the substrate surface during the corrosion product layer development was achieved using electrochemical impedance spectroscopy (EIS).

Surface Analysis of Iron Sulfide Layer

The surface SEM images presented in Figure 23 revealed that the morphologies of the corrosion product layers were similar irrespective of the rotational speed and

exposure time. Similarly, the sulfur and iron element detected on the surface of the metal confirms the corrosion product layers as iron sulfide.

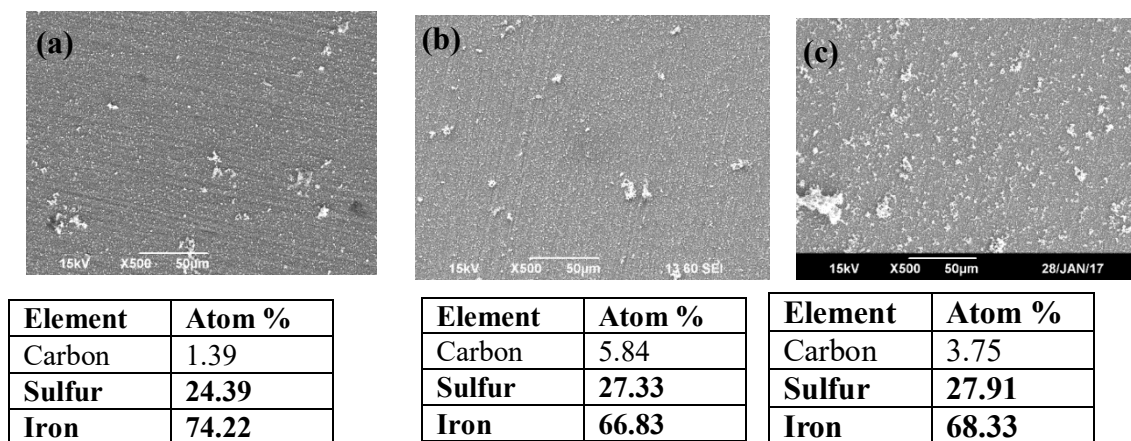


Figure 23: Surface SEM/EDS of FeS layer formed on 99.9% pure Fe at 30°C, 0.1 bar of H₂S and 50rpm impeller rotational speed (a.) 1 day (b) 3 days (c) 4 days

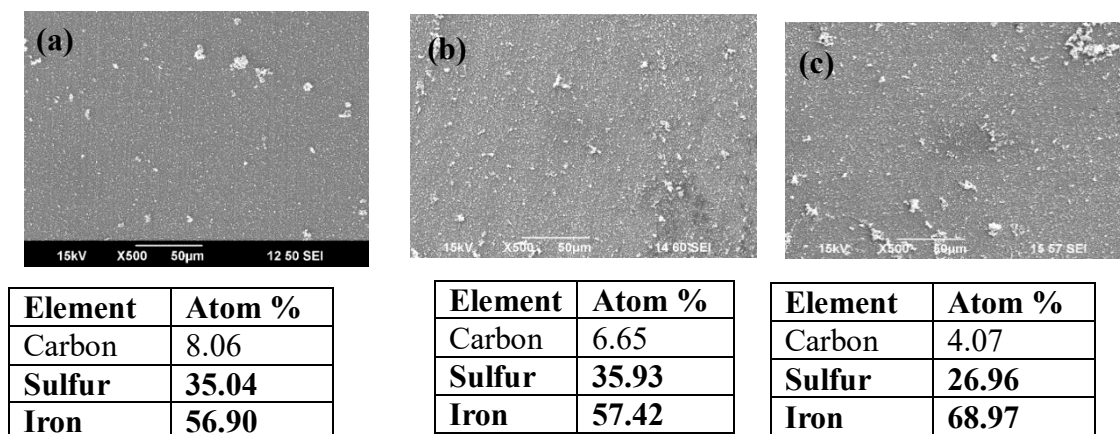


Figure 24: Surface SEM/EDS of the FeS layer formed on 99.9% pure Fe specimen exposed to a solution sparged with 10 vol.% H₂S/N₂ at pH 6.00, 30°C, and 50rpm impeller rotational speed for (a.) 1 day (b) 3 days (c) 4 days

The cross section of the corrosion product layers presented in Figure 25 and Figure 26 shows the presence of two distinct layers on the substrate: an inner layer and an

outer less compact (or fluffy) layer. This shows that the layers developed in this experimental setup are consistent. Since the outer fluffy FeS layer was present on the substrate after exposure to impeller velocity of 250rpm, it is inferred that the wall shear stress at this fluid velocity was insufficient to impede the formation or removal of this layer.

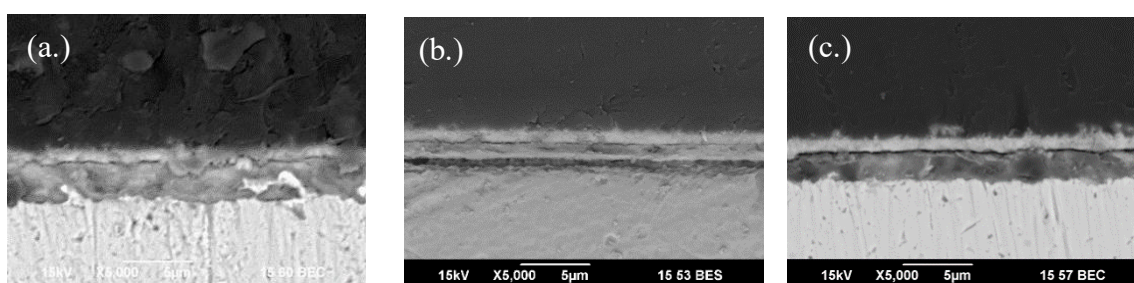


Figure 25: Cross-section of the FeS layer formed on 99.9% pure Fe specimen exposed to a solution sparged with 10 vol.% $\text{H}_2\text{S}/\text{N}_2$ at pH 6.00, 30°C, and 50rpm impeller rotational speed for (a.) 1 day (b) 3 days (c) 4 days

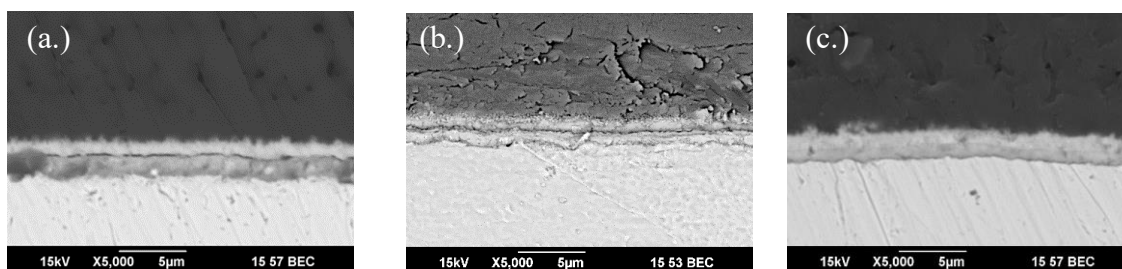


Figure 26: Cross section of the FeS layer formed on 99.9% pure Fe specimen exposed to a solution sparged with 10 vol.% $\text{H}_2\text{S}/\text{N}_2$ at pH 6.0, 30°C, and 250rpm impeller rotational speed for (a.) 1 day (b) 3 days (c) 4 days

The thickness of the corrosion product layers was measured with an inbuilt function in the SEM software. Figure 27 and Figure 28 indicate that thicker FeS layers

were formed at 50rpm in comparison to those formed at 250rpm. The charts also show that the thickness of the corrosion product layer decreased over time, irrespective of the rotational speed. If the properties of the layers formed in both conditions are assumed to be the same, the FeS formed at 50rpm is expected to have a higher tortuosity and make the layer more protective. This was observed from the corrosion rate data presented in Figure 21. At 50rpm, the corrosion rate dropped within 24 hours and remained constant thereafter (Figure 21). This shows that a more protective corrosion product layer was formed at this rotational speed in comparison to that formed at 250rpm.

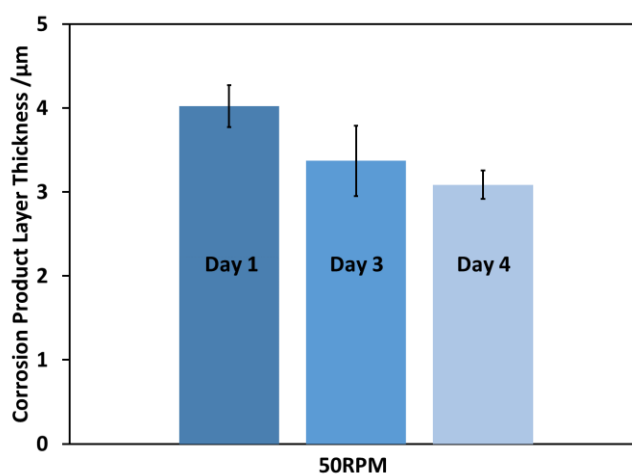


Figure 27: Thickness of corrosion product layer formed on 99.9% pure Fe in 1%. wt. NaCl solution at 30°C, 0.1bar of H₂S and 50rpm after day 1, day 3 and day 4.

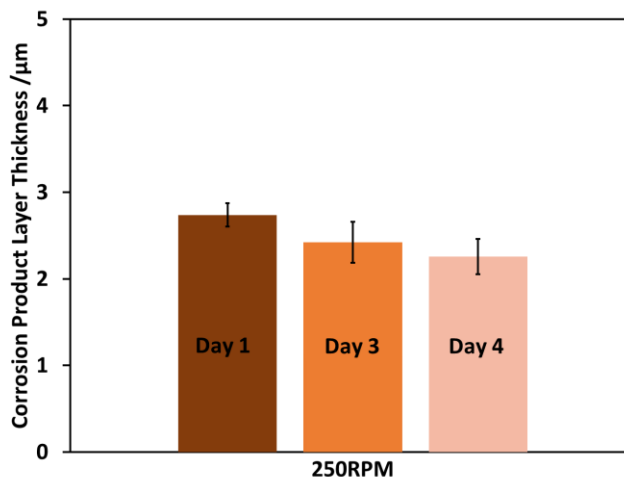


Figure 28: Thickness of corrosion product layer formed on 99.9% pure Fe in 1%. wt. NaCl solution at 30°C, 0.1bar of H₂S and 250rpm after day 1, day 3 and day 4.

EIS Analysis

The Nyquist plot for the 99.9% pure iron sample as function of immersion time in the test solution at impeller rotation speeds of 50rpm and 250rpm are presented in Figure 29 and Figure 30, respectively. The Nyquist plots obtained for both impeller rotational speeds (50 and 250rpm) show a more capacitive behavior in the first hour (Day 0) in comparison to the plots obtained for other days. This implies that the metal surface is more stable in the first hour of immersion. After one hour, the impedance of the metal increased with respect to time for both impeller speeds. However, the rate of increase is higher at 50rpm, suggesting a faster decrease in corrosion rates at this impeller speed. For all exposure times, a higher impedance was measured at 50rpm in comparison to 250rpm, which also suggests that the corrosion rate at this condition was lower. This was expected since the measured thickness of the FeS layer formed at 50rpm was higher than that

formed at 250rpm. These observation from the EIS data supports the corrosion rate trends obtained from LPR at the different impeller rotational speeds.

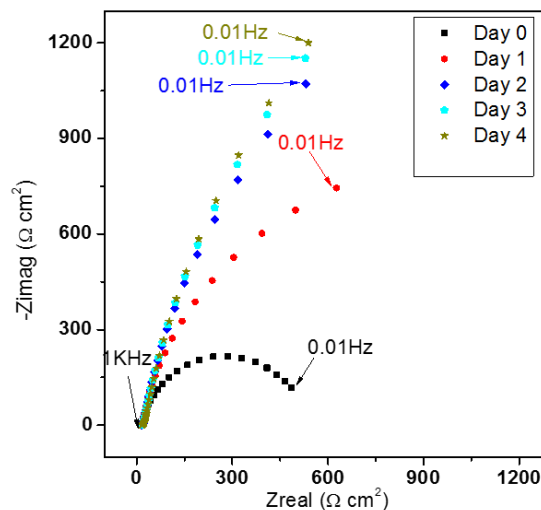


Figure 29: Nyquist plots for 99.9% pure Fe exposed to 1 wt. % NaCl solution at 30°C, 0.1bar of H₂S and 50rpm after day 0 (1hr), day 1, day 2, day 3 and day 4

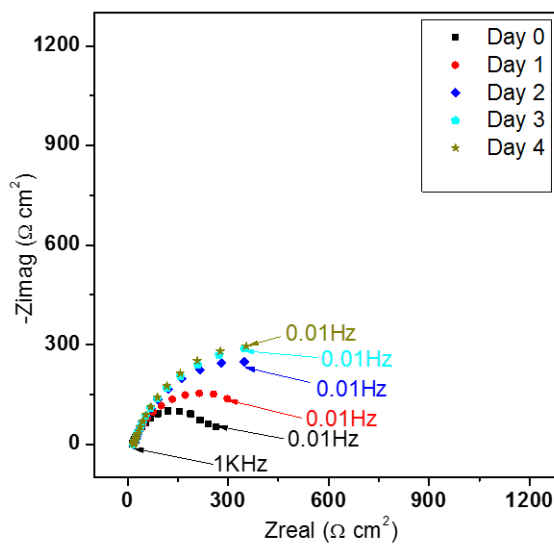


Figure 30: Nyquist plots for 99.9% pure Fe exposed to 1 wt. % NaCl solution at 30°C, 0.1bar of H₂S and 250rpm after day 0 (1hr), day 1, day 2, day 3 and day 4

With an LPR scan range of 10mV and scan rate of 0.125mV/sec, the frequency at which the polarization resistance measurements for all LPR measurements were taken was at 0.0125Hz. At this frequency, it can be seen that the resistance value was not taken at a point where the impedance data intersects the X axis for both plots (Figure 29 and Figure 30). The LPR data should have been taken at a lower frequency to accurately reflect the corrosion rate. Consequently, the data taken tend to give higher corrosion rate results. Nonetheless, the agreement between corrosion rates obtained by direct measurement and from Zheng's model [38] are within acceptable limits. Since the shear stress was not accounted for in Zheng's corrosion model, this similarity in the predicted and experimental corrosion rates confirmed the effectiveness of this setup for corrosion studies considering the negligible magnitude of shear stresses in this system (from CFD simulations and direct measurements). These results have shown that this newly developed experimental setup is suitable for investigating the development of corrosion product layers over an extended period while eliminating any possible influence of centrifugal forces or solution chemistry changes on the morphology of the corrosion product layer.

4.3 The Single-Phase Flow Loop

Channel flow systems such as thin channel flow cells have been used by researchers to conduct corrosion studies in conditions where achievement of high wall shear stresses is an important test parameter. This type of equipment has proven to be successful in the study of the development and retention of corrosion product layers especially in CO₂ conditions [23,131,132]. However, the use of such systems for sour

corrosion testing may bring up safety concerns due to the dangers associated with leaks. In order to address these challenges, a channel flow test cell system was developed in a single-phase flow loop to provide the desired high shear stress conditions and also ensure proper testing solution containment.

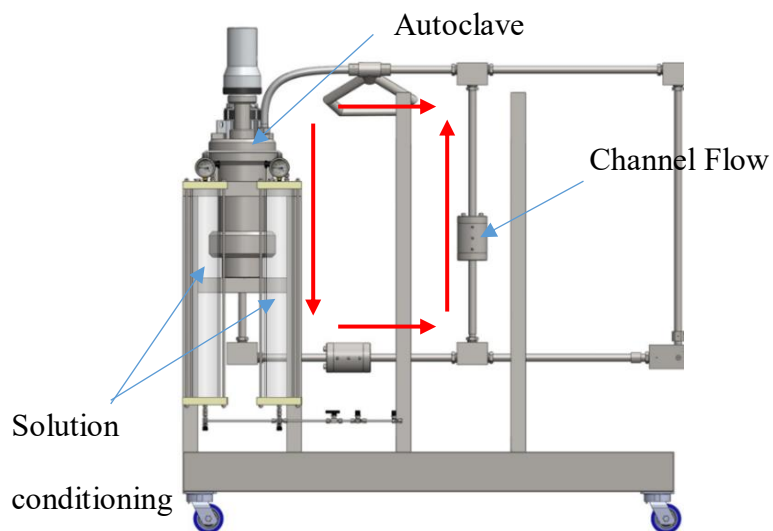


Figure 31: Single phase flow loop system showing the solution conditioning section, channel flow test section, autoclave.

The single-phase flow loop (SPFL), presented in Figure 31 comprises of a 5L autoclave, a test solution conditioning section, a $\frac{1}{2}$ " diameter flow pipe and a square duct test cell section. This system has the capability of achieving flow velocities as high as 13m/s, an operating temperature of 90°C, and pressure of 1330 Psia. The test cell section is designed as a duct with a rectangular cross section (0.75" x 0.04") and a 4" length. The schematic design of the test cell section, presented in Figure 32a, shows the locations for the reference electrodes, working electrodes and the weight loss specimen. Figure 32b

shows the inner schematics of the test cell set revealing the mounted position of the electrodes in the channel and the direction of flow (red arrow). It can also be seen from this diagram that the electrodes are mounted flush to the surface of the channel with the aid of a screw. The specimens used for testing in this equipment are circular shaped with a diameter of 0.5". The solution to specimen surface area ratio in this equipment is over 4000mL/cm², which is above the requirement according to ASTM G31 [110].

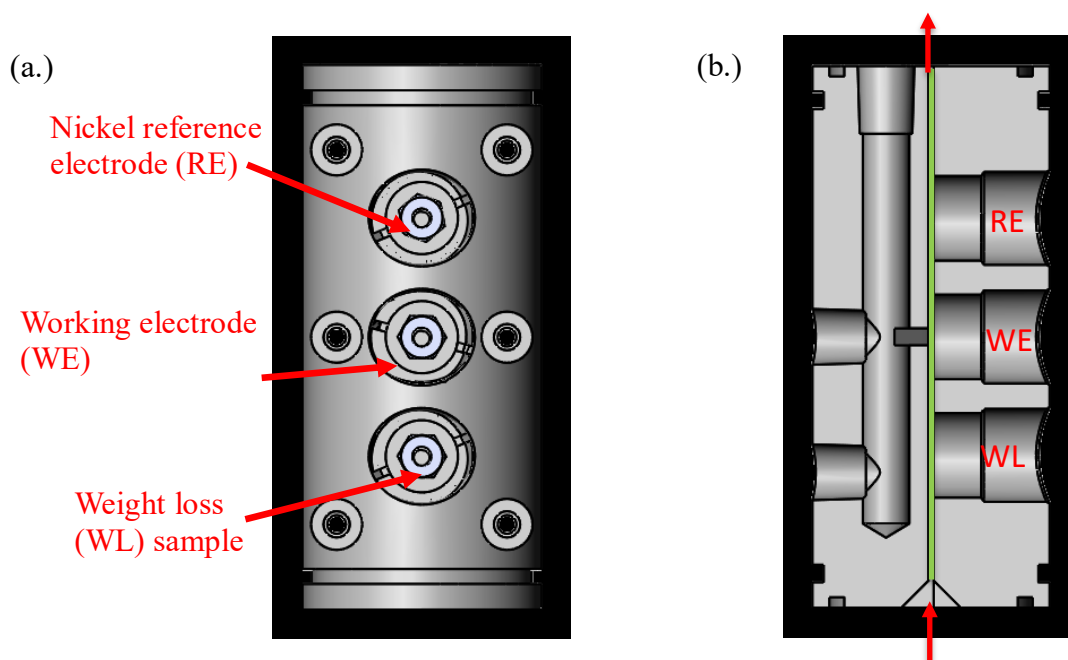


Figure 32: Diagram of the channel flow test cell showing the location of the reference electrode, working electrode, weight loss specimen, channel and the flow direction (a.) Schematic of the external body (b.) Schematic of the internal body

Since the flow entering the channel test cell emerges from a 0.5" diameter pipe, the geometry of the entry region of the test cell was modified to straighten the flow (Figure 33).

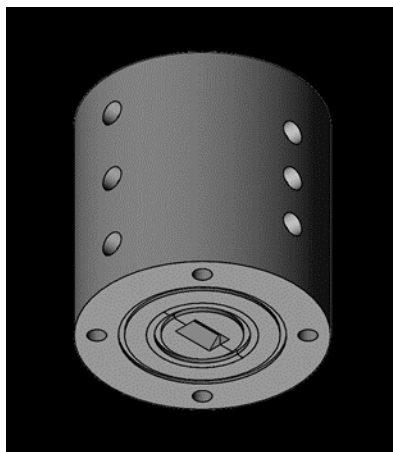


Figure 33: Assembly of the test cell showing the modified fluid entry region which ensures the removal of the flow entry region.

4.3.1 Mass Transfer in the Single-Phase Flow Loop.

Different correlations for the mass transfer characteristics of electrochemical species in a fully developed channel flow have been reported in the literature. These correlations were originally developed for heat transfer, but can be easily adapted to mass transfer calculations by implementing the concept of analogy between heat and mass transfer [133–135]. It was also reported that these correlations by Colburn[134] and Probststein [135], have been validated with experimental data and are generally accepted. The mass transfer coefficient of H_2S was extracted from each of the Sherwood correlations and compared with that developed by Aravinth [136] (Equations 69, 70 and 71). The mass transfer results obtained from these results are presented in Figure 34. Sherwood correlation by Colburn *et al.*[134]

$$Sh = 0.04Sc^{1/3}Re^{0.5} \quad (69)$$

Sherwood correlation by Probst *et al.* [135]

$$Sh = 0.021Sc^{1/3}Re^{7/8} \quad (70)$$

Sherwood correlation by Aravindh *et al.* [136]

$$Sh = 0.015Sc^{1/3}Re^{0.88} \quad (71)$$

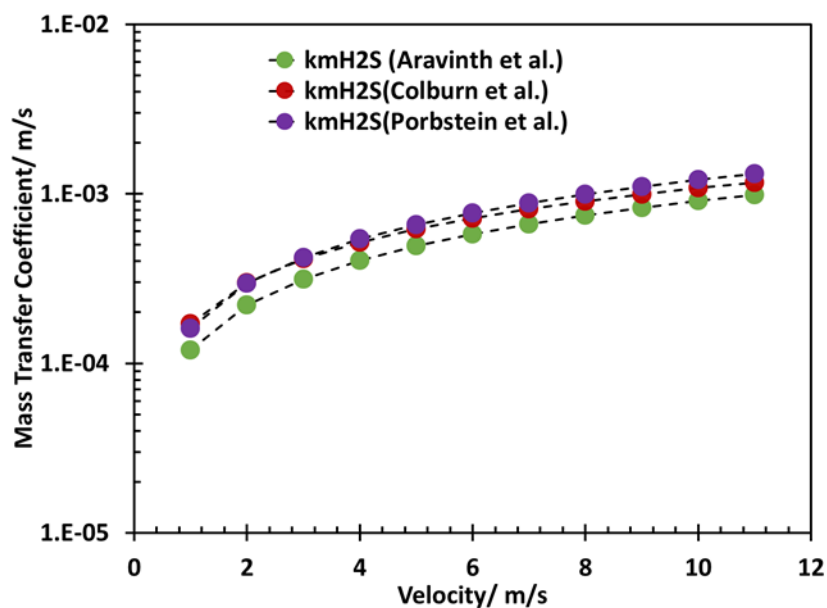


Figure 34: Comparison of mass transfer coefficient of H₂S in a fully turbulent channel using Sherwood correlations from different authors

4.3.2 Channel Flow Simulation and Wall Shear Stress Calculations

The flow in the SPFL system is such that the test solution that enters the inlet of the channel cell emerges from a 0.5" diameter pipe. This creates an entrance length [137,138] in the test cell which experiences non-uniformity in the flow. Ideally, the length of the entry region must be kept to a minimum. To address this problem, the design of the channel was modified, and computational fluid dynamics simulations were

conducted to verify that the flow across all the electrodes was fully developed and uniform. The same turbulence model used for the simulation of flow in the impeller flow in the glass cell was implemented in the simulation of flow in this system. The designed geometry, presented in Figure 35, of the channel cell consists of an entrance region, channel region housing the test cell and the exit region.

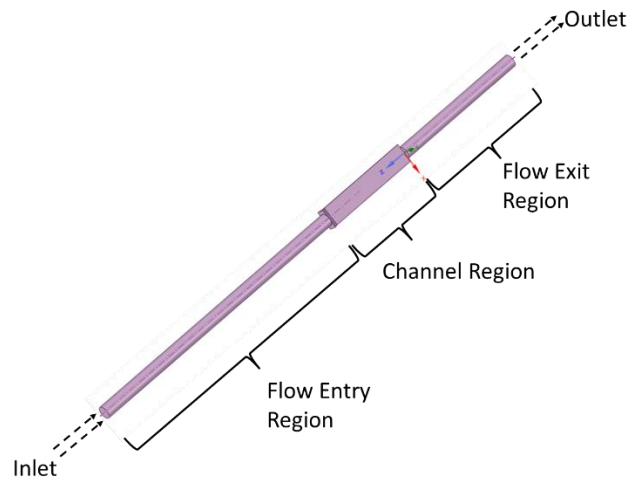


Figure 35: Geometry of the channel cell showing the flow entry region, the channel region (housing the test cell) and flow exit region

Figure 36 shows the meshed geometry of the channel cell showing a total of 2420244 nodes and 843083 elements. A mesh of smaller element size was used in the channel region while a coarser mesh was used in the entrance and exit regions. This meshing strategy was used to achieve a good near wall treatment (small y^+ value) in the region of interest while avoiding a high computational size.

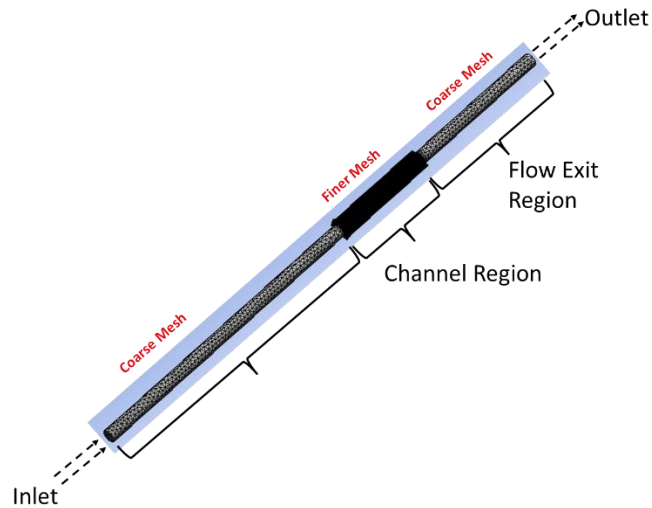


Figure 36: Meshing of channel cell into discrete elements

The simulation of flow in the channel cell was executed with water at 30°C, using atmospheric pressure and buoyancy properties of 9.8m/s^2 corresponding to the force of gravity. A no slip boundary condition was applied to the wall surfaces and an inlet and exit boundary conditions were applied on the entry and exit areas of the system. Since the fluid is moving and the solid body is stationary, a steady state method was used to execute the calculation.

Results:

The velocity profile of the fluid at the minimum (1.1m/s) and maximum (10.4m/s) flow capacity of the system shows a uniform distribution of the flow across the three samples. The velocity contours presented in Figure 37 and Figure 38 showed that the modified geometry of the entrance region of the channel cell effectively eliminated the entry length of the flow so that fluid characteristics are fully developed and uniform at

the specimen location. The Reynold's numbers corresponding to these 1.1m/s and 10.4m/s are 2614 and 24216, respectively.

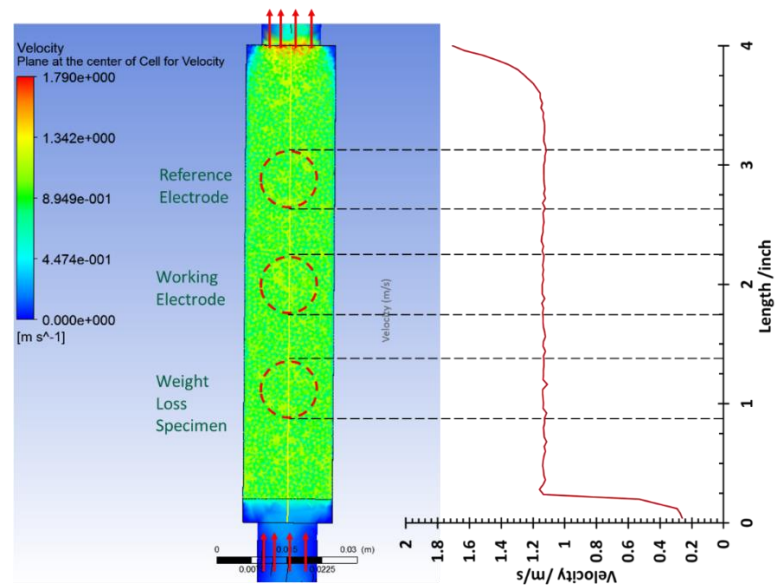


Figure 37: Velocity profile of the channel region at the lowest flow capacity ($V = 1.1\text{ m/s}$, $Re = 2614$) of the single-phase flow loop.

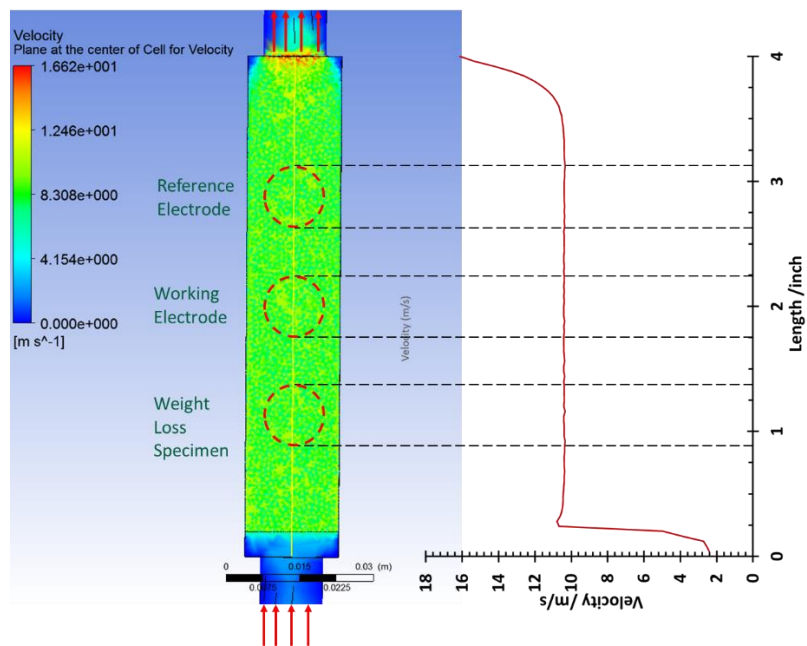


Figure 38: Velocity profile of the channel region at the highest flow capacity ($V = 10.4\text{m/s}$, $Re = 24216$) of the single-phase flow loop.

The wall shear stress contours corresponding to 1.1m/s and 10.4m/s presented in Figure 39a and Figure 39b shows that the minimum wall shear stress is 7.6 Pa while the maximum wall shear stress is 360 Pa .

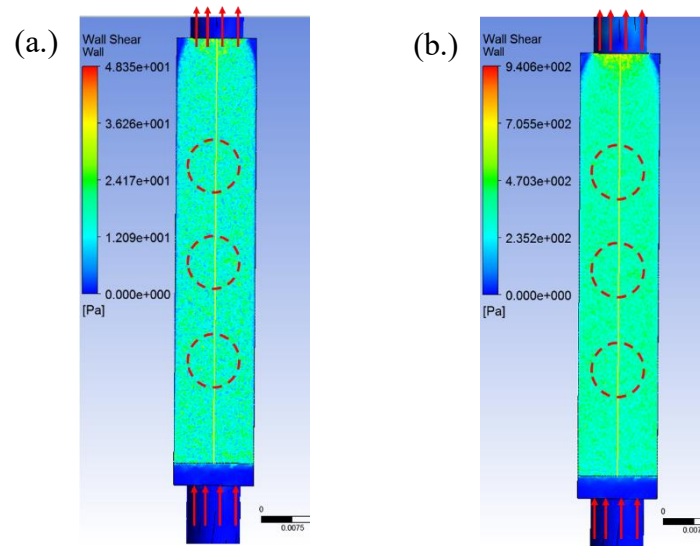


Figure 39: Contours of wall shear stress generated by a fully turbulent flow in the channel region at (a.) fluid velocity of 1.1m/s and (b.) fluid velocity of 10.4m/s

To check the validity of the simulation results, the wall shear stress values obtained from CFD simulations at different fluid velocities were compared with those obtained using Patel's [139] and Dean's [140] friction factors. The general equation for the calculation of wall shear stress is given as:

$$\tau = \frac{1}{2} \rho C_f V^2 \quad (72)$$

Where, ρ = density of the fluid kg/m³, V = fluid velocity m/s.

Friction factor given by Patel, *et al.* [139]:

$$C_f = 0.0376 Re^{-1/6} \quad (73)$$

Friction factor given by Dean [137]:

$$C_f = 0.073 Re^{-1/4} \quad (74)$$

Figure 40 shows a good agreement between the calculated wall shear stress with Dean's and Patel's friction factor with the wall shear stress obtained from CFD simulations.

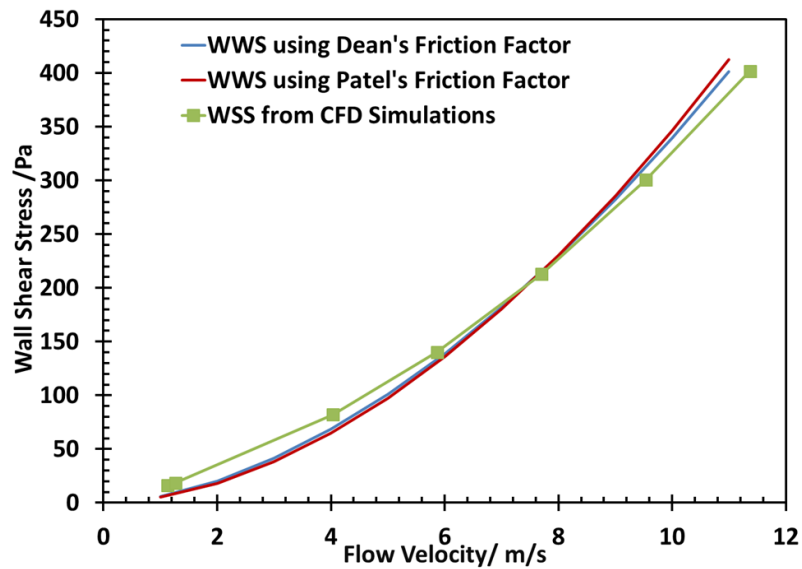


Figure 40: Comparison of wall shear obtained from the Patel and Dean friction factors with wall shear stress calculation from CFD simulations.

These results show that the single-phase flow loop system is suitable for achieving the part of the second research objective where the effect of flow on the development and retention of iron sulfide layers is investigated.

4.4 Summary

The results presented in this chapter relating to the development and characterization of the experimental equipment can be summarized as follows:

- The Sherwood correlation for the flow created by the Rushton-type Scada impeller in the glass cell is

$$Sh = 0.703 Re^{0.612} Sc^{1/3}$$

- The CFD simulation of the flow created by the Rushton-type Scada impeller and direct measurements on the sample wall revealed that the maximum shear stress on the sample is 1.3 – 2.0 Pa, while the WSS generated by the channel flow in the single-phase flow loop is 363 Pa.
- At equal mass transfer coefficients, the shear stress values on the sample surface resulting from the impeller flow are approximately one order of magnitude lower than those obtained in pipe flow (in a 0.2m diameter pipe).
- A good control of the solution chemistry was achieved with the new small-scale experimental setup.
- The measured corrosion rates from experiments conducted in a glass cell showed a good agreement with corrosion rate values predicted by Zheng's model[39].
- The solution to specimen surface area ratio of 4000mL/cm² in the single-phase flow loop experiment setup meets the requirement stated by ASTM G31 for maintaining of solution chemistry.
- The flow in the channel cell is fully developed and uniform across all the samples in the SPFL equipment.

CHAPTER 5: IMPACT OF IRON CARBIDE ON IRON SULFIDE LAYER DEVELOPMENT

5.1 Introduction and Research Goal

The degradation of carbon steel materials used to construct oil and gas pipelines is of immense concern to both production and corrosion engineers, as well as metallurgists. For this reason, significant resources have been devoted to enhancing the corrosion resistance and mechanical strength of these steels. By modifying their microstructure, usually through heat treatments, carbon steels are better able to withstand the performance demands encountered in oil and gas applications. Furthermore, modification of their microstructure may also impact the general corrosion behavior of such steels.[32] For example, a heat treatment which results in distinction of phases in the microstructure, such as the case in ferritic/pearlitic steels, may lead to local separation of cathodic and anodic sites which can impact the general corrosion behavior of the metal[141].

Corrosion in sour environments is an electrochemical reaction occurring at the metal surface, which includes the iron dissolution process as the anodic reaction and the reduction of hydrogen ion and hydrogen sulfide as the main cathodic reactions. Iron sulfide starts to precipitate on the steel surface when its saturation value is above one. However, the morphologies of these iron sulfide corrosion product layers may be dependent on the surface of the substrate metals upon which they precipitate. In sweet conditions, Farelas, *et al.*, [22] demonstrated that the presence of a residual iron carbide matrix enhanced the formation of a protective iron carbonate layer. In this study, it was reported that the formation of protective iron carbonate layers was more rapid in the

presence of a ferritic/pearlitic microstructure of a UNS G10180 steel in comparison to the martensitic microstructure of an API 5L X65 steel when these substrates were exposed to a 3 wt.% NaCl solution saturated with CO₂ at pH of 6.00, temperature of 80°C and fluid velocity of 0.5m/s. The author stated that in the initial active CO₂ corrosion stage, an iron carbide matrix formed a structure favorable for the formation of a protective corrosion product layer. Bonaventura[23] showed that with the removal of these iron carbide layers at a shear stress of 100Pa, the formation of iron carbonate layers was impeded. With these findings, iron carbide corrosion product residues on an actively corroding steel surface can significantly affect the formation of protective corrosion product layers if the operating conditions favor their exposure. In sour environments, it is generally understood that the formation of iron sulfide occurs rapidly [26,55]. This implies that the active stage of the corrosion process in sour environments, if at all present, is short. Therefore, the iron carbide residues may not be sufficiently exposed, as they are in CO₂ environments, and may have a reduced significance on the formation of protective iron sulfide layers.

One of the earliest studies conducted on the impact of iron carbide on the development of iron sulfide layers was conducted by Huang, *et al.*, [141] in 1996. In this study a grain coarsened heat affected zone (HAZ) of an ASTM-A516 low carbon steel with the ferritic/pearlitic microstructure was exposed to an aqueous solution saturated with 1 bar H₂S, at pH 2.8 and temperature of 25°C. Since cementite has a lower hydrogen overvoltage than ferrite[142], the iron dissolution (anodic reaction) was said to occur in the ferrite while the hydrogen reduction (cathodic reaction) occurred in the

cementite phase causing a local increase in pH. Presenting the formation of iron sulfides in grooves as proof, the author stated that there was an increase in the FeS precipitation on the cementite due to the increase in pH caused by the hydrogen reduction reactions occurring at this site. Zimer, *et al.*, [143] showed that iron sulfide precipitated preferentially on pearlite when AISI 1040 steel was exposed to $3.1 \times 10^{-3} \text{ mol dm}^{-3}$ of aqueous H₂S solution at a bulk pH of 4.5. However, with the addition of a 3.5 wt.% of NaCl, a non-preferential formation of iron sulfide across the surface of the metal was reported. These claims of preferential precipitation of iron sulfides on pearlite was refuted by Bai, *et al.*, [36] who reported that FeS layers developed equally on both the pearlite and the ferrite regions when an X52 ferritic/pearlitic steel is exposed to H₂O and H₂S at 50°C. These contrary claims on the impact of microstructure on FeS layer morphology highlights the need for a better understanding of this subject. While it is important to note that the microstructure of steel impacts the morphology of corrosion products, it is even more relevant to investigate how this affects the protectiveness of these layer as has been reported for CO₂ conditions. Kim, *et al.*, [32] compared the morphology of iron sulfide layers formed on pressure vessel steels with ferritic/pearlitic (F/P) and bainitic microstructures. The authors presented cross-section analyses of the corrosion product layers with claim that a greater degree of precipitation occurred over pearlite regions. It was concluded that the long range cementite network found in the F/P microstructure enhances the attachment of the FeS layer and also provided better protection. The cross-section analyses presented in this study were, however, somewhat

vague as the phase occupying the area directly above the pearlite region was not definitively identified as FeS.

The current research investigates any possible impact of iron carbide on the morphology of FeS layers developed on an UNS G10180 (F/P) in comparison to a 99.9% pure Fe substrate. The surfaces and cross-sections of the substrates were analyzed to ascertain any differences in the morphologies of the FeS layers developed after exposure to the test environment. The influence of these layer morphologies on their protectiveness was established by monitoring the corrosion rate trends of UNS G10180 and 99.9% pure Fe in the test solutions. Furthermore, the corrosion product layers developed on the substrate material were analyzed in order to identify both phase composition and identity.

5.2 Experimental Setup and Methodology

5.2.1 Equipment

Experiments were conducted in a 4-liter glass cell (Figure 4) which accommodates seven 0.50" x 0.50" x 0.08" square specimens, mounted in holders, with an impeller at the center to induce flow. The characteristics of the flow in this system were discussed in Chapter 4. One specimen was used for electrochemical measurements and the other six for weight loss and cross-section analyses. A three-electrode system was used for the electrochemical measurements, consisting of a platinized niobium wire counter electrode, an Ag/AgCl reference electrode and the test specimen as the working electrode.

5.2.2 Material Preparation and Microstructure Analysis

The materials used for the current research are commercially sourced 99.9% pure Fe and a UNS G10180 carbon steel material. The chemical composition of the UNS G10180 steel is shown in Table V.

Table V: Chemical composition of the UNS G10180 mild steel specimens

UNS G10180 mild steel (wt.%)										
Al	As	C	Co	Cr	Cu	Mn	Mo	Nb	Ni	P
0.008	0.006	0.180	0.003	0.120	0.180	0.750	0.020	0.002	0.065	0.011
S	Sb	Si	Sn	Ta	Ti	V	W	Zn	Zr	Fe
0.021	0.009	0.160	0.009	0.028	0.002	0.003	0.014	0.004	0.003	Balance

Specimens were polished with silicon carbide abrasive paper in the order 150, 400 and 600 grit. While polishing, specimens were rinsed with isopropanol and water to avoid heating up and to remove metal particles and other debris. Specimens were subsequently cleaned by immersion in a beaker with isopropanol and placed in an ultrasonicator for 5 minutes.

The microstructural analysis of the specimens was conducted by polishing the specimens further with a diamond suspension up to a finish of 0.25 microns. After polishing, specimens were rinsed in deionized water and degreased in isopropanol. Specimens were viewed under an optical microscope to ensure that no debris was still on the surface before being etched in a 5% Nital solution (5% HNO₃ in CH₃CH₂OH). The microstructures revealed from etching was examined by the scanning electron

microscopy (SEM). The same etching procedure was used for cross sectional analysis for all specimens after exposure to the test environment.

5.2.3 Test Methodology and Procedure

Specimens were exposed to a 1 wt.% NaCl solution saturated with 10% by volume of H₂S with N₂ as a gas mixture. The system was at atmospheric pressure. The test solution was deoxygenated by sparging with pure N₂ for 2 hours before introducing the desired 10% by volume of H₂S in N₂ gas mixture. The pH of the solution was adjusted to the desired value by adding drops of deoxygenated 1 molar NaOH solution. During experiments, the pH of the bulk solution was maintained by the solution chemistry control system described and discussed in Chapter 4. Two weight loss specimens were extracted on the first, third and final days of the experiment. At the time of extraction, specimen holders were withdrawn from the solution and the specimens themselves extracted from the holder. Immediately after extraction, the specimens were rinsed in a deoxygenated deionized water to rinse off any salt, further rinsed in isopropanol to remove the water, and dried afterwards in a desiccator under vacuum. Specimens were always stored in a vacuum desiccator prior to analysis. Surface SEM and cross-sectional analysis was conducted on one specimen while weight loss analysis was conducted on the other. The corrosion rates by mass loss were obtained by measuring the mass loss due to corrosion after exposing the specimen to the test solution for a particular time. The mass loss due to corrosion is the difference between the mass of the specimen before exposure and the mass after removal of the corrosion product layer, with Clarke solution, following extraction from the test solution. After removal of the corrosion

product layer, specimen surfaces were examined for the presence of localized corrosion using profilometry. XRD analysis was conducted on the specimen extracted on the last day.

5.2.4 Test Matrix

Table VI shows the test matrix for this study.

Table VI: Test Matrix for studying the impact of iron carbide on iron sulfide layer development

Operating Parameter	Specification	
Material	99.9% pure iron	UNS G10180
H ₂ S Partial Pressure	0.1 bar	
Total Pressure	1.01 bar	
Electrolyte	1 wt.% NaCl	
Solution pH	5.0	6.0
Temperature	30°C	
Expected FeS Phase	Mackinawite	
Impeller Rotational Speed	250rpm	
Test Duration	4 days	
Measurement Methods	LPR, EIS, WL	
Surface Analysis	SEM, EDS, XRD, Profilometry	

5.3 Results and Discussion

5.3.1 Microstructure of Test Specimens

The microstructures of the 99.9% pure Fe and the UNS G10180 carbon steel after etching in a 5% Nital solution are presented in Figure 41 (a.) and (b.), respectively. The etched surface of the 99.9% pure iron specimen shows a single-phase microstructure (ferrite) with large grain size, while the etched UNS G10180 surface revealed a ferritic-

pearlitic microstructure. The pearlite constituent has a lamellar structure which comprises of alternating cementite and ferrite regions.

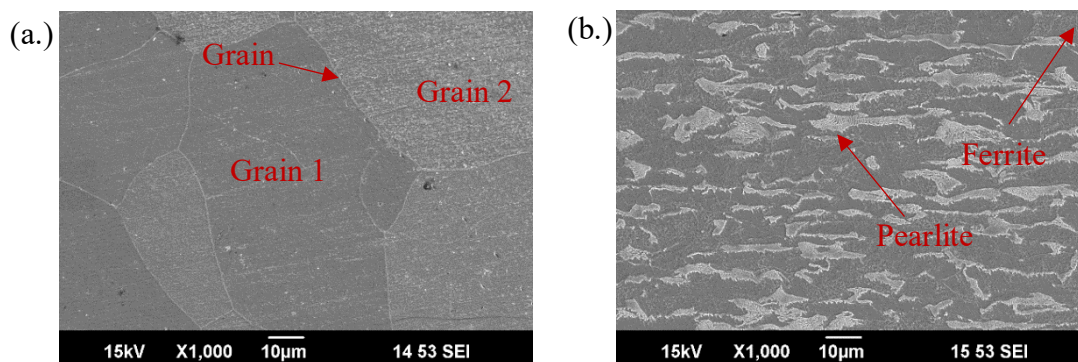


Figure 41: Microstructure of (a.) 99.9% pure Fe substrate (b.) UNS G10180 substrate, revealed after etching in 5% Nital solution, showing phases and grain boundaries.

5.3.2 Iron Sulfide Layer Development in Environment Promoting Fe_3C Formation (pH 5.00)

As stated earlier, the solution pH was controlled using an H^+ ion-exchange resin.

Figure 42 shows the ferrous ion concentration and the pH of the solution as monitored during the period of the experiment. These plots show how well the solution chemistry in this system is controlled with the pH maintained at 5.00 ± 0.07 , while the Fe^{2+} concentration remained below 3.1ppm throughout the duration of the experiment.

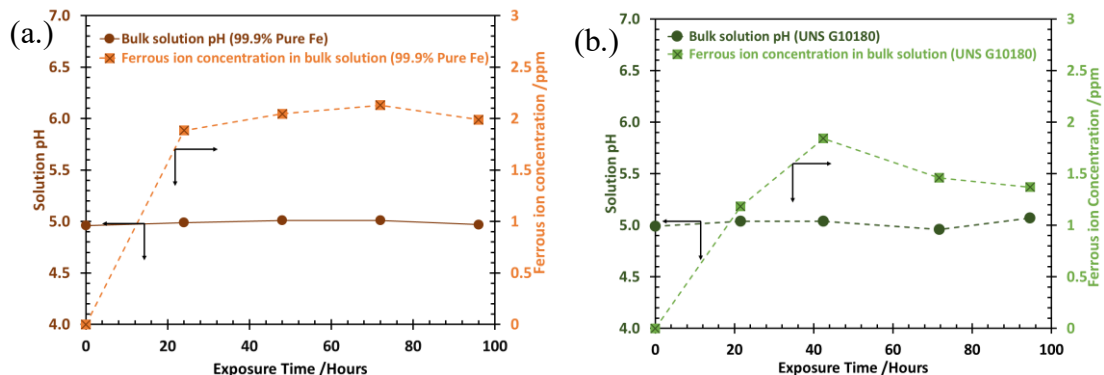


Figure 42: Bulk solution pH and ferrous ion concentration during the corrosion experiment in 1 wt.% NaCl solution, at pH 5.00, and for 0.1bar of H₂S at system temperature of 30°C and impeller rotational speed of 250rpm (a.) 99.9% pure Fe substrate and (b.) UNS G10180

The solution saturation was calculated by substituting the measured pH and ferrous ion concentration into the FeS saturation expression presented in Equation 33. The expression of the solubility constant at the solution temperature was calculated using Equation 36. Figure 43 shows that the saturation of FeS in the bulk solution for the experiments with the different substrates was between the value of 0 and 4.

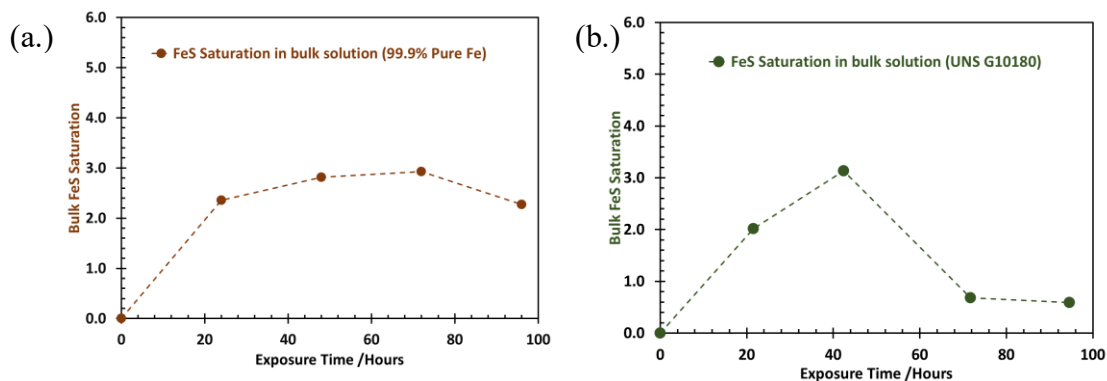


Figure 43: Bulk FeS saturation during corrosion experiment in 1 wt.% NaCl solution, at pH 5.00, and for 0.1bar of H₂S at system temperature of 30°C and impeller rotational speed of 250rpm (a.) 99.9% pure Fe substrate and (b.) UNS G10180

The weight loss measurements (Figure 44) suggest that in the first 24 hours, the corrosion rate of the 99.9% pure Fe substrate was higher than that of the UNS G10180 specimen. This could be an indication that the initial corrosion product layers formed on UNS G10180 within the first 24 hours of exposure was more protective than those formed on the 99.9% pure Fe. It can also mean that the kinetics of iron dissolution or/and cathodic reactions on the 99.9% pure Fe are different from that of UNS G10180. However, with extended exposure time, more corrosion product layers were developed and the corrosion rates of the substrate became similar. This observation suggests that, under these conditions, the formation of the initial corrosion product layers is very important, and the presence of the iron carbide favors its protectiveness.

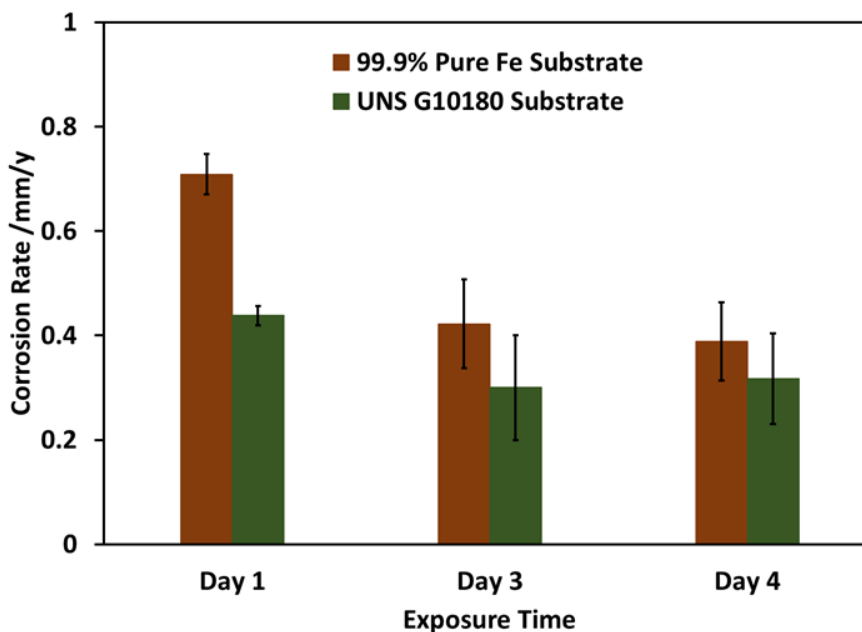


Figure 44: Weight loss corrosion rates of 99.9% pure Fe and UNS G10180 in 1 wt.% NaCl solution, at pH 5.00, for 0.1 bar of H₂S, 30°C and impeller rotational speed of 250rpm

Figure 45 shows the corrosion rate trends measured by LPR. The corrosion rate trends suggest the corrosion product layer formed on UNS G1018 achieved its maximum protectiveness within the first 18 hours. With the 99.9% pure Fe substrate, the corrosion rates continued to decrease for the period the sample was exposed, suggesting a slower but continuous increase in the protectiveness of the layer as it develops. These corrosion rate trends corroborate the corrosion rates measured by weight loss methods.

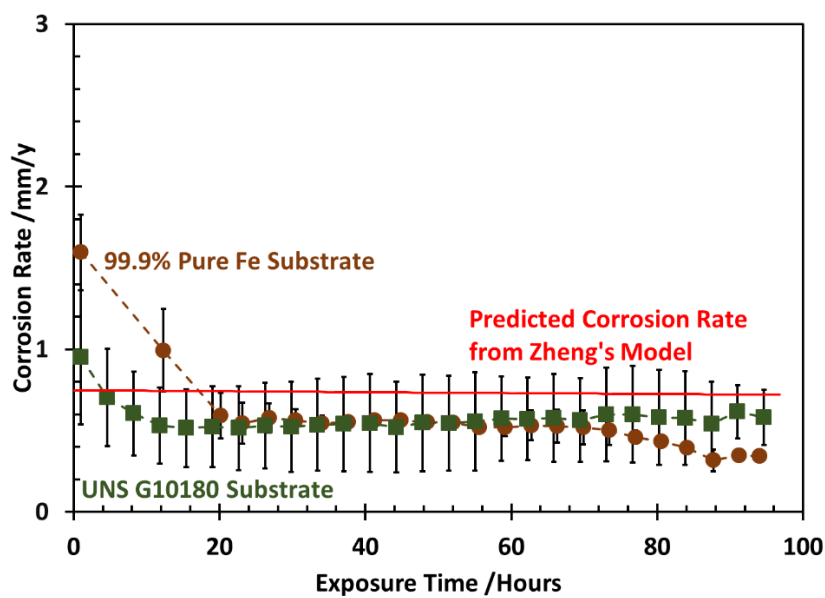


Figure 45: LPR corrosion rate measurements of 99.9% pure Fe and UNS G1018, in 1 wt.% NaCl solution, at pH 5.00, for 0.1 bar of H₂S, 30°C and impeller rotational speed of 250rpm

The corrosion rate results and the open circuit potential (Figure 45 and Figure 46) confirm the earlier suggestion that corrosion processes in sour (H₂S) environments are devoid of an active corrosion stage as observed in sweet (CO₂) environments.[22] With the immediate drop in the corrosion rate after the exposure of the specimens to the

corrosion environment, FeS layers can be said to rapidly form, cover any iron carbide network that may have developed and also offer some protection to the substrate metal.

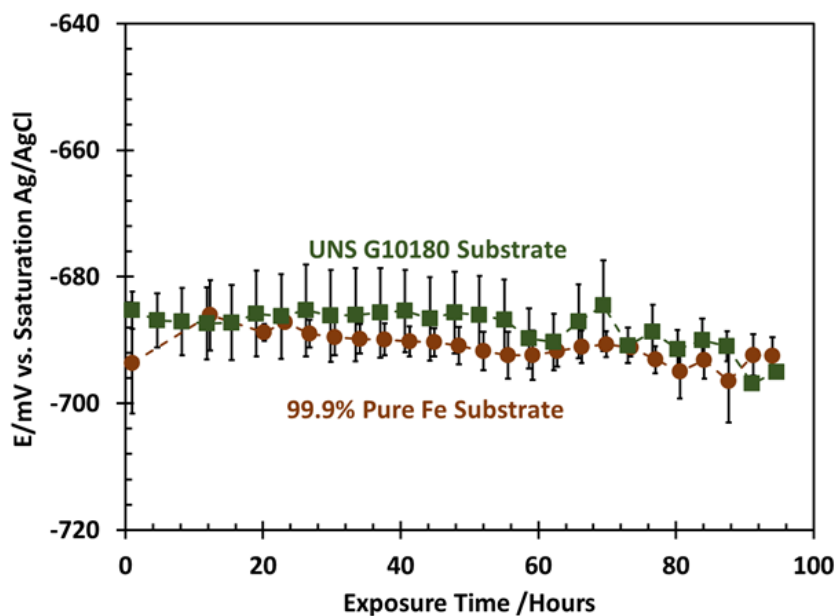


Figure 46: Open circuit potential (vs. Ag/AgCl) of 99.9% pure Fe and UNS G10180 in 1 wt.% NaCl solution, at pH 5.00, for 0.1 bar of H₂S, 30°C and impeller rotational speed of 250rpm

Cross-section analysis of the corrosion product layer

The cross section of the specimens extracted at different exposure times were examined to determine if there were any morphological differences in the corrosion product layers. All cross-section specimens were etched in order to reveal the microstructure of the underlying substrate metal. A thin, continuous corrosion product layer developed after 24 hours exposure time, (Figure 47) irrespective of the substrate metal. However, UNS G10180 specimens extracted after 72 hours and 96 hours (Figure 48 and Figure 49) showed a preferential development of the FeS layer above the pearlite

region while the FeS layer developed uniformly on the 99.9% pure Fe substrate. The selective precipitation of iron sulfides in the pearlitic region may have caused differences in mass transfer rates to the surface.

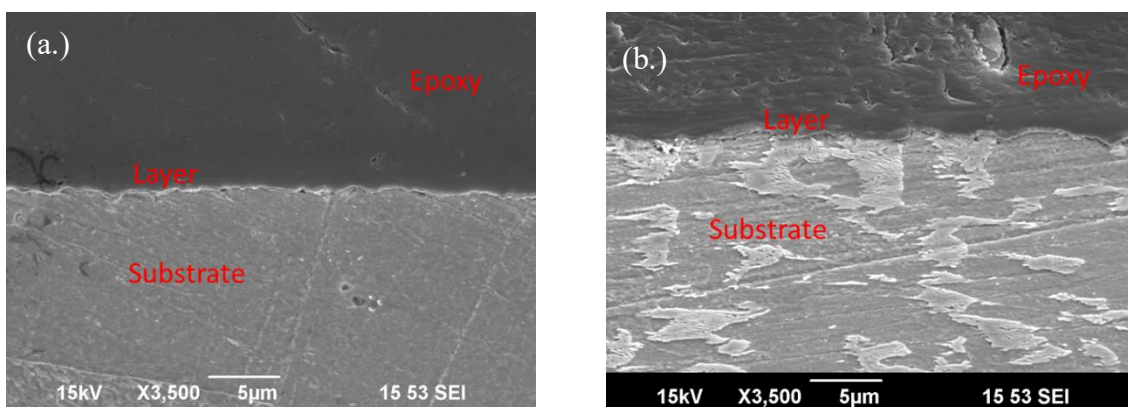


Figure 47: Cross-section of FeS layer formed after 1 day exposure in 1 wt.% NaCl solution at 30°C, at pH 5.00, for 0.1bar of H₂S and 250rpm impeller rotational speed (a) 99.9% pure Fe substrate (b) UNS G10180 substrate.

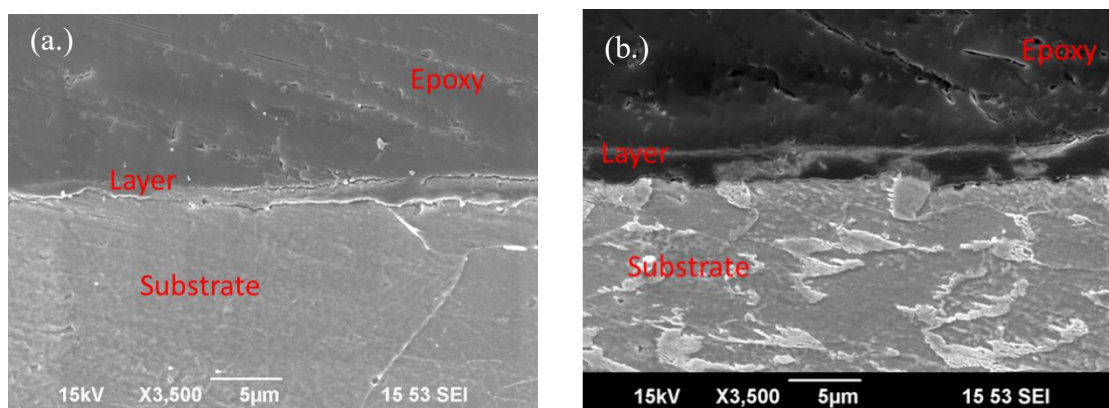


Figure 48: Cross-section of FeS layer formed after 3 days exposure in 1 wt.% NaCl solution at 30°C, at pH 5.00, for 0.1bar of H₂S and 250rpm impeller rotational speed (a) 99.9% pure Fe substrate (b) UNS G10180 substrate.

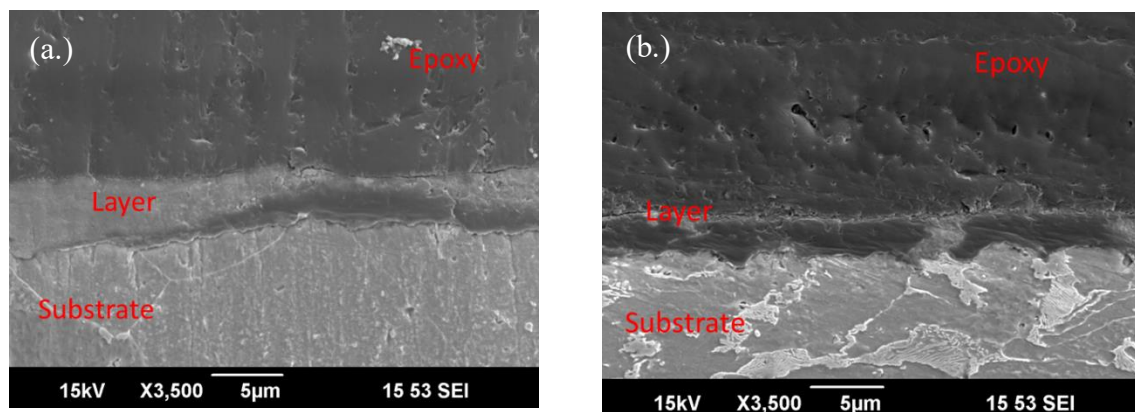


Figure 49: Cross-section of FeS layer formed after 4 days exposure in 1 wt.% NaCl solution at 30°C, at pH 5.00, for 0.1bar of H₂S and 250rpm impeller rotational speed (a.) 99.9% pure Fe substrate (b) UNS G10180 substrate.

Different authors have reported that the presence of a pearlite structure favors the formation of protective corrosion product layers.[32,141] In CO₂ environments, it was postulated that the enhanced FeCO₃ formation is a result of an increase in its local saturation within the iron carbide matrix, which provides both structural support and the right solution chemistry for the growth of the layer. [22–24] In H₂S conditions, a local galvanic couple can also formed between the iron carbide present in the pearlite region and the ferrite, where the iron carbide acts as a cathode and the ferrite as the anode[142]. The major cathodic reactions on the cementite phase are the hydrogen reduction (Equation 22) and hydrogen sulfide reduction reactions (Equation 23). The reduction of hydrogen ion at the cathode will lead to a local increase in pH. Ferrous ion dissolution (Equation 13), which occurs at the anode, is accelerated in the pearlite region due to the existence of the local galvanic couple in this region. In order to maintain electroneutrality, an increase in the ferrous ion concentration causes a decrease in the hydrogen ion concentration; and consequently, an increase in the local pH. With

reference to the saturation expression in Equation 32, an increase in the pH and ferrous iron concentration in the pearlite region favors the formation of FeS layers in this area.

Surface Analysis of Corrosion Product Layers

The detection of iron and sulfur in the EDS analyses of the corrosion product confirms the layer is an iron sulfide. Figure 50 and Figure 51 shows the elemental mapping of the cross-sections of the FeS layers formed on the pure Fe and UNS G10180 substrate after 4 days exposure time. The specimens were etched in order to reveal any influence of the pearlite on the morphology of the FeS layers. **Error! Reference source not found.** clearly shows that the iron sulfide grows above these pearlite regions, suggesting a possible influence of the iron carbide on the local layer growth.

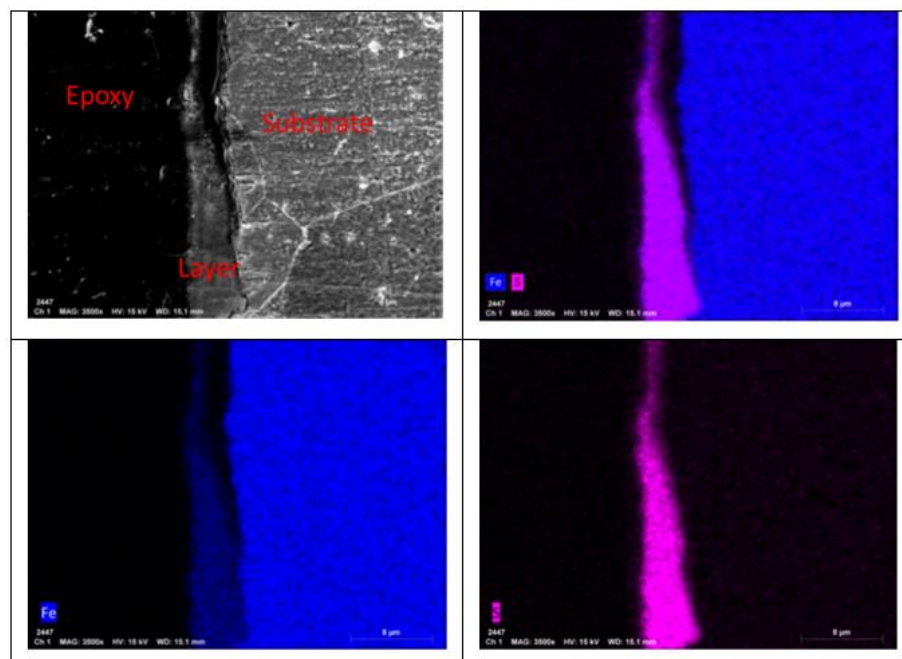


Figure 50: EDS mapping of FeS layer formed on 99.9% pure Fe substrate after a 4 days exposure period in 1 wt.% NaCl solution, at pH 5.00, at 30°C, for 0.1bar of H₂S and 250rpm impeller rotational speed

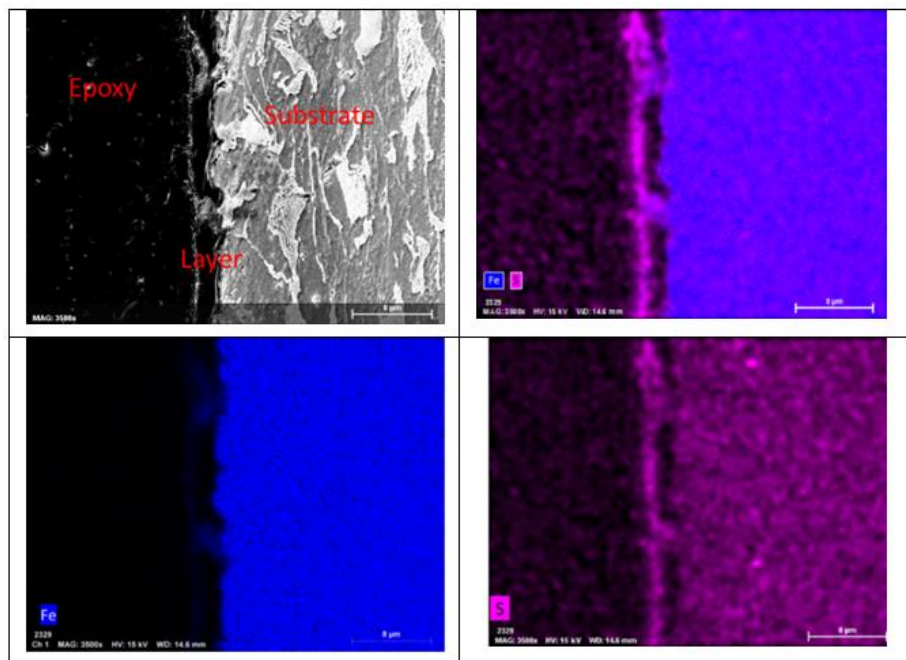


Figure 51: EDS mapping of FeS layer formed on UNS G1018 substrate after 4-day exposure period in 1 wt.% NaCl solution, at pH 5.00, at 30°C, for 0.1bar of H₂S and 250rpm impeller rotational speed.

However, XRD analyses conducted after 4days detected strong mackinawite peaks with the 99.9% pure Fe substrate (Figure 52). This may be due to the dense nature of the corrosion product layer that developed on the pure iron substrate as shown in the cross-section images presented earlier. Surprisingly, no mackinawite peak was detected with the UNS G10180, but this may be due to the very low thickness of the layers formed.

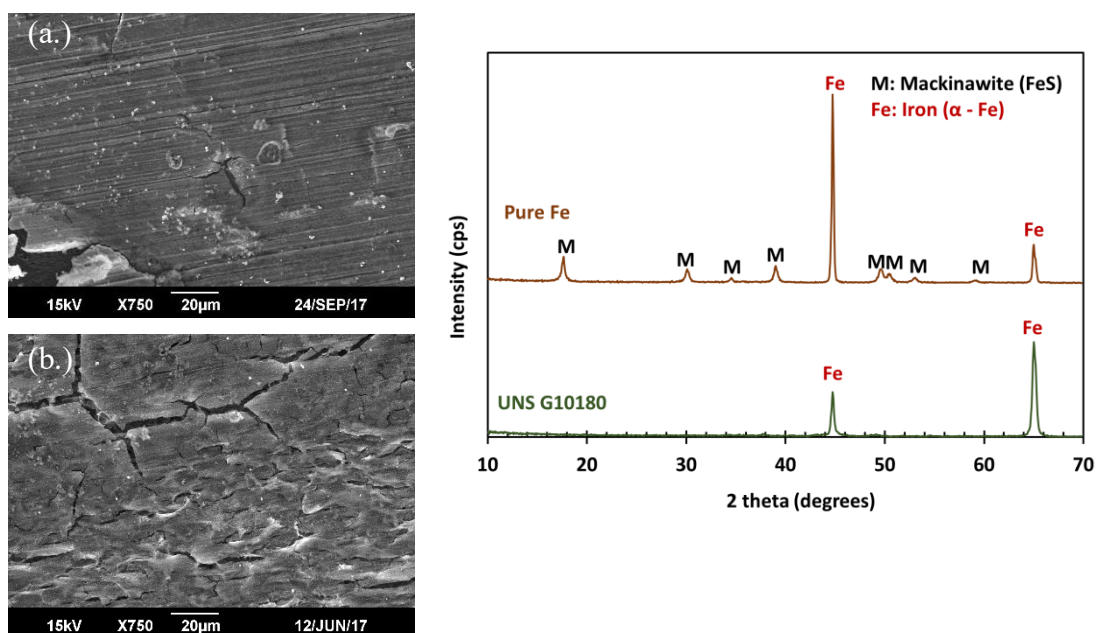


Figure 52: SEMs and XRD analyses of corrosion product layers formed on (a.) 99.9% pure Fe and (b.) UNS G10180 after a 4 day exposure in 1 wt. % NaCl solution, at pH 5.00, and for 0.1bar of H₂S at a system temperature of 30°C and impeller rotational speed of 250rpm

The fraction of corroded Fe in the FeS layer was calculated to evaluate the scaling tendency of the corrosion product layers developed on the two substrates. The mass of the corrosion product layer and the Fe corroded were obtained through mass loss methods. The difference between the mass of the specimens after extraction (after rinsing and drying) and their mass after the removal of the corrosion product layer with Clarke solution[144] represents the mass of the corrosion product layer, while the difference between the mass of the metal before exposure and the mass after removal of the corrosion product layer is the mass of the Fe corroded. These masses were converted to moles by dividing the obtained values with the molar mass (g/mol) of FeS (for moles of Fe in the corrosion product layer) and molar mass of Fe (for moles of Fe corroded). The

similarities in the fraction of corroded Fe in the FeS layers are shown in Figure 53, suggesting that the protectiveness of these layers is independent of the amount of FeS that precipitated. However, the low corrosion rates (measured by LPR and weight loss methods) of the UNS G10180 substrates within the first 24 hours suggests that the protectiveness of the layer is dependent on the attachment of the initial thin FeS layer closest to the metal substrate.

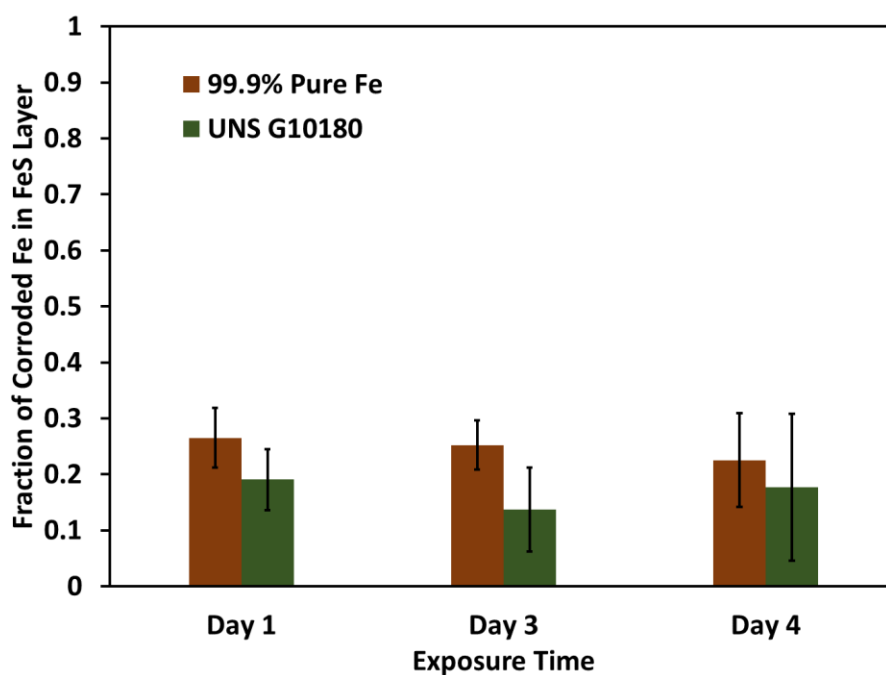


Figure 53: Fraction of corroded Fe in the FeS layer after exposure of 99.9% pure Fe and UNS G10180 substrates to 1 wt.% NaCl solution, at pH 5.00, and for 0.1bar of H₂S at system temperature of 30°C and impeller rotational speed of 250rpm.

Summary

- Precipitation of iron sulfide layer occurs preferentially on iron carbide, thereby affecting the morphology of the corrosion product layer.

- The iron sulfide layer developed on UNS G10180 in the first 24 hours provided a better protection to the underlying metal in comparison to that formed on 99.9% pure Fe.
- The protectiveness of the corrosion product layer is independent of the morphology of the FeS layer.

5.3.3 Iron Sulfide Layer Development under High FeS Saturation (pH 6.00)

Further experiments were conducted at pH 6.00, where FeS saturation in the bulk solution is higher. At pH of 5.00, the corrosion behavior of UNS G10810 and pure Fe were observed to be different; especially in the first 18 hours of specimen exposure. In addition, differences in the morphologies of the layers were observed, and were attributed to the preferential precipitation of the FeS layer in the pearlite region. With the pH of the solution increased to 6.00, a higher precipitation rate is expected due to the increase in bulk FeS saturation. Therefore, the aim of conducting the experiments at a pH of 6.00 was to investigate how much impact, or lack thereof, iron carbide would have on the FeS morphology of iron sulfide layers developed in high saturation conditions. Also, the corrosion rates were monitored for possible similarities to the trends observed at a pH of 5.00. The ferrous ion concentration and bulk solution pH during the period of the experiments conducted with the different substrates are presented in Figure 54.

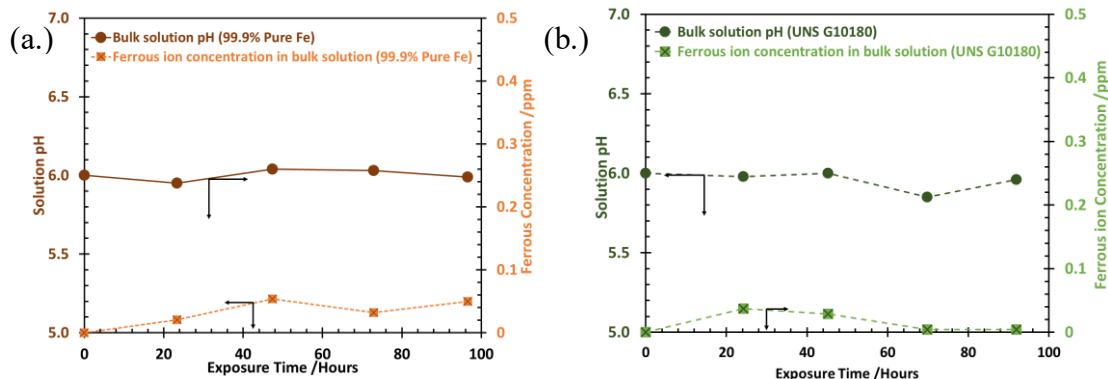


Figure 54: Bulk solution pH and ferrous ion concentration during corrosion experiments in 1 wt. % NaCl solution, a pH 6.00, and for 0.1bar of H₂S at system temperature of 30°C and impeller rotational speed of 250rpm (a.) 99.9% pure Fe substrate and (b.) UNS G10180

Figure 54 shows that the ferrous ion concentration was lower than 1ppm (lower than that measured in pH 5.00 conditions). This is expected since, at pH 6.00, the decreased hydrogen ion concentration will shift the equilibrium (Equations 28 and 29) of the FeS saturation reaction to the right, thereby leading to precipitation of more FeS. The saturation of FeS in solution, calculated from the measured pH and ferrous ion concentrations is also higher than that in pH 5.00 (Figure 43). This is expected to have an impact on the precipitation rate of FeS. After 60 hours exposure of UNS G10180, the Fe²⁺ concentration decreased to negligible values resulting in a saturation of slightly below 1. FeS saturation of below one is not thermodynamically possible and may be a result of error in Fe²⁺ concentration or the FeS solubility constant.

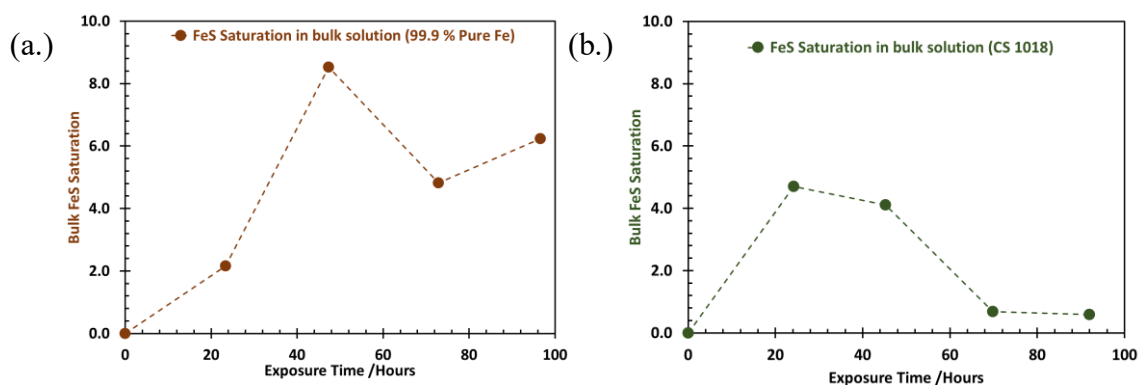


Figure 55: Bulk FeS saturation during corrosion experiment in 1 wt.% NaCl solution, at pH 6.00, and for 0.1bar of H₂S at system temperature of 30°C and impeller rotational speed of 250rpm (a.) 99.9% pure Fe substrate and (b.) UNS G10180

Similar to observations at pH 5.00, but to a decreased extent, the difference in the corrosion behavior of 99.9% pure Fe and UNS G10180 as presented in Figure 56 was observed only in the first day of exposure. No differences in the corrosion behavior between the two substrates were observed on the 3rd and 4th day of exposure.

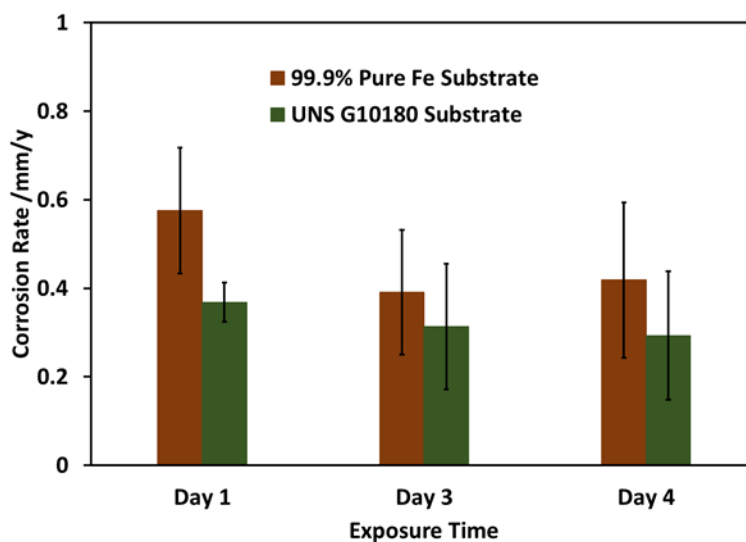


Figure 56: Weight loss corrosion rates of 99.9% pure Fe, and UNS G10180, in 1 wt.% NaCl solution, at pH 6.00, for 0.1 bar of H₂S, 30°C and impeller rotational speed of 250rpm

With bulk pH of 6.00, the impact of iron carbide on the protectiveness of the FeS layers may be masked by the fast saturation and precipitation of these FeS layers. However, the increase in the open circuit potential measured with the UNS G10180, in Figure 57, suggest the occurrence of pseudo-passivation of the substrate metal. Pseudo-passivation of carbon steel is usually associated with a corresponding increase in open circuit potential. [145,146]; this was not observed with the 99.9% pure Fe substrate. This may be an indication of a better attachment of the FeS layers facilitated by the iron carbides.

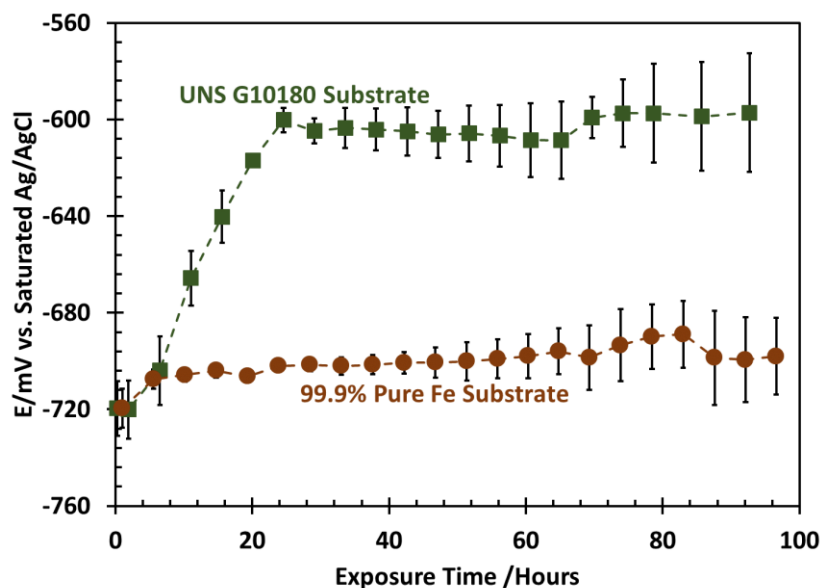


Figure 57: Open circuit potential (vs. Ag/AgCl) of 99.9% pure Fe, and UNS G10180, in 1 wt.% NaCl solution, at pH 6.00, for 0.1 bar of H₂S, 30°C and impeller rotational speed of 250rpm

Figure 58 shows that the corrosion rate trends in pH 6.00 solution were similar to that observed at pH 5.00 with the UNS G10180 substrate developing a more protective layer than 99.9% pure Fe.

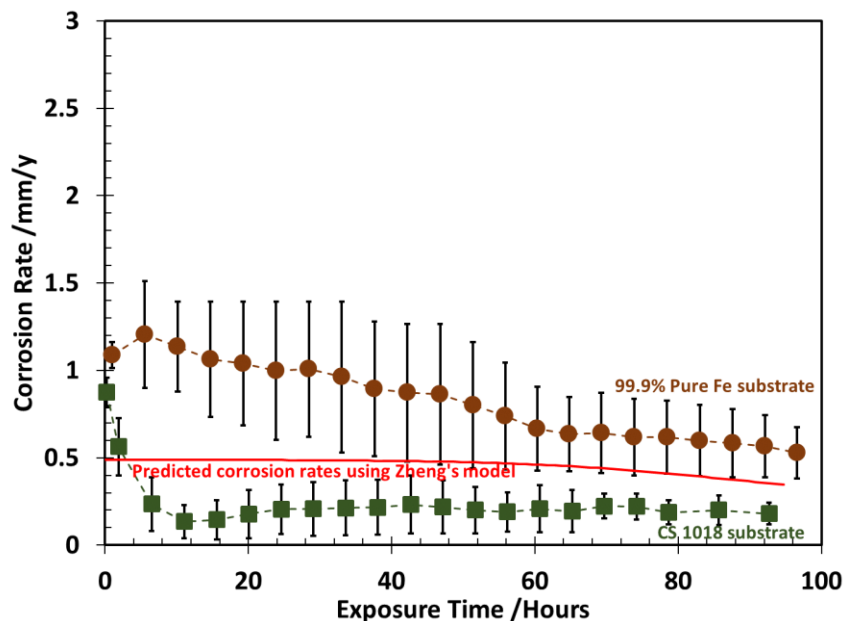


Figure 58: LPR corrosion rate measurements of 99.9% pure Fe and UNS G10180, in 1 wt.% NaCl solution, at pH 6.00, for 0.1 bar of H₂S, 30°C and impeller rotational speed of 250rpm

The corrosion of UNS G10180 reached a stable value of approximately 0.2mm/y within the first 10 hours of specimen exposure. However, the corrosion rates of the 99.9% pure Fe substrate continued to gradually decrease throughout the period of exposure. This indicates that UNS G10180 developed a protective FeS layer faster than the pure Fe substrate, which highlights the importance of the iron carbides in the protectiveness of the layers in the low shear stress condition.

Cross-section Analysis of the Corrosion Product Layer

Figure 59 – 61 show the cross-sections of the corrosion product layers developed on 99.9% pure Fe and UNS G10180 after 1, 3 and 4 days of exposure in the test solution.

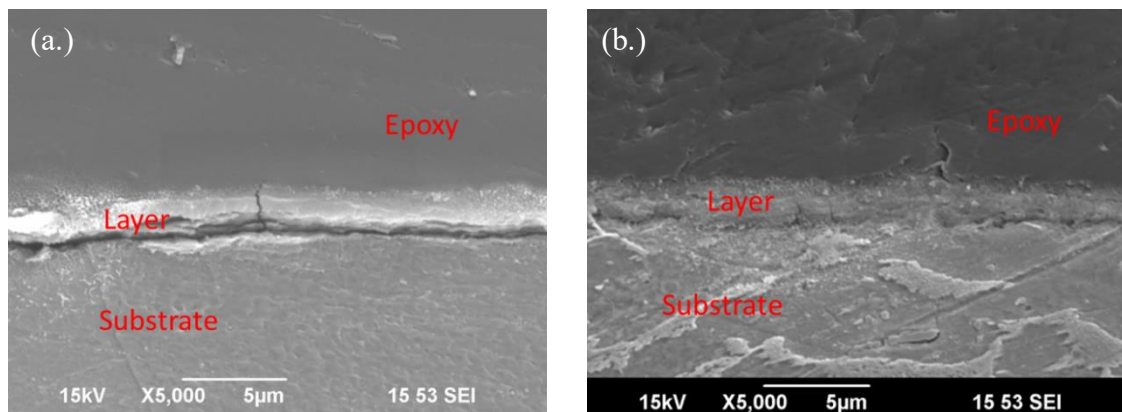


Figure 59: Cross-section of FeS layer formed after 1-day exposure in 1 wt.% NaCl solution at 30°C, at pH 6.00, for 0.1bar of H₂S and 250rpm impeller rotational speed (a.) 99.9% pure Fe substrate (b) UNS G10180 substrate.

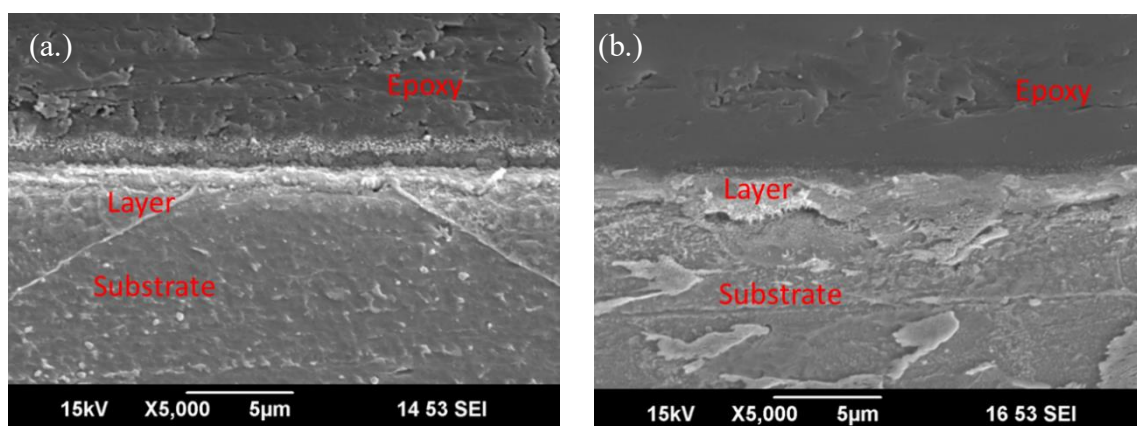


Figure 60: Cross-section of FeS layer formed after 3 days exposure in 1 wt.% NaCl solution at 30°C, at pH 6.00, for 0.1bar of H₂S and 250rpm impeller rotational speed (a.) 99.9% pure Fe substrate (b) UNS G10180 substrate.

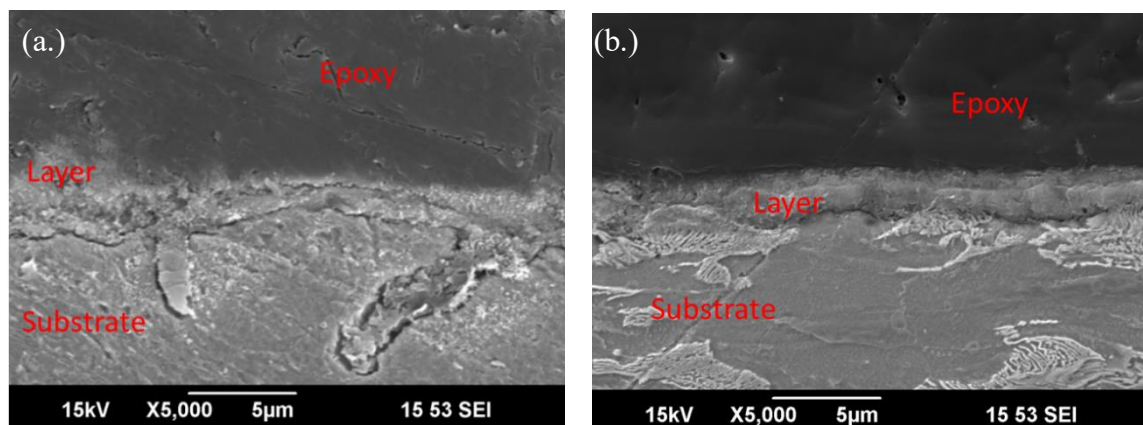


Figure 61: Cross-section of FeS layer formed after 4 days exposure in 1 wt. % NaCl solution at 30°C, at pH 6.00, for 0.1bar of H₂S and 250rpm impeller rotational speed (a.) 99.9% pure Fe substrate (b) UNS G1018 substrate.

The cross-section analyses of the corrosion product layers showed similarities in the overall morphologies of the corrosion product layers. However, a closer observation of the FeS layer formed over the pearlite regions shows the FeS layers filling-up the cementite skeletal framework. The formation of a continuous FeS layer over the pearlite region was revealed in the cross-section image of the UNS G10180 specimens extracted after 1 day (Figure 59b), 3 days (Figure 60b) and 4 days (Figure 61b). This shows that the presence of iron carbide enables the formation of a continuous iron sulfide layer and promotes the attachment of this layer, which supports the OCP and corrosion rate trends (Figure 57 and Figure 58). Bai, *et al.*, [36] demonstrated that the precipitation rate of the FeS layers was higher over the pearlite when a ferritic/pearlitic steel used to construct a pressure vessel was exposed to an H₂S saturated NACE TM0284-96A solution with an initial pH of 2.8. It was also reported that the iron sulfide layers formed on the steel with F/P microstructure provided more protectiveness when compared to a layer developed on

a steel with a bainitic microstructure exposed to the same environment. These reported behaviors of F/P steels support the findings from the current study in both pH 5.00 and 6.00 conditions. Figure 61a also revealed an area with an accelerated corrosion which raises the suspicion of localized attack. The surface profiles of the substrates after removal of the corrosion product layer were also analyzed to ascertain the occurrence of localized corrosion.

Surface Analysis of Corrosion Product Layers

The EDS mapping presented in Figure 62 (for 99.9% pure Fe) and Figure 63 (for UNS G10180) confirmed the corrosion products formed after 4 days exposure as iron sulfide.

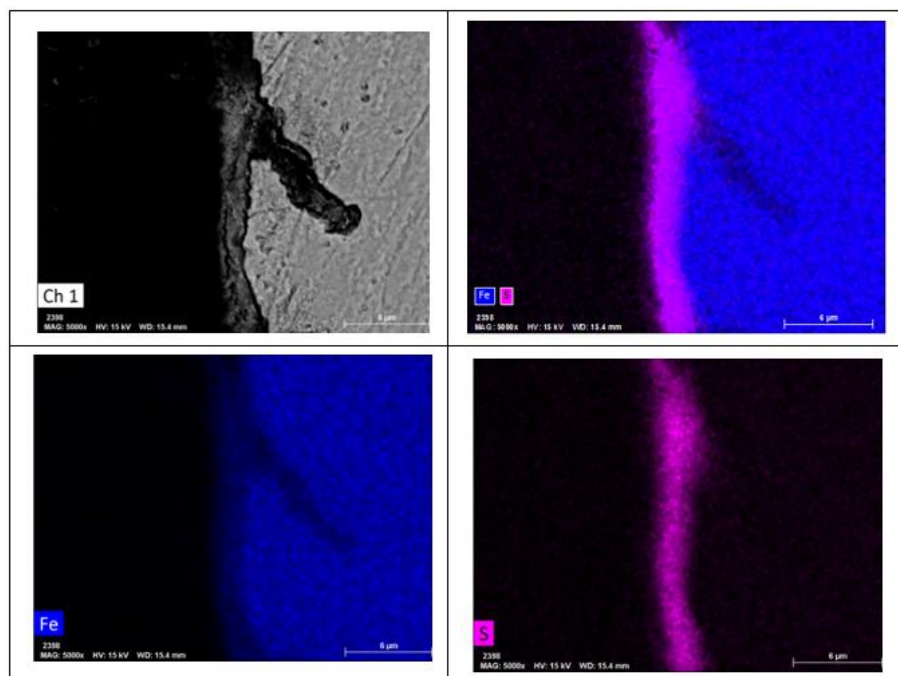


Figure 62: EDS mapping of FeS layer formed on 99.9% pure Fe substrate after 4-day exposure in 1 wt.% NaCl solution at 30°C, at pH 6.00, and 0.1bar of H₂S and 250rpm impeller rotational speed

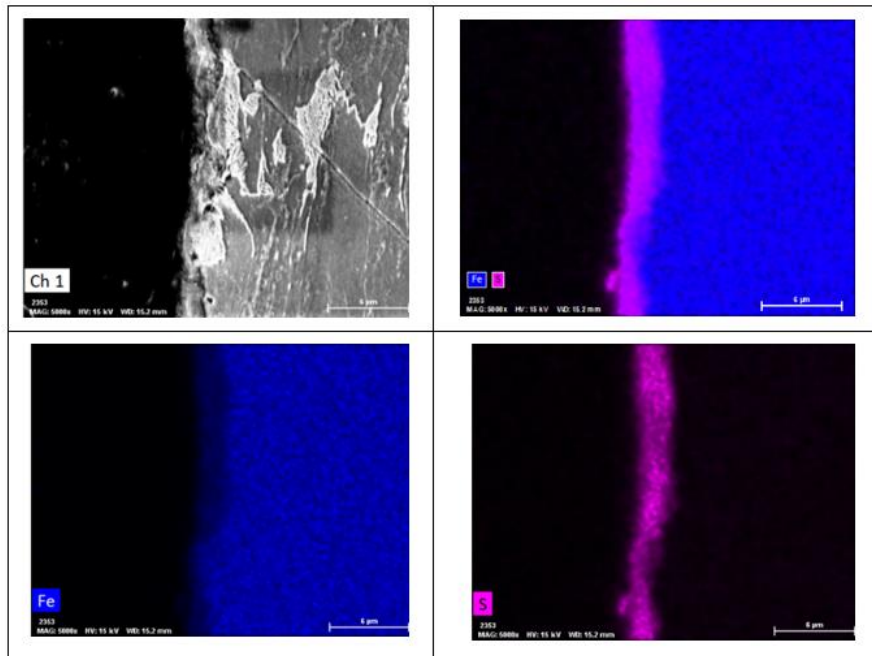


Figure 63:EDS mapping of FeS layer formed on UNS G10180 substrate after 4-day exposure in 1 wt.% NaCl solution at 30°C, at pH 6.00, and 0.1bar of H₂S and 250rpm impeller rotational speed

In the back scatter image of the UNS G10180 with the FeS layer presented in Figure 63, the upper part of the pearlite has a darker contrast than the bottom half, which confirms the formation of FeS layer within this pearlite region. Figure 64 shows the results from the EDS spot analysis of the FeS layer formed within the pearlite and those that formed on other areas of the specimen. The spots of the EDS were scaled to the actual size of the spot area from where data was collected.

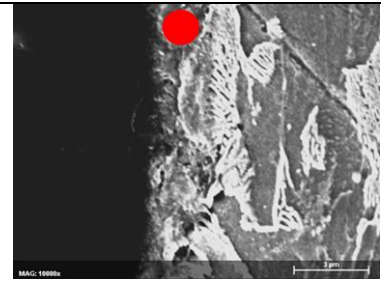
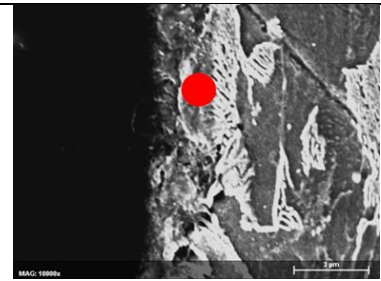
	Spot size radius of 0.7μm	Element	Atom %
		Carbon	44.58
		Oxygen	12.61
		Sulfur	15.58
		Iron	27.23
		Ratio Fe : S = 1 : 0.57	
	Spot size radius of 0.6μm	Element	Atom %
		Carbon	29.72
		Oxygen	13.51
		Sulfur	17.19
		Iron	39.57
		Ratio Fe : S = 1 : 0.43	

Figure 64: EDS spot analysis of the layer at different locations on the UNS G10180 substrate after 4 days exposure period in 1 wt.% NaCl solution at 30°C, pH 6.00, 0.1bar of H₂S and 250rpm impeller rotational speed (a.) outside the pearlite region (b.) in the pearlite region

The % carbon content of the layer formed in the pearlite region has a lower % carbon than that formed outside the pearlite region. Since the main source of carbon is the epoxy, it can be inferred that the layers with the lower % carbon content is more compact than those with higher carbon content. The layer formed above the pearlite region may be denser and more compact than the FeS layer formed in other areas on the specimen.

Surface SEM at different exposure times of the corrosion product layer formed on the different substrates showed no major difference in their morphology (Figure 65 and Figure 66). However, the XRD analysis (Figure 67) showed higher peaks for the mackinawite layer formed on 99.9% pure Fe.

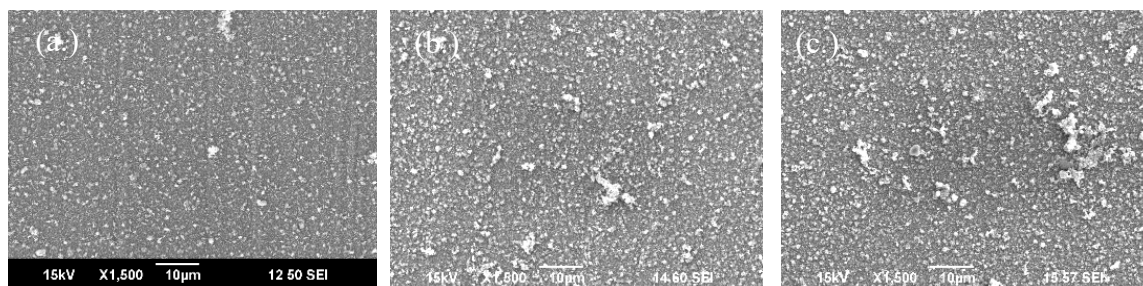


Figure 65: Surface SEM images of FeS layer formed on 99.9% pure Fe substrate exposed to 1 wt.% NaCl solution at 30°C, pH 6.00, 0.1bar of H₂S and 250rpm impeller rotational speed after (a.) 1 day, (b.) 3 days and (c.) 4 days

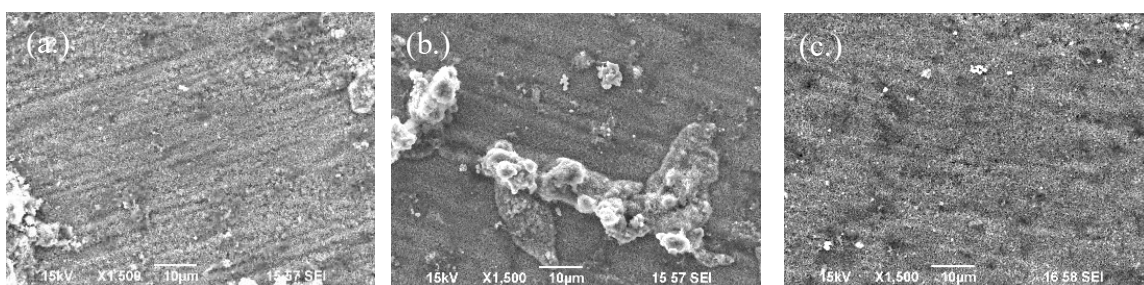


Figure 66: Surface SEM images of FeS layer formed on UNS G10180 exposed to 1 wt.% NaCl solution at 30°C, pH 6.00, 0.1bar of H₂S and 250rpm impeller rotational speed after (a.) 1 day, (b.) 3 days and (c.) 4 days

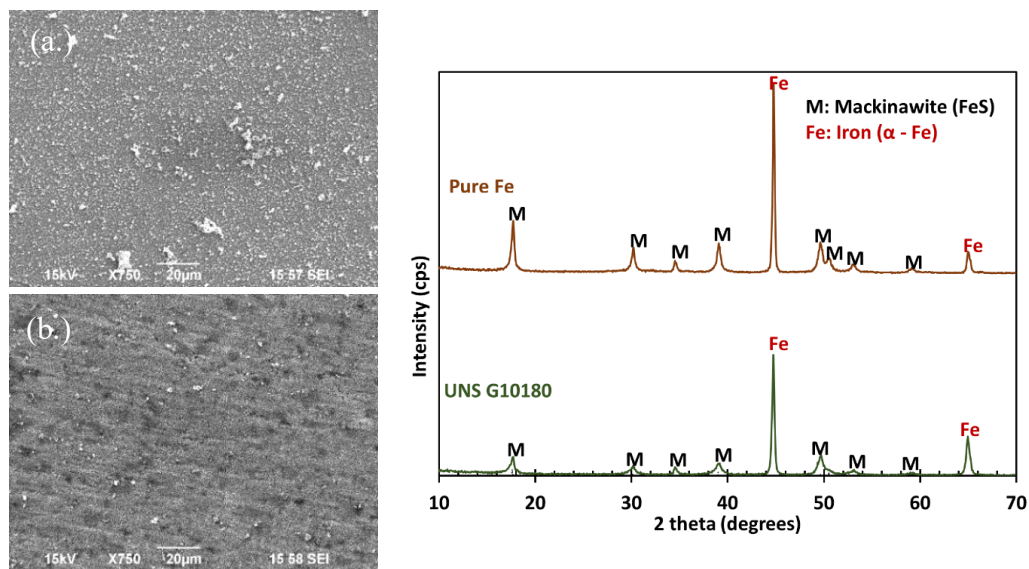


Figure 67: XRD analyses of corrosion product layers formed on (a.) 99.9% pure Fe and (b.) UNS G10180 after 4 days exposure in 1 wt.% NaCl solution, pH 6.00, and 0.1 bar of H_2S at system temperature of $30^\circ C$ and impeller rotational speed of 250rpm

Figure 68 shows the ratio of moles of Fe lost due to corrosion to moles of Fe precipitated on the substrate.

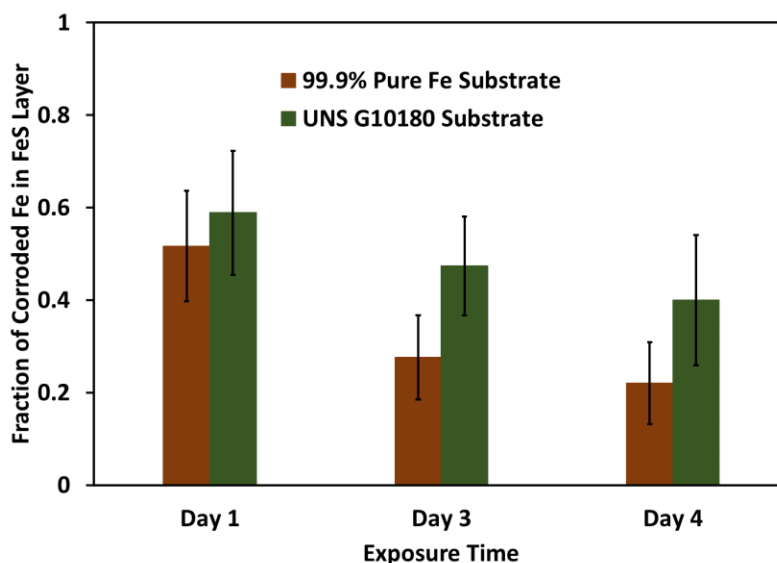


Figure 68: Fraction of corroded Fe in the FeS layer after exposure of 99.9% pure Fe and UNS G10180 substrates to 1 wt.% NaCl solution, pH 6.00, and 0.1bar of H₂S at system temperature of 30°C and impeller rotational speed of 250rpm.

The error bars in Figure 68 represents the spread of the measured fraction of corroded Fe in the FeS compared to the average fraction. While this average fraction value suggests that more of the Fe corroded was retained in the layer with UNS G10180 substrate, major conclusions cannot be made considering the error in the experiments. Therefore, it is inferred that the protectiveness of the corrosion product layers formed when UNS G10180 and 99.9% pure Fe were exposed to the test solution was independent of the layer characteristics. This is similar to the findings from the study conducted in the pH 5.00 solution.

Profilometry of Corroded Surfaces

The surfaces of the exposed metals were examined using a profilometer to detect any possible occurrence of localized corrosion. The mapped topography of the specimen

surfaces presented in Figure 69 and Figure 70 showed the possible occurrence of localized attacks on the pure Fe substrate and uniform corrosion occurred on the UNS G10180 substrate. With the absence of localized attack on the specimen after 1-day exposure and the occurrence of pitting on the specimen extracted on the third day, the localized corrosion can be said to initiate on/after the third day of exposure.

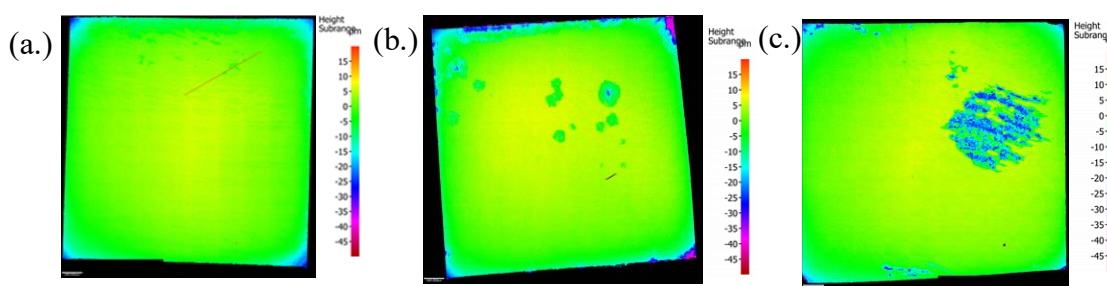


Figure 69: Topography of 99.9% pure Fe surface after removing the corrosion product layer with Clarke solution after exposure times of (a.) 1 day (b.) 3 days and (c.) 4 days.

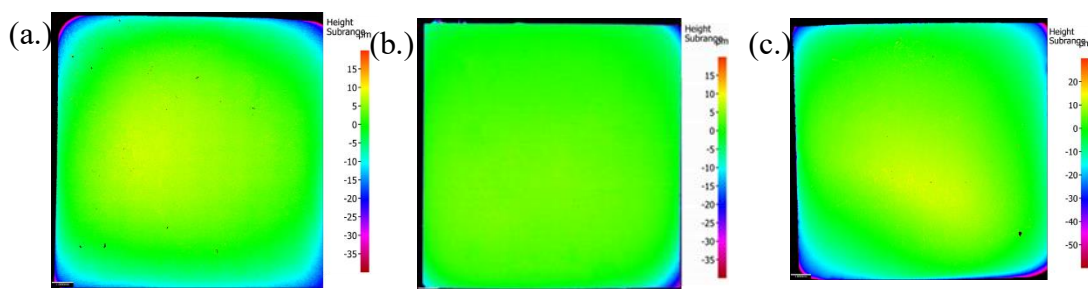


Figure 70: Topography of UNS G10180 surface after removing the corrosion product layer with Clarke solution after exposure times of (a.) 1 day (b.) 3 days and (c.) 4 days.

However, these localized attacks could not be reproduced as the repeat experiment showed an unevenly corroded surface on the 4th day of exposure (Figure 71).

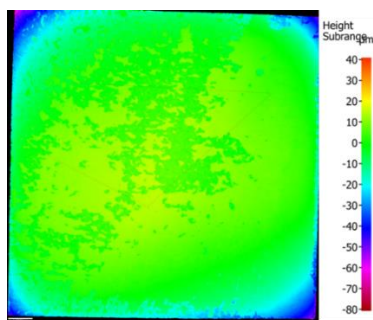


Figure 71: Topography of the UNS G10180 surface after removing the corrosion product layer with Clarke solution after 4 days (Repeat experiment).

Based on the available evidence, it is insufficient to infer the occurrence of localized corrosion on the 99.9% pure Fe substrate in the current test environment. However, with the difference in the surface profile of the substrates after the removal of the corrosion product layers, it can be concluded that, under the current experimental condition, the layers had a better attachment on the UNS G10180 substrate in comparison to the 99.9% pure Fe substrate.

Summary

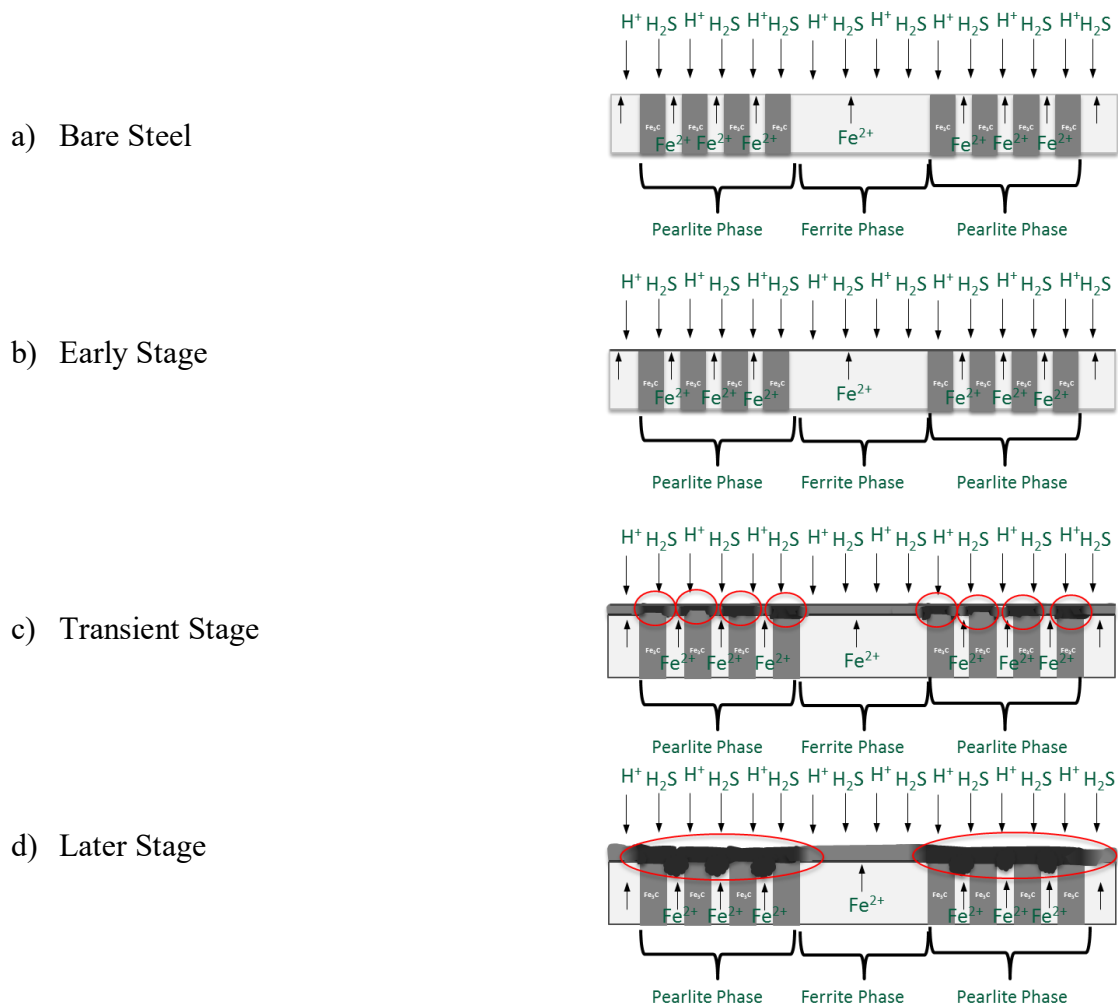
- A better attachment of iron sulfide layers was achieved on UNS G10180 substrate based on the following evidence:
 - A better FeS coverage inferred from open circuit potential trends
 - An unevenly corroded surface of the 99.9% pure Fe substrate observed after the removal of the FeS layer in comparison to the even surface of the UNS G10180 substrate.

- Corrosion rate results suggest that the FeS layer formed on UNS G10180 was more protective than that formed on the 99.9% pure Fe especially in the first day of specimen exposure.

5.4 Proposed Mechanism for FeS Development

5.4.1 FeS Development on UNS G10180 Substrate

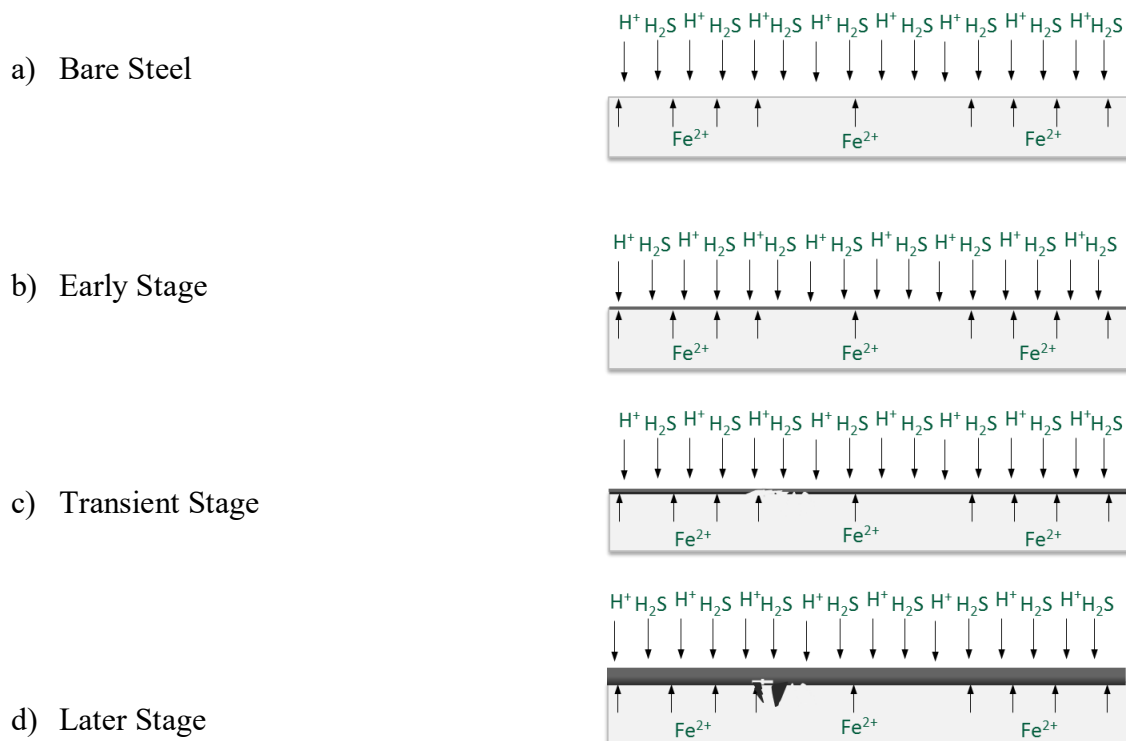
In the proposed mechanism for FeS development on the UNS G10180 substrate, the anodic reaction shown in Equation 13 occurs on the ferrite phase while the cathodic reactions shown Equations 22 and 23 occur on the cementite phase leading to a preferential precipitation of FeS in the pearlite region.



The early stage of the corrosion process involves the formation of the initial thin and continuous mackinawite layer. After the early stages, the layer starts to grow in such a way that there is a greater precipitation of FeS on the cementite (areas highlighted with the red circles). This is a transient stage and may not be captured during the experiment. The later stages of the FeS development involves the complete coverage of the surface with FeS with preferential precipitation on the pearlite phase (areas highlighted with red circles).

5.4.2 FeS Development on 99.9% Pure Fe Substrate

When 99.9% pure Fe is used, the anodic and cathodic reactions presented in Equation 13 and Equations 22 and 23 occur across the entire metal surface.



The formation of the thin mackinawite layer also occurs at the initial stages of the corrosion process. The transient stage involves the formation of new corrosion product layer which is affected by rate of corrosion that occurs underneath. The FeS may be loosely attached onto the substrate due to the undermining impact of corrosion. In the later stages of the layer development, localized corrosion may initiate in these regions where FeS is loosely attached due to high cathodic areas. This process is also accompanied by further growth of the FeS layers.

5.5 Summary

- The presence or absence of Fe_3C does not affect the final steady state corrosion rate.
- The presence of Fe_3C promotes precipitation of FeS in the pearlite region.
- The presence of Fe_3C favors the attachment of FeS layers and leads to a faster decrease in the corrosion rates.
- The pure Fe substrate showed possible susceptibility to localized corrosion at 250rpm impeller speed and solution pH 6.00. However, the evidences are not fully conclusive as the occurrence of localized corrosion could not be repeated.

CHAPTER 6: EFFECT OF FLOW ON THE DEVELOPMENT AND RETENTION OF IRON SULFIDE LAYERS

6.1 Introduction and Research Goal

The operating conditions of many wells often include the transport of fluids at high velocity, leading to the generation of high shear stresses on the surface of transport pipelines. However, the impact of high wall shear stress on the formation of protective iron sulfide corrosion product layers, which is critical to the overall integrity of the pipeline, is poorly understood. With the possible occurrence of localized corrosion associated with sour gas, it is important to clearly understand the influence of high flow conditions on the development and retention of the corrosion product layers formed and to be able to further relate this to their protective properties.

An important factor that has been considered in this research work is the influence of iron carbide on the development and retention of iron sulfide layers and how it influences their protectiveness. It has been reported that an exposed iron carbide matrix in a ferritic/pearlitic steel microstructure does not have the mechanical strength to withstand a high flow velocity that can impact a shear stress of the magnitude of 100 Pa [23]. With studies showing that an iron carbide network (especially related to an F/P steel) can enhance the formation of iron carbonate layers, its removal by high shear stress becomes critical to the formation of these protective corrosion product layers. However, results discussed in the previous chapter, as well as other reported findings, have shown that the corrosion of an F/P steel in a sour environment is devoid of an active corrosion stage, primarily due to the fast precipitation kinetics of iron sulfides[26,53,55,60].

The results presented in Chapter 5 on the role of iron carbide on the development of iron sulfide layers in low shear stress conditions also showed morphological differences in the layers developed on a 99.9% pure Fe and UNS G10180 substrate with an increased precipitation of iron sulfide observed in the pearlite region of the F/P steel. The behaviors of these layers at high shear stress and increased mass transfer rates may govern the overall corrosion behavior of the substrates. Therefore, in addition to investigating the role of shear stress on the development and retention of these layers, another goal of the current study is to investigate if the presence of iron carbide in an F/P steel has any effect on its corrosion behavior, especially in high shear stress conditions with concomitant enhanced mass transfer.

The choice of solution chemistry is critical to the information that can be deduced from the corrosion behavior of steel in sour environments. Depending on the concentration of hydrogen ion and sulfide species, the corrosion process in a sour environment can be either under charge transfer or mass transfer control. Also, systems which were hitherto under charge transfer limitation can become mass transfer controlled if protective corrosion product layers are developed. Zheng, *et al.*, [19] investigated the effect of mass transfer on the development of corrosion product layers formation by exposing an API X65 steel to a solution sparged with 0.05 bar H₂S at 80°C and pH 4.0. The protective properties of the layers formed in this condition could not be properly evaluated since the system was initially under mass transfer control, even before the formation of the corrosion products. This highlights the need to conduct the current studies in conditions where, prior to the formation of layers, the corroding system is

under charge transfer limitations such that any subsequent trends in corrosion rates can be directly attributed to the properties of the developed corrosion product layers.

In the current study, the effect of flow on the development of iron sulfide layers was investigated by exposing a UNS G10180 carbon steel and 99.9% pure Fe to different flow conditions. Similarly to the studies described in Chapter 4, the different substrates were used in the current study to highlight any possible influence of iron carbide on the morphology and protectiveness of FeS layers developed. The integrity of these FeS layers were tested under high shear stress and mass transfer rates.

6.2 Experimental Setup and Methodology

6.2.1 Equipment

Experiments were conducted in the 5-liter single phase flow loop system (Figure 31) which can accommodate three $\frac{1}{2}$ " diameter cylindrical specimens. These specimens were flush mounted in a channel test cell where the electrolyte flowed across the specimen surface. A three electrode system was used for all electrochemical measurements with a nickel sample placed in the topmost (downstream) sample location as the reference electrode (Figure 32), the electrochemical specimen placed in the middle location as the working electrode while the body of the SPFL system was used as the counter electrode. A test specimen was placed in the lowest sample location (upstream) for mass loss measurements. The description of different parts of this system, and the flow characteristics is discussed in Chapter 4.

6.2.2 Material

The materials used for the current study are commercially sourced 99.9% pure Fe and UNS G10180 carbon steel substrates. The chemical composition and the microstructure of these materials are presented in Figure 41b and Table V, respectively.

Specimens were prepared using the same procedure presented in Chapter 5. After preparation, test specimens were placed in their holders (Figure 32) and the assembly was fastened into place in the channel cell. To ensure the specimens are flush mounted, a shim with thickness similar to the height of the channel was inserted inside the channel while the specimens were assembled into place.

6.2.3 Test Methodology and Procedure

5 liters of 1 wt. % NaCl electrolyte was introduced into the solution conditioning section of the test system and sparged with nitrogen gas for 2 hours. At this time, the cell assembly was installed in the test section of the SPFL and nitrogen gas was passed through the system in order to keep the environment inert, thereby preserving the sample surface. Thereafter, the system was kept at a pressure of 20psi with nitrogen gas until the test solution was ready to be introduced into the system. A valve connecting the test section to the autoclave and the solution conditioning section was shut off in order to direct the test solution to the autoclave section without coming in contact with the sample.

After two hours of nitrogen sparging, the desired 10% by volume of H₂S gas in a mixture with N₂ was sparged into the electrolyte for an additional 45 minutes. The pH of the solution was adjusted to the desired value by adding deoxygenated 1 M aqueous

NaOH. After conditioning, the solution was introduced into the test system by applying a positive pressure between the solution conditioning section and the test system. After transferring the test solution to the autoclave, the system was pressurized with nitrogen to 15 psi and the valve connecting the test section to the autoclave was opened. The flow loop section of the system, consisting of the autoclave, the test section and the flow pipes, was isolated from other parts of the system with the aid of a valve. The test solution velocity and temperature were set to the desired values and electrochemical measurements started. For safety reasons, all the lines that supplied H₂S to the system during test preparation were cleaned by passing nitrogen gas through the line to the combustion system.

At the end of the experiment, the solution was discharged into a container with sodium hydroxide to react with the dissolved H₂S. The test section was detached from the system and the test cell was rinsed with deoxygenated water to remove all the salt on the specimen surface, and subsequently with isopropanol to complete the drying process. The test specimens were extracted and dried in a stream of nitrogen gas. SEM/EDS analysis, surface profilometry and mass loss measurements were conducted on one specimen, while cross-sectional analysis was conducted on the second test specimen. After removal of the corrosion product layers, specimens were characterized with a profilometer to check for the occurrence, or not, of localized corrosion. XRD analyses were conducted on specimens after exposure to identify the phase(s) present in the FeS layers formed under the current test conditions.

6.2.4 Test Matrix

The test matrix for studying of the effect of flow on the development of iron sulfide on UNS G10180 steel and 99.9% pure Fe are presented in Table VII. These experiments were conducted by applying the same fluid velocities from the start to the end of the experiment. Experiments were conducted at mass transfer rates similar to those in the glass cell and the corrosion behavior of the materials in the two systems were compared.

Table VII: Test Matrix for the study of the effect of flow on the development of iron sulfide on UNS G10180 steel and 99.9% pure Fe

Operating Parameter	Specification	
Material	UNS G1018	99.9% Pure Fe
H ₂ S Partial Pressure	0.1 bar	
Total Pressure	1.01 bar	
Electrolyte	1 wt.% NaCl	
Solution pH	6.00	
Temperature	30°C	
Expected FeS Phase	Mackinawite	
Fluid Velocity	1.1 m/s ($\tau = 7.2$ Pa, $k_{\text{H}_2\text{S}} = 1.3 \times 10^{-4}$ m/s) 10.4 m/s ($\tau = 363$ Pa, $k_{\text{H}_2\text{S}} = 9.4 \times 10^{-4}$ m/s)	
Test Duration	4 days	
Measurement Methods	LPR, EIS	
Surface Analysis	SEM, EDS, XRD	

The test matrix for the study of the effect of flow on the retention of iron sulfide layers on UNS G10180 is presented in Table VIII. In this study, the layer was developed at low flow conditions, 1.1 m/s and exposed to a gradually increased shear stress.

Table VIII: Test Matrix for the study of the effect of flow on the retention of iron sulfide on UNS G10180 and 99.9% pure Fe

Operating Parameter	Specification
Material	UNS G10180
H ₂ S Partial Pressure	0.1 bar
Total Pressure	1.01 bar
Electrolyte	1 wt.% NaCl
Solution pH	6.0
Temperature	30°C
Expected FeS Phase	Mackinawite
Test Duration	7 days
Measurement Methods	LPR, EIS
Surface Analysis	SEM, EDS, XRD

The graph presented in Figure 72 shows the different fluid velocities applied and the different specimen exposure times corresponding to the layer development and layer retention test stages. The development stage is the period where the corrosion product layer was developed at a low shear stress condition (7.2Pa) while the retention stage is the period where the developed FeS layer was challenged under a gradually increasing shear stress conditions.

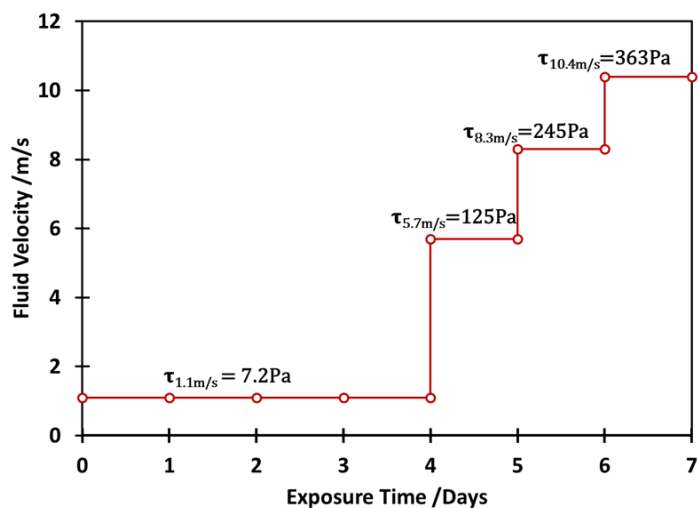


Figure 72: Fluid velocities and sample exposure times for FeS retention experiment on UNS G10180 substrates.

6.3 Results and Discussion

To ensure that the initial corrosion process in the stated experimental conditions is under charge transfer control, the polarization curve at the 1.1 m/s and 10.4 m/s fluid velocities were modeled. To model the polarization curves at these flow velocities, the anodic and individual cathodic current densities for the different species with respect to potential were calculated. In the current system, the main anodic reaction is the iron dissolution reaction (Equation 13) while the cathodic reactions include the hydrogen reduction (Equation 22), H₂S reduction (Equation 23) and water reduction reactions (Equation 24). The calculation for the current density associated with the anodic reaction and the cathodic reactions, with the exception of the H₂S reduction reaction, is discussed in Section 4.2.1. In calculating the mass transfer current density for the H⁺ reduction reaction, the flow dependent mass transfer coefficient of hydrogen ion, k_{m,H^+} , in Equation 55 was calculated with the Sherwood correlation for channel flow presented in Equation

71 [136]. Similar to H^+ reduction reaction, the current density for the H_2S reduction reaction is a harmonic mean of the charge transfer and mass transfer current densities:

$$\frac{1}{i_{H_2S}} = \frac{1}{i_{ct,H_2S}} + \frac{1}{i_{lim,H_2S}^d} \quad (75)$$

i_{H_2S} is the total current density for the H_2S reduction reaction while i_{ct,H_2S} and i_{lim,H_2S}^d are the charge transfer and mass transfer current densities. The unit for all current density values is A/m^2 .

The charge transfer current density in Equation 75 is calculated by using the Tafel equation for H_2S reduction:

$$i_{ct,H_2S} = i_{0,H_2S} \times 10^{\frac{\eta}{b_c}} \quad (76)$$

The Tafel slope, b_c , for the reduction of H_2S has been reported [39] in the literature as 0.12V/decade. η is the overpotential in mV, which is the difference between the applied potential and the reversible potential. The calculation for the exchange current density and reversible potential was discussed by Zheng, *et al.*, [39] and was implemented in the same way in the current study.

The mass transfer current density, i_{lim,H_2S}^d , was calculated with an equation similar to that of hydrogen reductions (Equation 55).

$$i_{lim,H_2S}^d = k_{m,H_2S} F C_{H_2S} \quad (77)$$

Where k_{m,H_2S} is the mass transfer coefficient of H_2S (in m/s) calculated with Equation 71, F is Faraday's constant (in C/mol), and C_{H_2S} is the molar concentration of H_2S in solution (in M).

The modelled anodic and cathodic potentiodynamic curves at flow velocities of 1.1m/s and 10.4m/s in the current experimental conditions are presented in Figure 73 and Figure 74.

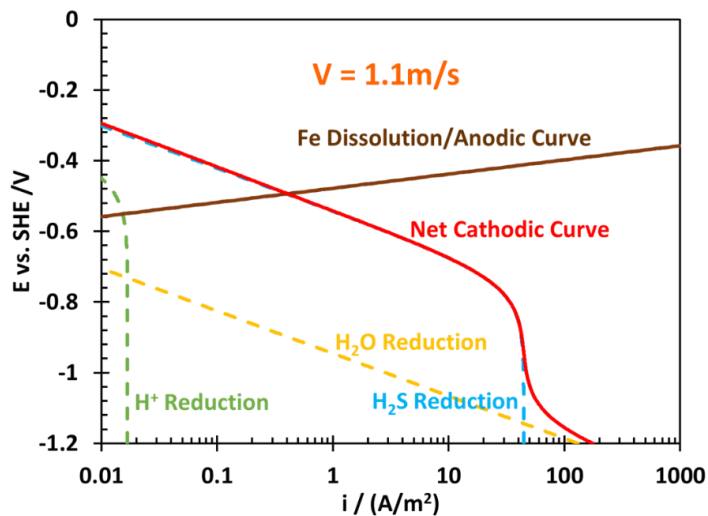


Figure 73: Modelled anodic and cathodic potentiodynamic curves for 10% vol. H₂S/N₂ at pH 6.00, 30°C and flow velocity of 1.1m/s

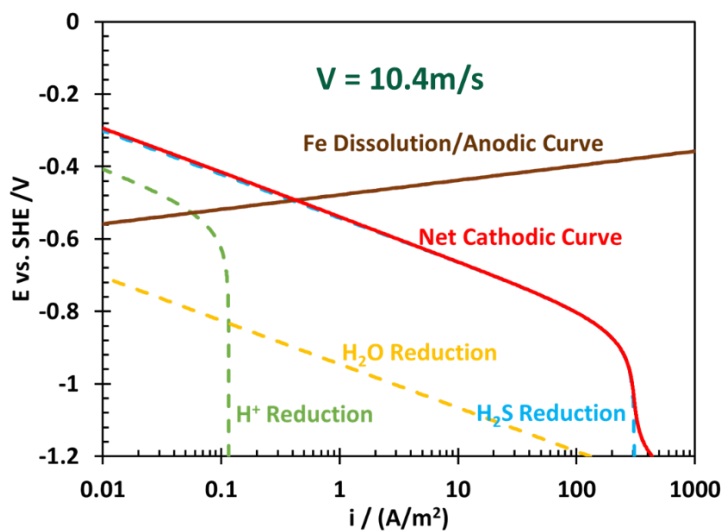


Figure 74: Modelled anodic and cathodic potentiodynamic curves for 10% vol. H₂S/N₂ at pH 6.00, 30°C and flow velocity of 10.4m/s

Figure 73 and Figure 74 show that the corrosion current densities at 1.1m/s and 10.4 m/s are similar, at approximately 0.5 A/m^2 , confirming that the initial corrosion process (in the absence of FeS layers) is under charge transfer control. Consequently, any difference in the corrosion behavior of the substrates during exposure to the test condition can be attributed to the layers formed at the different fluid velocities.

6.3.1 Development of Iron Sulfide Layer on UNS G10180 Substrate

Figure 75 shows the corrosion rate of UNS G10180 at flow velocities of 1.1m/s and 10.4m/s, corresponding to shear stresses of 7.2Pa and 363Pa, respectively. This plot shows the initial corrosion rates at the different velocities were similar at an average value of 0.75 mm/y. However, with time the corrosion rate at 1.1m/s decreased after 38 hours to a stable corrosion rate of 0.5mm/y, whereas at fluid velocity of 10.4 m/s, the corrosion rates remained approximately the same all through the exposure time. This corrosion rate trends suggest a possible effect of different fluid velocities on the protectiveness of the corrosion product layers.

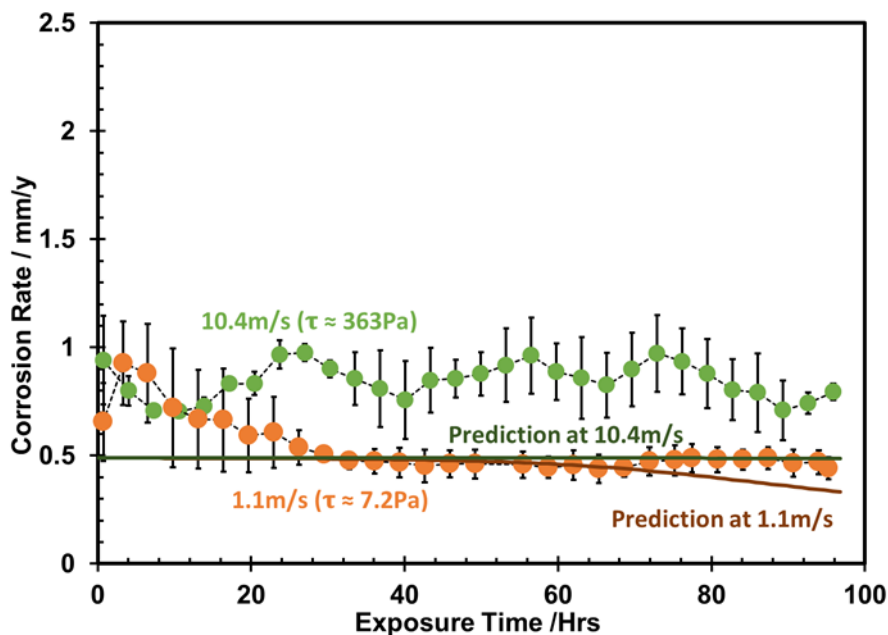


Figure 75: Corrosion rate trend of UNS G10180 during a 4 days exposure to 1 wt.% NaCl solution sparged with a 10% vol. H₂S in admixture with nitrogen at pH 6.0, 30°C and flow velocities of 1.1 m/s and 10.4 m/s

Figure 76 shows the corrosion rates obtained by mass loss methods at the different flow velocities compared with the time averaged instantaneous corrosion rates measured by LPR. This chart shows slight differences in corrosion rate measurements obtained from different methods. However, both corrosion measurement methods confirmed the occurrence of higher corrosion rates at increased fluid velocity (10.4m/s). Although the corrosion process under the current conditions was initially under charge transfer limitation, the formation of FeS layers provided a diffusion barrier, thereby changing the rate determining step to mass transfer of species through the layer. By implication, the mass transport rate is dependent on the properties (porosity, tortuosity and thickness) of the corrosion product layers developed at the different flow velocities.

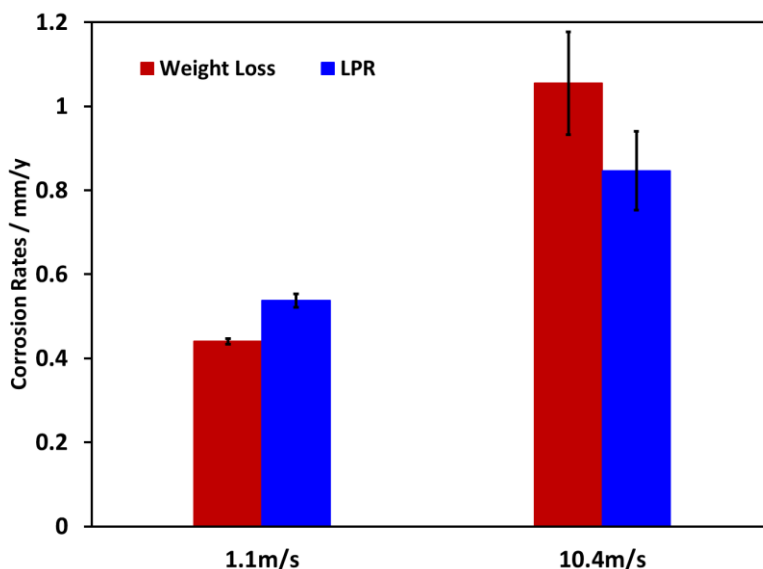


Figure 76: Corrosion rate measurement by weight loss compared with time-averaged corrosion rates from LPR measurement after 4 days exposure of UNS G10180 to 1 wt.% NaCl solution sparged with 10% vol. H₂S in admixture with nitrogen at pH 6.0, 30°C and flow velocities of 1.1m/s and 10.4m/s

It can also be seen that the mass transfer of H₂S at 1.1m/s flow velocity in the SPFL is similar to that at a 250rpm impeller rotational speed in the glass cell apparatus are similar. With the test solution conditions the same, the corrosion rates of UNS G10180 at 250rpm impeller speed was similar to corrosion rates obtained at 1.1m/s fluid velocity in the channel. This suggests that the corrosion product layers developed in these flow conditions have similar properties so that the mass transfer rate of electroactive species through them is similar.

Analysis of the Corrosion Product Layer

Figure 77 shows the surface SEM and the cross section of the corrosion product layers developed after 4 days exposure at fluid velocities of 1.1m/s and 10.4m/s, respectively. The surface SEM images of the FeS layers showed different features with

the layer developed at 10.4m/s having cracks which were not observed on the layers develop at 1.1m/s. It is unknown if these cracks occurred *in situ* or during the extraction of the specimens. However, since the same extraction procedure was implemented in all experiments, the differences in the layer morphologies raises suspicions about the possible differences in the hardness of the layers. This is addressed extensively in Chapter 7 of this dissertation. If the cracks seen on the corrosion product layers occurred *in situ* (i.e. during the experiment), it implies that this layer has a tortuous path affecting the diffusion of species to the electrode surface. However, if the cracks occurred *ex situ*, during specimen extraction and post-processing, it shows that the corrosion product layer possessed weak elastic properties since only the strongly attached corrosion product layers can retain their shape. In both scenarios, i.e. *in situ* or *ex situ* formation of cracks, the porosity of the layers developed at 10.4m/s would have a higher porosity which should provide a lower resistance to mass transfer compared to the layer formed at 1.1m/s (7.2Pa). Even with the difference in morphologies, the thickness of these layers formed under different flow velocities was similar.

Another difference in the layer morphology was revealed from the cross-sectional analysis of the FeS layer formed in the flow conditions. The layer formed at 1.1m/s comprised of an outer non-adherent “fluffy” layer and an inner compact layer, while at 10.4m/s the outer non-adherent layer did not form. Sun, *et al.*, [59] obtained a layer of similar morphology in low shear stress conditions, when a X65 carbon steel was exposed for 24hours to 1 wt.% NaCl solution sparged with a 1% H₂S in a mixture with N₂ (1 bar total pressure), at pH of 5.00 and temperature of 80°C. A two layer structure, comprising

of an inner compact and outer “fluffy” part, was reported in the cross-sectional analysis of the FeS layers. The formation of the outer fluffy layer was attributed to undersaturation of the bulk solution. This may not be the case in the current study since the calculated FeS saturation in the bulk solution was in excess of one. On the contrary, the increase of FeS saturation due to Fe^{2+} accumulation and increase in pH may be the reason for the precipitation that occurs on the specimen surface. It is not certain if the diffusion barrier caused by the layers is dependent on the difference in morphology. However, the absence of the outer less adherent layer at a high shear stress of 363Pa highlights the possible impact of shear stress on the morphology of the layer formed.

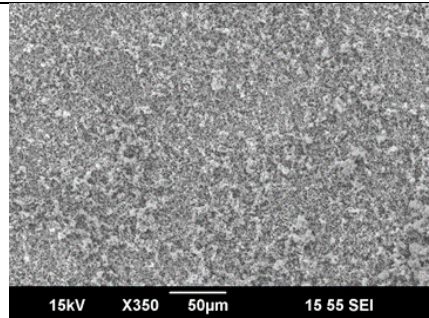
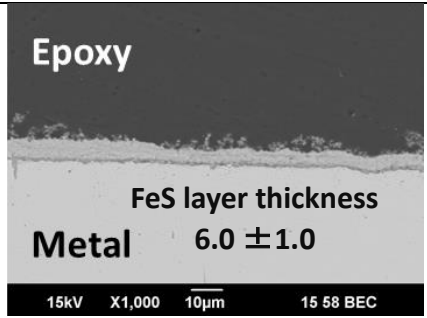
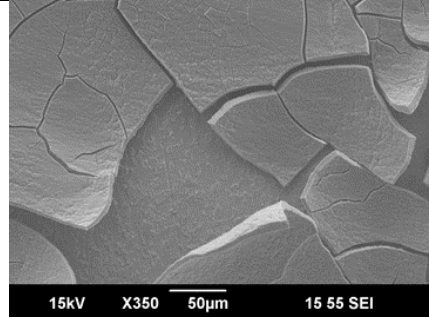
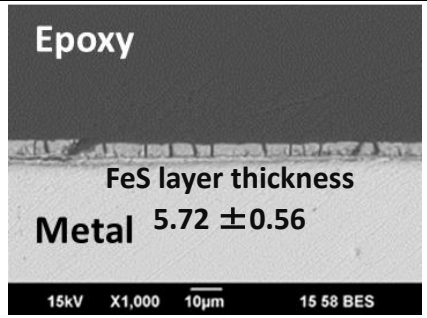
Condition	Surface	Cross Section
1.1m/s $\tau = 7.2\text{Pa}$, $k_{\text{H}_2\text{S}} = 1.3 \times 10^{-4}\text{m/s}$	 <p>15kV X350 50μm 15 55 SEI</p>	 <p>Epoxy</p> <p>FeS layer thickness</p> <p>Metal 6.0 ± 1.0</p> <p>15kV X1,000 10μm 15 58 BEC</p>
10.4m/s $\tau = 363\text{Pa}$ $k_{\text{H}_2\text{S}} = 9.4 \times 10^{-4}\text{m/s}$	 <p>15kV X350 50μm 15 55 SEI</p>	 <p>Epoxy</p> <p>FeS layer thickness</p> <p>Metal 5.72 ± 0.56</p> <p>15kV X1,000 10μm 15 58 BES</p>

Figure 77: Surface SEM and cross section analysis of corrosion product layers developed after 4 days exposure to 1 wt.% NaCl solution sparged with 10% H_2S in a mixture with N_2 at pH of 6.00, 30°C and flow velocity of 1.1m/s and 10.4m/s

Having confirmed the presence of corrosion product layers, the differences in the trends in corrosion rates may be a result of the diffusion barrier presented by these layers. Figure 78 shows the effect of layer porosity on the total mass transfer coefficient of H₂S at the different fluid velocities while considering an equal layer thickness of 6 μm and H₂S diffusivity of 2.3x10⁻⁹ m²/s [39]. The total mass transfer coefficient of H₂S was calculated using Equation 38 and the layer porosity was varied from 0 (representing layer with no pores and maximum diffusion resistance) and 1 (representing a bare electrode surface).

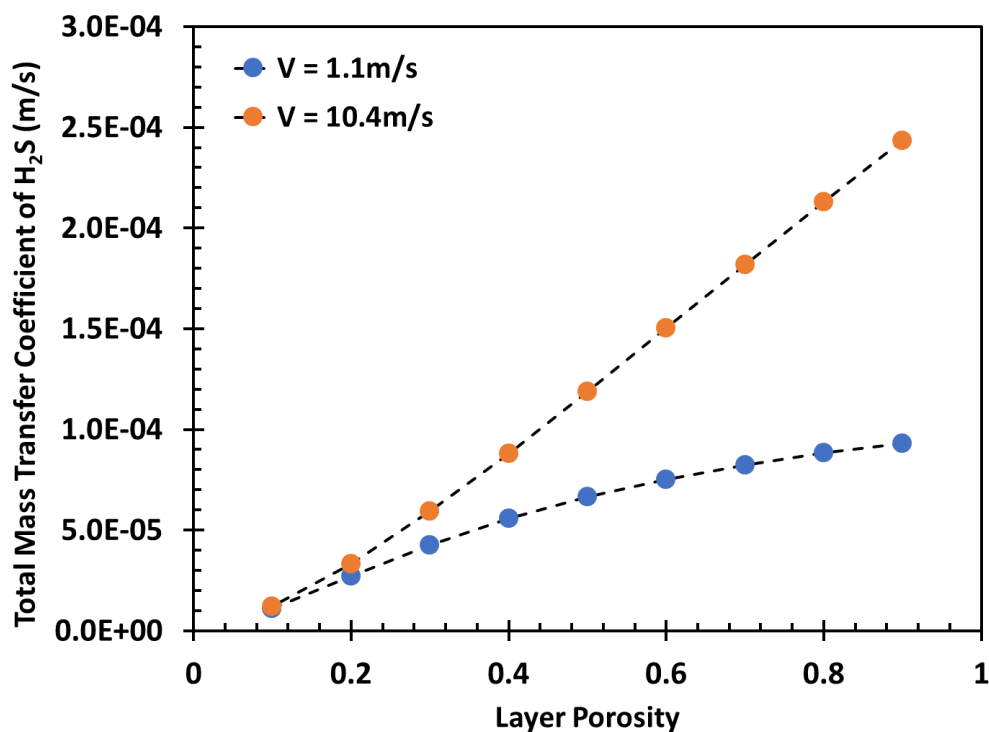


Figure 78: Effect of layer porosity on the total mass transfer coefficient of H₂S from the bulk through the layer to the specimen surface at equal layer thickness

It can be seen from Figure 78 that the response of the total mass transfer coefficient to layer porosity is higher at 10.4m/s than at 1.1m/s. This is because at 10.4m/s the mass transfer coefficient of H₂S in the bulk is very high so that the mass transport rate to the substrate surface is dominated by the diffusion through the layer, which increases monotonously with an increase in porosity. At a velocity of 1.1m/s, the total mass transfer coefficient is dominated by the mass transfer coefficient through the boundary layer, which is not affected by layer porosity.

It is important to mention that the layer porosity could not be calculated directly from layer mass and thickness measurements. Theoretically, the porosity of the developed iron sulfide layers could be determined by dividing its density with the density of iron sulfide mineral which is assumed to have a porosity of zero. The layer density at 1.1m/s and 10.4m/s was estimated at 4.27 g/cm³ and 5.49 g/cm³, respectively, from measurement of mass and average thickness of the layers. However, the density of these layers was higher than the density of pure mackinawite (4.17 g/cm³). This would yield a porosity higher than 1 which is clearly incorrect. This is most likely due to the presence of iron carbide matrix embedded in the FeS layers. For this reason, layer density, and consequently layer porosity calculations generated misleading results in this case.

At a flow velocity of 1.1m/s, it is thought that the shear stress (7 Pa) was too low to remove any formed corrosion product layer. Therefore, at this velocity, corrosion product layers of lower porosity were developed, compared to cases with higher velocity, and this resulted in a lower mass transport rate of species through it. However, at flow velocity of 10.4m/s, the shear stress generated at (363Pa) removed the outer weakly

attached corrosion products which decreased the overall mass transfer coefficient thereby enabling higher mass transfer rates of species through it. This condition may also favor galvanic effect by directly exposing the iron carbide network to the bulk solution. These are evident from the higher corrosion rates measured at 10.4m/s in comparison to those at 1.1m/s.

Chemical Analysis of Corrosion Product Layers

Figure 79 shows the EDS analysis of the corrosion product layers formed after the exposure of the UNS G10180 mild steel specimen to fluid velocities of 1.1m/s and 10.4m/s. The detection of iron and sulfur in the EDS maps confirmed the corrosion product layers as iron sulfide.

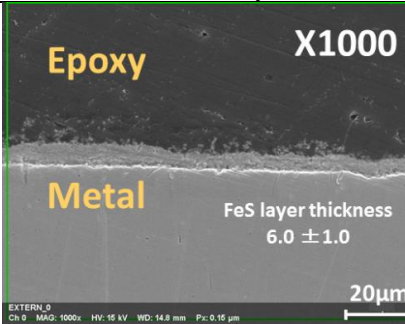
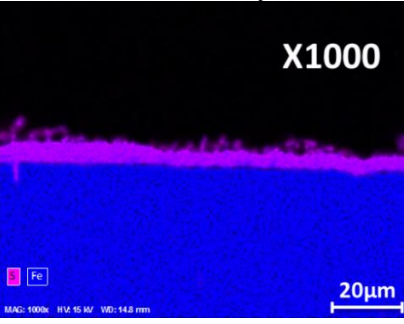
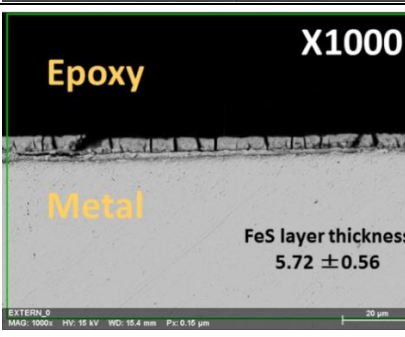
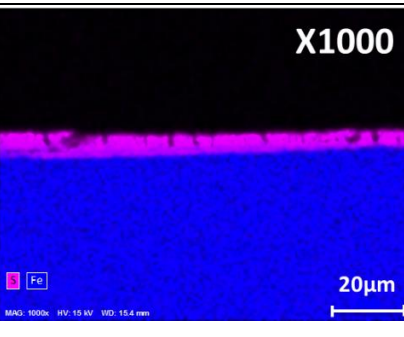
Condition	Thickness of Corrosion Product Layer	EDS Analysis of Corrosion Product Layer
<p>1.1m/s $\tau = 7.2\text{Pa}$, $k_{\text{H}_2\text{S}} = 1.3 \times 10^{-4}\text{m/s}$</p>		
<p>10.4m/s $\tau = 363\text{Pa}$ $k_{\text{H}_2\text{S}} = 9.4 \times 10^{-4}\text{m/s}$</p>		

Figure 79: EDS maps detecting iron and sulfur in the corrosion product layers developed after 4 days exposure to 1 wt.% NaCl solution sparged with 10% H₂S in admixture with N₂ at pH of 6.00, 30°C and flow velocity of 1.1m/s and 10.4m/s

Figure 80 shows the XRD patterns of the corrosion product layer formed on the specimens extracted after 4 days of exposure to the test solution at 1.1m/s and 10.4m/s.

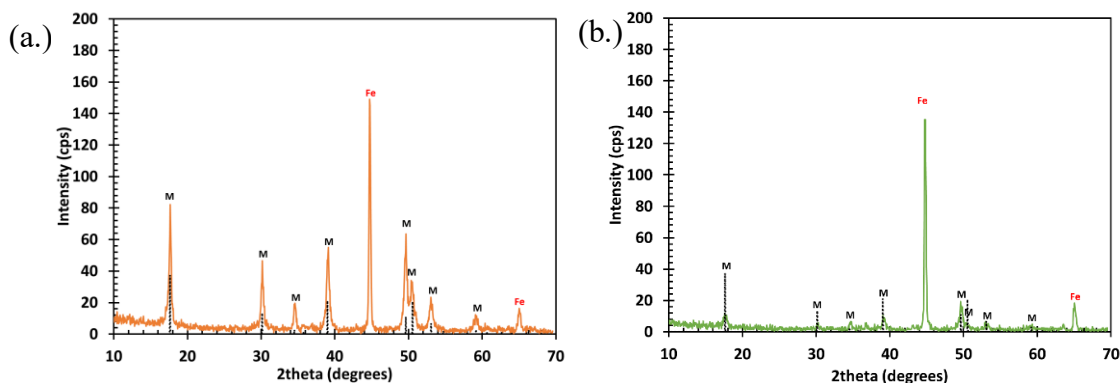


Figure 80: XRD analysis of iron sulfide layers developed on UNSG 10180 mild steel specimens after 4 days of exposure to 1 wt.% NaCl solution sparged with a 10% vol. H_2S in admixture with N_2 at pH 6.00, 30°C and flow velocities of (a.) 1.1 m/s and (b.) 10.4m/s

The mackinawite peaks detected in these XRD patterns confirmed the iron sulfide layer that developed after the exposure of the substrate to the corrosive environment was mackinawite.

Di Bonaventura[23] demonstrated that the removal of the anchoring structures of iron carbide with a shear stress of 100Pa prevented the formation of iron carbonates. With the identification of these layers as iron sulfide, specifically mackinawite, it has been confirmed that iron sulfide layers of $5.72 \pm 0.56 \mu m$ thickness developed at a shear stress approximately 3.5 time higher than that in which iron carbonates could not develop. This difference on the effect of flow on the development of iron sulfide and iron carbonate on a F/P steel was expected based on the established fact that the kinetics of iron sulfide layer precipitation is faster than that of iron carbonate layers[26]. Consequently, iron carbides are not readily removed from the steel surface as it always exists in the company of iron sulfides which reinforces its resistance to high shear stresses. However, it is unknown if these iron sulfides can develop in the absence of the

iron carbide structure. This can be elucidated by conducting a similar study with a 99.9% pure Fe, as discussed below in Section 6.3.2.

Metal Loss and FeS layer Thickness

The number of moles of Fe lost during corrosion was calculated by dividing the measured mass loss by the molar mass of iron, 55.85g/mol. The moles of Fe precipitated was calculated from the mass of the FeS layer, which is the difference between the mass of the substrate with the corrosion product layer and the mass of the substrate after removal of the corrosion product layer. This calculated mass of the FeS layer was then divided by the molar mass of FeS (87.91g/mol) to obtain the moles of FeS precipitated. Since the mole ratio of Fe to FeS in the precipitation reaction (Equation 33) is 1:1, the moles of Fe precipitated is, therefore, equal to the calculated moles of FeS. All calculated mole values are converted to molar density (mol/m^2) by dividing with the area of the exposed specimen surface. Figure 81 shows the moles of Fe corroded and the moles of Fe precipitated as FeS while the fraction of corroded Fe in the FeS layer is presented in Figure 82. These bar charts show a lower retention of corroded Fe at 10.4m/s fluid velocity in comparison to 1.1m/s.

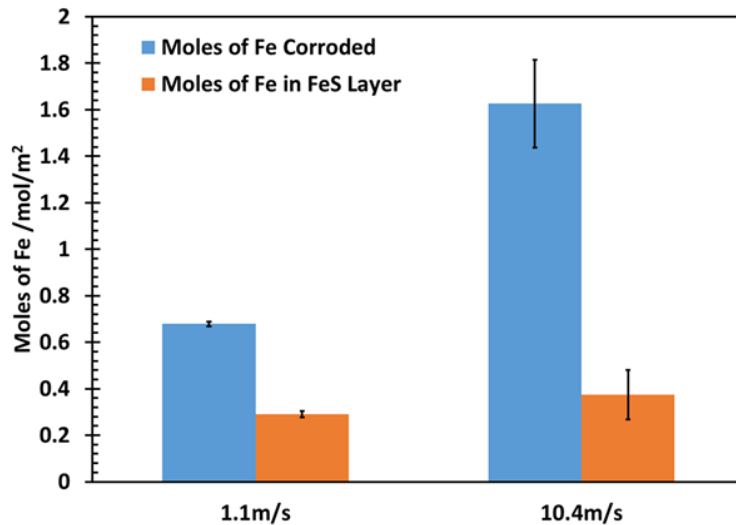


Figure 81: Moles of Fe corroded compared with moles of Fe precipitated (Fe in FeS layers) after exposure of UNS G10180 mild steel substrates to 1 wt.% NaCl solution, at pH 6.00, and 0.1bar of H₂S at 30°C and flow velocities of 1.1 m/s and 10.4m/s

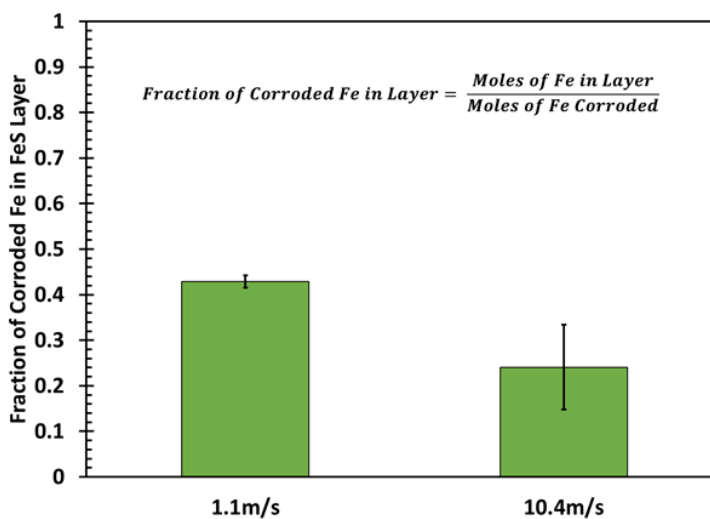


Figure 82: Fraction of corroded Fe in the FeS layers after exposure of UNS G10180 mild steel substrates to 1 wt.% NaCl solution, at pH 6.0, and 0.1bar of H₂S at 30°C and flow velocities of 1.1 m/s and 10.4m/s

For a more visual representation of the comparison of the retention of Fe at both fluid velocities, the mass loss of the metal due to corrosion and the mass of the FeS layers were converted to thickness by dividing with the area of the exposed surface and the densities of iron (7.86g/cm^3) and mackinawite (4.17g/cm^3), respectively. Figure 83 shows the retention of the corroded Fe is higher in the layer that developed at 1.1m/s than the layer that developed at 10.4m/s .

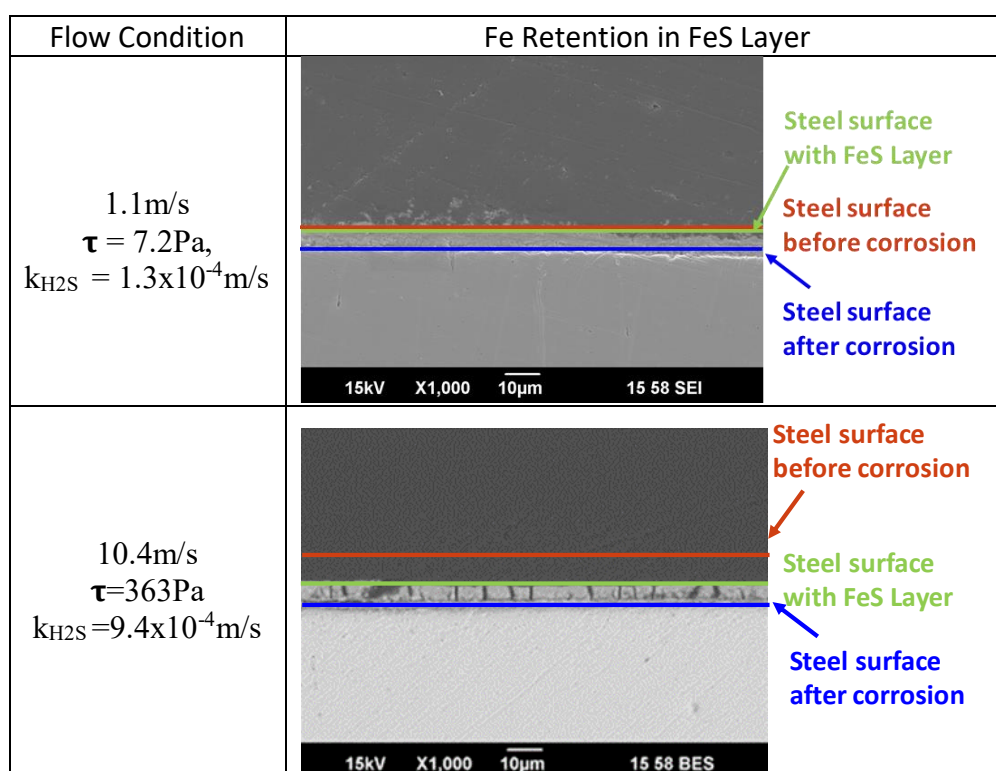


Figure 83: Level of steel surface before corrosion, with FeS layer and after removal of FeS layer developed after exposure of UNS G10180 to 1 wt.% NaCl solution at pH 6.0, and 0.1bar of H_2S at 30°C and flow velocities of 1.1 m/s and 10.4m/s

The results presented in Figure 83 further confirm the impact of wall shear stress on the morphology of the layer that developed at 1.1m/s and 10.4m/s .

Profile of Specimen Surface

Figure 84 shows the image of the specimen surface with the corrosion product layer formed at 1.1m/s (7.2 Pa) and 10.4m/s (363 Pa) and the corresponding profiles of the surfaces after removal of the FeS layers.

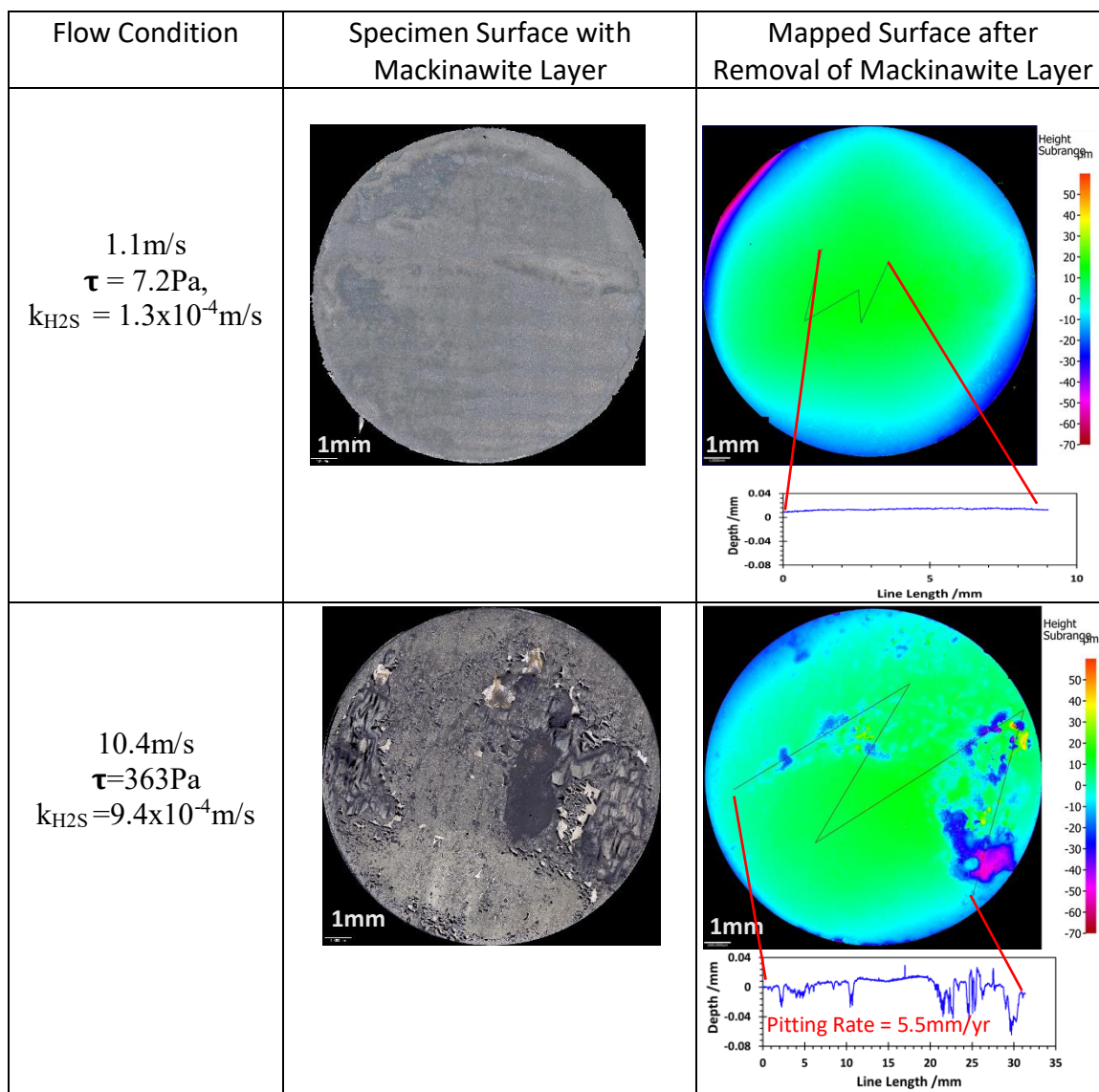


Figure 84: Specimen surface with FeS layer and the mapped specimen surface after the removal of the mackinawite layer formed after exposure of UNS G10180 to 1 wt.% NaCl solution at pH 6.0, and 0.1bar of H₂S at 30°C and flow velocities of 1.1 m/s and 10.4m/s

A difference can be observed in the FeS layers formed in the different flow velocities, with the layers formed at 1.1m/s more uniform than those formed at 10.4m/s. The profile of the surface of the specimen after removal of the FeS layers with Clarke solution[144] revealed the occurrence of localized corrosion on the specimen exposed to a solution at a flow rate of 10.4m/s, in contrast to the uniform corrosion on the specimen exposed to 1.1m/s flow velocity. At 10.4m/s, the mass transfer rate of corrosive species is higher due to the higher porosity of the FeS layer, resulting in an increase in undermining corrosion. This leads to a diminution in the scaling tendency of the layers formed in this condition. Therefore, the occurrence of localized corrosion at high flow velocity can be attributed to the undermining corrosion caused by the increased mass transport and inhomogeneity of the specimen surface due to the presence of iron carbide.

Summary

Based on the above results, it has been demonstrated that high shear stress, applied from the onset of the experiment, did not prevent the formation of mackinawite layers on the steel substrate. However, at 363 Pa shear stress, the formation of the top fluffy FeS layer observed at 7.2 Pa was impeded. With less retention of the corroded Fe in the layers observed at 363 Pa, and a resulting increase in mass transport rates through the layers, the pearlite and ferrite phases are exposed to the aggressive solution that constitutes the corrosive environment. Therefore, the higher undermining corrosion and the occurrence of localized corrosion observed at 10.4m/s can be postulated to be due to a synergy between wall shear stress and mass transport. Experiments were conducted with 99.9%

pure Fe to confirm the postulate that cementite (iron carbide) undermines the protectiveness of the layers.

6.3.2 Development of Iron Sulfide Layer on 99.9% Pure Fe Substrate

To determine the role of cementite in the development of FeS layers on UNS G10180 mild steel, experiments were conducted under similar condition with a pure Fe substrate.

Figure 85 shows the corrosion rate trend of a 99.9% pure Fe exposed to flow velocities of 1.1m/s and 10.4m/s.

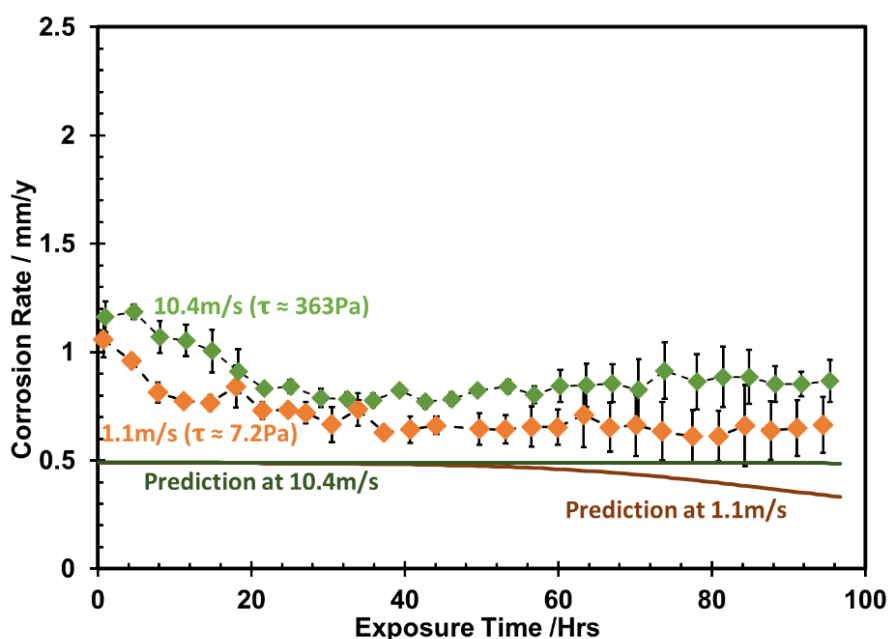


Figure 85: Corrosion rate trend of 99.9% pure Fe during a 4 days exposure to 1 wt.% NaCl solution sparged with a 10% vol. H₂S in admixture with N₂ at pH 6.00, 30°C and flow velocities of 1.1 m/s and 10.4 m/s

The corrosion rate trends suggest that the corrosion product layers developed on 99.9% pure Fe at the different fluid velocities showed fewer differences in terms of their

protective properties than what was observed with the UNS G10180 mild steel. Contrary to observations for the UNS G10180 substrate, a slight decrease in the corrosion rate can also be observed with 99.9% pure Fe at 10.4m/s. This suggests that the layers developed on pure Fe at this velocity may have a better protective property than those developed on the UNS G10180. These findings are contrary those from the study of the effect of iron carbide on FeS development in Chapter 5 (Figure 56 and Figure 58), where results showed that the FeS layers that developed on UNS G10180 is more protective than those that developed on 99.9% pure Fe. This highlights the possibility of a combined effect of mass transfer rates through the layers and the galvanic effect of iron carbide on the corrosion behavior of the F/P steel. The comparison of corrosion rates obtained with WL and LPR at the different fluid velocities are presented in Figure 86.

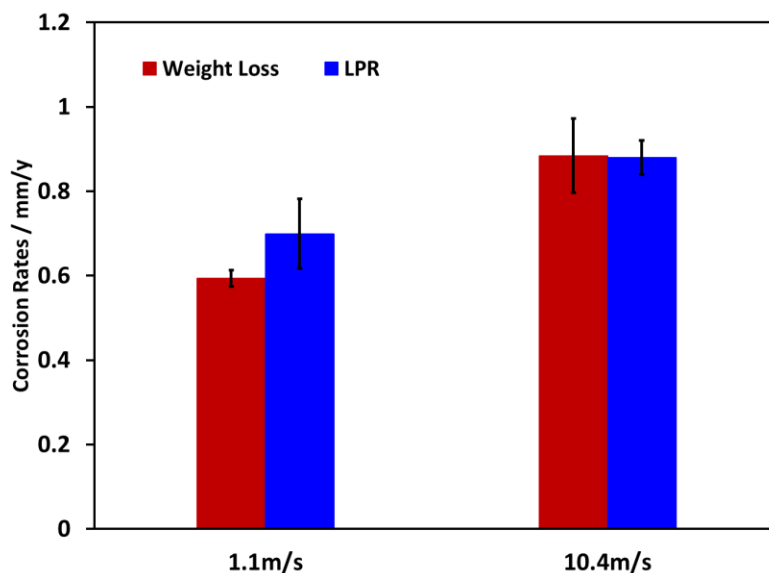


Figure 86: Corrosion rate measurement by weight loss compared with time averaged corrosion rates from LPR measurement after 4 day exposure of 99.9% pure Fe to 1 wt.% NaCl solution sparged with a 10% vol. H₂S in admixture with N₂ at pH 6.00, 30°C and flow velocities of 1.1 m/s and 10.4 m/s

While the corrosion rate measured at 1.1m/s was lower than the corrosion rate measured at 10.4m/s, less difference was observed between the two fluid velocities with pure Fe in comparison to UNS G10180. In the case of the pure Fe substrate, the increase in corrosion rates may be solely due to the higher mass transport rate from the bulk to the substrate surface. In contrast, it can be further postulated that, for the UNS G10180, electrical inhomogeneity between the cementite and ferrite, as well as mass transport rates through the layers, lead to an enhanced undermining corrosion.

Analysis of Corrosion Product Layers

Figure 87 shows that the corrosion product layers developed on the 99.9% pure Fe substrate after exposure to both fluid velocities.

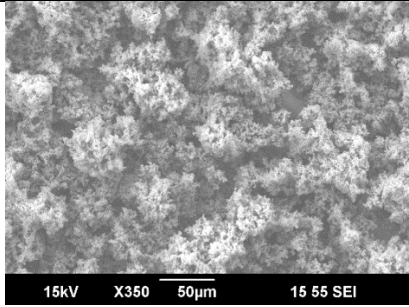
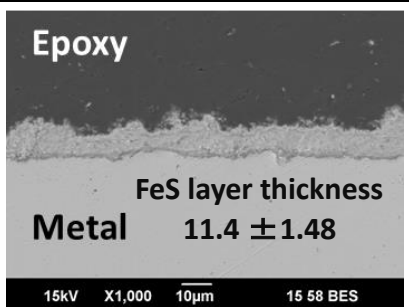
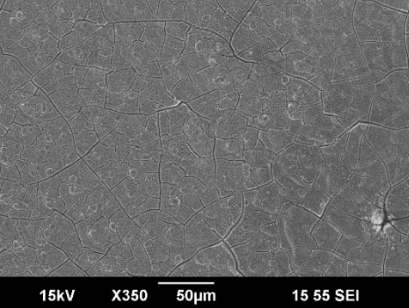
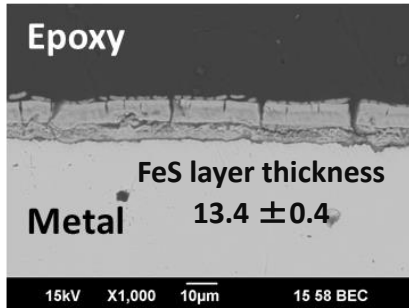
Condition	Surface	Cross Section
1.1m/s $\tau = 7.2\text{Pa}$, $k_{\text{H}_2\text{S}} = 1.3 \times 10^{-4}\text{m/s}$		
10.4m/s $\tau = 363\text{Pa}$ $k_{\text{H}_2\text{S}} = 9.4 \times 10^{-4}\text{m/s}$		

Figure 87: Surface SEM and cross-section analyses of corrosion product layers developed on 99.9% pure Fe after 4 days of exposure to 1 wt.% NaCl solution sparged with 10% H₂S in admixture with N₂ at pH of 6.00, 30°C and flow velocity of 1.1m/s and 10.4m/s

Similar to the observation with UNG 10180, the outer fluffy layer only formed at 7.2 Pa, confirming the initial postulate that such sulfide layers do not possess the mechanical strength to withstand 363 Pa shear stress. Even with the removal of the outer layer by shear stress, thicker corrosion product layers were developed at 363 Pa. With the corrosion product layers comprising of only FeS alone (absence of iron carbide network), the density of the layers formed at the different velocities (3.08 g/cm^3 at 1.1m/s and 3.28 g/cm^3 at 10.4m/s) was lower than the density of mackinawite mineral. In this case, the layer porosity corresponding to layers formed at 1.1m/s and 10.4m/s could be determined at 0.74 and 0.75, respectively. These results show that the layer properties were similar. Therefore, the mass transfer coefficient through these layers should be similar ($1.29 \times 10^{-4} \text{ m/s}$ at 1.1 m/s and $1.20 \times 10^{-4} \text{ m/s}$ at 10.4 m/s). Using the harmonic mean of the mass transfer coefficient through the layer and that through the bulk (Equation 37), the total mass transfer coefficient at 1.1m/s was $6.5 \times 10^{-5} \text{ m/s}$ and that at 10.4m/s was $1.1 \times 10^{-4} \text{ m/s}$.

With the increase in corrosion rates observed at the 10.4m/s flow condition, the increase in the thickness of the corrosion product layer can be attributed to an increased FeS saturation resulting from higher ferrous ion concentration and pH conditions close to the surface of the corroding substrate. A similar behavior was reported by Zheng, *et al.*, [19] where it was demonstrated that an increase in corrosion rates of API X65 from 1.5mm/y to 7.5mm/y, caused by an increase in fluid velocity, resulted in an increase in the thickness of the FeS layer developed from 20 μm to 96 μm . This behavior also confirms that the wall shear stress itself cannot remove the more compact inner FeS

layers. EDS analyses were conducted to identify the chemical composition of these layers.

Chemical Analysis of Corrosion Product Layers

EDS mapping, presented in Figure 88, reveal that the corrosion product layers consisted of sulfur and iron, confirming the layers as iron sulfide.

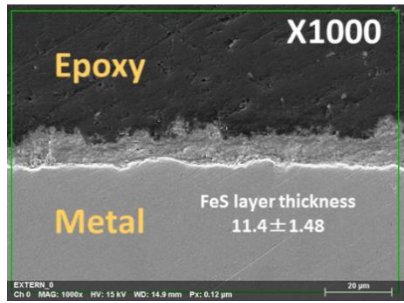
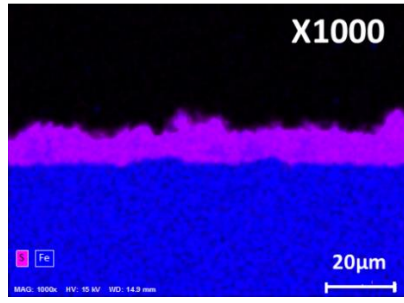
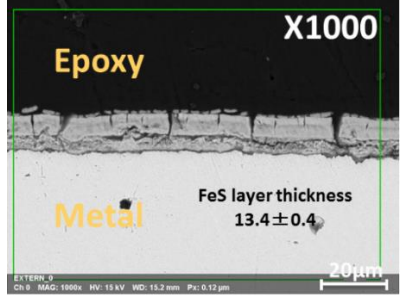
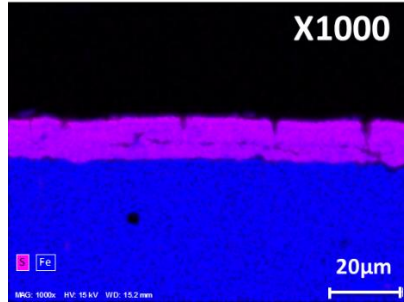
Condition	Thickness of Corrosion, Product Layer	EDS Analysis of Corrosion Product Layer
1.1m/s $\tau = 7.2\text{Pa}$, $k_{\text{H}_2\text{S}} = 1.3 \times 10^{-4}\text{m/s}$		
10.4m/s $\tau = 363\text{Pa}$ $k_{\text{H}_2\text{S}} = 9.4 \times 10^{-4}\text{m/s}$		

Figure 88: EDS maps detecting iron and sulfur in the corrosion product layers developed after a 4 day exposure of 99.9% pure Fe to 1wt.% NaCl solution sparged with 10% H₂S in admixture with N₂ at pH 6.00, 30°C and flow velocity of 1.1m/s and 10.4m/s

Considering the similarities in the current experiment conditions to those with a UNS G10180 substrate (Section 6.3.1) the same phase of iron sulfide, mackinawite, is expected. These results confirm that iron sulfide layers can develop in high shear stress conditions even in the absence of iron carbides.

Metal loss and FeS Layer Thickness

Figure 89 shows the mole density of iron lost due to corrosion and the iron precipitated as FeS and the ratio of these two values, which represents the fraction of the corroded Fe that precipitated is presented in Figure 90.

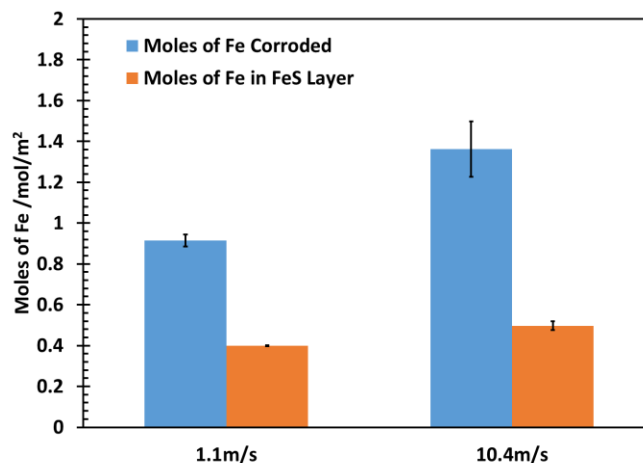


Figure 89: Moles of Fe corroded compared with moles of Fe precipitated (Fe in FeS layers) after exposure of 99.9% pure Fe substrates to 1 wt. % NaCl solution, pH 6.0, and 0.1bar of H₂S at 30°C and flow velocities of 1.1 m/s and 10.4m/s

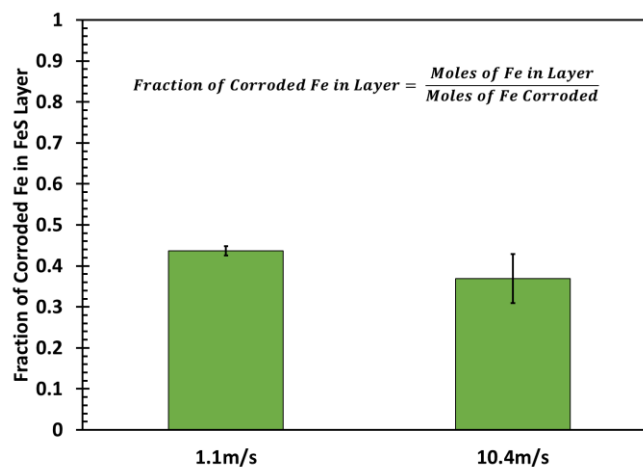


Figure 90: Fraction of corroded Fe in the FeS layers after exposure of 99.9% pure Fe substrates to 1 wt. % NaCl solution, at pH 6.0, and 0.1bar of H₂S at 30°C and flow velocities of 1.1 m/s and 10.4m/s

Even with the higher number of moles of Fe lost due to enhanced corrosion at 10.4m/s, there was also a proportional increase in the number of moles of Fe that precipitated as FeS. Thus, there was no significant difference in the fraction of Fe corroded in the FeS layer indicated in Figure 90. This is in contrast to observations with UNS G10180, where there was a decrease in the fraction of Fe in the FeS layer at 10.4m/s. The surface of the substrates after removal of the corrosion product layers were examined for the occurrence of localized corrosion. Figure 91 shows a representation of the steel surface after corrosion and after formation of FeS layers calculated from mass loss measurements.

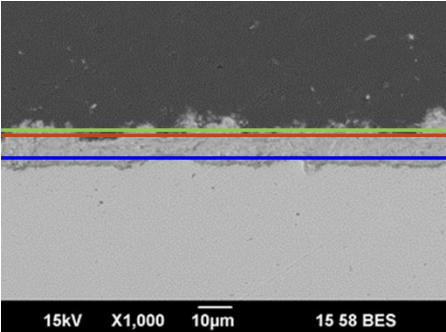
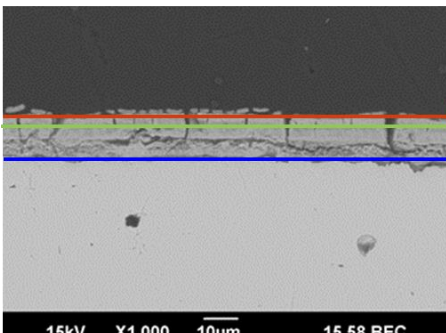
Flow Condition	Fe Retention in FeS Layer
<p>1.1m/s $\tau = 7.2\text{Pa}$, $k_{\text{H}_2\text{S}} = 1.3 \times 10^{-4}\text{m/s}$</p>	 <p>Steel surface with FeS Layer Steel surface before corrosion Steel surface after corrosion</p> <p>15kV X1,000 10µm 15 58 BES</p>
<p>10.4m/s $\tau = 363\text{Pa}$ $k_{\text{H}_2\text{S}} = 9.4 \times 10^{-4}\text{m/s}$</p>	 <p>Steel surface before corrosion Steel surface with FeS Layer Steel surface after corrosion</p> <p>15kV X1,000 10µm 15 58 BEC</p>

Figure 91: Level of steel surface before corrosion, with FeS layer and after removal of FeS layer developed after exposure of 99.9% pure Fe to 1 wt.% NaCl solution at pH 6.00, and 0.1bar of H₂S at 30°C and flow velocities of 1.1 m/s and 10.4 m/s

The similarities in the level of FeS layer relative to the steel surface after corrosion showing no significant difference in the retention of Fe between the two fluid velocities.

Profile of Specimen Surface

Figure 92 shows the image of the surface of the substrates with the developed FeS layer and the mapped surface after the removal of the layers.

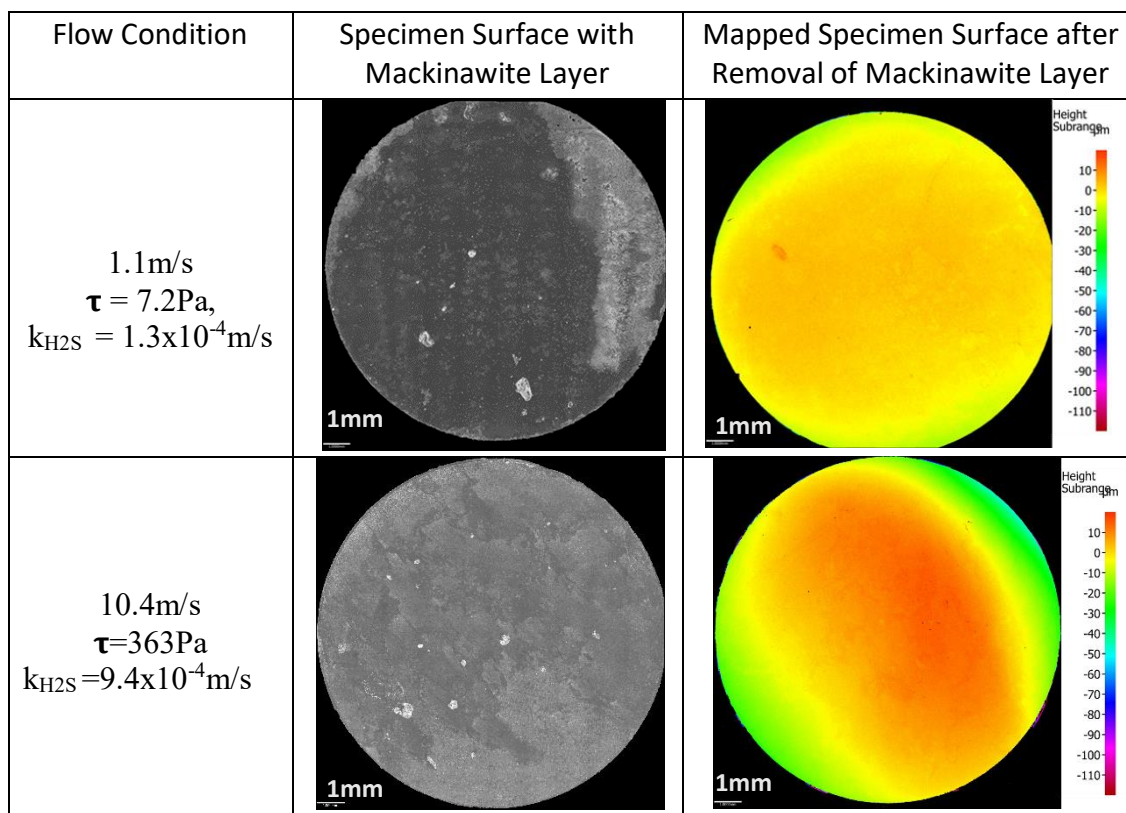


Figure 92: Specimen surface with FeS layer and the mapped specimen surface after the removal of the mackinawite layer formed after exposure of 99.9% pure Fe to 1 wt.% NaCl solution at pH 6.00, and 0.1bar of H₂S at 30°C and flow velocities of 1.1 m/s and 10m/s.

Figure 92 shows that the surface of the substrates was uniformly covered by the FeS layer irrespective of the fluid velocity. The less uniform FeS layer coverage observed with the UNS G10180 substrate at 10.4m/s could be an indication that these layers possess weaker adhesive properties than those developed on the 99.9% pure Fe. This proposal can be further confirmed by evaluating the adhesive properties of the FeS layers formed on the different substrates at shear stress of 363 Pa.

The profiles presented in this figure revealed the occurrence of uniform corrosion on the specimens exposed to both fluid velocities, 1.1m/s and 10.4m/s. This is in contrast to observations with the UNS G10180 substrate where localized corrosion was observed at 10.4m/s. With the major difference between 99.9% pure Fe and UNS G10180 being the presence of iron carbide, the results presented suggests that iron carbides may contribute to the extent of undermining effect on the protectiveness of the corrosion product layers formed at high shear stress conditions.

Summary

The results presented in this section have demonstrated that FeS layers developed on pure Fe in the absence of the iron carbide matrices. Similar to observations with UNS G10180 substrates, the formation of the outer fluffy FeS layer was impeded by the high shear stress of 363Pa. The higher corrosion rates observed at 10.4m/s favored the formation of thicker corrosion product layers. However, this did not confer better protection as higher corrosion rates were measured at higher fluid velocity. The absence of localized corrosion when the 99.9% pure Fe substrate was exposed to high flow

velocity strengthens the argument that iron carbide accelerates the undermining corrosion process with the UNS G10180 substrate.

6.3.3 Retention of iron sulfide layer on UNS G10180

The mechanical properties and protectiveness of iron sulfide layers developed at 1.1m/s were challenged by subjecting them to high flow conditions. As shown in Figure 93, high flow velocities were applied in three steps, 5.7m/s, 8.3m/s and 10.4m/s corresponding to shear stresses of 125 Pa, 245 Pa and 363 Pa, respectively. Figure 93 compares the corrosion rates obtained from the retention experiment to those obtained from the layer development experiments at 1.1m/s and 10.4m/s.

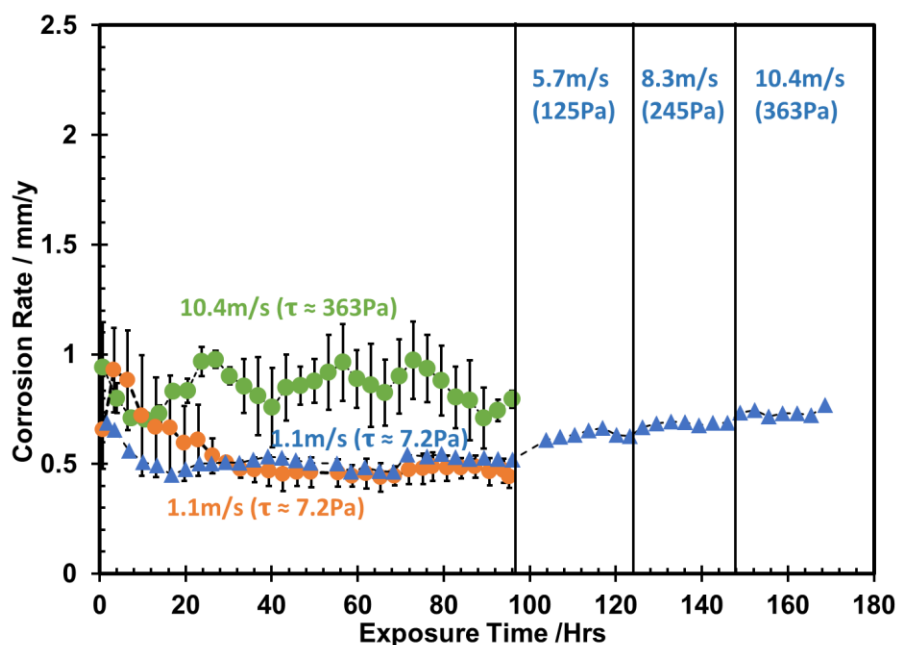


Figure 93: Corrosion rate trend of the retention test of iron sulfide layer developed on UNS G10180 during a 4-day exposure to 1 wt.% NaCl solution sparged with a 10% vol. H₂S in admixture with N₂ at pH 6.00, 30°C and initial flow velocities of 1.1 m/s

The first 100 hours of the experiment, where the specimen is only exposed to low flow conditions (velocity of 1.1 m/s and shear stress of 7.2 Pa), shows a corrosion trend very similar to the one obtained earlier in similar conditions (orange curve on Figure 93). An increase in the flow velocity logically resulted in a corresponding increase in corrosion rates. The corrosion rate at the final stage of the test, corresponding to a velocity of 10.4 m/s, was also equivalent to the corrosion rates obtained when the specimen had been exposed to similar flow conditions for the entire test (green curve on Figure 93). These results further confirm that the removal of the loosely attached corrosion products resulted in an increase in the overall mass transfer coefficient which enhanced the mass transport of the corrosive species to the electroactive sites.

Analysis of Corrosion Product Layer

The surface and the cross-sectional analyses of the corrosion product layers formed at the end of the retention experiment are presented in Figure 94.

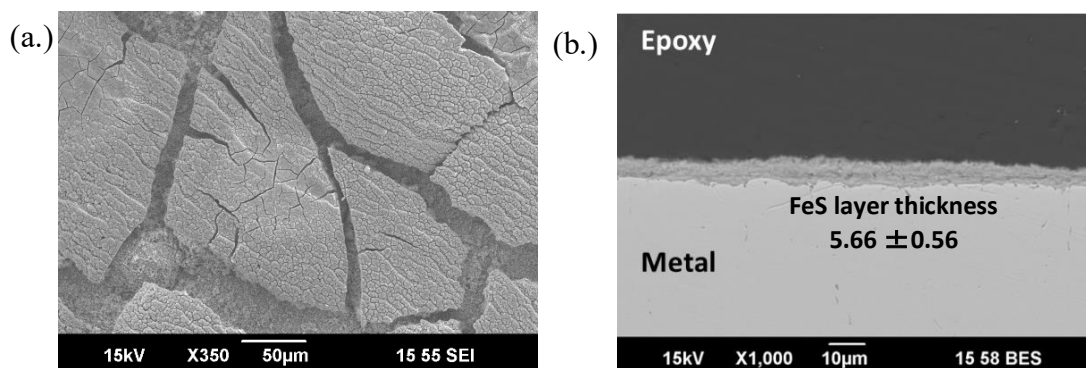


Figure 94: Surface SEM and cross-section analyses of FeS layers after the retention experiment

The surface SEM showed similar features to the FeS layers formed in conditions where a 10.4m/s (363Pa) flow velocity was applied from the onset of sample exposure, suggesting similarities in layer mechanical properties. The cross-section analysis of the FeS layer formed under this condition lacked the outermost, less adherent, “fluffy” layer that formed at 1.1m/s velocity, confirming the inability of this outer layer to withstand a flow with a shear stress of 363Pa.

Chemical Analysis of Corrosion Product Layers

The EDS analysis of the layer shown in Figure 95 detected iron and sulfur elements, confirming the layer as iron sulfide.

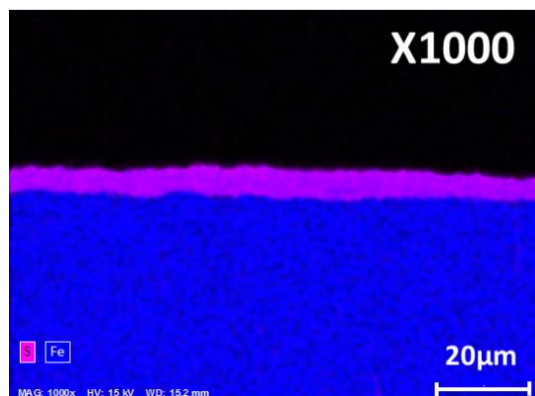


Figure 95: EDS analysis of corrosion product layer after the retention experiment confirming the formation of iron sulfide

Although no XRD analysis was conducted, mackinawite is the expected FeS phase since the test conditions were very similar to the ones of the FeS development study (Section 6.3.1).

Profile of Specimen Surface

The surface profile of the specimen after removal of the corrosion product layer revealed the occurrence of localized corrosion at a rate 7.3mm/y. The rate of localized attack was calculated from the maximum of depth on the corroded surface detected from the profilometry and the entire exposure time. Figure 96 also revealed the formation of non-uniform corrosion product layers across the specimen surface, which can be related to the areas of localized attack. The black areas on the Figure 96(a.) are spots where the FeS layers are exfoliated and, thus, are above the selected limits for image capture.

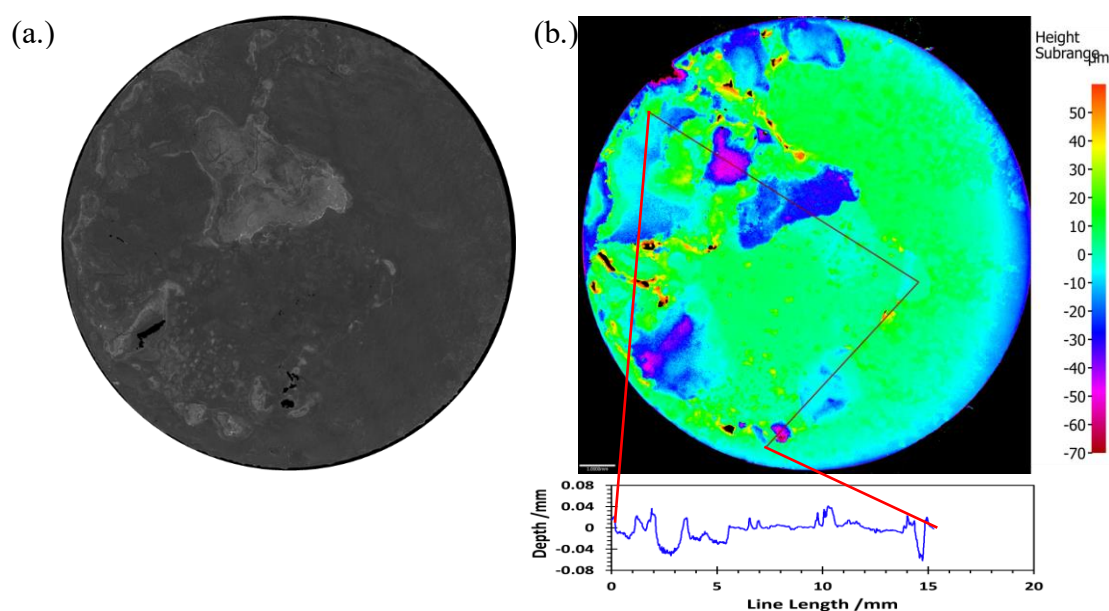


Figure 96: Specimen with FeS layer (a.) and profilometry (b.) of its surface after the removal of the mackinawite layer formed in the FeS retention experiment.

The occurrence of localized attack further confirms the synergistic effect of wall shear stress and mass transfer on the corrosion behavior of the material. Similar to the

proposition presented for the development experiment at high flow velocity (section 6.3.1), by subjecting the FeS covered specimen to high shear stress conditions the loosely attached outer layer is sheared off leaving behind a tightly attached layer. Corrosion rate measurements suggest increased mass transport rates through the layer which may be an indication of the porosity or tortuosity of the layer. In addition, electrical inhomogeneities at the steel surface (due to steel microstructure) resulted in an increase in the undermining corrosion and the occurrence of localized corrosion.

6.4 Summary

The results presented in this section demonstrated that high shear stress, applied after the development of FeS corrosion production layer, did not remove the inner mackinawite layer on the steel substrate. Similar to the observation from the development experiments with 99.9% pure Fe and UNS G10180, the top “fluffy” FeS layer, which was observed at 7.2 Pa, was not retained after the stepwise increase in shear stress. Increase in fluid velocity influenced the properties of the FeS layer such that mass transfer rates through them was enhanced, thus, resulting in higher undermining corrosion rates. The difference in FeS morphology and the occurrence of localized corrosion suggests that shear stress and mass transfer both play a role in the protectiveness of the layer formed.

CHAPTER 7: CHARACTERIZATION OF THE MECHANICAL PROPERTIES OF IRON SULFIDE LAYERS

7.1 Introduction and Research Goal

The integrity management of oil and gas pipelines is usually associated with the control of corrosion threats which occur as a result of the production processes. While many studies have focused on understanding the chemical/electrochemical aspects of corrosion mechanisms associated with the transport of produced fluids[19,26,38,116], little attention has been given to the mechanical properties of scales or corrosion products forming on the pipe surface. These layers are constantly exposed to stresses generated by fluid flow, and other dynamic events (cavitation, droplet impingement), which may lead to their partial removal. The mechanical damage of iron carbonate or iron sulfide, typically encountered in oil and gas production, increases the likelihood of occurrence of localized corrosion. It is therefore critical to understand their mechanical properties. Studies have been conducted to evaluate the ability of FeCO_3 to withstand typical flow related wall shear stresses as it occurs in the field[21][20][147], but similar studies have not been done for FeS layers until now.

Different methods have been used by researchers to determine the stress required to remove an iron carbonate layer. Modified tensile test experiments have been performed[147], where the iron carbonate layer was detached from the surface by an applied tensile force normal to the substrate surface. These experiments used epoxy to attach to an iron carbonate layer and test for layer detachment over an area of the order of 1cm^2 . Another method used atomic force microscopy to apply a shear force of the order

of nanonewtons on an individual iron carbonate crystals with the intent to cause full detachment [21]. The reported shear stress required to remove iron carbonate layer in both cases was of the order of 10^6 Pa, which is 3 orders of magnitude higher than the maximum flow related wall shear stress typically encountered in a multiphase pipe flow[20]. Even though both methods of evaluating the shear stress values involved iron carbonate layers pre-formed in ex-situ conditions, these results, when extrapolated to FeCO_3 layers formed in production conditions, show clearly that flow related shear stresses in pipelines are not sufficient to generate damage. Similar studies have not yet been conducted on iron sulfide layers probably because of the complexity of corrosion product layers formed in sour environment.

The aim of the current study was to investigate the magnitude of shear stress required to damage an iron sulfide layer up to the point of exposing the substrate. This study was conducted on mackinawite due to its significance as the first and most common iron sulfide layer [83–85]. To achieve this research goal, a well-defined iron sulfide layer developed under controlled conditions was tested for mechanical properties using a mechanical scratch tester. Indentation measurements and scratch test were used to determine the hardness and interfacial shear strength of a pre-formed iron sulfide layer.

7.1.1 Indentation Measurement

An indentation measurement involves the application of a load by an indenter in contact with a specimen and the subsequent removal of this load when the preset force is reached[148][149].

Figure 97 shows a typical elastic-plastic loading and elastic unloading curve from an indentation measurement. The hardness of the material is determined by dividing the load by the impressed area on the substrate.

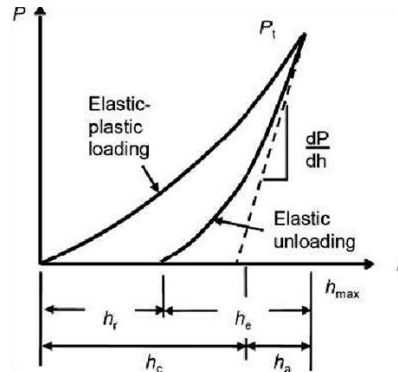


Figure 97: A typical loading and unloading curve from an indentation test[148]

Where h_f is the plastic deformation depth in m, h_e is the elastic deformation depth in m, h_c is the contact depth of the indenter otherwise known as the effective height of the indenter in m, h_a is the sink in depth, in m, which is the difference of the total depth, h_{max} and h_c .

The substrate hardness, H , can be calculated according to the following equation:

$$H = \frac{P}{A_{proj}} \quad (78)$$

Where H is the substrate hardness in Pa, P is the maximum load in N and A_{proj} is the projected area m^2 .

The impressed area, also known as the projected area, can be calculated from the penetration depth of the indenter. The projected area shown in Equation 78 is dependent

on the indenter shape that is used. For the current studies a Vickers indenter, shown Figure 98, was used for all the hardness measurements and the projected areas can be calculated using Equation 79 below[148].

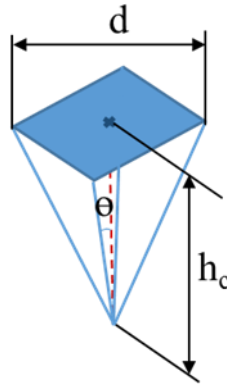


Figure 98: A schematic of a Vickers indenter tip with dimensions

$$A_{proj} = 24.5h_c^2 \quad (79)$$

Where h_c , is the effective height of the indenter.

The d in Figure 98 is the diagonal length of the indentation mark in m and θ is the face angle of the indentation in degrees.

7.1.2 Scratch Testing

A scratch test involves the movement of an indenter tip across a surface it is in contact with and observing the surface for any possible surface layer failure. This test method has been used for many years to test the adhesive properties of coatings on substrates.[150–155] Owing to the success of this test method in area of coatings, its operating principles were considered useful in the evaluation of the adhesive properties of corrosion product layer. To successfully execute a quantitative scratch test, certain

requirements have to be met such as: an identifiable failure mode, a clear mechanism of failure, a method for identifying the occurrence, location and extent of failure, and a method of calculating the interfacial shear stress.[156] A scratch test can be either progressive or constant. In conducting a progressive load scratch test, the indenter is moved across the surface with a linearly increasing normal force until failure occurs at critical load (CL). In contrast, a constant load test involves the movement of an indenter tip across a surface while maintaining the normal force at a constant level. The progressive load scratch test is appropriate for obtaining an estimated range of force for the occurrence of failure. The actual CL can be determined from constant load tests, by conducting scratch tests at different constant loads within the range of forces established by the progressive load test.

Modes of Failure in Scratch Testing

The failure mode that occurs during a scratch test can be either cohesive or adhesive[157,158].

Cohesive Failure: Cohesive failure occurs within the layer attached to a substrate. The different types of cohesive failure are, chevron, arc tensile, hertzian and conformal cracks. The schematics of these cohesive failure types are presented in Figure 99[159].

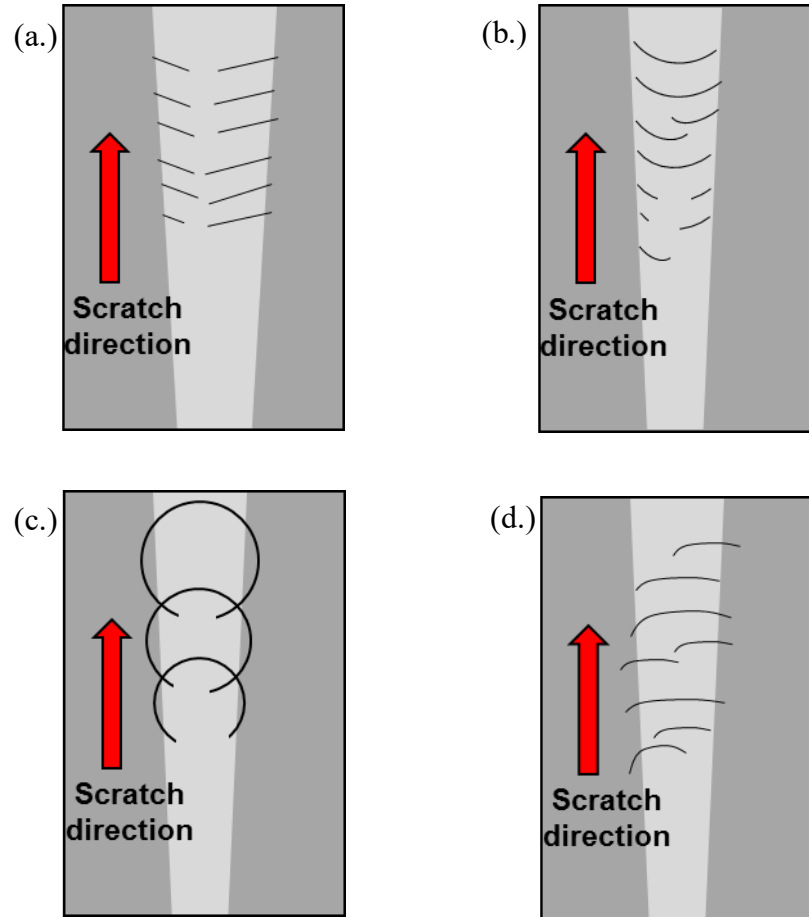


Figure 99: Schematics of different types of cohesive failure (a.) chevron cracks (b.) arc tensile cracks (c.) hertzian cracks (d.) conformal cracks (design idea courtesy of Claudia Prietto)

Adhesive Failure: Adhesive failure occurs at the layer-substrate interface where there is a separation of the layer from the surface either by cracking or by full separation. Some examples of adhesive failure are buckling cracks, wedging, recovery and gross spallation[159].

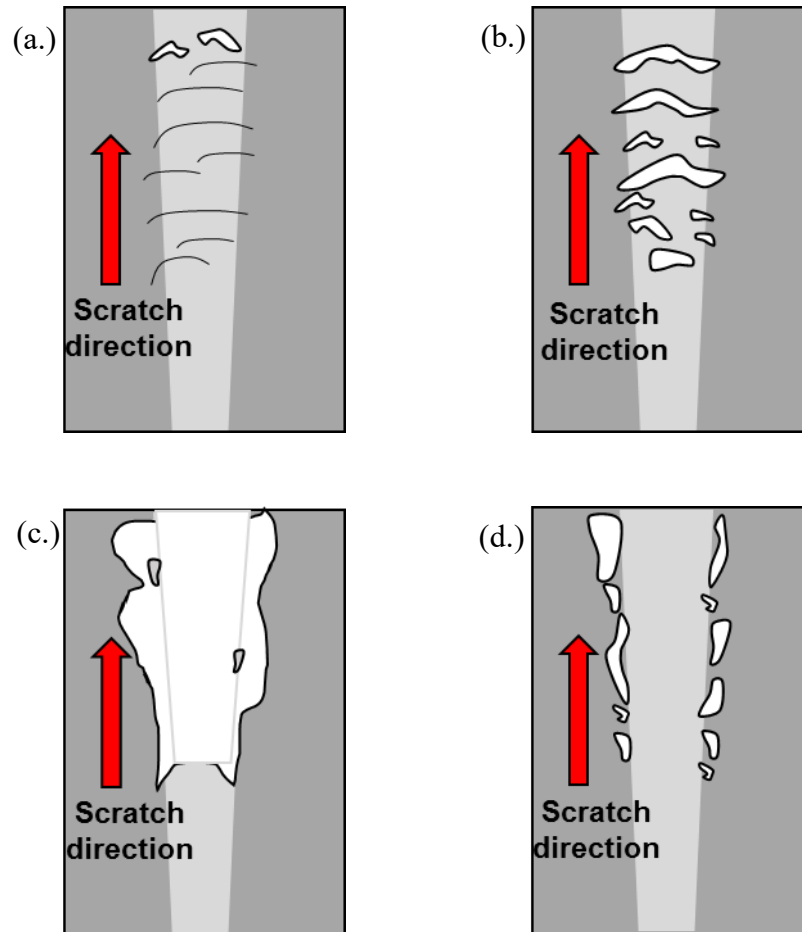


Figure 100: Schematics of different types of cohesive failure (a.) buckling cracks (b.) wedging spallation (c.) recovery spallation (d.) gross spallation (design idea courtesy of Claudia Prietto)

Table IX illustrates how these different types of failures that occur during a scratch test are dependent on the layer and substrate hardness.

Table IX: Failure modes from layer and substrate hardness[158]

		Substrate Hardness	
		Low	High
Layer Hardness	Low	Possible cohesive failure: Conformal Cracking Possible adhesive failure: Buckling Failure	Possible cohesive failure: Conformal Cracking Possible adhesive failure: Spallation and Buckling Failure
	High	Possible cohesive failure: Tensile and Hertzian cracks Possible adhesive failure: Chipping and Spallation Failure	Possible cohesive failure: Tensile cracks Possible adhesive failure: Chipping and Spallation Failure

Shear Stress Calculation from Scratch Test Measurements

Early models[160][161] used the hardness of the substrate, obtained from indentation measurements, to calculate the interfacial shear strength of the layer. Equations 80 - 82 shows the expressions for calculating the shear stresses with parameters from Figure 101 which illustrates an indenter tip with the different forces acting on it during scratch test.

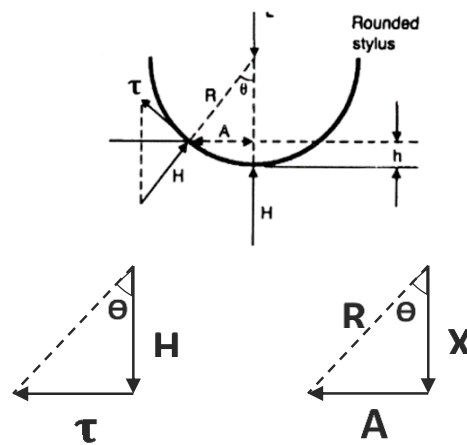


Figure 101: Schematics of the forces and dimensions associated with an indenter tip in contact with a surface during a scratch test.

$$\tau = H \tan \theta \quad (80)$$

$$\tan \theta = \frac{A}{\sqrt{R^2 - A^2}} \quad (81)$$

$$\tau = \frac{AH}{\sqrt{R^2 - A^2}} \quad (82)$$

Where

τ = shear stress (Pa)

H = Hardness of the substrate (Pa)

R = Radius of the indenter (m)

A = Half width of the scratch (m)

θ = angle of friction (degrees)

h = scratch depth (m)

x = introduced variable used for calculation (length in m)

An improved shear stress calculation model developed by Ollivier, *et al.*, [162] uses the critical load from a scratch test to determine the interfacial shear strength. This new model replaces the hardness of the substrate, H, in Equation 5 with $L_c/\pi A^2$. Equation 83 shows the new equation according to Ollivier and Matthew [162].

$$\tau = \frac{L_c}{\pi A \sqrt{R^2 - A^2}} \quad (83)$$

Where L_c is the critical load for the occurrence of failure in Newtons.

This model has been shown to be more accurate than the Benjamin and Weaver model [162] and this was used for all the shear stress evaluations in the current study.

7.2 Experimental Methods

Iron sulfide layers were developed in the 4-liter glass cell (Figure 4), under controlled chemistry and mass transfer conditions and the mechanical properties of the layers, such as hardness and adhesive strength, were investigated using a mechanical tester. In growing the iron sulfide layer, specimens were inserted in 1 wt.% NaCl solution saturated with 10% by volume of H₂S in a mixture with nitrogen at pH of 6.0. Six specimens were individually inserted and exposed in each experiment. The same procedures used for solution preparation, specimen preparation and sample extraction discussed in section 4.2 was implemented in developing the iron sulfide layer. Three specimens were extracted after 1 day and three specimens were extracted after 3 days and immediately stored in a vacuum desiccator for further analysis. For the three specimens extracted on each stipulated day, SEM and cross-sectional analyses were conducted on one, adhesive strength tests on the second, and hardness measurements on the third. XRD analysis was only conducted on a sample extracted after 3 days exposure time. For these experiments, FeS layers were developed at two temperatures, 30°C and 80°C, in order to investigate the impact of temperature on the mechanical properties of these layers.

7.2.1 Equipment for Iron Sulfide Layer Development

As mentioned above, the FeS layers were developed in a 4-liter glass cell with impeller (Figure 4). The development and characterization of this experimental setup was comprehensively discussed in Chapter 4. This system has been shown to provide good control of the solution chemistry and mass transport of species. For this set of experiments, the iron sulfide layer was developed at 250 rpm rotational speed, which

corresponds to Fe^{2+} and H_2S mass transfer of $6.8 \times 10^{-5}\text{m/s}$ and $1.2 \times 10^{-4}\text{m/s}$, respectively.

7.2.2 Equipment for Mechanical Testing of Iron Sulfide layers

The mechanical properties of the FeS layers developed in the glass cell were investigated using the Nanovea™ CB500 mechanical tester[163]. This system can be used to perform a hardness measurement and a scratch adhesion tests in the range of forces between 0.1mN to 800mN. The three indenters which can be used in this system are:

- Conical indenter: suitable for scratch tests.
- Berkovich indenter: suitable for nanoindentation.
- Vickers indenter: suitable for micro and nanoindentation.

The tip of these indenters, shown in Figure 102, have different shapes making them suitable for variety of tests[164].

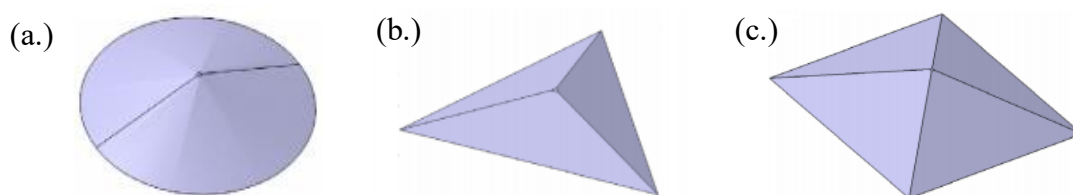


Figure 102: Tip geometry for (a.) Conical, (b.) Berkovich and (c.) Vickers indenter [11]

7.2.3 Materials Test

The materials used for the current studies are 99.9% pure iron and carbon steel UNS G10180. The chemical composition and microstructure of the UNS G10180 carbon

steel are presented in Table V and Figure 41(b.), respectively. The microstructure of 99.9% pure Fe is shown in Figure 41(a.).

7.2.4 Procedure for the Mechanical Testing of the Developed Iron Sulfide Layers

The hardness of a UNS G10180 carbon steel was measured by conducting an indentation measurement at maximum force of 300mN. Indentation measurements were also conducted on the FeS layer developed at 30°C and 80°C after 1-day and 3-days exposure periods. Afterwards, a progressive load test was conducted on the specimens with corrosion product layers from 0.1mN to 300mN at a loading rate of 75mN/min, a scratch speed of 0.25mm/min and a scratch length of 1mm. The scratched specimen was examined under the SEM for the occurrence of the adhesive failure and EDS analysis was conducted to ascertain the extent of failure. After the detection of the adhesive failure, a constant load test was conducted to determine the critical load (CL) for the adhesive failure of the FeS layer.

7.3 Results and Discussion

Figure 103 (a.) and (b.) show the results from the five indentation measurements conducted on a bare UNS G10180 and 99.9% pure Fe specimens, respectively, using with a Vickers indenter.

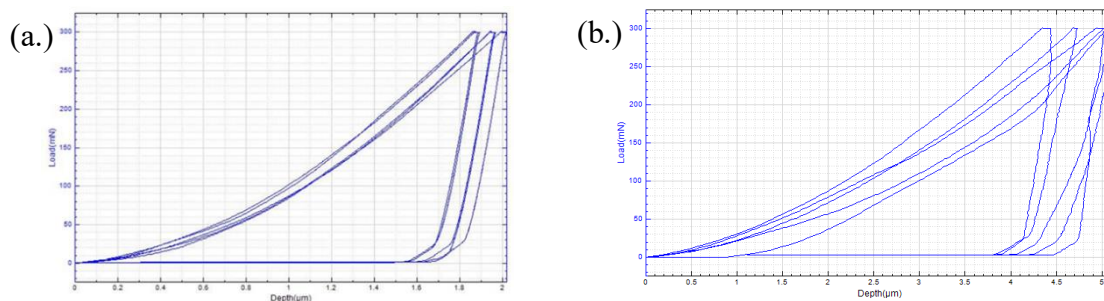


Figure 103: Loading and unloading curve from hardness measurements on (a.) a bare UNS G-10180 carbon steel and (b.) a bare 99.9% pure Fe

The average hardness value for these measurements for UNS G10180 and 99.9% pure Fe, presented in Table X, are 357HV (= 3.78GPa) and 60.2HV (=0.64GPa), respectively. The measured hardness of UNS G10180 agrees with the findings from studies conducted by Jian et al. in which a Vickers hardness of 330 HV was reported for a UNS G10180 carbon steel[165].

Table X: Summary of measured hardness of UNS G10180 from indentation tests using a Vickers indenter

	UNS G10180		99.9% Pure Fe	
Repeat Test #	Hardness (GPa)	Hardness (HV)	Hardness (GPa)	Hardness (HV)
1	3.69	348.7	0.56	52.90
2	4.02	380.1	0.62	58.5
3	3.99	377.3	0.61	57.6
4	3.48	329.3	0.72	68.4
5	3.70	349.6	0.67	63.8
Average	3.78	357	0.64	60.2
Std Dev	0.23	21.428	0.057	5.36

The higher hardness value measured with UNS G10180 substrate in comparison in 99.9% pure Fe was expected since several studies have shown that the hardness of carbon steel can be improved by an increase in the carbon content.[166,167]

7.3.1 Effect of Temperature on the Mechanical Properties of Iron Sulfide Layers

Some reports in literature suggests that iron sulfide layers developed at high temperature have a lower adhesive strength than those developed at low temperature[7]. This observation can be further investigated by comparing the interfacial shear strength of the iron sulfide layers developed at different temperatures.

Mechanical Characterization of FeS layer developed on UNS G10180 Exposed to 1 wt.% Solution at pH 6.0, 30 °C, 0.1bar H₂S and 250rpm Impeller Rotation Speed

The SEM analysis of sample surface presented in Figure 104 (a.) and (b.) shows that the surface FeS layers formed after 1 day and 3 days have similar morphologies.

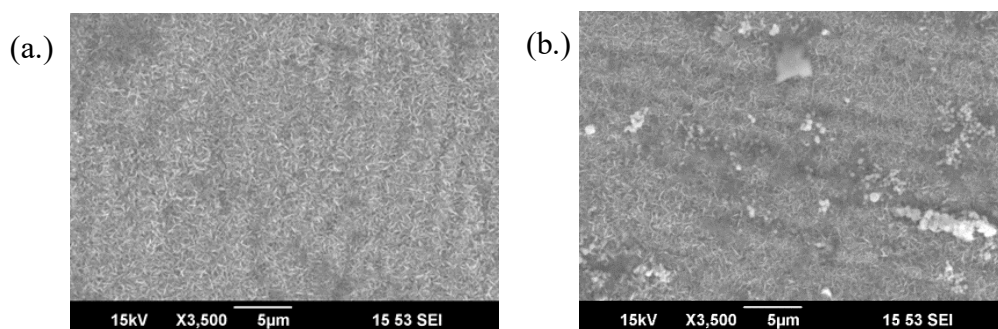


Figure 104: Surface SEM of FeS layer developed on UNS G10180 immersed in 1% wt. NaCl solution at 30°C, pH 6.0, 0.1bar of H₂S and 250rpm impeller speed (a.) 1 day exposure (b.) 3 days exposure

The thickness of the FeS layers formed after 1 day and 3 days exposure period, shown in Figure 105 (a.) and (b.), were also similar at approximately 2.3 μm .

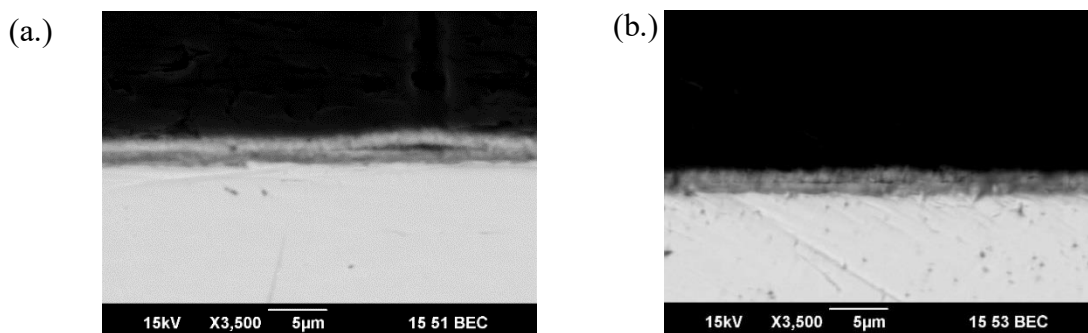


Figure 105: Cross section of FeS layers on UNS G10180 immersed in 1%. wt. NaCl solution at 30⁰C, pH 6.0, 0.1bar of H₂S and 250rpm impeller speed (a.) 1-day exposure (b.) 3 days exposure

The results from the XRD analysis shown in Figure 106 confirmed mackinawite as the phase of FeS layers formed.

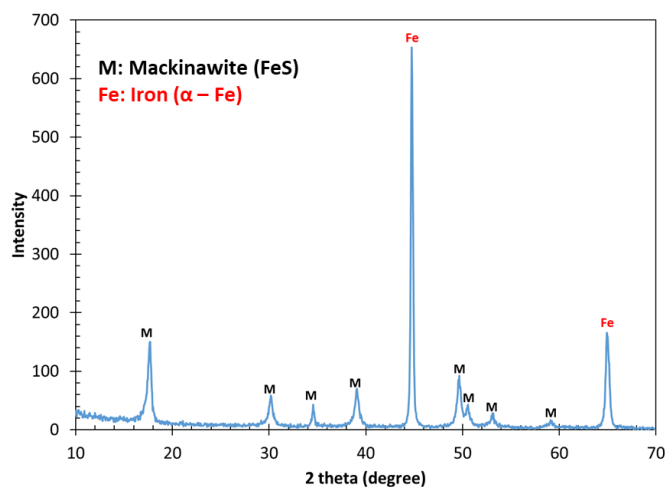


Figure 106: XRD analysis of FeS layer formed after 3 days exposure time in 1%. wt. NaCl solution at 30⁰C, pH 6.0, 0.1bar of H₂S and 250rpm impeller rotational speed

Hardness Measurements of Mackinawite Layers

The hardness of the corrosion product layers developed after 1 day and 3 days exposure time was estimated by conducting 5 different indentation tests on the layers using a Vickers indenter. The penetration depth of the indenter shown in the x-axis of the loading and unloading curves (Figure 107) is less than the thickness of the corrosion product layers shown in Figure 105(a.) and Figure 105(b.). This shows that the hardness measurements were not influenced by the metal substrate.

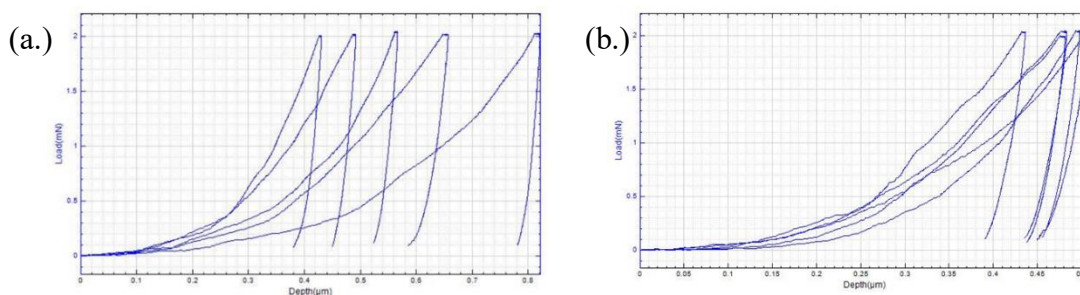


Figure 107: Loading and unloading curve from hardness measurements of mackinawite layer formed on UNS G10180 immersed in 1%. wt. NaCl solution at 30^oC, pH 6.0, 0.1bar of H₂S and 250rpm impeller speed after (a.) 1 day (b.) 3days

Table XI shows that the average hardness of the mackinawite layer formed after 1 day and 3 days exposure of UNS G10180 steel is 28.4HV and 38.3HV, respectively. These hardness measurements show that the FeS layer became harder with time.

Table XI: Summary of measured hardness of mackinawite layer formed on UNS G10180 exposed to 1 wt.% solution at pH 6.00, 0.1bar of H₂S, 30°C, and 250rpm impeller rotation speed from from indentation tests using a Vickers indenter

Repeat Test #	Day 1		Day 3	
	Hardness (GPa)	Hardness (HV)	Hardness (GPa)	Hardness (HV)
1	0.29	27.1	0.49	46.4
2	0.38	35.8	0.39	37.1
3	0.49	46.5	0.41	38.4
4	0.21	20.3	0.36	34.3
5	0.13	12.4	0.37	35.3
Average	0.30	28.4	0.40	38.3
Std Dev	0.12	11.9	0.045	4.3

These results show that the metal substrate has a hardness approximately 13 times higher than that of the corrosion product layer. According to the failure map developed by Bull[156][158] (Table IX), the expected mode of cohesive failure for this layer is conformal cracking, while spallation or buckling would be indicative of an adhesive failure. The results from scratch tests were inspected under the SEM to ascertain the occurrence of these forms of failures.

Determination of the Interfacial Shear Strength of Mackinawite Layer

To determine the interfacial shear strength of the layers, a progressive load test was conducted and the specimens after 1-day exposure time to establish the range of force required for the occurrence of an adhesive failure. Constant load scratch tests were conducted within this force range to determine the critical load for adhesive failure. Studies on the mechanical properties of materials have shown a similarity in hardness results when conical and Vickers indenters were used in contrast to the large variation in results when conical indenters are compared to those from Berkovich indenters[164].

Therefore, to have better correlation of hardness measurements (conducted with a Vickers indenter) and scratch test results, the conical indenter was used to conduct all the scratch tests.

Progressive Load Test on Mackinawite Layer Formed after 1 Day Exposure

The chart in Figure 108 shows the loading vs scratch length chart of the progressive load test from 0.1mN to 300mN.

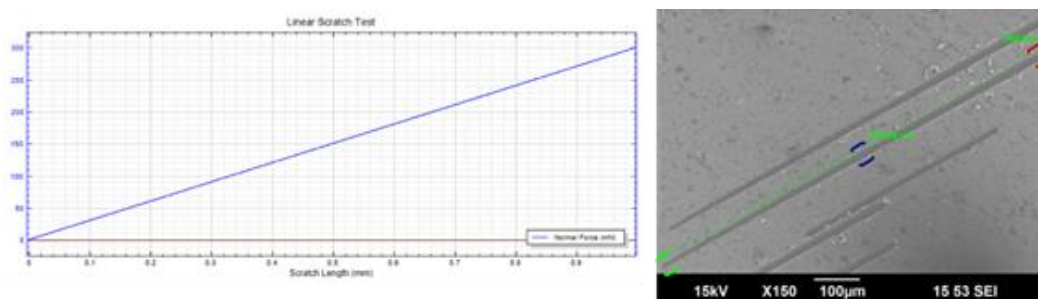


Figure 108: Progressive load scratch test from 0.1mN to 300mN on the mackinawite layer formed after 1 day exposure of UNS G10180 to 1 wt.% solution at pH 6.00, 0.1bar of H_2S , 30°C , and 250rpm impeller rotation speed, conducted at a scratch speed of 0.25mm/min and loading rate of 75mN/min.

Since the force loading rate is linear, the range of force where an adhesive failure occurred was identified visually by inspecting the beginning, the middle and the end of the scratch, which corresponds to the minimum (0.1mN), median (150mN) and maximum (300mN) load. In addition to direct observation of changes in the contrast between area with adhesive failure and areas with cohesive failure, energy-dispersive X-ray spectroscopy (EDS) technique was used to confirm the occurrence of adhesive failure. The EDS analysis of the scratch marks presented in Figure 109 shows a high iron to sulfur atom % ratio at maximum load of 300mN while an approximately equal iron and

sulfur atom % was detected at 150mN and 0.1mN. This indicates that the critical load for adhesive failure lies between 150 and 300mN.

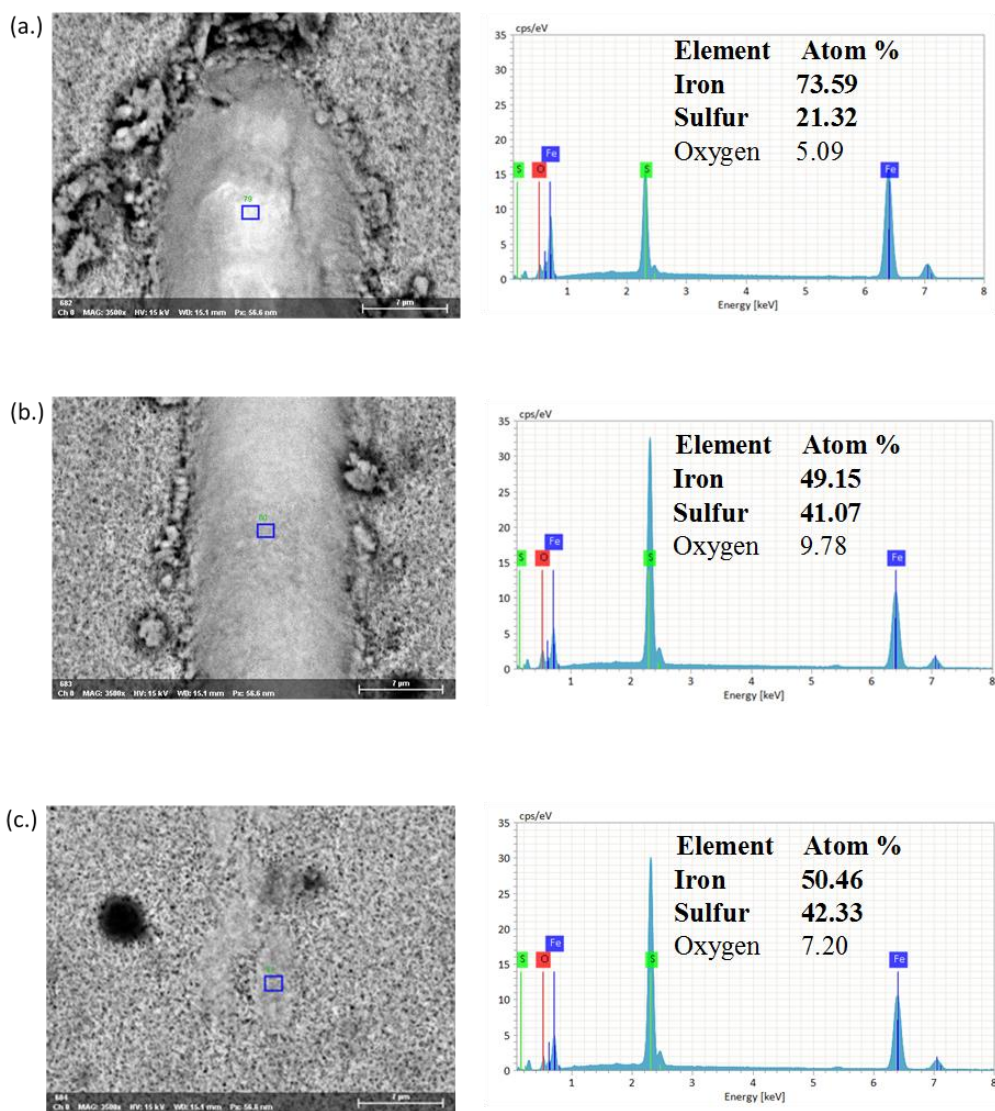


Figure 109: EDS Analysis of progressive load scratch from 0.1mN to 300mN on mackinawite layer formed after 1 day exposure of UNS G10180 to 1 wt.% solution at pH 6.00, 0.1bar of H₂S, 30⁰C, and 250rpm impeller rotation speed, (a.) 0.1mN (b.) 150mN and (c.) 300mN

It was assumed that the critical load for adhesive failure of the FeS layer formed after 3 days would be within the same range of force since the layer thickness and layer hardness were similar in magnitude. These results also show that a force less than 0.1 mN is required to remove the outer FeS layer.

Constant Load Test on Mackinawite Layer Formed on UNS G10180 after 1 Day Exposure

Constant load tests at forces between 150 and 300 mN were expected to reveal the critical load for the occurrence of adhesive failure. A constant load test was performed on the mackinawite layer at a normal force of 200 mN and a scratch speed of 0.25 mm/min, which resulted in a cohesive form of failure presented in Figure 110.

The EDS mapping presented in Figure 110(b) shows an area of slightly higher iron intensity, however, the back scatter image presented in Figure 110(a) does not show areas of different contrast, which would be expected if the substrate metal was exposed. Therefore, the evidence was not strong enough to conclude that adhesive failure occurred at 200 mN.

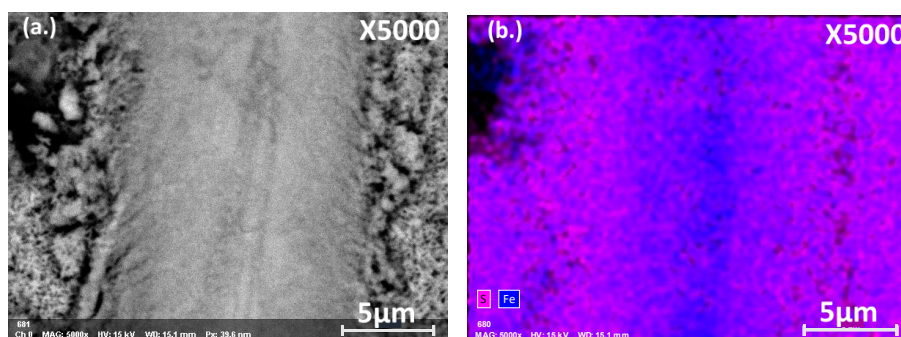


Figure 110:(a.) Scratch track and (b.) EDS mapping of scratch mark from a constant load test at 200mN constant load test on a mackinawite layer formed after 1-day exposure to 1 wt.% solution at pH 6.00, 0.1bar of H₂S, 30°C, and 250rpm impeller rotation speed.

However, the EDS mapping of the scratch produced by a higher load of 230mN (Figure 111b.) showed distinct areas with higher Fe intensities indicating the occurrence of an adhesive form of failure. Additionally, the backscatter analysis of the scratch mark at this force (Figure 111a.) shows areas of different contrasts which also corresponds to the areas of higher Fe intensity on the EDS map. This evidence is strong enough to conclude that an adhesive failure of the FeS layer occurred. This will also be used as a criterion for ascertaining the occurrence of adhesive failure in all scratch analysis presented in this work.

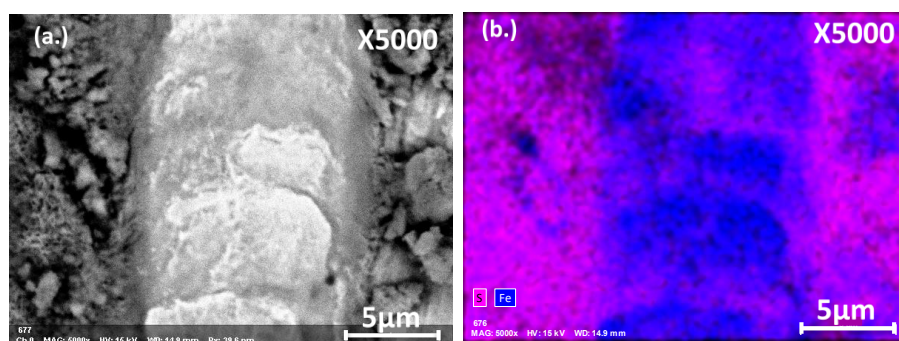


Figure 111: (a.) Scratch track and (b.) EDS mapping of scratch track from a constant load test at 230mN constant load test on a mackinawite layer formed after 1-day exposure to 1 wt.% solution at pH 6.00, 0.1bar of H₂S, 30⁰C, and 250rpm impeller rotation speed.

Figure 112 shows a point EDS analysis that was conducted on the scratch area which shows a high iron atom % in comparison to S atom % confirming the occurrence of an adhesive form of failure.

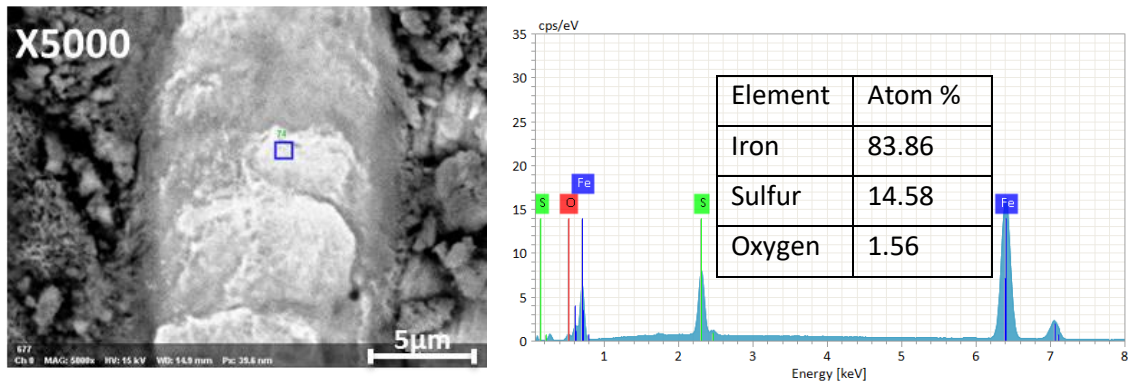


Figure 112: EDS analysis of scratched area from a 230mN constant load test on a mackinawite layer formed after 1-day Exposure to 1 wt.% Solution at pH 6.0, 0.1bar of H₂S, 30°C, and 250rpm Impeller Rotation Speed.

An important parameter in the Benjamin and Weaver model [160] for calculation of the interfacial shear strength is the scratch width. Therefore, it was important to measure the scratch width from the constant load test on the mackinawite layer using a measurement feature in the SEM software. The scratch width was determined to be approximately $18 \pm 1.27 \mu\text{m}$. Using half of the scratch width, the indenter radius and the critical load in Equation 81, the interfacial shear strength was estimated to be 470 MPa.

The profilometry of the scratched areas presented in Figure 113 showed that the depth of the scratch mark resulting from 400 MPa shear stress was $1.2 \mu\text{m}$ while that at 470 MPa was $2.3 \mu\text{m}$.

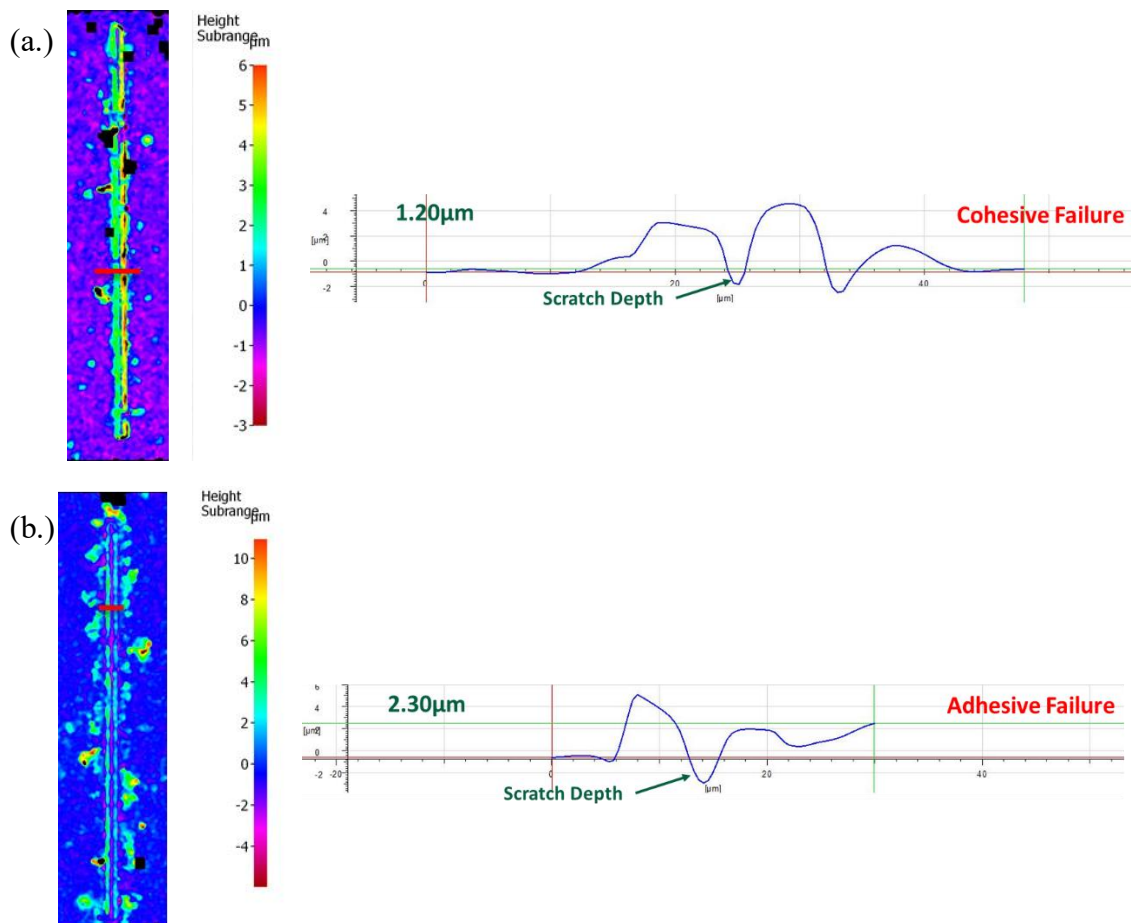


Figure 113: Profilometry of scratch track left by a shear stress of (a.) 400 MPa and (b.) 470 MPa on a Mackinawite layer developed UNS G10180 after 1 days exposure to 1 wt. % NaCl solution at 30°C, pH 6.0, 0.1bar H₂S and 250rpm impeller rotational speed

Figure 113(b) shows that the depth of the scratch track associated with the observed adhesive failure was 2.3 μm, which agrees with the measured layer thickness presented in Figure 105(a). This confirmed that adhesive failure occurred at the layer/substrate interface.

Constant Load Test of FeS Layer Formed on UNS G10180 after 3 Day Exposure

The adhesive failure of the FeS layer developed after 3 days exposure period occurred at a critical load of 250mN. This was confirmed by the EDS mapping of the scratch mark presented in Figure 114.

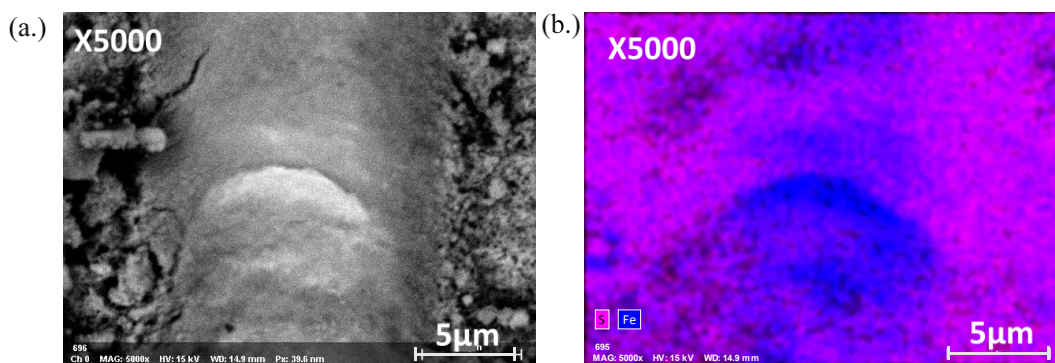


Figure 114: (a.) Scratch track and (b.) EDS mapping of scratch track from a constant load test at 250mN (500MPa) constant load test on a mackinawite layer formed after 3-day Exposure to 1 wt.% Solution at pH 6.0, 0.1bar of H₂S, 30⁰C, and 250rpm impeller rotation speed

The approximate width of the scratch at this force is 18 μm, which corresponds to an interfacial shear strength of 500 MPa.

The profilometry analysis of the scratch area, presented in Figure 115, showed that the scratch depth was 1.70 μm.

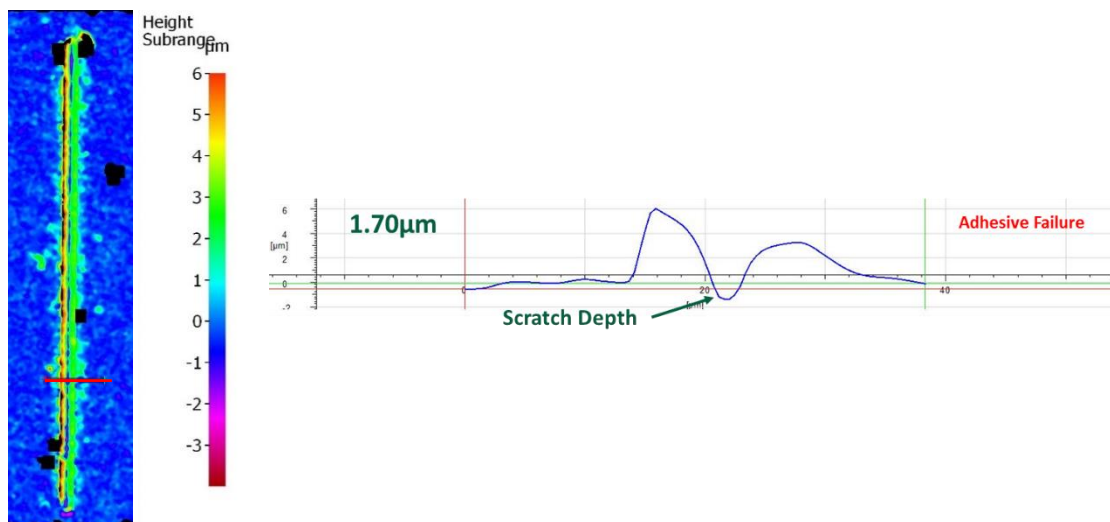


Figure 115: Profilometry of scratch track left by a shear stress of 500 MPa on a Mackinawite layer developed UNS G10180 after 3 days exposure to 1 wt. % NaCl solution at 30°C, pH 6.0, 0.1bar H₂S and 250rpm impeller rotational speed.

The measured scratch depth agrees with the range of the FeS layer thickness ($2.2 \pm 0.5 \mu\text{m}$) presented in Figure 105(b) and further confirms the occurrence of adhesive failure which occurs at the layer substrate interface.

To validate the finding from the retention test which suggests that the outer fluffy FeS layer possesses a weak adhesive strength, a constant load scratch test was conducted at a normal force of 0.1 mN, the lowest force obtainable in this system. The result of this experiment, presented in Figure 116, suggests that at this normal force (corresponding to a shear stress of 0.41 MPa), the outer FeS layer is removed. This agrees with the findings from the retention experiment which revealed that the weak adhesive property of the outer fluffy FeS layer.

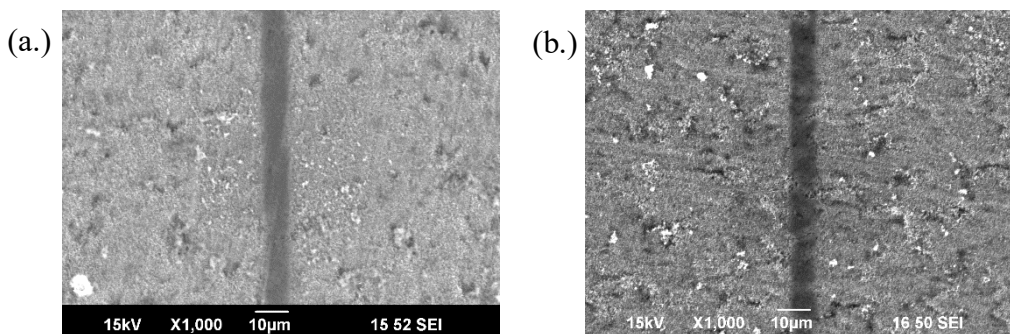


Figure 116: Scratch mark from a 0.1mN constant load test on layers developed in 1 wt. % solution sparged with 10% H₂S/N₂ at 30°C, pH 6.00 and 250rpm (a.) 1-day exposure (b.) 3 days exposure

The summary of the results obtained from the mechanical analysis of the corrosion product layers formed after 1 and 3 days in a 30°C environment is presented in Table XII.

Table XII: Summary of results obtained for mechanical characterization of mackinawite layer formed on UNSG 1018 is exposed to a solution sparged, pH 6.0 and impeller speed of 250 rpm

Exposure Time	FeS Layer Hardness	Critical Load	Scratch Depth	Interfacial Shear of Inner Mackinawite Layer
1 Day	0.3 GPa	230mN	2.3µm	0.47 GPa
3 Days	0.4 Gpa	250mN	1.7µm	0.5 GPa

Mechanical Characterization of FeS layer developed on UNS G10180 Exposed to 1 wt.% Solution at pH 6.0, 80 °C, 0.1bar H₂S and 250rpm Impeller Rotation Speed.

The cross section of the corrosion product layers formed on UNS G10180 exposed to the test solution at 80°C after 1 day and 3 days exposure time is shown in Figure 117.

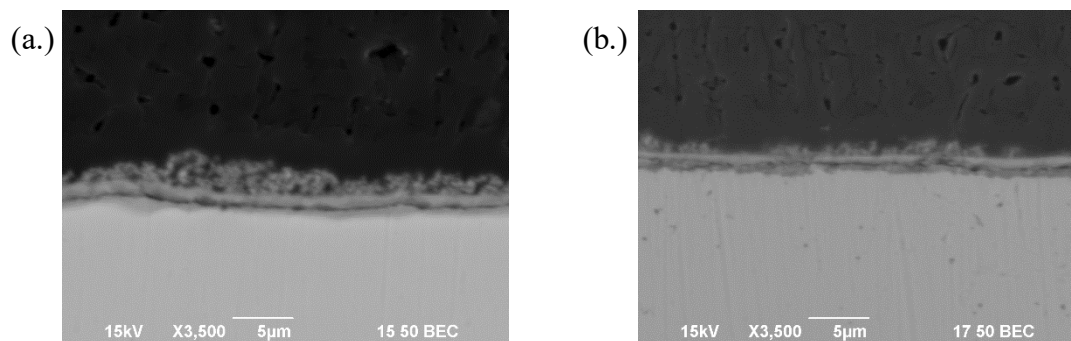


Figure 117: Cross section of FeS layers developed on UNS G10180 immersed in 1% wt. NaCl solution at 80°C, pH 6.0, 0.1bar of H₂S and 250rpm impeller speed (a.) 1-day exposure (b.) 3 days exposure

Similarly to the corrosion product layers formed in 30°C solution, two distinct layers can be observed, an outer fluffy layer and an inner compact layer. However, the outer fluffy layer appears to be more porous and loosely attached than that formed at 30°C. Ning et al.[40] developed FeS layers of similar morphology under these conditions. It was reported that the corrosion rates under these conditions started from an initial value of 1.1mm/year and decreased to 0.07mm/year. This decrease in corrosion rates suggests that these layers are protective. Although X65 carbon steel with tempered martensitic microstructure was used in this study, the corrosion behavior is not expected to differ significantly from that of UNS G1018, especially under the testing conditions where precipitation rates are high. Therefore, the mackinawite layers presented in Figure 118 can be assumed to be protective.

The SEM analysis of sample surface presented in Figure 118 shows that the exposure time did not play a major role in the morphology of the FeS layers. These surface SEM images confirmed the presence of two distinct layers, the outer fluffy FeS layer and the inner compact FeS layer.

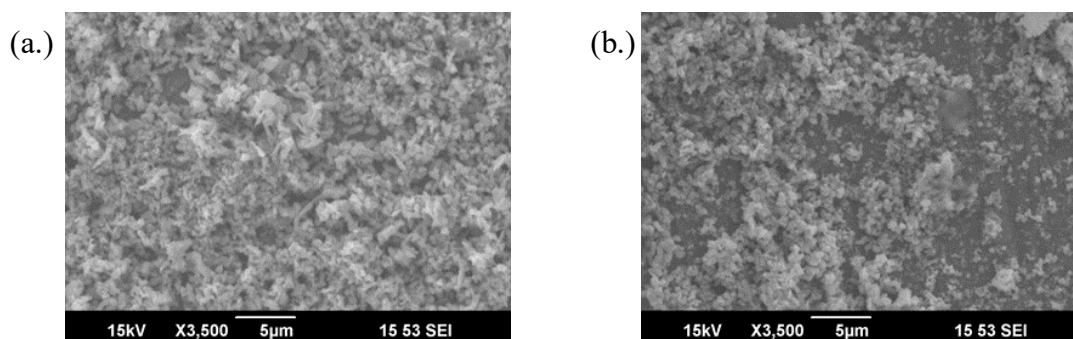


Figure 118: Surface SEM of FeS layer developed on UNS G10180 immersed in 1%. wt. NaCl solution at 80°C, pH 6.00, 0.1bar of H₂S and 250rpm impeller speed (a.) 1 day exposure (b.) 3 days exposure

The phase of FeS layers was confirmed as mackinawite from the XRD analysis presented in Figure 119. This shows that iron sulfide of the same phase can possess different macroscopic morphological characteristics.

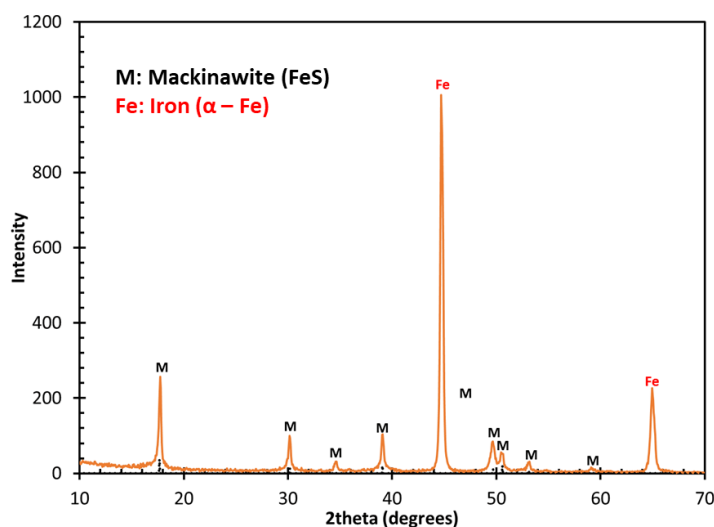


Figure 119: XRD analysis of FeS layer formed on UNS G10180 after 3 days exposure to 1%. wt. NaCl solution at 80°C, pH 6.00, 0.1bar of H₂S and 250rpm impeller speed

Hardness Measurements of Mackinawite Layers on UNS G10180

The loading and unloading chart for the indentation test conducted on the FeS layer formed at 80°C after 1 day and 3 days exposure time are presented in Figure 120 (a.) and (b.).

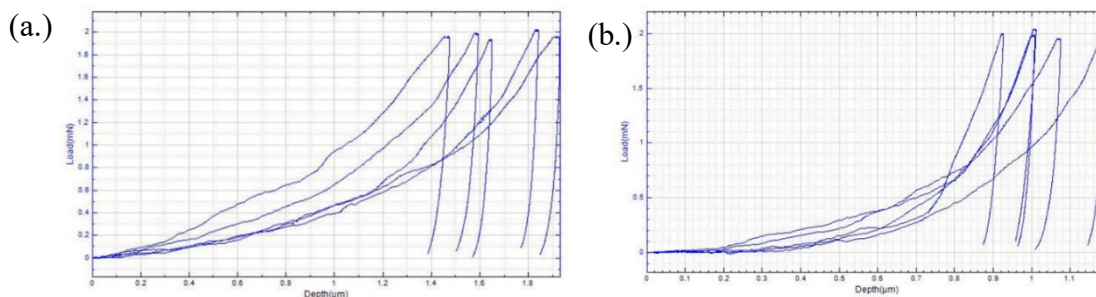


Figure 120: Loading and unloading curve from hardness measurements of mackinawite layer formed on UNS G10180 at 80°C after (a.) 1 day (b.) 3 days

Table XIII shows the hardness measurements obtained for these layers.

Table XIII: Summary of measured hardness of mackinawite layer formed on UNS G10180 exposed to 1 wt.% solution at pH 6.0, 80°C, and 250rpm impeller rotation speed from indentation tests using a Vickers indenter

Repeat Test #	Day 1		Day 3	
	Hardness (GPa)	Hardness (HV)	Hardness (GPa)	Hardness (HV)
1	0.023	2.1	0.087	8.2
2	0.040	3.6	0.101	9.6
3	0.034	3.2	0.073	6.9
4	0.025	2.4	0.060	5.6
5	0.030	2.9	0.084	7.9
Average	0.030	2.9	0.081	7.6
Std Dev	0.006	0.58	0.014	1.3

Similarly to the indentation test results on the layers formed at 30°C, the hardness of the FeS layer formed at 80°C is more than 10 times lower than the hardness of the substrate. A failure mode similar to that observed for the layers formed at 30°C is expected with these layers: a conformal crack mode is expected for the cohesive failure and a buckling crack mode is expected in the case of an adhesive failure.

Determination of the Interfacial Shear Strength of Mackinawite Layer on UNS G10180

Similar progressive load tests were conducted on specimens after 1-day exposure to the environment at 80°C. Constant load scratch tests were then conducted to determine the critical load for adhesive failure using the conical indenter.

Progressive Load Test on Mackinawite layer formed on UNS G10180 after 1 Day

Exposure

The chart in Figure 121 shows the loading vs scratch length chart of the progressive load test from 0.1mN to 300mN on the FeS layer formed on UNS G10180 after 1-day exposure to solution at 80°C.

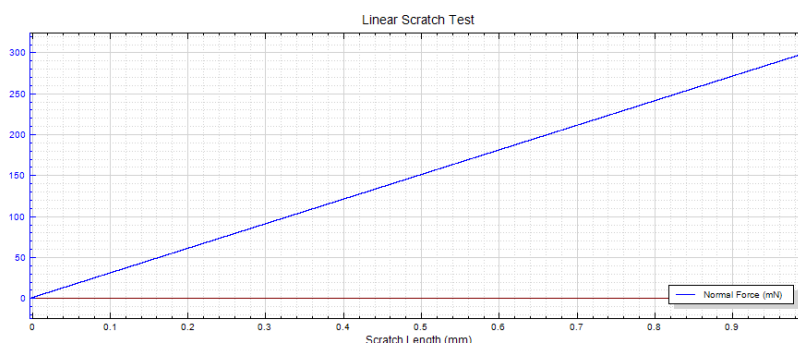


Figure 121: Progressive load scratch test from 0.1mN to 300mN on the mackinawite layer formed after 1 day exposure of UNS G10180 to 1 wt.% solution at pH 6.0, 80°C, and 250rpm impeller rotation speed, conducted at a scratch speed of 0.25mm/min and loading rate of 75mN/min.

The EDS analysis of the scratch track from the progressive load test (Figure 122) shows that adhesive failure occurred at 150mN and 300mN. This is indicated by the high iron to sulfur atom % ratio detected in the scratched area. However, at 0.1mN, the approximately equal Fe to S atom % ratio indicates that only a cohesive form of failure occurred. From these results, it can be inferred that the critical load for adhesive failure is between 0.1mN and 150mN. Constant load tests were conducted at forces between 0.1mN and 150mN to confirm the critical load for adhesive failure.

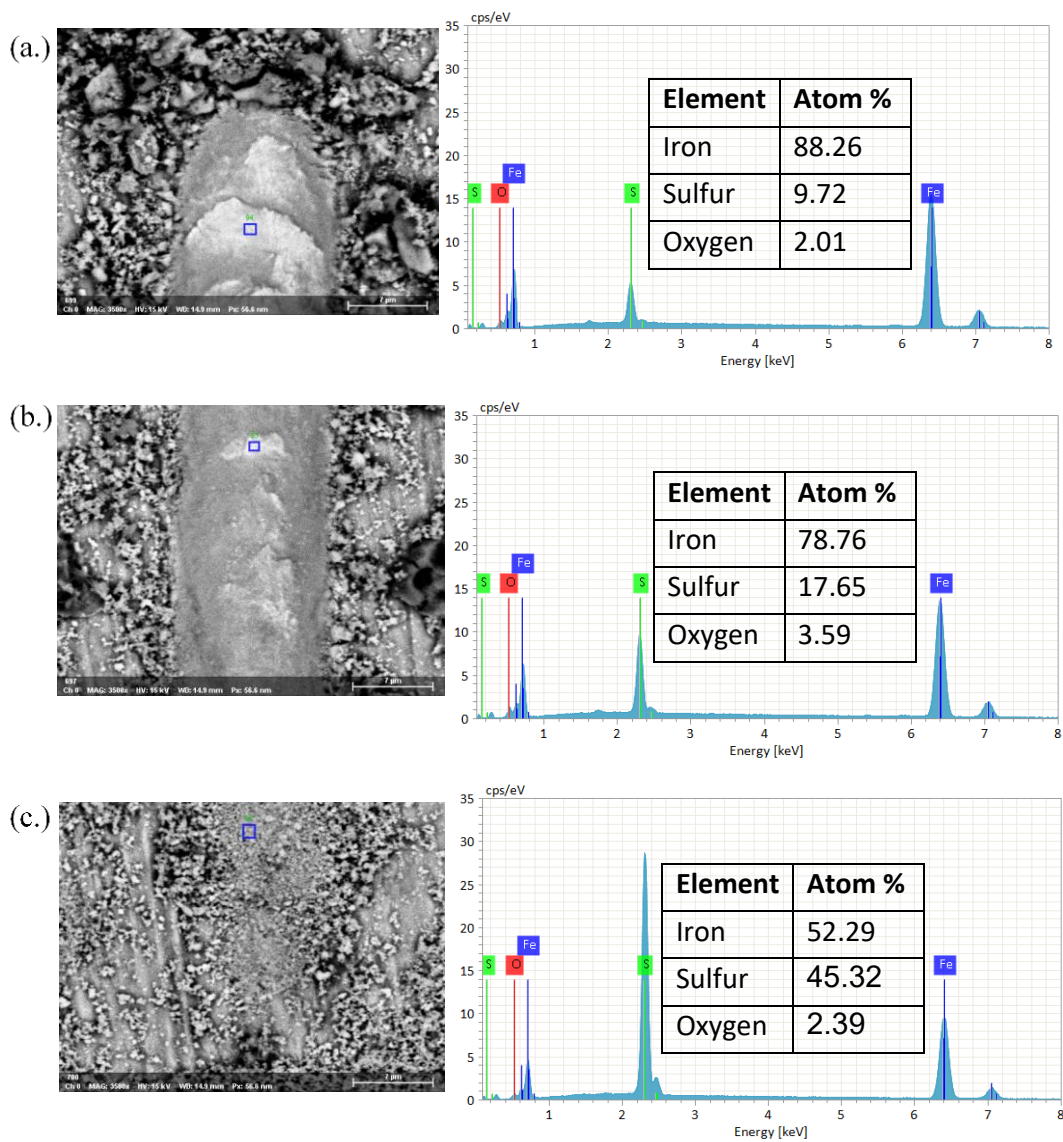


Figure 122: EDS Analysis of progressive load scratch from 0.1mN to 300mN on mackinawite layer formed on UNS G10480 after 1-day exposure to 1 wt.% solution at pH 6.0, 80°C, and 250rpm impeller rotation speed at (a.) 0.1mN (b.) 150mN and (c.) 300mN

Constant Load Test of Mackinawite Layer Formed on UNS G10180 after 1 Day

Exposure

A constant load test was conducted at 100mN since results from the progressive load test revealed the occurrence of adhesive failure at a load between 0.1mN and 150mN. For reasons of uniformity, the scratch rate during testing was also maintained at 0.25mm/min. The EDS map of the scratch presented in Figure 123 confirmed the occurrence of a cohesive form of failure at this force. The EDS map of the scratch presented in Figure 123 confirmed the occurrence of a cohesive form of failure at this force.

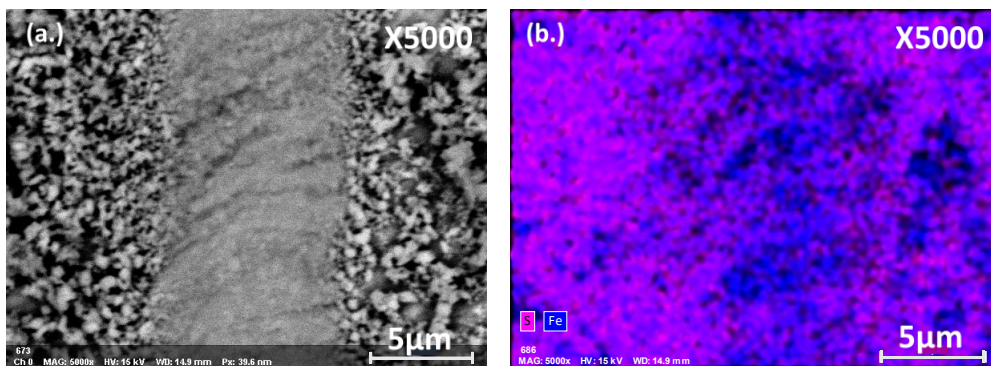


Figure 123: (a.) Scratch mark from a constant load test at 100mN (b.) EDS mapping of scratch mark with uniform distribution of Fe and S

However, a constant load test at an increased force of 150mN resulted in the occurrence of an adhesive form of failure. The failure at these different forces was confirmed from the EDS mapping of the scratched surface (Figure 124). Distinct areas within the scratch track showed higher iron intensities confirming adhesive failure at 150mN. These were not observed at 100mN.

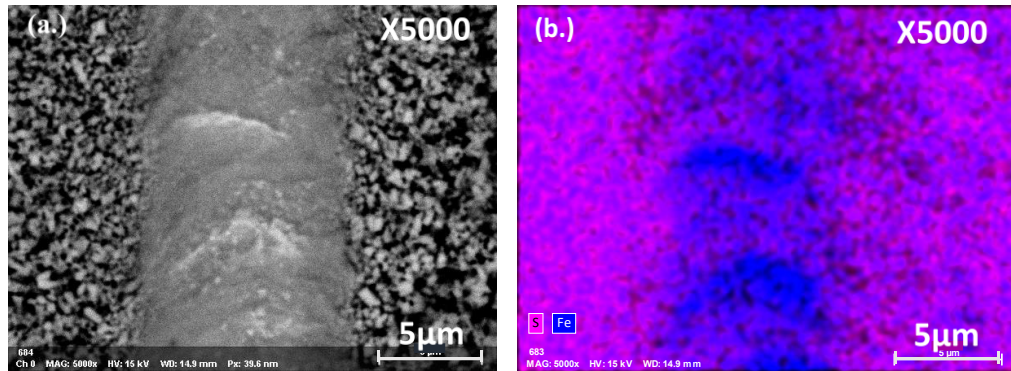


Figure 124: (a.) Scratch mark from a constant load test at 150mN (b.) EDS analysis of scratch mark showing distinct area of high iron intensities.

The scratch width from the 150mN constant load test (Figure 124) was $12\mu\text{m}$ corresponding to an interfacial shear strength of 410MPa. This value is within the same magnitude of shear strength obtained for layers developed at 30°C .

The profilometry analysis of the scratch marks obtained at 310 MPa and 410 MPa shear stresses (Figure 125) revealed that the depth of the scratches was $1.50\mu\text{m}$ and $3.0\mu\text{m}$, respectively. The $3.0\mu\text{m}$ scratch depth resulting from the 410 MPa shear stress is within the range of the FeS layer thickness confirming that the failure occurred at the substrate layer interface.

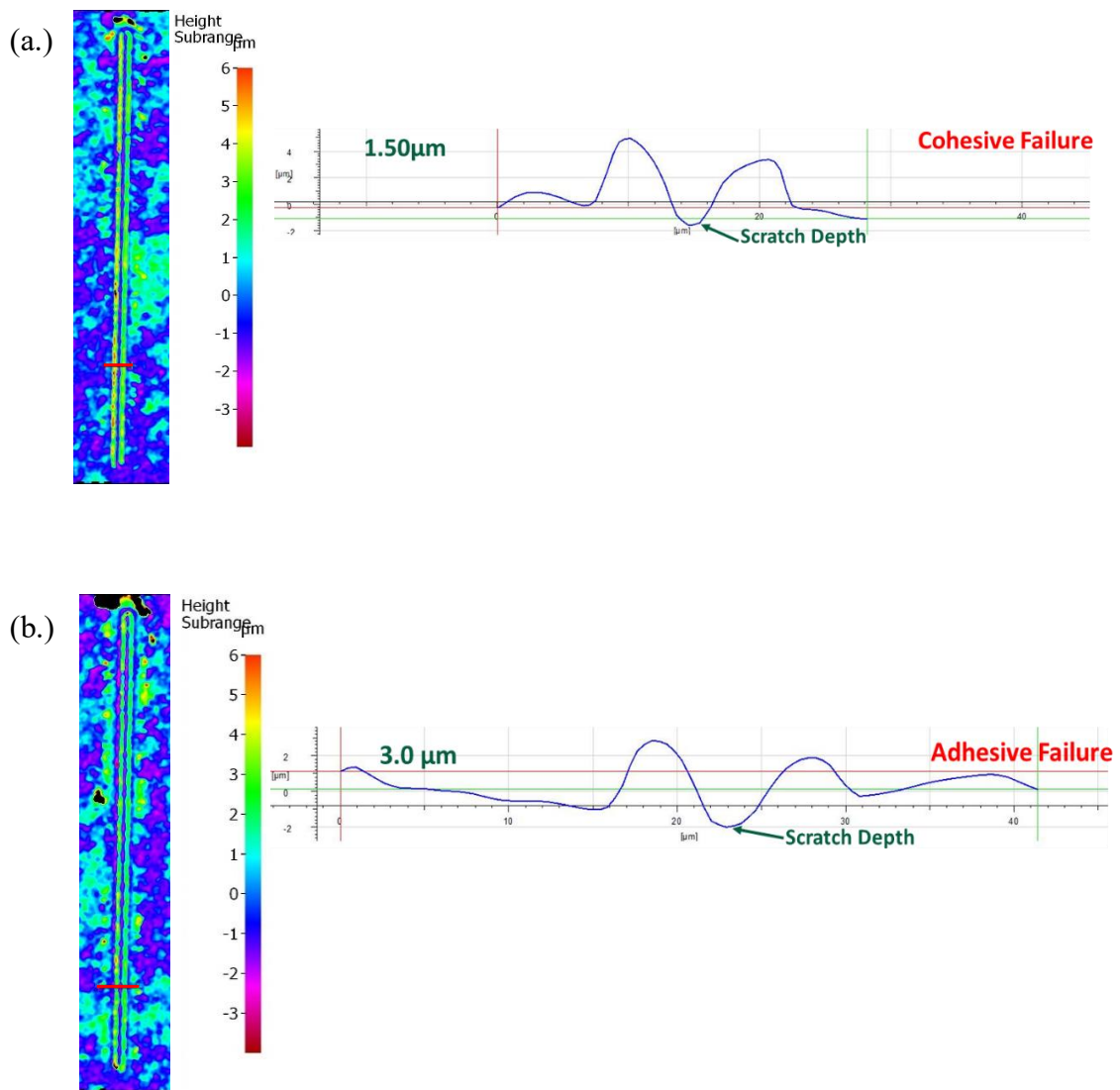


Figure 125: Profilometry of scratched area resulting from a shear stress of (a.) 310 MPa and (b.) 410 MPa

Constant Load Test of Mackinawite Layer Formed on UNS G10180 after 3 Days

Exposure

The adhesive failure of the layer developed after 3 days exposure period occurred at a constant load force of 150mN. The EDS mapping presented in Figure 126 shows the distinct areas with higher Fe intensity which confirms the occurrence of adhesive failure.

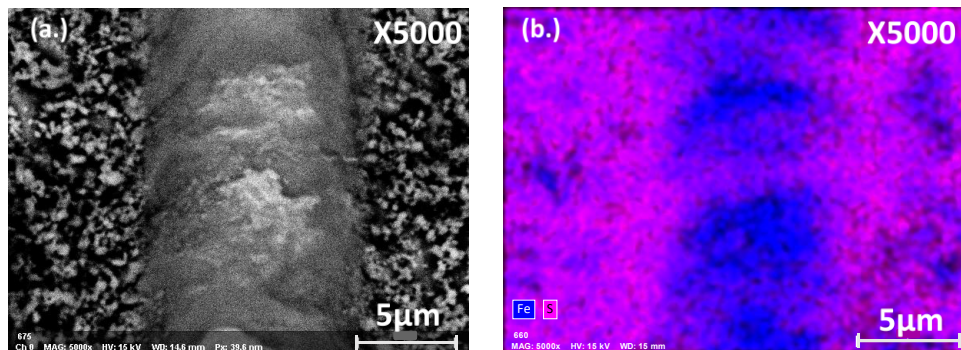


Figure 126: (a.) Scratch mark from a constant load test at 150mN (b.) EDS analysis of scratch mark showing distinct area of high iron intensities

With the equal critical load observed for the layers developed after 1 day and 3 days, it can be inferred that these layers have a very similar adhesion to the substrate. The higher scratch width ($14\ \mu\text{m}$) observed on the 3 days sample is an indication that more corrosion product layer was removed during the scratching process. The calculated interfacial shear strength of the layer developed after 3 days was 370 MPa, which is slightly lower than that of the layer developed after 1 day, 410 MPa. This difference may not be significant enough considering the magnitude of interfacial shear strength in question.

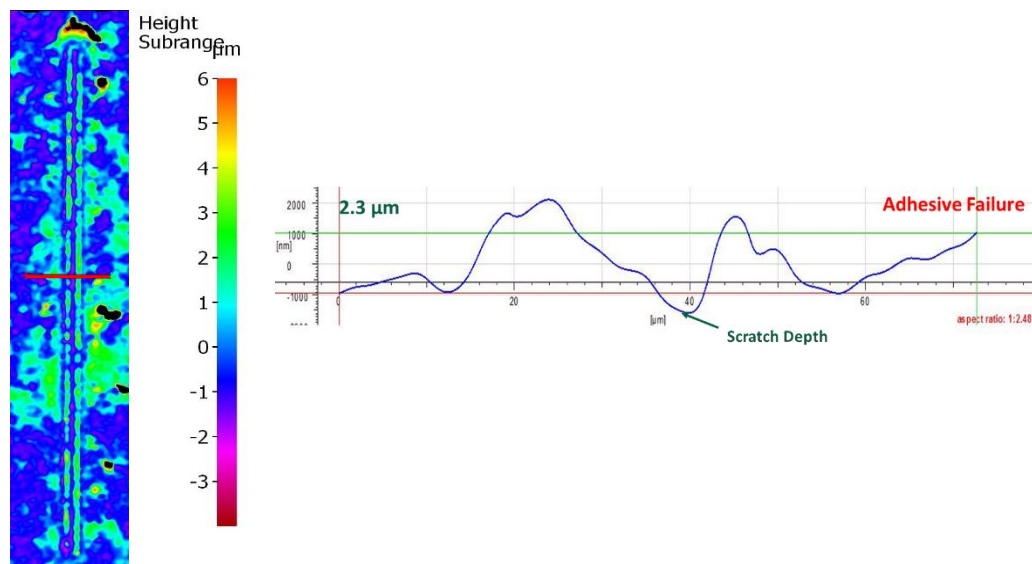


Figure 127: Profilometry of the scratched area resulting from a shear stress of 370MPa

The depth profile presented in Figure 127 shows the scratch depth is within range of the corrosion product layer thickness.

The resistance of the outer FeS layer to a scratch test at a normal force 0.1mN was also evaluated. The results from this test, presented in Figure 128 also showed that these layers are easily removable at this shear stress equivalent to 0.28MPa. With the use of an equal normal force, a lower shear strength was calculated for layers that formed at 80°C, in comparison to those that formed at 30°C. This indicates that the outer FeS layer formed at higher temperature has a lower adhesive property than those formed at 30°C.

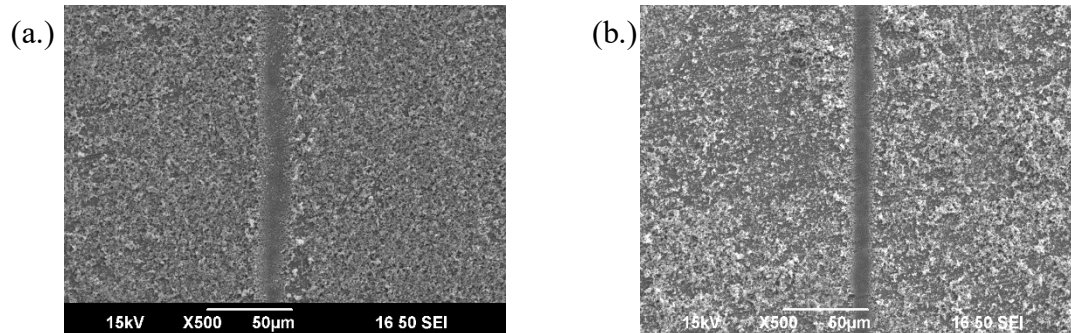


Figure 128: Scratch mark from a 0.1mN constant load test on layers developed in 1 wt. % solution sparged with 10% H₂S/N₂ at 80°C, pH 6.00 and 250rpm (a.) 1 day exposure (b.) 3 days exposure

The summary of the results obtained from the indentation and the adhesion tests is presented in Table XIV.

Table XIV: Summary of results obtained for mechanical characterization of mackinawite layer formed on UNS G1018 exposed to a solution sparged with 10% H₂S/N₂ at 80°C, pH 6.00 and impeller speed of 250rpm

Exposure Time	Hardness	Critical Load	Scratch Depth	Interfacial Shear of Inner Mackinawite Layer
1 Day	0.03 GPa	150mN	3.0µm	0.41 GPa
3 Days	0.08 GPa	150mN	2.3µm	0.37Pa

Summary

The mechanical properties mackinawite corrosion product layers formed on UNS G1018, at 30°C and 80°C, pH 6, with 10% H₂S/N₂ and considering exposure times of 1 and 3 days, were investigated using hardness and scratch tests measurements. The mode of adhesive failure obtained for all the layers tested was buckling. The mode of cohesive failure expected was conformal cracking considering the hardness of the layers and the

substrate. While this mode of cohesive failure was evident for the scratches in layers formed at higher temperature, the appearance of conformal cracks was less pronounced in the layer formed at lower temperature. This may be due to the fact that the layers formed at 80°C had a lower hardness than those formed at 30°C, which is more favorable for the formation of conformal cracks.

The chart presented in Figure 129 shows the interfacial shear strength of the different layers tested while the red line on the chart shows the maximum wall shear stress that can be generated by flow alone. Furthermore, the calculated interfacial shear strength suggests that the adhesive force of the layer formed at 80°C is slightly lower than that of the layer formed at 30°C. These results agree with recent findings in literature where it was reported that a denser but weakly attached FeS layer forms at higher temperature H₂S environments in comparison to a lower temperature environment. [84]

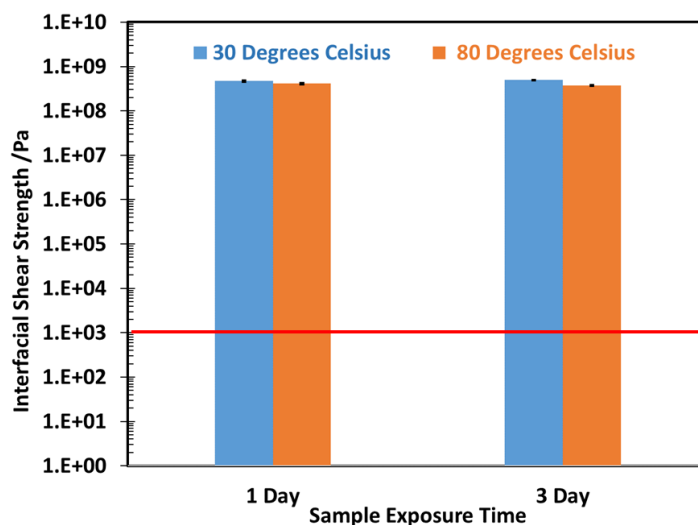


Figure 129: Summary of the interfacial shear strength of mackinawite layers formed in 30°C and 80°C solutions compared to the highest possible flow related shear stress in pipelines

7.3.2 Effect of Substrate material on the Mechanical Properties of Iron Sulfide Layers Formed in Low Flow Conditions

The mackinawite layer developed on a 99.9% pure Fe substrate after 3 days exposure to a 1 wt. % NaCl solution sparged with 10% H₂S solution in admixture with N₂ at pH of 6.0, temperature of 30°C and 250 impeller rotational speed was evaluated for their mechanical properties. Indentation and scratch test measurements were conducted to evaluate the hardness and the adhesive strength of these layers on 99.9% pure Fe and the results were compared with the values obtained for FeS layers developed on UNS G10180 substrates after 3 days exposure to similar solution at similar conditions. Figure 130 (a.) and (b.) shows the surface SEM and cross section of the FeS layer developed on pure Fe substrate after 3 days exposure to 1 wt. % NaCl solution at 30°C, pH 6.0, 0.1bar H₂S and 250rpm impeller rotational speed.

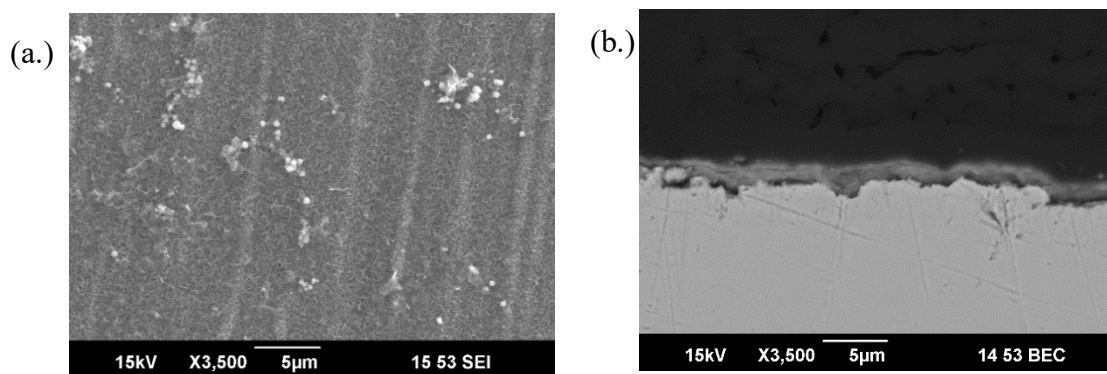


Figure 130: (a.) Surface SEM and (b.) Cross section of FeS layer developed on 99.9% pure Fe after 3 days exposure to 1 wt. % NaCl solution at 30°C, pH 6.0, 0.1bar H₂S and 250rpm impeller rotational speed

The SEM image of 99.9% pure Fe after 3 days exposure shows similarity to the morphology of the layer formed on UNS G10180. Cross section analysis showed that the thickness of this FeS layer is $2.12 \pm 0.36 \mu\text{m}$. This is approximately the same thickness of the FeS layer developed on UNS G10180 after three days exposure to similar solution.

The EDS analysis of the corrosion product layer presented in Figure 131 detected iron and sulfur as the main atomic components confirming this layer as iron sulfide. Mackinawite is the expected phase of FeS that forms in this condition according to the earlier reported XRD analysis of the FeS layer developed under similar conditions and exposure time.

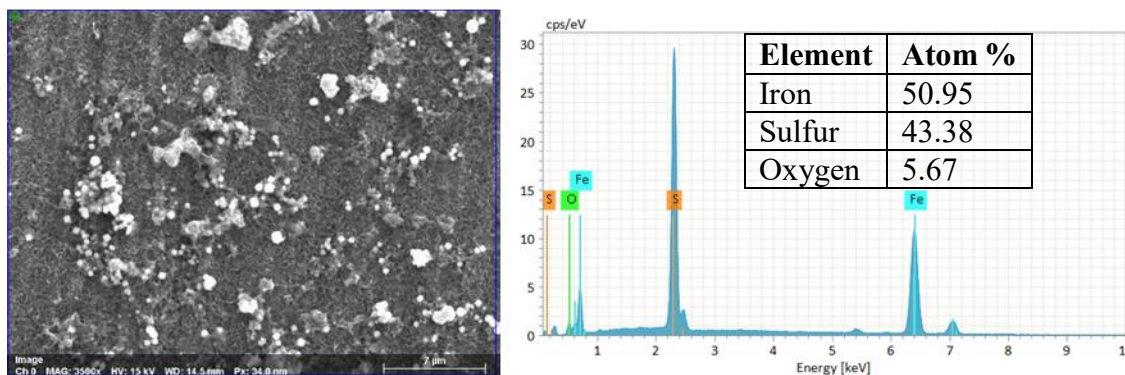


Figure 131: EDS analysis of FeS layer developed on 99.9% pure Fe after 3 days exposure to 1 wt. % NaCl solution at 30°C, pH 6.00, 0.1bar H₂S and 250rpm impeller rotational speed

Hardness Measurement of Mackinawite Layer Formed on 99.9% Pure Fe after 3-days Exposure to 1 wt.% Solution at pH 6.0, 30°C, and 250rpm Impeller Speed.

The hardness measurement of the mackinawite layer from five indentation measurements is presented in Figure 132. The penetration depth shown on the x axis of

the indentation measurement is lower than the thickness of the FeS layer, indicating that hardness substrate hardness did not influence the indentation measurements.

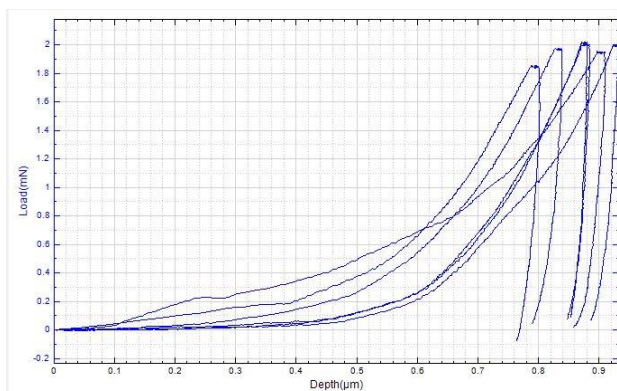


Figure 132: Loading and unloading curve from hardness measurements of mackinawite layer formed on 99.9% pure Fe after 3 days exposure to 1 wt. % NaCl solution at 30°C, pH 6.0, 0.1bar H₂S and 250rpm impeller rotational speed

The average values of the layer hardness, presented in Table XV, shows that the average hardness of the FeS layer formed on pure Fe substrate from the six indentation measurements is 10.59HV (0.11 GPa).

Table XV: Summary of measured hardness of mackinawite layer formed on 99.9% pure Fe exposed to 1 wt.% solution at pH 6.0, 0.1bar H₂S 30°C, and 250rpm impeller rotation speed from from indentation tests using a Vickers indenter

Repeat Test #	Hardness (GPa)	Hardness (HV)
1	0.11	10.45
2	0.11	10.46
3	0.10	9.71
4	0.10	9.42
5	0.12	11.58
6	0.13	11.93
Average	0.11	10.59
Std Dev	0.01	0.91

These results show that the hardness of the mackinawite layer formed on 99.9% pure Fe substrate is approximately three times lower than the hardness of the mackinawite layer formed on UNS G10180 under the same condition. In Chapter 5, an increase in the precipitation rate of iron sulfides was observed in the pearlite phase due to the favorable water chemistry in this region. Therefore, the higher hardness values of the mackinawite layer formed on UNS G10180 can be attributed to the iron carbide network which is present within the iron sulfide layers formed on this substrate.

Determination of the Interfacial Shear Strength of Mackinawite Layer Formed on 99.9% Pure Fe after 3-days Exposure to 1 wt.% Solution at pH 6.00, 30 °C, and 250rpm Impeller Speed.

Progressive load experiments were initially conducted to establish the range of force for the occurrence of adhesive failure. Afterwards, constant load experiments were performed to identify the actual force for adhesive failure.

Progressive Load Test on Mackinawite Layers on 99.9% Pure Fe after 3 Days Exposure

Figure 133 shows the chart and scratch track from the progressive load test conducted from a normal force of 0.1mN to 300mN.

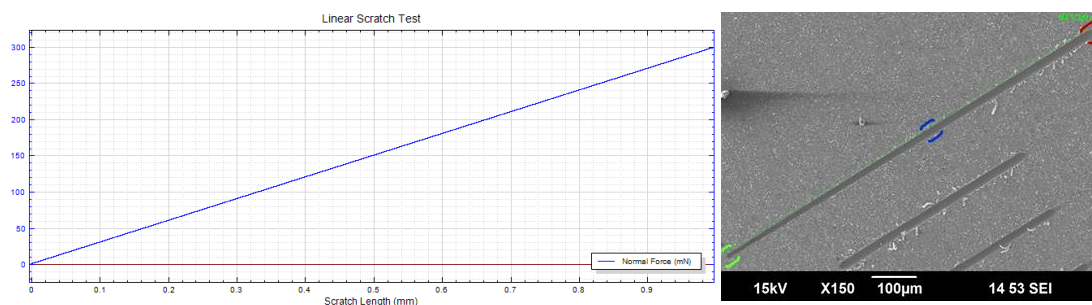


Figure 133: Progressive load scratch test from 0.1mN to 300mN on the mackinawite layer formed on 99.9% pure Fe after 3 days exposure to 1 wt.% solution at pH 6.00, 30⁰C, and 250rpm impeller rotation speed, conducted at a scratch speed of 0.25mm/min and loading rate of 75mN/min.

Figure 134 shows the EDS analysis of the scratch track conducted on the force location of 0.1mN, 150mN and 300mN corresponding to the locations marked as green, blue and red on the progressive scratch track presented in Figure 133.

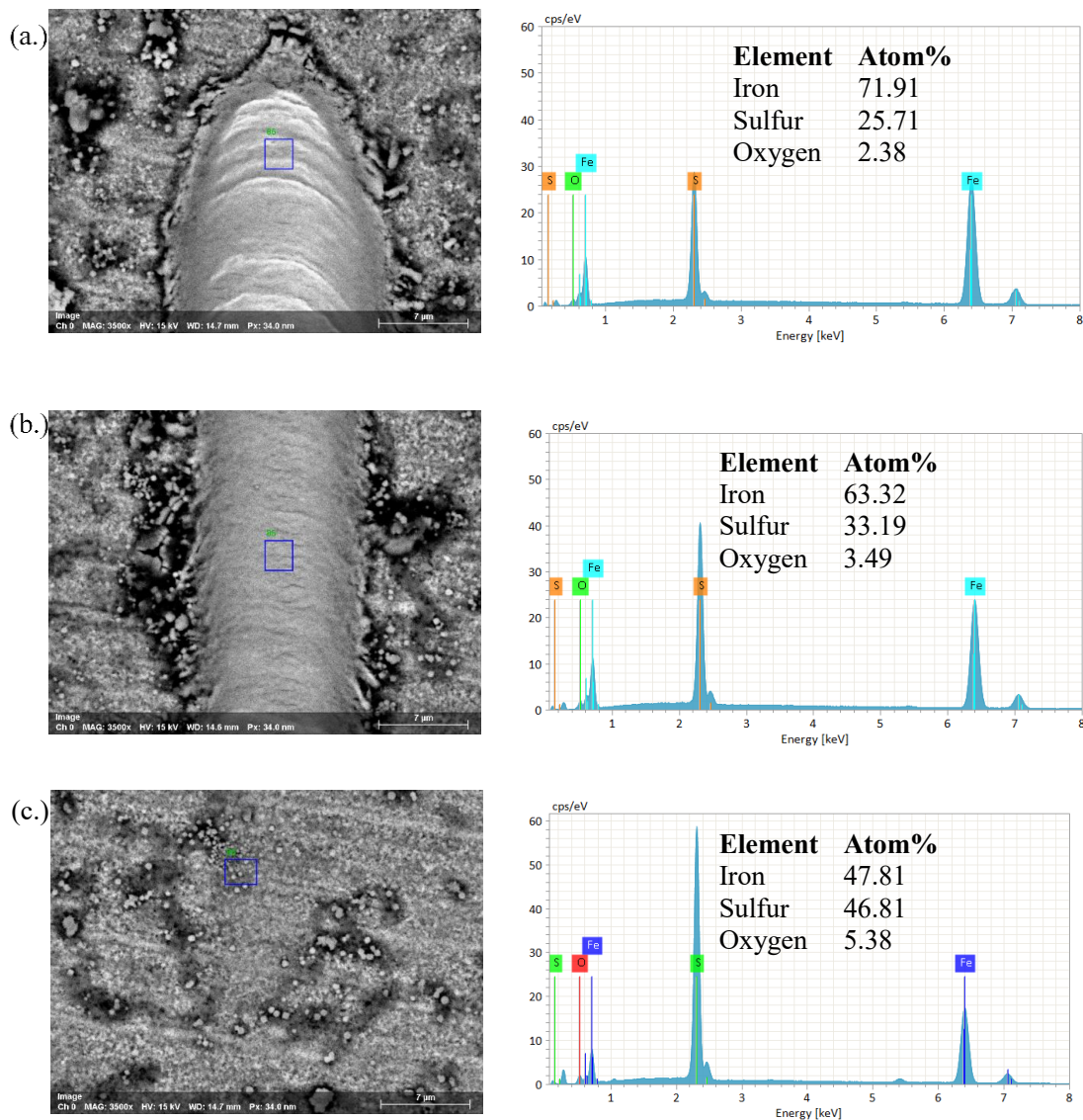


Figure 134: EDS analysis of progressive load scratch from 0.1mN to 300mN on mackinawite layer formed on 99.9% pure Fe after 3 days exposure to 1 wt. % NaCl solution at 30°C, pH 6.00, 0.1bar H₂S and 250rpm impeller rotation speed at (a.) 0.1mN (b.) 150mN and (c.) 300mN

Similarly to observations with the UNS G10180, the EDS analysis of the scratch track at different force locations showed that the adhesive failure occurred between 150mN and 300mN. A reduction in the atom % of sulfur at the force location of 150mN was observed without the actual failure of the layer usually indicated by cracks. This

behavior may be due to the fact that this layer is soft and has a hardness three times lower than the layer formed on UNS G10180. Constant load test was conducted at a force above 150 mN to identify the critical load for the adhesive failure of this layer.

Constant Load Test on Mackinawite Layers on 99.9% Pure Fe after 3 Days Exposure

The constant load experiment conducted at 200mN (Figure 135) shows the occurrence of an adhesive failure along the scratch track. Similarly to results obtained with UNS G10180, the mode of both cohesive and adhesive failure is conformal and buckling cracks, respectively. According to the failure mode chart presented in Table IX, the more pronounced conformal cracks observed with 99.9% pure Fe is due to the reduced hardness of the layers formed on this substrate in comparison to UNS G10180.

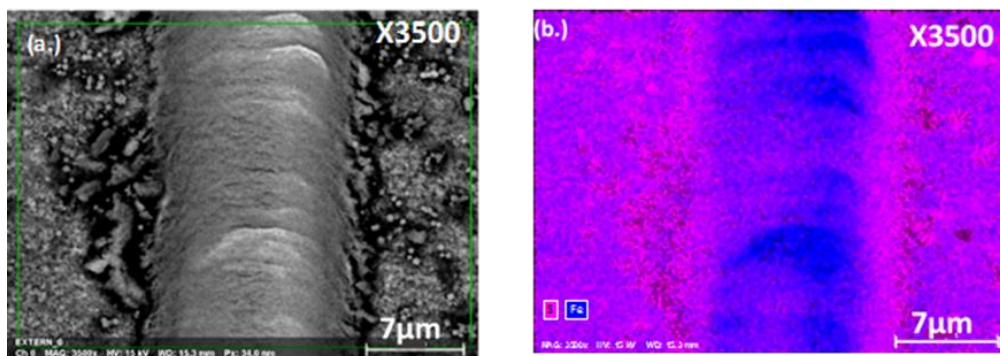


Figure 135: Scratch track left by a shear stress of 500MPa on a Mackinawite layer developed on 99.9% Pure Fe after 3 days exposure to 1 wt. % NaCl solution at 30°C, pH 6.0, 0.1bar H₂S and 250rpm impeller rotational speed. (b.) EDS analysis of scratch track showing distinct area of high iron intensities.

EDS analysis of the scratch track also showed areas of higher iron peak intensity indicating exposure of the substrate due to removal of the mackinawite layer. These results confirm that 200mN is the critical load for adhesive failure. With the measured scratch width of $17.26 \pm 0.06 \mu\text{m}$, the interfacial shear strength corresponding to 200mN

was calculated to be 410MPa. This value is smaller by 90MPa compared to that obtained for the mackinawite layer formed on UNS G10180 (Section 7.3.1) suggesting less adherence of the layer to the 99.9% pure Fe substrate. These results agree with the findings from Chapter 5, the study of effect of iron carbide on FeS layer development, where under similar conditions, the FeS layer showed less attachment to the Fe substrate than the UNS G10180.

The profilometry of the scratched surface, presented in Figure 136 showed that the depth of the scratch track left by a shear stress of 410MPa is $1.80\mu\text{m}$.

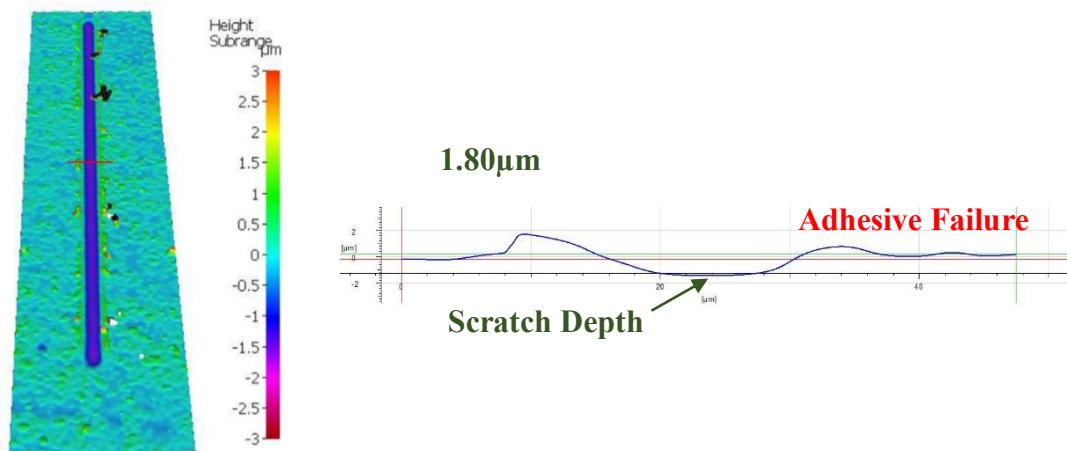


Figure 136: Profilometry of scratch track left by a shear stress of 500MPa on a Mackinawite layer developed on 99.9% Pure Fe after 3 days exposure to 1 wt. % NaCl solution at 30°C , pH 6.0, 0.1bar H_2S and 250rpm impeller rotational speed

The depth of the scratch track revealed from the profilometry of the specimen surface agrees with the thickness of the layer measured as $2.12\pm 0.36\mu\text{m}$ from the cross section confirming the failure at the substrate/layer interface.

The results obtained from the indentation and scratch tests conducted on the mackinawite layer developed both UNS G10180 and 99.9% pure Fe substrate have been summarized in the Table XVI.

Table XVI: Summary of results obtained for mechanical characterization of mackinawite layer formed on UNSG 1018 and 99.9% pure Fe after 3 days exposure to 1 wt. % NaCl solution at 30°C, pH 6.0, 0.1bar H₂S and 250rpm impeller rotational speed of 250 rpm.

Substrate	FeS Layer Hardness	Critical Load	Scratch Depth	Interfacial Shear of Inner Mackinawite Layer
UNS G10180	0.40 GPa	250mN	1.7μm	0.5 GPa
99.9% Pure Fe	0.11 GPa	200mN	1.8μm	0.41 GPa

Summary

The effect of iron carbide on the mechanical properties of FeS layers formed in low shear stress conditions was investigated by comparing the hardness and interfacial shear strength of the mackinawite layers formed on 99.9% pure Fe after 3 days exposure to 1 wt. % NaCl solution (at 30°C, pH 6.0, 0.1bar H₂S and 250rpm impeller rotational speed of 250 rpm) with that of the layers formed on UNS G10180. The summary of the results presented in Table XVI shows that the layers formed on Pure Fe had a lower hardness than the layers formed on UNS G10180. This can be attributed to the presence of iron carbide in the FeS layer formed on UNS G10180. Results from this study also showed that the layers formed on pure Fe have a lower interfacial shear strength (approximately 90 MPa lower) than that for layers formed on UNS G10180. This observation agrees with findings from the effect of iron carbide on FeS development

(Chapter 5), where it was demonstrated that a more attached FeS layer formed 99.9% pure Fe in comparison to that formed on UNS G10180.

7.3.3 Effect of Substrate on the Mechanical Properties of Layers Developed in High flow conditions

The mackinawite layers formed during a three-day exposure of 99.9% pure Fe and UNS G10180 to a 1 wt. % NaCl solution at 0.1bar H₂S/N₂, pH 6.00 and temperature of 30°C flowing at a velocity of 10.4m/s in the single-phase flow loop. The surface and cross section analysis of the corrosion product layer were presented in Figure 77 and Figure 87 in Chapter 6. These layers exhibited different protective properties as the occurrence of localized corrosion was observed with the layer formed on the UNS G10180 substrate in contrast to the uniform corrosion of the 99.9% pure Fe. The indentation measurements of the layers formed on the pure Fe and the UNS G10180 substrates are presented in Figure 137(a.) and (b.).

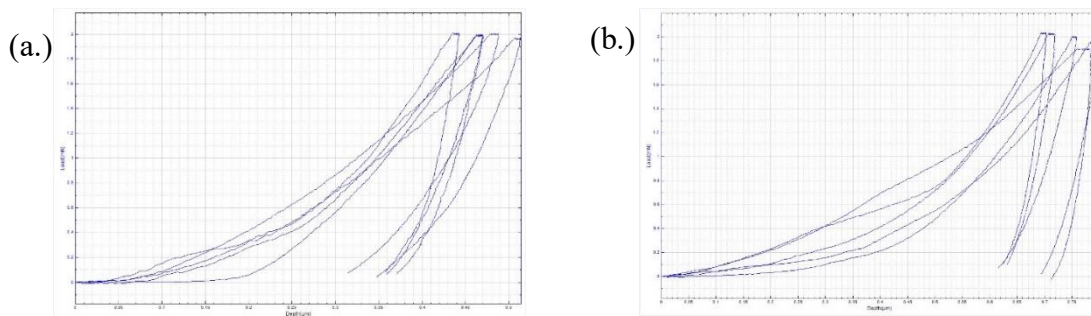


Figure 137: Loading and unloading curve from hardness measurements of mackinawite layer formed on (a.) UNS G10180 and (b.) 99.9% pure Fe substrate after 4 days exposure to 1 wt. % NaCl solution at 30°C, pH 6.0, 0.1bar H₂S and 10.4m/s fluid velocity.

The average hardness obtained from the indentation measurements for the different substrates are presented in Table XVII.

Table XVII: Summary of measured hardness of mackinawite layer formed on UNS G10180 and 99.9% pure Fe after 4 days exposure to 1 wt.% solution at pH 6.0, 30°C, 0.1bar H₂S and 10.4m/s fluid velocity.

Repeat Test #	UNS G10180		99.9% Pure Fe	
	Hardness (GPa)	Hardness (HV)	Hardness (GPa)	Hardness (HV)
1	0.490	46.3	0.189	17.82
2	0.520	49.1	0.162	15.31
3	0.436	41.2	0.144	13.62
4	0.471	44.5	0.148	14.01
5	0.513	48.4	0.176	16.64
Average	0.486	45.9	0.164	15.48
Std Dev	0.030	2.8	0.017	1.58

The hardness of the layers formed on the different substrates was higher than the hardness of the layers formed at a low flow velocity (250rpm impeller speed) by about 5 - 8HV. These results were expected since previously reported results showed that only the more compact inner mackinawite layer forms in high shear stress flow conditions. Similarly to the reported hardness of the layers formed at lower shear stress, Table XVII also shows that the hardness of the layer formed on 99.9% pure Fe is 3 times less than the layer formed on UNS G101080. This difference is also attributed to presence of iron carbide in the FeS layer formed on UNS G10180.

Critical Load for Adhesive Failure of Mackinawite Layer formed on UNS G10180 and 99.9% pure Fe after 4 days exposure to 1 wt.% solution at pH 6.0, 30 °C, 0.1bar H₂S and 10.4m/s fluid velocity.

The progressive load tests on the layers formed at 10.4m/s from 0.1mN to 300mN did not yield an adhesive failure of the layers. However, at a higher load of 800mN, an adhesive failure was observed on the mackinawite layer formed on UNS G10180. The layer formed on 99.9 % pure Fe did not undergo an adhesive form of failure at this force. A constant load experiment at a higher load could not be achieved since the limit of the current mechanical tester is 800mN. The EDS analysis of the scratch track resulting from the 800mN constant load tests on the layers formed on the different substrate is presented in Figure 138.

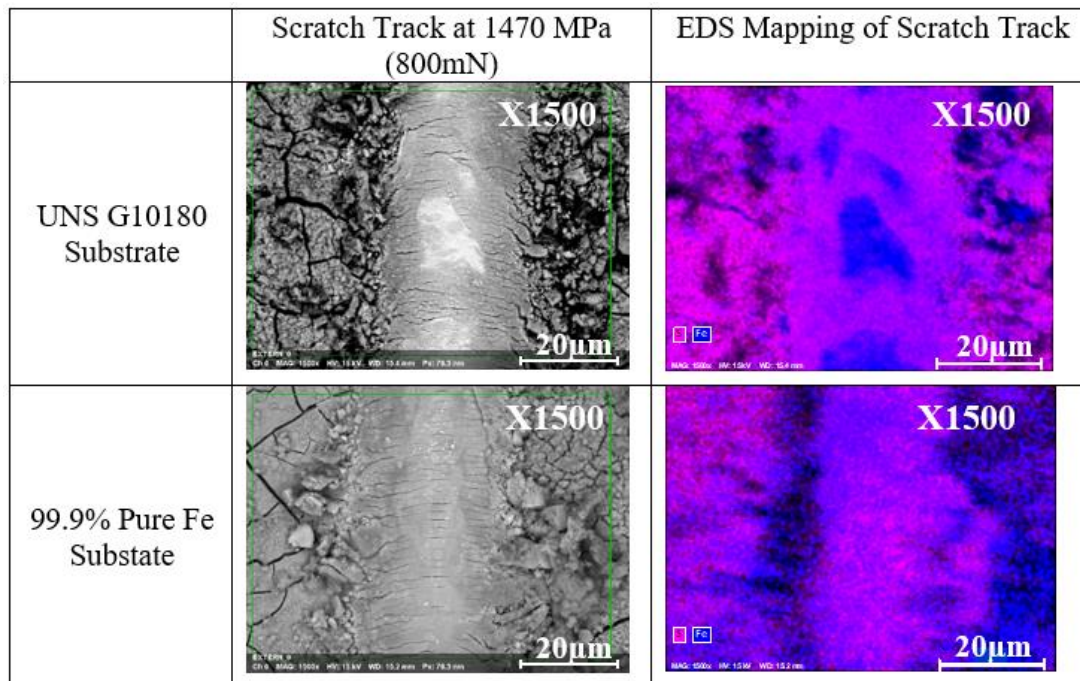


Figure 138: EDS analysis of scratch tracks from 1470 MPa shear stress on a mackinawite layer formed on UNS G10180 and 99.9% pure Fe after 4 days exposure to 1 wt. % NaCl solution at 30°C, pH 6.0, 0.1bar H₂S and 10.4m/s fluid velocity.

With the scratch track diameter of 20 μ m, the interfacial shear strength corresponding to 800mN is 1470MPa. While the mackinawite layer formed on UNS G10180 exhibited adhesive failure at 1470MPa, the layer formed on 99.9% pure Fe required a force higher than this to fully delaminate. The lower interfacial shear strength exhibited by the layers formed on the UNS G10180 implies less attachment of the mackinawite layer on the carbon steel at high flow condition. This is consistent with findings from the studies conducted at high flow velocity condition (in Chapter 6) where localized attacks were observed on UNS G10180, in contrast to the uniform corrosion of 99.9% pure Fe. The results from this study also showed that the mackinawite layer formed at high flow velocity conditions (10.4m/s) has interfacial shear strength 3 times

higher than that exhibited by the mackinawite layer formed at low flow conditions (250rpm impeller speed). Corrosion studies revealed the occurrence of higher corrosion rates caused by an increase in the mass transport rate of species through the initial FeS layer. The increase in sulfide species concentration and ferrous ion concentration favors higher precipitation rates of iron sulfides which may result in the formation of a more adhesive layer.

The depth profile of the scratch tracks from a shear stress of 1470 MPa is presented in Figure 139.

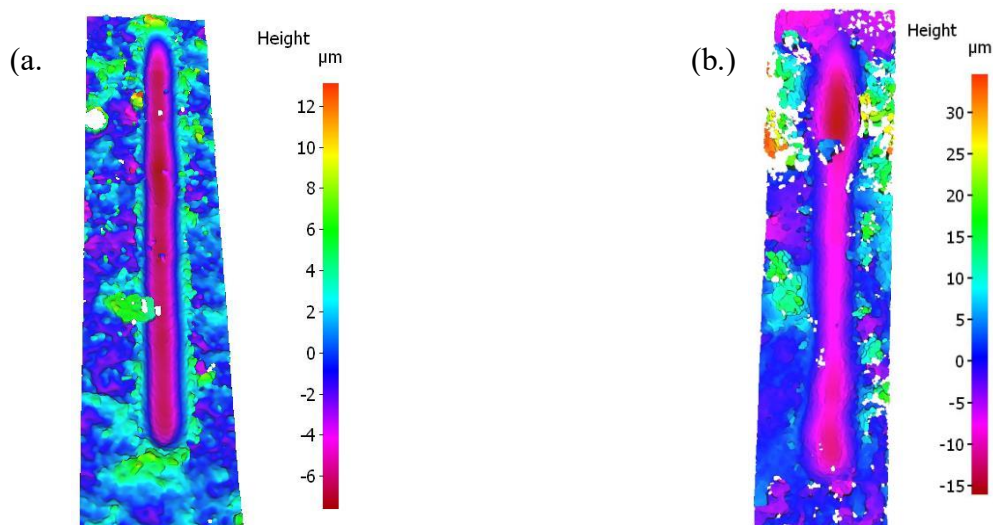


Figure 139: Profilometry of scratch track left by a shear stress of 1470MPa on a Mackinawite layer developed on (a.) UNS G10180 and (b.) 99.9% Pure Fe after 3 days exposure to 1 wt. % NaCl solution at 30°C, pH 6.0, 0.1bar H₂S and 10.4m/s

Due to higher substrate hardness and the hardness of the mackinawite layer formed on UNS G10180, the scratch depth on the UNS G10180 was lower than that on the pure Fe substrate. Since the depth of the scratch tracks is higher than the thickness of

the layer on both substrates, the adhesive strength of the layers can be said to be higher than the yield strength of the substrates.

The results obtained from the indentation and scratch tests conducted on the mackinawite layer developed both UNS G10180 and 99.9% pure Fe substrate at 363Pa have been summarized in the Table XVIII.

Table XVIII: Summary of results obtained for mechanical characterization of mackinawite layer formed on UNSG 1018 and 99.9% pure Fe after 3 days exposure to 1 wt. % NaCl solution at 30°C, pH 6.0, 0.1bar H₂S and 10.4m/s

Substrate	FeS Layer Hardness	Critical Load	Scratch Depth	Interfacial Shear of Inner Mackinawite Layer
UNS G10180	0.486 GPa	800mN	6μm	1.47GPa
99.9% Pure Fe	0.164 GPa	>800mN	15μm	>1.47GPa

Summary

The results presented in this section showed that the interfacial shear strength of the mackinawite layer formed on pure Fe and UNS G10180 at 10.4m/s (1470 MPa) was approximately 3 times higher than that of the layers formed at 1.1m/s (500MPa). This behavior was attributed to the increased precipitation rate of the FeS layers formed due to increase in mass transfer and corrosion rates. Results also showed that the layers formed on pure Fe substrate are more adhesive than those formed on UNS G10180. This further highlights the influence of iron carbide on the protectiveness of the layers formed in high flow conditions. Profilometry of the scratch tracks suggests the interfacial shear strength of the mackinawite layers formed at 10.4m/s is higher than the yield strength of the substrates.

7.4 Conclusions

- The outer mackinawite layer can be removed at a shear stress lower than 410 KPa (10^5 Pa). A more precise evaluation of the actual interfacial shear stress could not be done due to limitation of the mechanical tester. However, results from the retention test experiments showed that the outer fluffy mackinawite layer are removed at shear stress of 363Pa
- The inner mackinawite layer would require a shear stress on the order of 10^8 Pa magnitude or higher to be removed. This is two orders of magnitude higher than the shear stress required to remove an iron carbonate layer[21].
- The typical shear stress in oil and gas pipelines is five orders of magnitudes lower than the stress values required to remove the inner mackinawite layers.

CHAPTER 8: CONCLUSIONS AND FUTURE WORK

8.1. Conclusions

The focus of the current research was to investigate the effect of flow on the development and retention of iron sulfide layers in conditions representative of oil and gas production conditions. In conducting this research, the following tasks were accomplished:

- Development and characterization of corrosion testing setups which enabled solution chemistry control and representative flow conditions, ensuring consistent physiochemical environments for FeS layer development and retention studies.
- Characterization of the morphological and protectiveness properties of mackinawite corrosion product layers formed on 99.9% pure Fe and UNS G10180 using the developed glass cell with impeller flow system.
- Determination of the effects of high flow velocities on the development and protectiveness of mackinawite layers by exposing 99.9% pure Fe and UNS G1080 to 1.1m/s and 10.4m/s flow velocities in the single-phase flow loop (SPFL) setup. The retention of the mackinawite layers formed on UNS G10180 at 1.1m/s was also investigated by subjecting them to a shear stress of 363Pa in the SPFL.
- Evaluation of the mechanical properties of the mackinawite corrosion product layers on both 99.9% pure Fe and UNS G10180 by conducting indentation and adhesive scratch testing.

The results from the above studies were discussed to ascertain if they confirm or refute the hypotheses for the current research.

- 1st Hypothesis: High flow velocities influence the morphology of corrosion product layers in a way that enables higher mass transfer rates thereby promoting higher undermining corrosion rates.

This hypothesis is confirmed especially for a substrate with iron carbide matrix in its microstructure. Studies with UNS G10180 mild steel showed a higher undermining corrosion and the occurrence of localized corrosion in flow conditions where the shear stress is sufficiently high to remove the loosely attached outer corrosion product, thereby forming a less tortuous path for the diffusion of electroactive species. In comparison, with a 99.9% pure Fe substrate, greater mass transfer rates had a lower impact on the undermining corrosion rates suggesting the presence of a more protective FeS layer. Therefore, the undermining corrosion effect of high mass transfer rates on scaling tendency of the mackinawite layers formed in the current study is more pronounced in the presence of iron carbide residues.

- 2nd Hypothesis: The presence of iron carbide in the steel microstructure provides an “anchoring structure” for the formation of FeS precipitates.

The preferential precipitation of FeS layers in the iron carbide corrosion product residues in a low FeS saturation environment (pH 5.00) confirms this hypothesis. However, the iron carbide in the steel microstructure plays no role in the development of mackinawite layers in high FeS saturation conditions (pH 6.00) irrespective of the solution flow velocity.

- 3rd Hypothesis: Iron sulfide layers cannot be damaged by shear stress generated by flow in typical conditions encountered in oil and gas production.

This hypothesis was confirmed by the following findings:

- A shear stress of 363 Pa could not prevent the formation of mackinawite layers on both 99.9% pure Fe and UNS G10180 substrates.
- Mackinawite layers developed at shear stress of 7.2 Pa (low flow conditions) were retained on the surface of UNS G10180 when subjected to a shear stress of 363 Pa. Only the outer “fluffy” FeS layer was removed by this shear stress.
- The shear stress required to remove (adhesive failure) the inner mackinawite layers formed in low flow conditions (1.1m/s) is 1470 MPa while that of layers formed in high flow conditions (10.4m/s) was 500 MPa.

The results from the current research confirmed that shear stress generated by flow in typical oil and gas production conditions is not enough, by itself, to remove or prevent the formation of mackinawite corrosion product layers. However, a major finding from this study is that enhanced mass transfer rates can lead to significant undermining of the layer protectiveness. This seemed especially true in the presence of iron carbide in a ferritic/pearlitic microstructure which favored high undermining corrosion rates, possibly enhanced by the galvanic coupling between the substrate and cementite.

8.2.Future Work

- The current study showed that the presence of iron carbide is a governing factor with respect to the observed morphologies of FeS layers that developed at lower saturation conditions (where Fe₃C is promoted). This was also demonstrated in studies conducted by Zheng et al. Based on these findings, studies on the effect of

high shear stress on the development of iron sulfide layers in conditions that promote the formation of iron carbide layers is recommended.

- The study of the protectiveness of different phases of iron sulfide layers in flowing conditions is recommended for further studies. The effect of mass transfer and shear stress on the protectiveness of high sulfur FeS phases, such as pyrrhotite and pyrite, is achievable in the single-phase flow loop; findings from such studies will be of great interest to oil and gas producers.
- Most mechanical characterization tests in the current study were conducted in conditions where mackinawite layers were at risk of being oxidized. A design of a test system with an inert environment, where the chemical composition of corrosion product layers can be preserved while they undergo mechanical tests is recommended.

REFERENCES

- [1] R. G. Santos, W. Loh, A. C. Bannwart, and O. V. Trevisan, “An overview of heavy oil properties and its recovery and transportation methods,” *Brazilian J. Chem. Eng.*, vol. 31, no. 3, pp. 571–590, 2014.
- [2] “Pipeline Safety Excellence Performance Report & Strategic Plan 2017-2019,” 2017. [Online]. Available: <http://www.aopl.org/wp-content/uploads/2018/08/2017-API-AOPL-Pipeline-Safety-Excellence-Strategic-Plan-Performance-Report.pdf>. [Accessed: 22-Sep-2018]
- [3] “U.S. Liquids Pipeline Usage & Mileage Report,” 2015. [Online]. Available: <http://www.aopl.org/wp-content/uploads/2015/11/AOPL-API-Pipeline-Usage-and-Mileage-Report-2015.pdf>
- [4] M. Bonis, M. Girgis, K. Goerz, and R. Macdonald, “Weight loss corrosion with H₂S: Using past operations for designing future facilities,” in *Corrosion*, no. 6122, San Diego: NACE, 2006.
- [5] P. Wang, J. Wang, S. Zheng, Y. Qi, M. Xiong, and Y. Zheng, “Effect of H₂S/CO₂ partial pressure ratio on the tensile properties of X80 pipeline steel,” *Int. J. Hydrogen Energy*, vol. 40, no. 35, pp. 11925–11930, Sep. 2015.
- [6] G. H. Koch, M. P. Brongers, N. G. Thompson, Y. P. Virmani, and J. H. Payer, “Corrosion cost and preventive strategies in the United States,” 2002. [Online]. Available: <http://impact.nace.org/documents/ccsupp.pdf>
- [7] X. Wen, P. Bai, B. Luo, S. Zheng, and C. Chen, “Review of recent progress in the study of corrosion products of steels in a hydrogen sulphide environment,” *Corros.*

- Sci.*, vol. 139, pp. 124–140, Jul. 2018.
- [8] R. A. King, “Sulfide stress cracking,” *Trends Oil Gas Corros. Res. Technol.*, pp. 271–294, Jan. 2017.
- [9] H. J. Sussmann, “Sulfide Stress Crackin of Pipeline - Case History,” in *Corrosion*, no. 244, New Orleans: NACE, 2008.
- [10] M. Elboujdaini, “Hydrogen-Induced Cracking and Sulfide Stress Cracking,” in *Uhlig’s Corrosion Handbook*, R. Revie, Winston, Ed. 2011, pp. 183–194.
- [11] B. Beidokhti, A. Dolati, and A. H. Koukabi, “Effects of alloying elements and microstructure on the susceptibility of the welded HSLA steel to hydrogen-induced cracking and sulfide stress cracking,” *Mater. Sci. Eng. A*, vol. 507, no. 1–2, pp. 167–173, May 2009.
- [12] T. Chen, Q. Wang, F. Chang, and Y. Al-Janabi, “Iron Sulfide Scale Dissolution at High-Pressure, High Temperature,” in *Saudi Aramco Journal of Technology*, 2016, pp. 47–54.
- [13] H. Ma, X. Cheng, G. Li, S. Chen, Z. Quan, S. Zhao, and L. Niu, “The influence of hydrogen sulfide on corrosion of iron under different conditions,” *Corros. Sci.*, vol. 42, no. 10, pp. 1669–1683, 2000.
- [14] P. V. Scheers, “The effects of flow velocity and pH on the corrosion rate of mild steel in a synthetic minewater,” *J. South. African Inst. Min. Metall.*, vol. 92, no. 10, pp. 275–281, 1992.
- [15] E. Gulbrandsen and A. Grana, “Testing of carbon dioxide corrosion inhibitor performance at high flow velocities in jet impingement geometry. Effects of mass

- transfer and flow forces,” *Corros. Sci.*, vol. 63, no. 11, pp. 1009–1020, 2007.
- [16] M. Eisenberg, C. W. Tobias, and C. R. Wilke, “Ionic mass transfer and concentration polarization at rotating electrodes,” *J. Electrochem. Soc.*, vol. 101, no. 6, pp. 306–320, 1954.
- [17] D. C. Silverman, “Rotating Cylinder Electrode — Geometry Relationships for Prediction of Velocity-Sensitive Corrosion,” *CORROSION*, vol. 44, no. 1, pp. 42–49, Jan. 1988.
- [18] A. G. Wikjord, T. E. Rummery, F. E. Doern, and D. G. Owen, “Corrosion and deposition during the exposure of carbon steel to hydrogen sulphide-water solutions,” *Corros. Sci.*, vol. 20, no. 5, pp. 651–671, 1980.
- [19] Y. Zheng, J. Ning, B. Brown, D. Young, and S. Netic, “Mechanistic study of the effect of iron sulfide layers on hydrogen sulfide corrosion of carbon steel,” in *Corrosion*, no. 5933, Dallas: NACE, 2015, pp. 1–20.
- [20] W. Li, B. F. M. Pots, B. Brown, K. E. Kee, and S. Netic, “A direct measurement of wall shear stress in multiphase flow-Is it an important parameter in CO₂ corrosion of carbon steel pipelines?,” *Corros. Sci.*, vol. 110, pp. 35–45, 2016.
- [21] W. Li, Y. Xiong, B. Brown, K. E. Kee, and S. Netic, “Measurement of Wall Shear Stress in Multiphase Flow and Its Effect on Protective FeCO₃ Corrosion Product Layer Removal,” in *Corrosion*, no. 5922, Dallas: NACE, 2015, pp. 1–15.
- [22] F. Farelas, B. Brown, and S. Netic, “Iron Carbide and its Influence on the Formation of Protective Iron Carbonate in CO₂ Corrosion of Mild Steel,” in *Corrosion*, no. 2291, Orlando: NACE, 2013.

- [23] M. C. Di Bonaventura, "Effect of Flow on the Formation of Iron Carbonate and Influence of Exposed Iron Carbide Layer," Masters Thesis, Chem. Eng. Dept., Ohio University, 2017.
- [24] M. Di Bonaventura, B. Brown, M. Singer, and S. Nesic, "Effect of Flow and Steel Microstructure on the Formation of Iron Carbonate," in *Corrosion*, no. 11179, Phoenix: NACE, 2018.
- [25] P. H. Tewari, G. Wallace, and A. B. Campbell, "The solubility of iron sulfides and their role in mass transport in Girdler-Sulfide heavy water plants," 1978. [Online]. Available: https://inis.iaea.org/search/search.aspx?orig_q=RN:9410578. [Accessed: 19-Sep-2018]
- [26] W. Sun, S. Nesic, and S. Papavinasam, "Kinetics of iron sulfide and mixed iron sulfide/carbonate scale precipitation in CO₂/H₂S corrosion," in *Corrosion*, no. 6644, San Diego: NACE, 2006.
- [27] A. Vairavamurthy and K. Mopper, "Geochemical formation of organosulphur compounds (thiols) by addition of H₂S to sedimentary organic matter," *Nat. Int. J. Sci.*, vol. 329, no. 6140, pp. 623–625, Oct. 1987.
- [28] H. G. Machel, "Bacterial and thermochemical sulfate reduction in diagenetic settings - old and new insights," *Sediment. Geol.*, vol. 140, no. 1–2, pp. 143–175, 2001.
- [29] S. Zheng, C. Li, Y. Qi, L. Chen, and C. Chen, "Mechanism of (Mg, Al, Ca)-oxide inclusion-induced pitting corrosion in 316L stainless steel exposed to sulphur environments containing chloride ion," *Corros. Sci.*, vol. 67, pp. 20–31, Feb. 2013.

- [30] F. Pessu, R. Barker, and A. Neville, "Pitting and Uniform Corrosion of X65 Carbon Steel in Sour Corrosion Environments: The Influence of CO₂, H₂S, and Temperature," *CORROSION*, vol. 73, no. 9, pp. 1168–1183, Sep. 2017.
- [31] D. Rickard and J. W. Morse, "Acid volatile sulfide (AVS)," *Mar. Chem.*, vol. 97, no. 3–4, pp. 141–197, Dec. 2005.
- [32] S. J. Kim, J. H. Park, and K. Y. Kim, "Effect of microstructure on sulfide scale formation and corrosion behavior of pressure vessel steel in sour environment," *Mater. Charact.*, vol. 111, pp. 14–20, Jan. 2016.
- [33] H. Vedage, T. A. Ramanarayanan, J. D. Munford, and S. N. Smith, "Electrochemical growth of iron sulfide films in H₂S-saturated chloride media," *Corrosion*, vol. 49, no. 2, pp. 114–121, 1993.
- [34] R. D. Kane and M. S. Cayard, "Roles of H₂S in the behavior of engineering alloys: a review of literature and experience," *Corrosion*, no. 274, p. 28, 1998.
- [35] S. N. Smith, "Discussion of the History and Relevance of the CO₂/H₂S Ratio," *Nace Corros.*, no. October, p. No.11065, 2011.
- [36] P. Bai, H. Zhao, S. Zheng, and C. Chen, "Initiation and developmental stages of steel corrosion in wet H₂S environments," *Corros. Sci.*, vol. 93, pp. 109–119, 2015.
- [37] P. H. Tewari and A. B. Campbell, "Dissolution of iron during the initial corrosion of carbon steel in aqueous H₂S solutions," *Can. J. Chem.*, vol. 57, no. 2, pp. 188–196, Jan. 1979.
- [38] S. Nesic, Y. Zheng, B. Brown, and J. Ning, "Advancement in Predictive Modeling

- of Mild Steel Corrosion in CO₂ and H₂S Containing Environments,” in *corrosion*, no. 6146, Dallas: NACE, 2015.
- [39] Y. Zheng, “Electrochemical Mechanism and Model of H₂S Corrosion of Carbon Steel,” Ph.D. Dissertation, Chem. Eng. Dept., Ohio University, 2014.
- [40] J. Ning, Y. Zheng, B. Brown, D. Young, and S. Nesic, “Construction and Verification of Pourbaix Diagrams for Hydrogen Sulfide Corrosion of Mild Steel,” in *Corrosion*, no. 5507, Dallas: NACE, 2015.
- [41] H. Wu, L. Liu, L. Wang, and Y. Liu, “Influence of Chromium on Mechanical Properties and CO₂/H₂S Corrosion Behavior of P110 Grade Tube Steel,” *J. Iron Steel Res. Int.*, vol. 21, no. 1, pp. 76–85, Jan. 2014.
- [42] W. Sun, S. Nešić, D. Young, and R. C. Woollam, “Equilibrium Expressions Related to the Solubility of the Sour Corrosion Product Mackinawite,” *Ind. Eng. Chem. Res.*, vol. 47, no. 5, pp. 1738–1742, 2008.
- [43] A. E. Lewis, “Review of metal sulphide precipitation,” *Hydrometallurgy*, vol. 104, no. 2, pp. 222–234, Sep. 2010.
- [44] A. A. Migdisov, A. E. Williams-Jones, L. Z. Lakshantov, and Y. V. Alekhin, “Estimates of the second dissociation constant of H₂S from the surface sulfidation of crystalline sulfur,” *Geochim. Cosmochim. Acta*, vol. 66, no. 10, pp. 1713–1725, May 2002.
- [45] O. M. Suleimenov and R. E. Krupp, “Solubility of hydrogen sulfide in pure water and in NaCl solutions, from 20 to 320°C and at saturation pressures,” *Geochim. Cosmochim. Acta*, vol. 58, no. 11, pp. 2433–2444, Jun. 1994.

- [46] O. M. Suleimenov and T. M. Seward, "A spectrophotometric study of hydrogen sulphide ionisation in aqueous solutions to 350°C," *Geochim. Cosmochim. Acta*, vol. 61, no. 24, pp. 5187–5198, Dec. 1997.
- [47] Y. Kharaka, W. Gunter, and P. Aggarwal, "SOLMINEQ. 88: A computer program for geochemical modeling of water-rock interactions," *Water Resour. Rep.*, p. 408, 1989.
- [48] J. O. Bockris, D. Drazic, and A. R. Despic, "The electrode kinetics of the deposition and dissolution of iron," *Electrochim. Acta*, vol. 4, no. 2–4, pp. 325–361, Aug. 1961.
- [49] H. Ma, X. Cheng, S. Chen, C. Wang, J. Zhang, and H. Yang, "An ac impedance study of the anodic dissolution of iron in sulfuric acid solutions containing hydrogen sulfide," *J. Electroanal. Chem.*, vol. 451, no. 1–2, pp. 11–17, Jul. 1998.
- [50] D. Rickard and G. W. Luther, "Chemistry of iron sulfides," *Chem. Rev.*, vol. 107, no. 2, pp. 514–562, 2007.
- [51] D. E. Jiang and E. A. Carter*, "Adsorption, Diffusion, and Dissociation of H₂S on Fe(100) from First Principles," *J. Phys. Chem. B*, vol. 108, no. 50, pp. 19140–19145, 2004.
- [52] D. E. Jiang and E. A. Carter, "First principles study of H₂S adsorption and dissociation on Fe(1 1 0)," *Surf. Sci.*, vol. 583, no. 1, pp. 60–68, 2005.
- [53] Y. Zheng, B. Brown, and S. Nešić, "Electrochemical Study and Modeling of H₂S Corrosion of Mild Steel," *CORROSION*, vol. 70, no. 4, pp. 351–365, 2013.
- [54] A. Kahyarlian, "Mechanism and Prediction of Mild Steel Corrosion in Aqueous

- Solutions Containing Carboxylic Acids, Carbon Dioxide, and Hydrogen Sulfide,”
Ph.D. Dissertation, Chem. Eng. Dept., Ohio University, 2018.
- [55] W. Sun, “Kinetics of Iron Carbonate and Iron Sulfide Scale Formation In CO₂/H₂S Corrosion,” Ph.D. Dissertation, Chem. Eng. Dept., Ohio University, 2006.
- [56] D. W. Shoesmith, “The Formation of Ferrous Monosulfide Polymorphs during the Corrosion of Iron by Aqueous Hydrogen Sulfide at 21°C,” *J. Electrochem. Soc.*, vol. 127, no. 7, p. 1007, 1980.
- [57] F. H. Meyer, O. L. Riggs, R. L. McGlasson, and J. D. Sudbury, “Corrosion Products of Mild Steel In Hydrogen Sulfide Environments,” *CORROSION*, vol. 14, no. 2, pp. 69–75, Feb. 1958.
- [58] W. Sun and S. Nešić, “A Mechanistic Model of Uniform Hydrogen Sulfide/Carbon Dioxide Corrosion of Mild Steel,” *CORROSION*, vol. 65, no. 5, pp. 291–307, May 2009.
- [59] W. Sun and S. Nešić, “A Mechanistic Model of H₂S Corrosion of Mild Steel,” in *Corrosion*, no. 7655, Nashville: NACE, 2007.
- [60] S. N. Smith, B. N. Brown, and W. Sun, “Corrosion at Higher H₂S Concentrations and Moderate Temperatures,” in *Corrosion*, no. 11081, Houston: NACE, 2011.
- [61] D. Rickard, “Kinetics of fast precipitation reactions involving metal sulfides,” *Chem. Geol.*, vol. 70, no. 1–2, p. 81, Aug. 1988.
- [62] D. Rickard, “An apparatus for the study of fast precipitation reactions,” *Mineral. Mag.*, vol. 53, no. 737, pp. 527–530, 1989.
- [63] D. Rickard, “Experimental concentration-time curves for the iron(II) sulphide

- precipitation process in aqueous solutions and their interpretation*," *Chem. Geol.*, vol. 78, pp. 315–324, 1989.
- [64] E. W. van Hunnik, B. F. M. Pots, and E. L. J. A. Hendriksen, "The Formation of Protective FeCO₃ Corrosion Product Layers in CO₂ Corrosion," in *Corrosion*, no. 6, Denver: NACE, 1996.
- [65] K. Lee, "A mechanistic modeling of CO₂ corrosion of mild steel in the presence of H₂S," Ph.D. Dissertation, Chem. Eng. Dept., Ohio University, 2004.
- [66] Z. Ma, Y. Yang, B. Brown, S. Nescic, and M. Singer, "Investigation of FeCO₃ and FeS Precipitation Kinetics by EQCM," in *Corrosion*, no. 11192, Phoenix: NACE, 2018.
- [67] N. G. Harmandas and P. G. Koutsoukos, "The formation of iron(II) sulfides in aqueous solutions," *J. Cryst. Growth*, vol. 167, no. 3–4, pp. 719–724, Oct. 1996.
- [68] L. G. Benning, R. T. Wilkin, and H. L. Barnes, "Reaction pathways in the Fe–S system below 1008C," *Chem. Geol.*, vol. 167, pp. 25–51, 2000.
- [69] M. Liu, J. Wang, W. Ke, and E.-H. Han, "Corrosion Behavior of X52 Anti-H₂S Pipeline Steel Exposed to High H₂S Concentration Solutions at 90 °C," *J. Mater. Sci. Technol.*, vol. 30, no. 5, pp. 504–510, May 2014.
- [70] J. Ning, Y. Zheng, D. Young, B. Brown, and S. Nešić, "A Thermodynamic Study of Hydrogen Sulfide Corrosion of Mild Steel," in *Corrosion*, no. 2462, Orlando: NACE, 2013.
- [71] A. R. Lennie, K. E. R. England, and D. J. Vaughan, "Transformation of synthetic mackinawite to hexagonal pyrrhotite: a kinetic study," *Am. Mineral.*, vol. 80, no.

- 1992, pp. 960–967, 1995.
- [72] J. Ning, Y. Zheng, B. Brown, D. Young, and S. Nešić, “The Role of Iron Sulfide Polymorphism in Localized H₂S Corrosion of Mild Steel,” *CORROSION*, vol. 73, no. 2, pp. 155–168, Feb. 2017.
- [73] S. N. Smith, “A Proposed Mechanism for Corrosion in Slightly Sour Oil and Gas Production,” *Int. Corros. Congr.*, vol. 1304, 1993.
- [74] J. B. Sardisco and R. E. Pitts, “Corrosion of Iron in an H₂S-CO₂-H₂O System Composition and Protectiveness of the Sulfide Film as a Function off pH,” *CORROSION*, vol. 21, no. 11, pp. 350–354, Nov. 1965.
- [75] C. Ren, D. Liu, Z. Bai, and T. Li, “Corrosion behavior of oil tube steel in simulant solution with hydrogen sulfide and carbon dioxide,” *Mater. Chem. Phys.*, vol. 93, no. 2–3, pp. 305–309, Oct. 2005.
- [76] S. Gao, P. Jin, B. Brown, D. Young, S. Nešić, and M. Singer, “Effect of High Temperature on the Aqueous H₂S Corrosion of Mild Steel,” *CORROSION*, vol. 73, no. 10, pp. 1188–1191, Oct. 2017.
- [77] E. C. Dos Santos, M. P. Lourenço, L. G. M. Pettersson, and H. A. Duarte, “Stability, Structure, and Electronic Properties of the Pyrite/Arsenopyrite Solid–Solid Interface—A DFT Study,” *J. Phys. Chem. C*, vol. 121, no. 14, pp. 8042–8051, Apr. 2017.
- [78] C. I. Pearce, R. A. D. Patrick, and D. J. Vaughan, “Electrical and Magnetic Properties of Sulfides,” *Rev. Mineral. Geochemistry*, vol. 61, no. 1, pp. 127–180, Jan. 2006.

- [79] R. Schieck, A. Hartmann, S. Fiechter, R. Könenkamp, and H. Wetzel, “Electrical properties of natural and synthetic pyrite (FeS₂) crystals,” *J. Mater. Res.*, vol. 5, no. 7, pp. 1567–1572, Jul. 1990.
- [80] M. Cabán-Acevedo, M. S. Faber, Y. Tan, R. J. Hamers, and S. Jin, “Synthesis and Properties of Semiconducting Iron Pyrite (FeS₂) Nanowires,” *Nano Lett.*, vol. 12, no. 4, pp. 1977–1982, Apr. 2012.
- [81] J. Ning, Y. Zheng, B. Brown, D. Young, and S. Nesic, “The Role of Pyrite in Localized H₂S Corrosion of Mild Steel,” in *Corrosion*, no. 9251, Phoenix: NACE, 2017.
- [82] D. Csákberényi-Malasics, J. D. Rodriguez-Blanco, V. K. Kis, A. Rečnik, L. G. Benning, and M. Pósfai, “Structural properties and transformations of precipitated FeS,” *Chem. Geol.*, vol. 294–295, pp. 249–258, Feb. 2012.
- [83] S. N. Smith and M. Joosten, “Corrosion of Carbon Steel by H₂S in CO₂ Containing Oilfield Environments-10 Year Update,” in *Conference*, no. 5484, Dallas: NACE, 2015.
- [84] S. Zheng, C. Li, and C. Chen, “Effect of Temperature on the Corrosion Behaviours of L360QCS in the Environments Containing Elemental Sulphur and H₂S/CO₂,” *Metallofiz. i novejšie tekhnologii*, vol. 34, pp. 57–63, 2012.
- [85] H. Y. Jeong, J. H. Lee, and K. F. Hayes, “Characterization of synthetic nanocrystalline mackinawite: Crystal structure, particle size, and specific surface area,” *Geochim. Cosmochim. Acta*, vol. 72, no. 2, pp. 493–505, Jan. 2008.
- [86] H. Ohfuji and D. Rickard, “High resolution transmission electron microscopic

- study of synthetic nanocrystalline mackinawite,” *Earth Planet. Sci. Lett.*, vol. 241, no. 1–2, pp. 227–233, Jan. 2006.
- [87] S. Boursiquot, M. Mullet, M. Abdelmoula, J.-M. Génin, and J.-J. Ehrhardt, “The dry oxidation of tetragonal FeS 1- x mackinawite,” *Phys. Chem. Miner.*, vol. 28, no. 9, pp. 600–611, Oct. 2001.
- [88] D. Rickard, A. Griffith, A. Oldroyd, I. B. Butler, E. Lopez-Capel, D. A. C. Manning, and D. C. Apperley, “The composition of nanoparticulate mackinawite, tetragonal iron(II) monosulfide,” *Chem. Geol.*, vol. 235, no. 3–4, pp. 286–298, Dec. 2006.
- [89] D. A. Lopez, T. Perez, and S. N. Simison, “The influence of microstructure and chemical composition of carbon and low alloy steels in CO₂ corrosion. A state-of-the-art appraisal,” *Mater. Des.*, vol. 24, no. 8, pp. 561–575, 2003.
- [90] B. L. Bramfitt and B. S. Corporation, “Structure / Property Relationships in Irons and Steels,” in *Metals Handbook Desk Edition, Second Edition*, 2nd ed., J. R. Davis, Ed. ASTM International, 1998, pp. 153–173.
- [91] M. Bonis, “Weight Loss Corrosion With H₂S: From Facts To Leading Parameters And Mechanisms,” *Corros. 2009*, 2009.
- [92] V. G. Levich and C. W. Tobias, “Physicochemical Hydrodynamics,” *J. Electrochem. Soc.*, vol. 110, no. 11, p. 251C, Nov. 1963.
- [93] J. Genesca and B. Galicia, “Effect of Flow On the Corrosion Behavior of Carbon Steel In CO₂/H₂S Containing Solutions,” in *Corrosion*, no. 1213, Salt Lake: NACE, 2012.

- [94] R. Galvan-Martinez, J. Mendoza-Flores, R. Duran-Romero, and J. Genesca-Llongueras, "Effects of turbulent flow on the corrosion kinetics of X52 pipeline steel in aqueous solutions containing H₂S," *Mater. Corros.*, vol. 55, no. 8, pp. 586–593, Aug. 2004.
- [95] J. G. Llongueras, R. G.- Martinez, J. Mendoza-, and R. Duran-Romero, "Effects of Turbulent Flow on the Corrosion Kinetics of X52 Pipeline Steel in Aqueous Solutions Containing H₂S," in *Corrosion*, no. 3641, San diego: NACE, 2003.
- [96] D. C. Silverman, "**Technical Note:** On Estimating Conditions for Simulating Velocity-Sensitive Corrosion in the Rotating Cylinder Electrode," *CORROSION*, vol. 55, no. 12, pp. 1115–1118, Dec. 1999.
- [97] S. Arzola-Peralta, J. Mendoza-Flores, R. Duran-Romero, and J. Genesca, "Cathodic kinetics of API X70 pipeline steel corrosion in H₂S containing solutions under turbulent flow conditions," *Corros. Eng. Sci. Technol.*, vol. 41, no. 4, pp. 321–327, 2006.
- [98] N. Zhang, D. Zeng, Z. Zhang, W. Zhao, and G. Yao, "Effect of flow velocity on pipeline steel corrosion behaviour in H₂S/CO₂ environment with sulphur deposition," *Corros. Eng. Sci. Technol.*, vol. 53, no. 5, pp. 370–377, Jul. 2018.
- [99] I. H. Omar, Y. M. Gunaltun, J. Kvarekval, and A. Dugstad, "H₂S corrosion of carbon steel under simulated kashagan field conditions," in *Corrosion*, no. 5300, Houston: NACE, 2005.
- [100] S. Nešić, G. T. Solvi, and J. Enerhaug, "Comparison of the Rotating Cylinder and Pipe Flow Tests for Flow-Sensitive Carbon Dioxide Corrosion," *CORROSION*,

- vol. 51, no. 10, pp. 773–787, Oct. 1995.
- [101] B. Brown, K.-L. Lee, and S. Nestic, “Corrosion in Multiphase Flow Containing Small Amounts of H₂S,” in *Corrosion*, no. 3341, San Diego: NACE, 2003.
- [102] W. H. Ahmed, M. M. Bello, M. El Nakla, A. Al Sarkhi, and H. M. Badr, “Experimental investigation of flow accelerated corrosion under two-phase flow conditions,” *Nucl. Eng. Des.*, vol. 267, pp. 34–43, Feb. 2014.
- [103] B. Brown and A. Schubert, “The Design and Development of A Large-scale, Multiphase Flow Loop for The Study of Corrosion in Sour Gas Environment,” in *Corrosion*, no. 2502, Denver: NACE, 2002.
- [104] W. Sun, C. Li, S. Ling, R. V. Reddy, J. L. Pacheco, M. Asmann, G. Wilken, and R. J. Franco, “Laboratory Study of Sour Localized / Pitting Corrosion,” in *Corrosion*, no. 11080, Houston: NACE, 2011.
- [105] E. Heitz, “Chemo-mechanical effects of flow on corrosion,” *Corrosion*, vol. 47, no. 2, pp. 135–145, 1991.
- [106] D. R. Morris, L. P. Sampaleanu, and D. N. Veysey, “The corrosion of steel by aqueous solutions of hydrogen sulfide,” *J. Electrochem. Soc.*, vol. 127, no. 6, pp. 1228–1235, 1980.
- [107] S. Ieamsupapong, “Mechanisms of Iron Carbonate Formation on Mild Steel in Controlled Water Chemistry Conditionse,” Ph.D. Dissertation, Chem. Eng. Dept., Ohio University, Athens, OH, 2016.
- [108] F. R. Menter, M. Kuntz, and R. Langtry, “Ten Years of Industrial Experience with the SST Turbulence Model,” *Turbul. Heat Mass Transf. 4*, vol. 4, pp. 625–632,

2003.

- [109] S. Nešić and K.-L. J. Lee, “A Mechanistic Model for Carbon Dioxide Corrosion of Mild Steel in the Presence of Protective Iron Carbonate Films—Part 3: Film Growth Model,” *CORROSION*, vol. 59, no. 7, pp. 616–628, 2003.
- [110] “Standard Practice for Laboratory Immersion Corrosion Testing of Metals,” *ASTM G 31 -72*, 1999.
- [111] J. Banaś, U. Lelek-Borkowska, B. Mazurkiewicz, and W. Solarski, “Effect of CO₂ and H₂S on the composition and stability of passive film on iron alloys in geothermal water,” *Electrochim. Acta*, vol. 52, no. 18, pp. 5704–5714, May 2007.
- [112] K. D. Efirid, E. J. Wright, J. A. Boros, and T. G. Hailey, “Correlation of Steel Corrosion in Pipe Flow with Jet Impingement and Rotating Cylinder Tests,” *CORROSION*, vol. 49, no. 12, pp. 992–1003, Dec. 1993.
- [113] S. Nestic, G. T. Solvi, and J. Enerhaug, “Comparison of the rotating cylinder and pipe flow tests for flow-sensitive carbon dioxide corrosion,” *Corrosion*, vol. 51, no. 10, pp. 773–787, 1995.
- [114] X. Zhong, B. Brown, W. Li, S. Nestic, and M. Singer, “How to Maintain a Stable Solution Chemistry when Simulating CO₂ Corrosion in a Small Volume Laboratory System,” in *Corrosion*, no. 7780, Vancouver: NACE, 2016.
- [115] F. P. Berger and K.-F.-L. Hau, “Mass transfer in turbulent pipe flow measured by the electrochemical method,” *Int. J. Heat Mass Transf.*, vol. 20, no. 11, pp. 1185–1194, 1977.
- [116] S. Nestic, J. Postlethwaite, and S. Olsen, “An Electrochemical Model for Prediction

- of Corrosion of Mild Steel in Aqueous Carbon Dioxide Solutions,” *CORROSION*, vol. 52, no. 4, pp. 280–294, Apr. 1996.
- [117] F. G. Schmitt, “About Boussinesq’s turbulent viscosity hypothesis: historical remarks and a direct evaluation of its validity,” *Comptes Rendus Mécanique*, vol. 335, no. 9–10, pp. 617–627, Sep. 2007.
- [118] H. Singh, D. F. Fletcher, and J. J. Nijdam, “An assessment of different turbulence models for predicting flow in a baffled tank stirred with a Rushton turbine,” *Chem. Eng. Sci.*, vol. 66, no. 23, pp. 5976–5988, Dec. 2011.
- [119] M. Jenne and M. Reuss, “A critical assessment on the use of k - ϵ turbulence models for simulation of the turbulent liquid flow induced by a Rushton-turbine in baffled stirred-tank reactors,” *Chem. Eng. Sci.*, vol. 54, no. 17, pp. 3921–3941, Sep. 1999.
- [120] A. Brucato, M. Ciofalo, F. Grisafi, and G. Micale, “Numerical prediction of flow fields in baffled stirred vessels: A comparison of alternative modelling approaches,” *Chem. Eng. Sci.*, vol. 53, no. 21, pp. 3653–3684, Nov. 1998.
- [121] Z. Jaworski and B. Zakrzewska, “Modelling of the Turbulent Wall Jet Generated by a Pitched Blade Turbine Impeller: The Effect of Turbulence Model,” *Chem. Eng. Res. Des.*, vol. 80, no. 8, pp. 846–854, Nov. 2002.
- [122] Nandkishor K. Nere, A. Ashwin W. Patwardhan, and J. B. Joshi*, “Liquid-Phase Mixing in Stirred Vessels: Turbulent Flow Regime,” *Ind. Eng. Chem. Res.*, vol. 42, pp. 2661–2698, 2003.
- [123] J. Aubin, D. . Fletcher, and C. Xuereb, “Modeling turbulent flow in stirred tanks

- with CFD: the influence of the modeling approach, turbulence model and numerical scheme,” *Exp. Therm. Fluid Sci.*, vol. 28, no. 5, pp. 431–445, Apr. 2004.
- [124] G. A. Zhang, Y. Zeng, X. P. Guo, F. Jiang, D. Y. Shi, and Z. Y. Chen, “Electrochemical corrosion behavior of carbon steel under dynamic high pressure H₂S/CO₂ environment,” *Corros. Sci.*, vol. 65, pp. 37–47, Dec. 2012.
- [125] W. Rodi, “Experience with two-layer models combining the k-epsilon model with a one-equation model near the wall,” in *29th Aerospace Sciences Meeting*, 1991.
- [126] F. R. Menter, “Improved two-equation k-omega turbulence models for aerodynamic flows,” in *NASA Technical Memorandum*, NASA, 1992, pp. 1–31.
- [127] F. R. Menter, “Two-equation eddy-viscosity turbulence models for engineering applications,” *AIAA J.*, vol. 32, no. 8, pp. 1598–1605, Aug. 1994.
- [128] P. A. C. Rocha, H. H. Barbosa Rocha, F. O. Moura Carneiro, M. E. Vieira Da Silva, and A. V. Bueno, “k- ω SST (shear stress transport) turbulence model calibration: A case study on a small scale horizontal axis wind turbine,” *Energy*, vol. 65, pp. 412–418, 2014.
- [129] Z. Chara, B. Kysela, J. Konfrst, and I. Fort, “Study of fluid flow in baffled vessels stirred by a Rushton standard impeller,” *Appl. Math. Comput.*, vol. 272, pp. 614–628, Jan. 2016.
- [130] R. Alcamo, G. Micale, F. Grisafi, A. Brucato, and M. Ciofalo, “Large-eddy simulation of turbulent flow in an unbaffled stirred tank driven by a Rushton turbine,” *Chem. Eng. Sci.*, vol. 60, no. 8–9, pp. 2303–2316, Apr. 2005.
- [131] F. Farelas, M. Singer, D. Nugraha, S. Whitehurst, and B. Kinsella, “Localized

- Corrosion in the Presence of Corrosion Inhibitors at High Flow Velocities in CO₂ Environments,” in *Corrosion*, no. 11269, Phoenix: NACE, 2018.
- [132] W. Li, “Mechanical Effects of Flow on CO₂ Corrosion Inhibition of Carbon Steel Pipelines,” Ph.D. Dissertation, Chem. Eng. Dept., Ohio University, 2016.
- [133] M. S. Isaacson and A. A. Sonin, “Sherwood Number and Friction Factor Correlations for Electrodialysis Systems, with Application to Process Optimization,” *Ind. Eng. Chem. Res.*, vol. 15, no. 2, pp. 313–321, 1976.
- [134] A. P. Colburn, “A method of correlating forced convection heat-transfer data and a comparison with fluid friction,” *Trans. Am. Inst. Chem. Eng.*, vol. 29, pp. 174–210, 1933.
- [135] R. F. Probstein, A. A. Sonin, and E. Gur-Arie, “A turbulent flow theory of electro dialysis,” *Desalination*, vol. 11, no. 2, pp. 165–187, Oct. 1972.
- [136] S. Aravinth, “Prediction of heat and mass transfer for fully developed turbulent fluid flow through tubes,” *Int. J. Heat Mass Transf.*, vol. 43, pp. 1399–1408, 2000.
- [137] E. Rieschel, “A Study on the Flow of Viscous Fluids in a Square Duct,” 2016.
- [138] F. D. Young, R. B. Munson, and H. T. Okiishi, “Viscous Flow in Pipes,” in *A Brief Introduction to Fluid Mechanics*, Canada: John Wiley & Sons, Inc., 1996, pp. 323–375.
- [139] V. C. Patel, “Some Observations on Skin Friction and Velocity Profiles in Fully Developed Pipe and Channel Flows,” *J. Fluid Mech.*, vol. 38, pp. 181–201, 1969.
- [140] R. B. Dean, “Reynolds Number Dependence of Skin Friction and Other Bulk Flow Variables in Two-Dimensional Rectangular Duct Flow,” *J. Fluids Eng.*, vol. 100,

no. 2, p. 215, Jun. 1978.

- [141] H.-H. Huang, W.-T. Tsai, and J.-T. Lee, "Electrochemical behavior of the simulated heat-affected zone of A516 carbon steel in H₂S solution," *Electrochim. Acta*, vol. 41, no. 7–8, pp. 1191–1199, May 1996.
- [142] R. Revie, R. Winston, and H. H. Uhlig, *Corrosion and corrosion control : an introduction to corrosion science and engineering*, 4th ed. Canada: A John Wiley & Sons, Inc., Publication, 2008.
- [143] A. M. Zimer, E. C. Rios, P. de C. D. Mendes, W. N. Gonçalves, O. M. Bruno, E. C. Pereira, and L. H. Mascaro, "Investigation of AISI 1040 steel corrosion in H₂S solution containing chloride ions by digital image processing coupled with electrochemical techniques," *Corros. Sci.*, vol. 53, no. 10, pp. 3193–3201, Oct. 2011.
- [144] S. G. Clarke, "The Use of Inhibitors (with Special Reference to Antimony) in the Selective Removal of Metallic Coatings and Rust," *Trans. Electrochem. Soc.*, vol. 69, no. 1, p. 131, Jan. 1936.
- [145] J. Han, S. Nešić, Y. Yang, and B. N. Brown, "Spontaneous passivation observations during scale formation on mild steel in CO₂ brines," *Electrochim. Acta*, vol. 56, no. 15, pp. 5396–5404, Jun. 2011.
- [146] W. Li, B. Brown, D. Young, and S. Nešić, "Investigation of Pseudo-Passivation of Mild Steel in CO₂ Corrosion," *CORROSION*, vol. 70, no. 3, pp. 294–302, Mar. 2014.
- [147] Y. Yang, B. Brown, S. Nešić, M. E. Gennaro, and B. Molinas, "Mechanical

- strength and removal of a protective iron carbonate layer formed on mild steel in CO₂ corrosion,” in *Corrosion*, no. 10383, San Antonio: NACE, 2010.
- [148] M. F. Doerner and W. D. Nix, “A method for interpreting the data from depth-sensing indentation instruments,” *J. Mater. Res.*, vol. 1, no. 4, pp. 601–609, Aug. 1986.
- [149] W. C. Oliver and G. M. Pharr, “An improved technique for determining hardness and elastic modulus using load and displacement sensing indentation experiments,” *J. Mater. Res.*, vol. 7, no. 6, pp. 1564–1583, Jun. 1992.
- [150] A. J. Perry, “The adhesion of chemically vapour-deposited hard coatings to steel—the scratch test,” *Thin Solid Films*, vol. 78, no. 1, pp. 77–94, Mar. 1981.
- [151] P. A. Steinmann and H. E. Hintermann, “Adhesion of TiC and Ti(C,N) coatings on steel,” *J. Vac. Sci. Technol. A Vacuum, Surfaces, Film.*, vol. 3, no. 6, pp. 2394–2400, Nov. 1985.
- [152] J. Valli, “A review of adhesion test methods for thin hard coatings,” *J. Vac. Sci. Technol. A Vacuum, Surfaces, Film.*, vol. 4, no. 6, pp. 3007–3014, Nov. 1986.
- [153] H. E. Hintermann, “Adhesion, friction and wear of thin hard coatings,” *Wear*, vol. 100, no. 1–3, pp. 381–397, Dec. 1984.
- [154] A. J. Perry, “Scratch adhesion testing of hard coatings,” *Thin Solid Films*, vol. 107, no. 2, pp. 167–180, Sep. 1983.
- [155] S. Bull and D. Rickerby, “New developments in the modelling of the hardness and scratch adhesion of thin films,” *Surf. Coatings Technol.*, vol. 42, no. 2, pp. 149–164, Nov. 1990.

- [156] S. J. Bull and E. G.-Berasetegui, “An overview of the potential of quantitative coating adhesion measurement by scratch testing,” *Tribol. Interface Eng. Ser.*, vol. 51, pp. 136–165, 2006.
- [157] P. J. Burnett and D. S. Rickerby, “The relationship between hardness and scratch adhesion,” *Thin Solid Films*, vol. 154, no. 1–2, pp. 403–416, Nov. 1987.
- [158] S. J. Bull, “Failure modes in scratch adhesion testing,” *Surf. Coatings Technol.*, vol. 50, no. 1, pp. 25–32, Jan. 1991.
- [159] C1624-05, “Standard test method for adhesion strength and mechanical failure modes of ceramic coatings by quantitative single point scratch testing,” *ASTM Int.*, no. Reapproved 2010, pp. 1–29, 2012.
- [160] P. Benjamin and C. Weaver, “Measurement of Adhesion of Thin Films,” *Proc. R. Soc. A Math. Phys. Eng. Sci.*, vol. 254, no. 1277, pp. 163–176, Feb. 1960.
- [161] C. Weaver, “Adhesion of thin films,” *J. Vac. Sci. Technol.*, vol. 12, no. 1, pp. 18–25, Jan. 1975.
- [162] B. Ollivier and A. Matthews, “Adhesion of diamond-like carbon films on polymers: an assessment of the validity of the scratch test technique applied to flexible substrates,” *J. Adhes. Sci. Technol.*, vol. 8, no. 6, pp. 651–662, Jan. 1994.
- [163] “Mechanical Tester For Mechanical Properties Testing.” [Online]. Available: <https://nanovea.com/mechanical-testers/>. [Accessed: 16-Jul-2018]
- [164] N. A. Sakharova, J. V. Fernandes, J. M. Antunes, and M. C. Oliveira, “Comparison between Berkovich, Vickers and conical indentation tests: A three-dimensional numerical simulation study,” *Int. J. Solids Struct.*, vol. 46, no. 5, pp.

1095–1104, Mar. 2009.

- [165] W. H. Jiang and R. Kovacevic, “Feasibility study of friction stir welding of 6061-T6 aluminium alloy with AISI 1018 steel,” *Proc. Inst. Mech. Eng. Part B J. Eng. Manuf.*, vol. 218, no. 10, pp. 1323–1331, 2004.
- [166] I. Konyashin, B. Ries, D. Hlawatschek, Y. Zhuk, A. Mazilkin, B. Straumal, F. Dorn, and D. Park, “Wear-resistance and hardness: Are they directly related for nanostructured hard materials?,” *Int. J. Refract. Met. Hard Mater.*, vol. 49, pp. 203–211, Mar. 2015.
- [167] M. A. Moore, “The relationship between the abrasive wear resistance, hardness and microstructure of ferritic materials,” *Wear*, vol. 28, no. 1, pp. 59–68, Apr. 1974.

APPENDIX A: DEVELOPMENT OF IRON SULFIDE LAYER IN A 2-LITER GLASS CELL WITHOUT SOLUTION CHEMISTRY CONTROL

The goal of this preliminary set of experiments was to develop an iron sulfide layer in conditions where the chemistry of the solution is not controlled in order to identify the extent of solution pH and Fe^{2+} concentration changes with respect to exposure time.

Equipment

The experiment was conducted in a two-liter glass cell as shown in Figure 140. The H_2S gas outlet is connected to a scrubber before being released to the atmosphere. In carrying out this experiment, five specimens made out of API 5L X65 carbon steel were used; four square specimens and one cylindrical specimen. The square specimens, which were suspended in the solution with a string, were used for mass loss measurements and surface analysis, while the cylindrical specimen was used for the electrochemical measurements (LPR and EIS). A three-electrode system was used for the electrochemical measurements with an Ag/AgCl electrode used as the reference electrode, a platinized niobium gauze used as the counter, and the electrochemical specimen used as the working electrode.

Test Conditions

The test conditions for the current experiment are shown in Table XX

Table XX: Test conditions for the glass cell experiment

Operating Parameter	Specification	Notes
Material	API 5L X65	
H ₂ S Partial Pressure	1 mbar (1000 ppm)	
Total Pressure	1.01 bar	
Electrolyte	1 wt. % NaCl	
Initial Solution pH	6.00	
Temperature	30°C	
Stirring Rate	200 rpm	
Measurement Method	LPR	Scan rate: 0.125mV/s±5mV vs. OCP
	EIS	Frequency: 0.2 Hz – 5000 Hz AC voltage: 5mV

Corrosion rate measurements were taken using both electrochemical and weight loss methods. For the electrochemical methods, both linear polarization resistance and electrochemical impedance spectroscopic measurements were made to obtain the corrosion rate of the API 5L X65 test specimens. The scan rate of these electrochemical measurements is specified in Table XX. The solution resistance obtained from the EIS measurement was subtracted from the resistance obtained by LPR (which is a combination of polarization and solution resistance). Specimens were extracted for further examination of the corrosion product layer. The surface analyses conducted on the specimen after testing were achieved using scanning electron microscopy (SEM), energy dispersive X-ray spectroscopy (EDX) and X-ray diffraction (XRD).

Procedure

The 1 wt. % NaCl electrolyte was prepared by adding 20.2g of NaCl in 2L of deionized water and deoxygenated by purging with N₂ for two hours. H₂S was introduced into the inlet gas stream to achieve a H₂S/nitrogen gas mixture with an H₂S/N₂ partial pressure of 1mbar. The solution was purged with this stream for an additional 30 minutes while stirring the solution with a stir bar at 200 rpm. The solution temperature was maintained at 30°C and pH was adjusted to 6.00 with deoxygenated 1M NaOH solution. The rotating cylinder electrode (RCE) specimen and the weight loss sample were polished using silicon carbide abrasive papers in the order 150 grit, 400 grit and 600 grit. While polishing, specimens were rinsed with isopropanol to remove metal particles debris and to prevent them from heating up. The dimensions of the specimen were measured. The samples were cleaned by putting them in a beaker with isopropanol and placed in an ultrasonicator for 5 minutes. The mass of the specimens was taken and recorded. The RCE specimen was installed on the rotator shaft and introduced into the glass cell. Mass loss specimens were introduced into the solution with the aid of a nylon string fastening. The corrosion rate trends of the RCE specimen was monitored by LPR after a stable OCP of $\pm 5\text{mV}$ was achieved (which is usually after the first hour of immersion). The solution resistance was measured using EIS and compensated for in the polarization obtained from LPR. At the end of the test, the RCE specimen was removed and rinsed with N₂ purged deionized (DI) water and then isopropanol and was afterwards dried in a stream of N₂ gas. The same sample extraction process was carried out for the

weight loss specimens and all the post-test analyses of the layer were conducted immediately after their extraction.

Results and Discussion

The corrosion rates from LPR and open circuit potential data obtained with repeat experiments are shown in Figure 141 and Figure 142, respectively. The corrosion rates obtained from weight loss for both experiments were also overlaid with the corrosion rate obtained from the LPR measurements. There were differences in the initial corrosion rate measured in the two experiments. This can be attributed to the possible slight differences in the sample preparation. The measured open circuit potential when compared with that obtained from Zheng's model[38,39] had a good agreement, as shown in Figure 142.

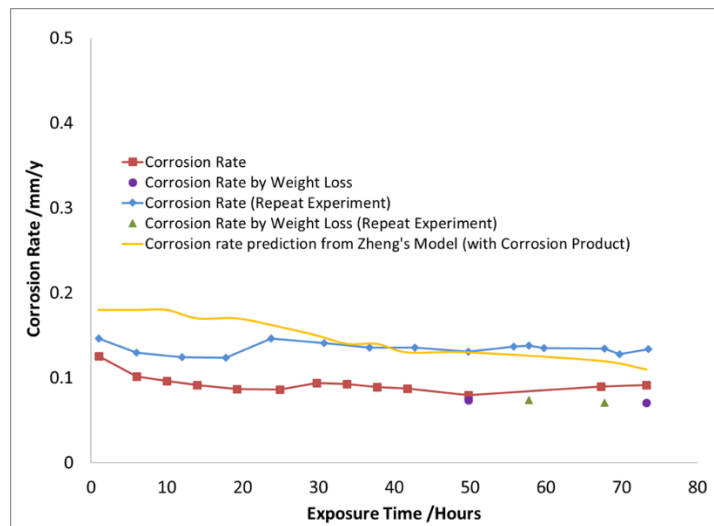


Figure 141: Corrosion rate measurement (from LPR and weight loss) of X-65 carbon steel sample in 1 wt. % NaCl solution, pH 6.00, 30°C and 0.1mbar of H₂S compared with predicted corrosion rate values from Zheng's model.

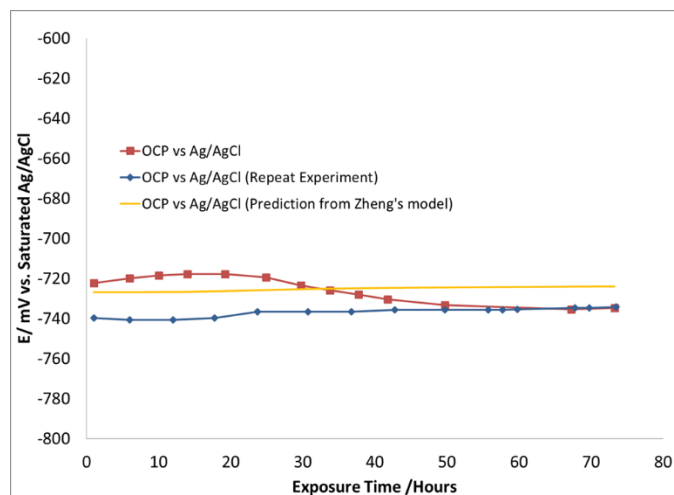


Figure 142: Open circuit potential measurement of X-65 carbon steel sample in 1 wt. % NaCl solution, pH 6.00, 30°C and 0.1mbar of H₂S compared with predicted corrosion rate values Zheng's model.

The solution pH and the saturation values of iron sulfide in solution are shown in Figure 143 and Figure 144, respectively. The solution pH went up to 6.7 in the first 20 hours of the experiment due to the initial high corrosion rate and the consequent release of ferrous ions into solution. The formation of a protective iron sulfide layer is expected due to the high initial iron sulfide saturation value in the bulk solution. At the end of the experiments a reduced supersaturation value was measured due to lower corrosion rates and continuous precipitation of FeS on the specimen surface.

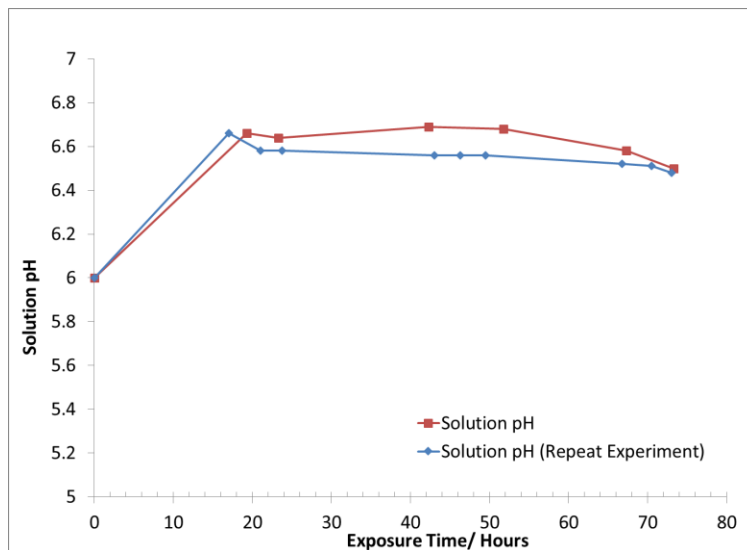


Figure 143: Solution pH measurements for experiment conducted at 30°C, $p_{H_2S} = 1 \text{ mbar}$, $[\text{Fe}^{2+}] = 0$ and initial solution pH = 6.00

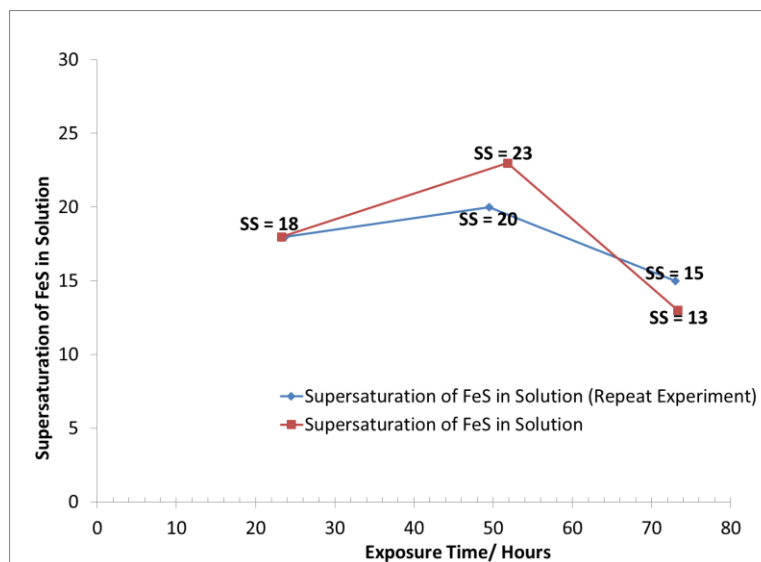


Figure 144: Supersaturation (SS) of FeS in solution for experiment conducted at 30°C, $p_{H_2S} = 1 \text{ mbar}$, $[\text{Fe}^{2+}] = 0$ and initial solution pH= 6.00

The surface morphologies of the sample surfaces from both experiments (Figure 145 and Figure 146) were similar and revealed the formation of more corrosion products on the metal surface with time.

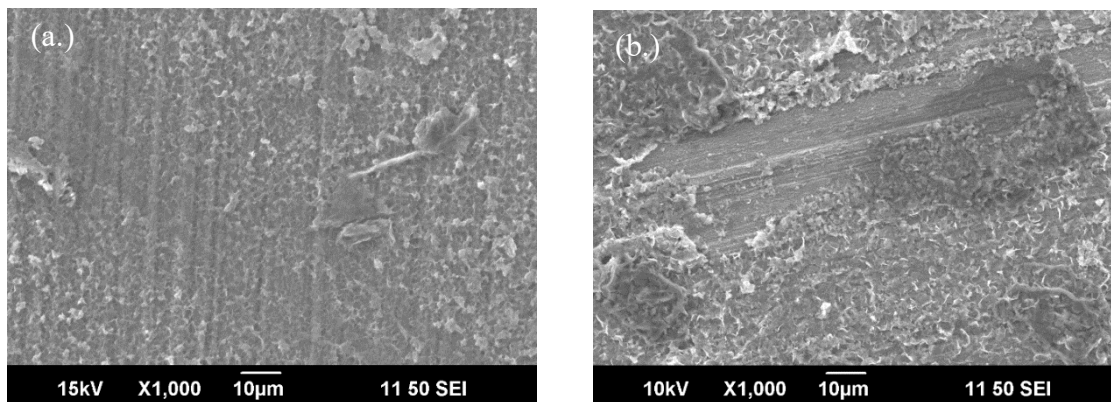


Figure 145: Surface morphology of iron sulfide layers after 2 days exposure in solution at 30°C, 1mbar H₂S, pH 6.00 (a) Test 1 (b) Repeat experiment

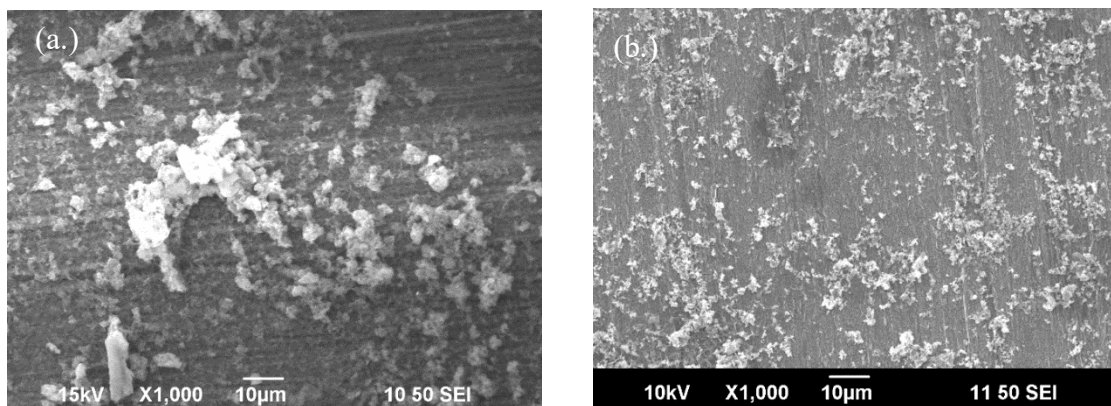


Figure 146: Surface morphology of iron sulfide layers after 3 days exposure in solution at 30°C, 1mbar H₂S, pH 6.00 (a) Test 1 (b) Repeat experiment

The cross-sectional analysis also showed corrosion product with an average thickness of 1.88µm on the second day Figure 147 and 2.84µm on the third day Figure 148.

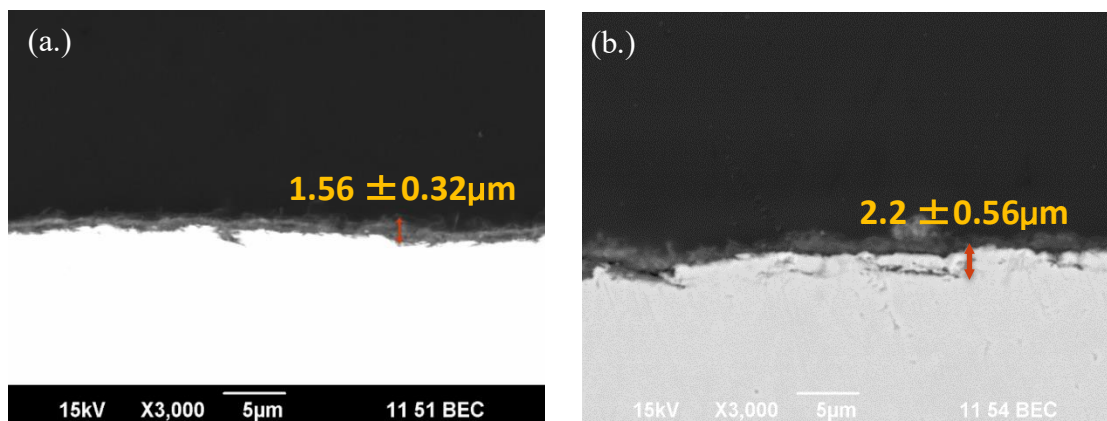


Figure 147: Cross section of iron sulfide layers after 2 days exposure in solution at 30°C, 1mbar H₂S (a) Test 1 (b) Repeat experiment

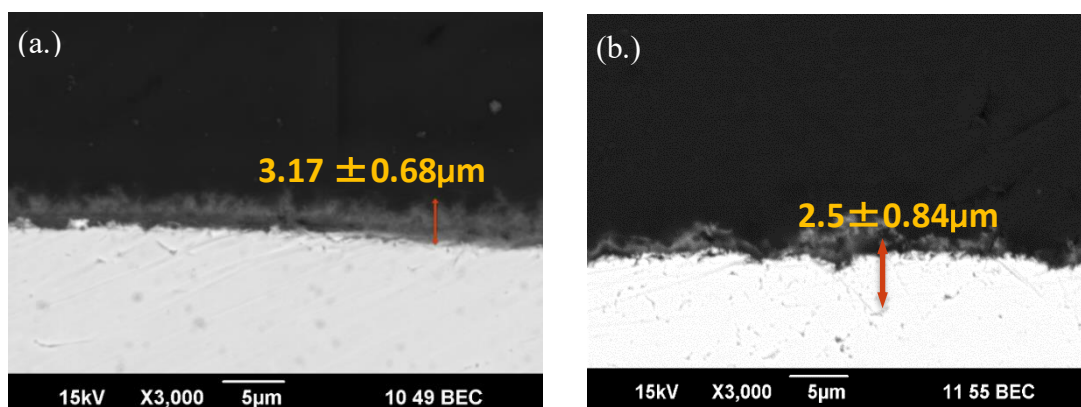


Figure 148: Cross section of iron sulfide layers after 3 days exposure in solution at 30°C, 1mbar H₂S (a) Test 1 (b) Repeat experiment

A closer look at the corrosion product layer in Figure 148(a.) also revealed a fluffy outer corrosion product layer on top of an iron sulfide layer, especially after three days of exposure. The morphology of the corrosion product supports the argument that the initial iron sulfide layer formed on the sample surface may be due to the precipitation process occurring closer to the sample surface and the upper flaky iron sulfide layer is due to the precipitation process occurring at the bulk.

The XRD pattern (Figure 149) confirmed the corrosion product as mackinawite.

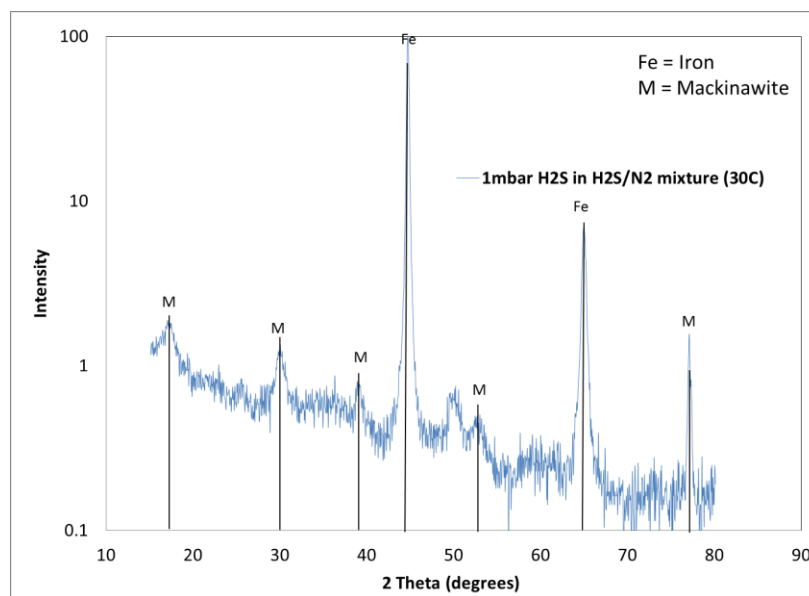


Figure 149: XRD analysis of the X65 carbon steel surface after testing in 1 wt. % NaCl solution, pH 6.00, 30°C and with 1mbar of H₂S

Preliminary experimental results presented above show that the FeS layer was formed in systems under mild agitation. However, the drift in the pH of the solution shows that this solution chemistry was very unstable during the period of specimen exposure. This highlights the need to conduct experiments in a test set-up that enables solution chemistry control.

APPENDIX B: CHARACTERIZATION OF THE MECHANICAL STRENGTH OF MACKINAWITE LAYERS IN THE PRESENCE OF OTHER IRON SULFIDE PHASES

The aim of this study was to evaluate the mechanical properties of a layer comprising of mackinawite and other phases of FeS and make comparison with layers comprising of mackinawite alone. The findings from this study were intended to be a precursor to a study on the protectiveness of other phases of FeS in comparison to mackinawite, especially in flowing conditions.

Equipment

The FeS layer was developed in a 7 L Hastelloy autoclave, as shown in Figure 150.

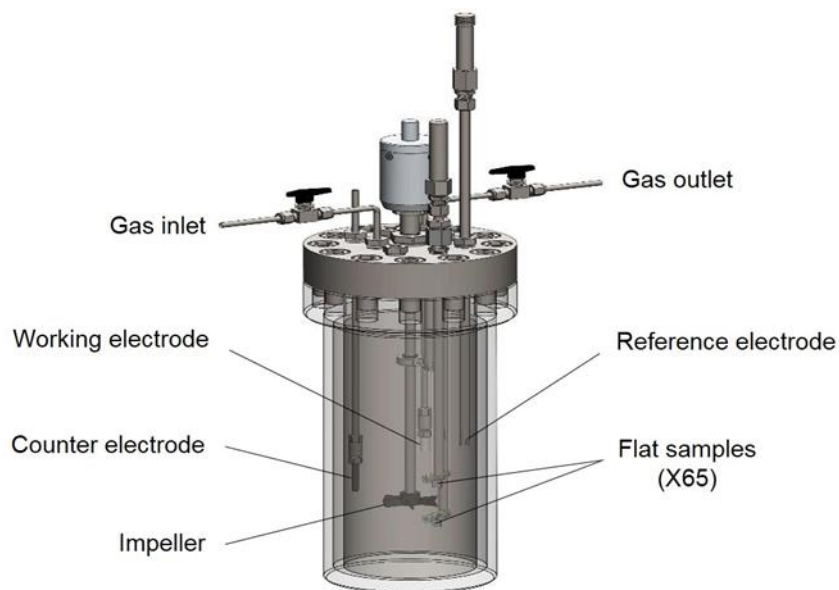


Figure 150: 7L Hastelloy autoclave for FeS layer development (image courtesy of Cody Shafer, ICMT)

The interfacial shear strength of the corrosion product layer was characterized using a mechanical tester.

Test Condition

The test conditions for the current experiment are presented in Table XXI

Table XXI: Test conditions for the development of an iron sulfide layer in the 7L Hastelloy autoclave

Operating Parameter	Specification
Material	UNSG 10180
H ₂ S Partial Pressure	2 bars
Electrolyte	1 wt.% NaCl
Solution pH	4.0
Temperature	80°C,
Exposure Time	2 weeks
Mechanical Testing Technique	Hardness Progressive Load Test Constant Load Tests
Surface Analysis	SEM, EDS, XRD

Procedure

The electrolyte solution (1 wt.% NaCl) was deoxygenated for 2 hours. The pH of the solution was adjusted to the desired initial value obtained from water chemistry calculations. Test specimens were introduced into the test solution and the autoclave was closed. The test solution was sparged for an additional hour. A pressure of 100psi was applied on the autoclave with N₂ gas and the pressure released to a value of 10psi. The cycle of adding nitrogen pressure and its removal was done 3 times to ensure proper deoxygenation of the solution. The autoclave was then put under the desired H₂S

pressure. The H₂S concentration in the gas phase of the system was measured by gas chromatography. The desired temperature and impeller rotation speed (250rpm) were set. At the end of the experiment, the temperature of the autoclave system was cooled to 50°C and the H₂S concentration was measured by gas chromatography in order to compare with initial values. The valve connecting the autoclave to a gas vent was opened and the H₂S gas was released to the combustion chamber. The solution in the autoclave was released into a container with sodium hydroxide crystals in order to scrub the solution of any dissolved H₂S. The autoclave lid was now opened, and the test specimens were extracted. The extracted specimens were rinsed with deoxygenated deionized water, then with isopropanol, and stored in a vacuum desiccator before being characterized.

Mechanical Characterization of FeS layer Developed on UNS G10180

The SEM of the specimen surface and the cross-section of the specimen after exposure to the corrosive environment are presented in Figure 151 (a.) and (b.).

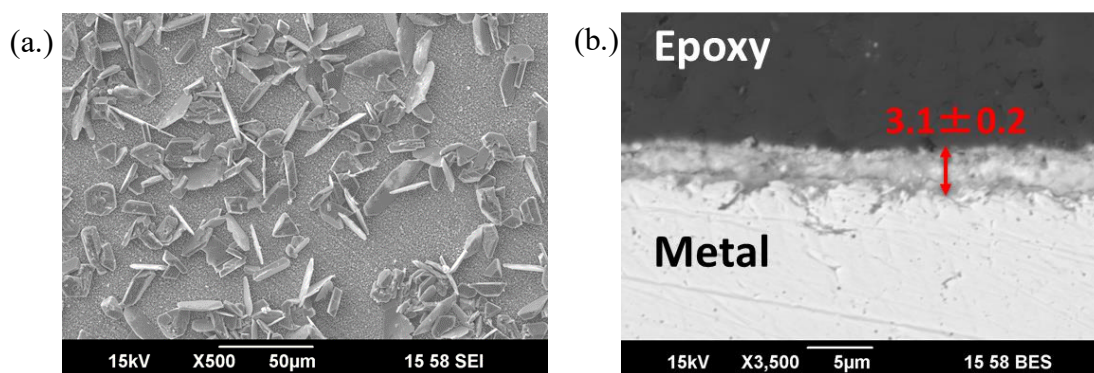


Figure 151: (a.) Surface SEM and (b.) Cross section of UNS G10180 exposed to 1 wt.% NaCl solution with 2 bars H₂S, pH 4.00, 80°C and 2 weeks exposure.

The EDS analysis of the surface presented in Figure 152(a.) detected iron and sulfur as the component of the corrosion product layer confirming it as iron sulfide.

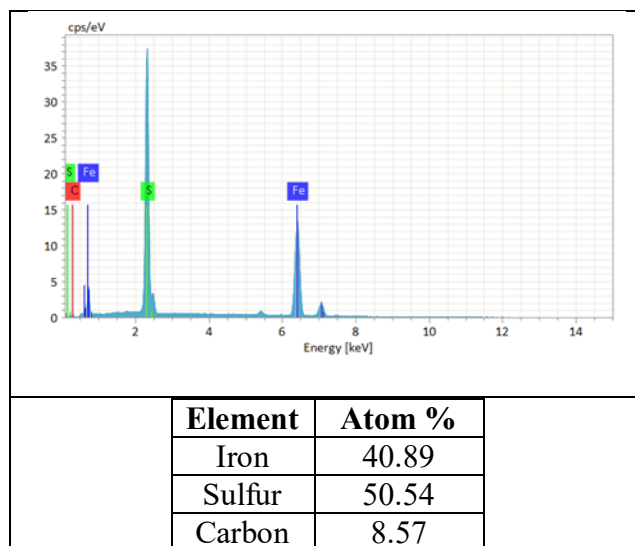


Figure 152: EDS Analysis of iron sulfide layer formed on UNS G10180 exposed to 1 wt.% NaCl solution with 2 bars H₂S, pH 4.00, 80°C and 2 weeks exposure.

The XRD analysis, shown in Figure 153 of the specimen surface confirmed mackinawite with other FeS phases, such as pyrrhotite and troilite. This is in contrast to the mackinawite layers analyzed for their mechanical properties and discussed in Chapter 7.

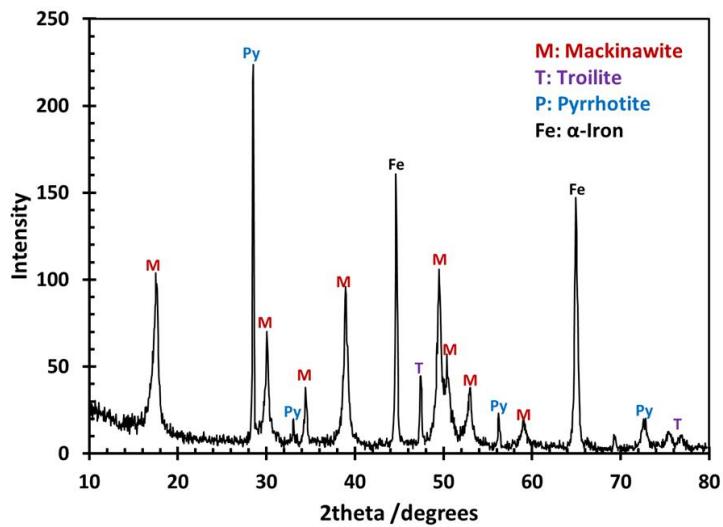


Figure 153: XRD analysis of iron sulfide layer formed on UNS G10180 exposed to 1 wt.% NaCl solution with 2 bar H₂S, pH 4.00, 80°C and 2 weeks exposure

Progressive Load Test

The scratch track from a progressive load test from 0.1mN to 400mN is presented in Figure 154.

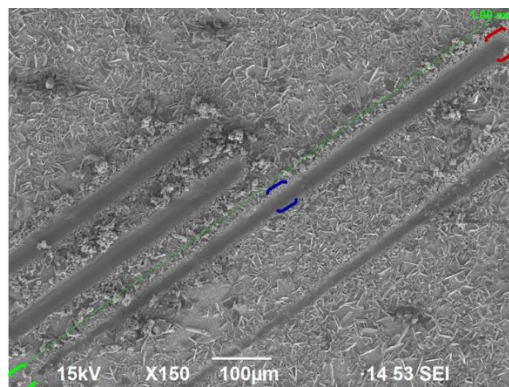


Figure 154: Progressive load test from 0.1mN to 400mN on iron sulfide layers formed on UNS G10180 exposed to 1 wt.% NaCl solution with 2 bar H₂S, pH 4.00, 80°C and 2 weeks exposure

Analyses of the different areas (shown in Figure 155) of the scratch track, corresponding to 800mN, 400mN, and 0.1mN, showed that the critical load for adhesive failure was not achieved.

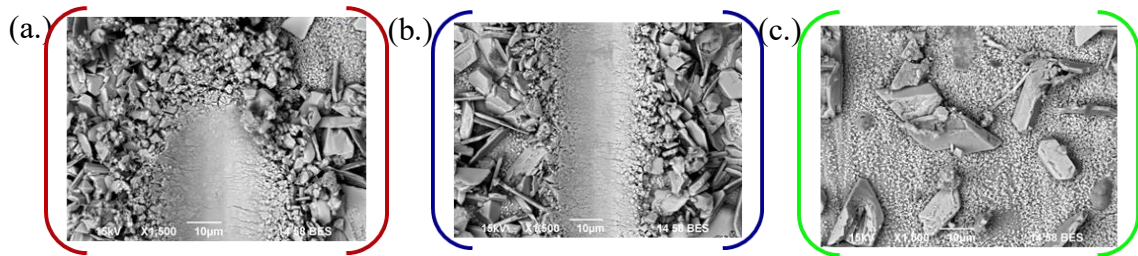


Figure 155: Scratch tracks corresponding to the (a.) 800mN, (b.) 400mN and (c.) 0.1mN from the progressive load scratch test.

Constant Load Tests

The SEMs of the different constant load scratch tests at different constant loads are presented in Figure 156.

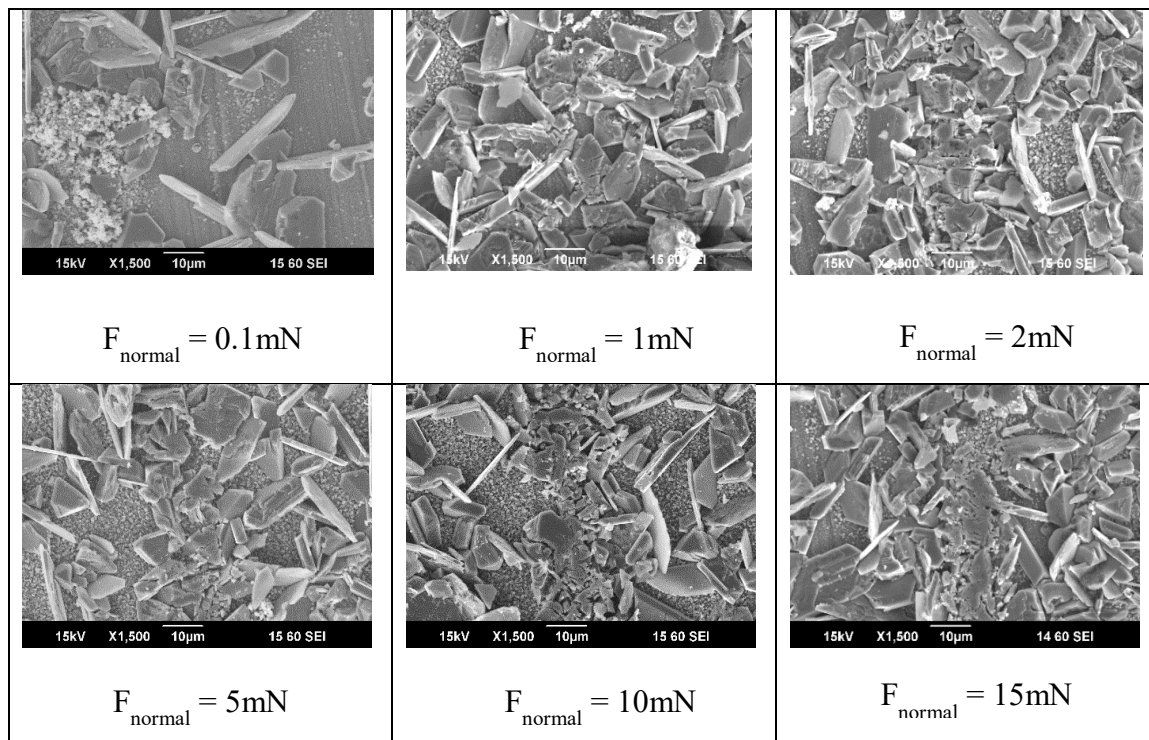


Figure 156: Constant load tests at different normal forces

Figure 156 shows that the pyrrhotite crystals, which constitute the outer layer, was damaged at a normal force of 1mN, while a scratch track was evident at normal force of 10mN corresponding to a shear stress of 37MPa.

The EDS mapping of the scratch test from constant load test conducted at 800mN corresponding to 1.3GPa is shown in Figure 157.

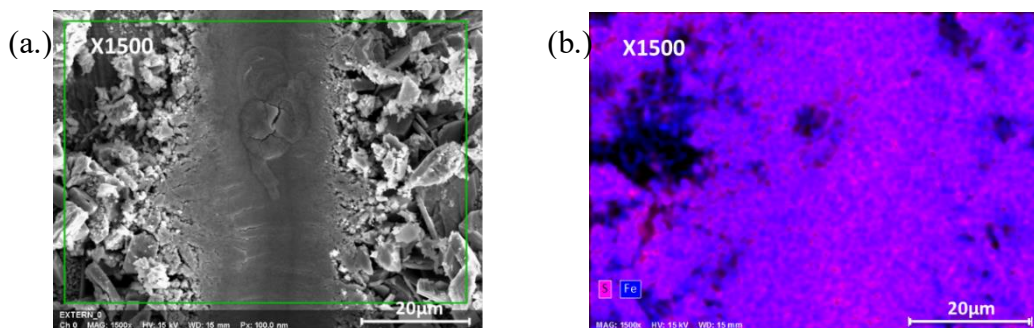


Figure 157: (a.) Scratch track and (b.) EDS mapping of scratch track left by a shear stress of 1.3 GPa on a layer formed on UNS G10180 after 2 weeks exposure to 1wt.% NaCl after exposure to 2bar H₂S, pH 4.00, 80°C

The uniform distribution of Fe and S atoms across the surface suggests that only a cohesive form of failure occurred. Further confirmation of this was achieved by conducting EDS spot analyses on areas inside and outside the scratch track, as presented in Figure 158(a.) and (b.).

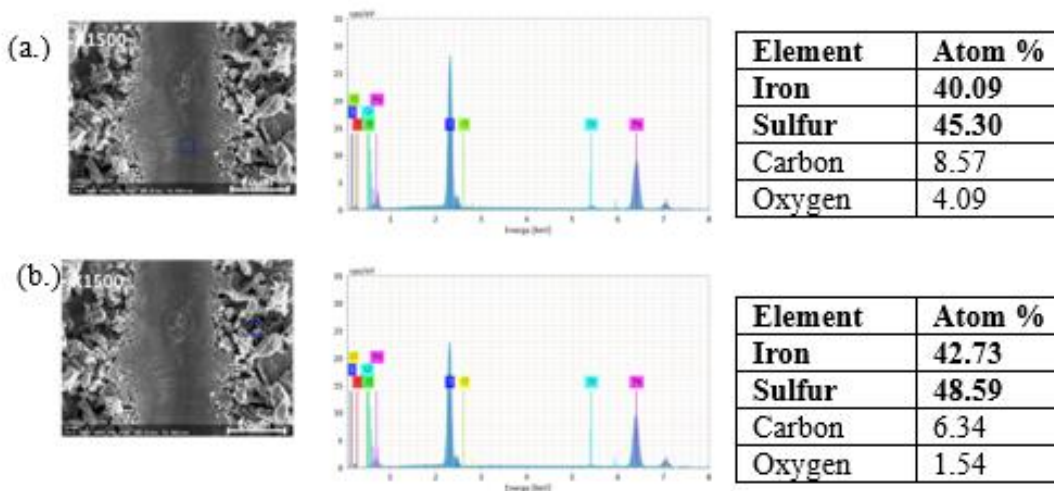


Figure 158: EDS spot analyses on areas inside and outside the scratch track from a shear stress of 1.3GPa on a layer formed on UNS G10180 after 2 weeks exposure to 1wt.% NaCl after exposure to 2 bar H₂S, pH 4.00, 80°C

The results from the current study shows the removal of the outer layer requires a shear stress of 37 MPa while the inner layer required a shear stress above 1.3GPa.

APPENDIX C: MODELLING OF CORROSION RATES

The corrosion prediction model developed by Nesic, *et al.*, [38] was used to test the validity of the corrosion rates measured. This prediction model described H₂S corrosion as a process of two parts: (a.) the electrochemical corrosion process and (b.) the iron sulfide layer formation and growth. More focus is placed on the latter part of the model since the conditions selected in this study correspond to a layer forming condition. In a layer forming condition, the entire corrosion process is affected by the presence of the corrosion product layer which forms a barrier to the diffusion of species from the bulk solution to the metal surface. These changes in surface concentration are described with the following equation [38]:

$$\frac{\partial \varepsilon C_{Surface,j}}{\partial t} = \frac{N_{e,j} - N_{w,j}}{\Delta x} + R_j \quad (84)$$

R_j is the source and sink term for both homogenous and heterogeneous chemical reactions. As shown in Figure 3, $N_{e,j}$ is the flux of species (in mol./m².s), j , from the bulk to the surface. $N_{w,j}$ is the mass flux of species, j , from the surface to the bulk (in mol./m².s). The homogenous reaction in the present conditions involve sulfide species and occurs very fast in comparison to other processes that contribute to the overall corrosion process. The heterogeneous reaction, presented in Equation 30, involve the formation of iron sulfides when the solubility limit of iron sulfide is exceeded.

The precipitation rate of FeS, which occurs when the solubility exceeds 1, can be calculated using the equation [38]:

$$R_{FeS(s)} = e^{48 - \frac{40,000}{RT}} \frac{S}{V} K_{sp,S^2-} (S_{FeS} - 1) \quad (85)$$

R_{FeS} is the precipitation rate of FeS in mol/(m³.s), s/v is the surface per volume ratio of iron sulfide in m⁻¹, S_{FeS} is the saturation value of FeS and $K_{sp,S^{2-}}$ is the solubility limit (mol/L)² of iron sulfide, which can be calculated using the Benning equation[68].

$N_{w,j}$ is the flux of species due to the electrochemical reactions that occur at the metal surface.

$$N_{w,j} = \pm \frac{i_j}{n_j F} \quad (86)$$

Where n_j is the number of electrons and F is the faradays constant. The current density, i_j , is affected by the porosity of the corrosion product layer and calculated as follows:

$$i_j = \varepsilon i_o 10^{\pm \eta/b} \quad (87)$$

The second flux term in Equation 84, $N_{e,j}$ is due to the mass transfer of species from the bulk, through the layer, to the substrate surface, given by:

$$N_{e,j} = k_{T,j} \times (C_{bulk,j} - C_{surface,j}) + k_{T,j} \times \frac{z_j F}{RT} c_{bulk,j} \Delta \Phi \quad (88)$$

The first term in the equation above is the contribution of mass transfer in the bulk to the flux of species. The second term is the contribution of ion electron-migration to the overall flux in the system and is only considered for major species such as Na⁺ and Cl⁻. The mass transfer coefficient, $k_{T,j}$, is the harmonic mean of the mass transfer coefficient through the corrosion product layer and the mass transfer coefficient in the bulk (Equation 37).

The mass transfer coefficient through the corrosion product layer is a function of the layer properties and presented in Equation 38.

The porosity, ε , changes with time and is given by

$$\frac{\partial \varepsilon}{\partial t} = -\frac{M_{FeS}}{\rho_{FeS}} R_{FeS} - CR \frac{\partial \varepsilon}{\partial x} \quad (89)$$

The thickness of the layer, δ_s , also changes with time and is calculated using the following equation:

$$\Delta \delta_s = \frac{\Delta x R_{FeS(s)} M_{FeS} \Delta t}{\rho_{FeS} (1 - \varepsilon)} \quad (90)$$

The mass transfer coefficient through the bulk, $K_{m,j}$, is calculated with the Sherwood correlation for the different flow systems (Equations 50 and 71).

Corrosion rate calculation are carried out in discrete time steps with the initial corrosion rate evaluated in the absence of a layer. The subsequent evolution of the corrosion process is dependent on changes in layer thickness and porosity.



OHIO
UNIVERSITY

Thesis and Dissertation Services